

Academic Press is an imprint of Elsevier  
Linacre House, Jordan Hill, Oxford OX2 8DP, UK  
32 Jamestown Road, London NW1 7BY, UK  
Radarweg 29, PO Box 211, 1000 AE Amsterdam, The Netherlands  
30 Corporate Drive, Suite 400, Burlington, MA 01803, USA  
525 B Street, Suite 1900, San Diego, CA 92101-4495, USA

First edition 2010

Copyright © 2010 Elsevier Ltd. All rights reserved

No part of this publication may be reproduced, stored in a retrieval system or transmitted in any form or by any means electronic, mechanical, photocopying, recording or otherwise without the prior written permission of the publisher

Permissions may be sought directly from Elsevier's Science & Technology Rights Department in Oxford, UK: phone (+44) (0) 1865 843830; fax (+44) (0) 1865 853333; email: [permissions@elsevier.com](mailto:permissions@elsevier.com). Alternatively you can submit your request online by visiting the Elsevier web site at <http://elsevier.com/locate/permissions>, and selecting *Obtaining permission to use Elsevier material*

#### Notice

No responsibility is assumed by the publisher for any injury and/or damage to persons or property as a matter of products liability, negligence or otherwise, or from any use or operation of any methods, products, instructions or ideas contained in the material herein. Because of rapid advances in the medical sciences, in particular, independent verification of diagnoses and drug dosages should be made

#### British Library Cataloguing in Publication Data

A catalogue record for this book is available from the British Library

#### Library of Congress Cataloging-in-Publication Data

A catalog record for this book is available from the Library of Congress

ISBN: 978-0-08-089054-8

ISSN: 0066-4103

For information on all Academic Press publications visit our web site at <a href="http://elsevierdirect.com">elsevierdirect.com</a>
--

Printed and bound in Great Britain

10 11 12 10 9 8 7 6 5 4 3 2 1

Working together to grow  
libraries in developing countries

[www.elsevier.com](http://www.elsevier.com) | [www.bookaid.org](http://www.bookaid.org) | [www.sabre.org](http://www.sabre.org)

ELSEVIER

BOOK AID  
International

Sabre Foundation

## CONTRIBUTORS

**Zoltán Gáspári**

Laboratory of Structural Chemistry and Biology, Institute of Chemistry, Eötvös Loránd University, Pázmány Péter sétány 1/A, Budapest, Hungary

**Lana Kaiser**

Agilent Technologies, Walnut Creek, California, USA

**Flemming H. Larsen**

Department of Food Science, Quality and Technology, University of Copenhagen, Rolighedsvej 30, Frederiksberg, Denmark

**András Perczel**

Laboratory of Structural Chemistry and Biology, Institute of Chemistry, Eötvös Loránd University, Pázmány Péter sétány 1/A, Budapest, Hungary; Protein Modeling Group HAS-ELTE, Institute of Chemistry, Eötvös Loránd University, Budapest, Hungary

**K. P. Ramesh**

Department of Physics, Indian Institute of Science, Bangalore, India

**Brian J. Soher**

Department of Radiology, Duke University Medical Center, Durham, North Carolina, USA

**Karl Young**

Department of Radiology, University of California San Francisco/VAMC San Francisco, USA

**John A. Weil**

Department of Chemistry, University of Saskatchewan, Saskatoon, Canada

## PREFACE

It is my pleasure to present Volume 71 of Annual Reports on NMR, which consists of a collection of reports on advances in many scientific areas due to the application of NMR techniques. The volume commences with an account of 'Magnetic Resonance of Systems with Equivalent Spin-1/2 Nuclides' by J.A. Weil; 'Protein Dynamics as Reported by NMR' is presented by Z. Gaspari and A. Perczel; 'Virtual MRS: Spectral Simulation and its Applications' is covered by B.J. Soher, K. Young and L. Kaiser; F.H. Larsen reports on 'Simulation of Molecular Motion of Quadrupolar Nuclei in Solid State NMR'; finally, 'NMR Studies of Disorder in Condensed Matter Systems' is discussed by K.P. Ramesh. My thanks are due to all of these reporters for their interesting and timely contributions.

G. A. Webb  
*Royal Society of Chemistry  
Burlington House  
Piccadilly, London, UK*

## Magnetic Resonance of Systems with Equivalent Spin-1/2 Nuclides

**John A. Weil**

---

<b>Contents</b>		
	1. Preamble	2
	2. Introduction	5
	3. Exchange Actions and Interactions	5
	3.1. Electrons	5
	3.2. Nuclei	6
	4. Equivalent Nuclides within a Molecular Species	6
	4.1. NMR in gases	6
	4.2. NMR in non-viscous liquids	7
	4.3. NMR in crystalline solids	8
	5. The Effects of Motions	8
	5.1. Internal molecular rotations and interchanges	8
	5.2. Intermittent crystal rotations	8
	5.3. Random molecular rotations	9
	5.4. Sample rotations	9
	6. Exchange Degeneracy	10
	7. Spin-Spin Interactions of Sets of Distinct Particles	10
	7.1. Basics 1	10
	7.2. Basics 2	12
	8. Selected Molecules with Equivalences	12
	8.1. Molecular hydrogen	12
	8.2. Methane	14
	8.3. The hydrazines	14
	8.4. Benzene and the C <sub>6</sub> H <sub>6</sub> isomers	15
	8.5. Cyclopropane	17
	8.6. Fluxional molecules	17
	9. Spin-Hamiltonian Parameters	18
	9.1. Zeeman term	19
	9.2. Coupling parameters	21

Department of Chemistry, University of Saskatchewan, Saskatoon, Canada

Annual Reports on NMR Spectroscopy, Volume 71  
ISSN 0066-4103, DOI: 10.1016/S0066-4103(10)71001-2

© 2010 Elsevier Ltd.  
All rights reserved.

9.3. Reported NMR measurements of matrix $\mathbf{g}_n$ and/or $\mathbf{J}$ properties	22
10. Spectral Degeneracy	23
Acknowledgement	23
References	29

## Abstract

The terms 'equivalent' and 'exchange' are defined and discussed, beginning at a fairly elementary level. In contemplating the fields of NMR and EPR spectroscopies, we pursue the concept that the principles and pursuits of one give us access to those of the other. It is discussed herein that for  $n > 2$  nuclei, the NMR spectra have a more complicated form than anticipated from the usual oversimplified analysis, the latter predicting  $n + 1$  multiplet lines with intensity ratios given by the coefficients of the binomial expansion. Discussion of the underlying theory, invoking exchange degeneracy and the appropriate permutation group theory, is included or referred to. Numerous molecular examples featuring equivalence of nuclides are presented. A discussion of the parameter matrices and 'tensors' encountered in magnetic resonance spectroscopy is included, with attention paid to their measurability and symmetry properties.

**Key Words:** NMR, EPR, Spin–spin coupling, Equivalent nuclides, Spin-Hamiltonian energies and eigenstates, Exchange degeneracy.

## 1. PREAMBLE

We begin by stating details of our assumptions, definitions and nomenclature, largely summarizing information to be found in the standard textbooks.<sup>1–7</sup>

- 1.1 We shall restrict ourselves to electronic ground-state properties of the chemical species to be encountered. This implies the lowest energy manifold of spin states as well as lowest energy angular momenta (herein: spins). We shall deal only with nuclides having spin of  $1/2$ . We shall invoke only ordinary quantum mechanics, staying clear of the relativistic aspects as much as possible. This includes, of course, the curvature of our space.
- 1.2 The angular momentum variables all enter as quantum-mechanical operators, whose eigenvalues may be measurable.
- 1.3 The total angular momentum of a particle is given via its square: the expression  $[J(J+1)](h/2\pi)^2$ , where  $2J$  is a non-negative integer. We shall call  $J$  the primary spin quantum number. The angular-momentum vector  ${}^{\text{op}}\mathbf{J}$  cannot be measured with exactness; only its magnitude  $[J(J+1)]^{1/2}(h/2\pi)$  and one  $M_J(h/2\pi)$  of its spatial components can be simultaneously known. For nuclides,  $J$  is denoted by  $I$ , and for electrons  $S$ . We ignore relativistic situations (appreciable spin–orbit coupling where these are not good quantum numbers). In what follows, every angular momentum will be taken as unit-less.

- 1.4 The other quantum number,  $M_J$ , describing the same angular momentum is of course its projection in some direction, called the quantization axis, which is chosen for our convenience. There are  $2J + 1$  values allowed for the secondary spin quantum number:  $-J, -J + 1, \dots, J - 1, J$ . One can usefully think of a classical analogue of  ${}^{\text{op}}\mathbf{J}$ : vector  $\mathbf{J}$ , as precessing about the axis of quantization.
- 1.5 The word ‘particle’ (e.g. nuclide or electron) is used routinely, and has ascribed to it measured properties such as total energy  $E$ , as well as spin parameters  $J$  and  $M_J$ . However its actual definition is fraught with danger (particle/wave conundrum, and its sub-structure mystery), and the concept of its exact size is nebulous. Its electrical charge too does not bear too close a scrutiny, because of its potential sub-structure composed of other smaller ‘particles’. It seems clear that all the particles in our Universe interact, at some range, to some extent.
- 1.6 We shall not need to explicitly consider herein the linear momentum of any particle.
- 1.7 The total energy  $E$  of a particle too can never be known exactly, since there always are unknown additive contributions to it, and also if there is any probability that it can change to some other energy state: leading to ‘lifetime’ broadening of the energies of both states.
- 1.8 The property ‘magnetic moment’  $\mu$  too has similar limitation. A non-zero such dipolar moment implies presence of charge within the particle (even though its total charge may be zero, e.g. the neutron). We can consider only ‘paramagnetism’, and hence take  $\mu$  as proportional to the angular momentum  $J$ . Thus the moment too can be thought of as a vector,  ${}^{\text{op}}\boldsymbol{\mu}$ , known via its magnitude and one projection. As indicated, it too in fact is a quantum-mechanical operator.

The proportionality can be expressed as  ${}^{\text{op}}\boldsymbol{\mu} = \pm \beta \mathbf{g} \cdot {}^{\text{op}}\mathbf{J}$ , where  $\beta$  (called the magneton, in usual units J/T) is a collection of natural constants, and  $\mathbf{g}$  is a  $3 \times 3$  dimensionless real matrix in three-space. Some authors refer to  $\mathbf{g}$  as a second-rank tensor, but in fact (strictly speaking) it is not.<sup>8</sup> For a detailed discussion, consult [Section 9](#) below. We shall not use the term ‘tensor’, unless this is unavoidable.

For all electrons,  $\beta_e \equiv |e|(\hbar/2\pi)/(2m_e)$  called the Bohr magneton, and for free electrons:  $\mathbf{g} = g_e \mathbf{U}_3$ , where  $\mathbf{U}_3$  is the  $3 \times 3$  unit matrix. Here  $m_e$  is the mass of the electron.

For all nuclides,  $\beta_n \equiv |e|(\hbar/2\pi)/(2m_p)$  called the nuclear magneton. Here  $m_p$  is the mass of the proton. For bare unshifted nuclides,  $\mathbf{g} = g_n \mathbf{U}_3$ . The precession frequency, called the Larmor frequency, is defined to be  $g\beta B/\hbar$ , where  $B$  is the magnitude of the external magnetic field acting as the quantization axis for the spin.

The nuclear paramagnetism too is given via a matrix  $\mathbf{g}$ . When a nucleus experiences a chemical shift, due to neighbouring electrons, one writes  $\mathbf{g}_n = {}^{\circ}\mathbf{g}_n(\mathbf{U}_3 - \boldsymbol{\sigma})$ , where  $\boldsymbol{\sigma}$  is called the shift matrix. The latter represents the effect of the neighbouring electrons circulating in applied field  $\mathbf{B}$ , and tending to oppose it (hence the minus sign). It is important to properly define the parameters related to nuclear shielding and chemical shift, as discussed by Jameson.<sup>9</sup>

## 1.9 Parameter matrices, their principal values and directions

The principal values constitute the quantum-mechanical (energy, interaction) information about the spin system at hand. The principal directions are orientational information, and in fact are not true directions, since they have no sense of pointing, that is no polarity. Their axis length is for convenience taken to be +1, that is normalized. Any principal value and any axis component may have either algebraic sign, to be measured.

The Zeeman splitting parameter matrices are called  $\mathbf{g}$  both for electrons and nuclei. {However, for electrons, it is not customary to depict the deviations from  $g_e$  by expression  $\mathbf{g} = g_e(\mathbf{U}_3 - \boldsymbol{\sigma})$ .} Matrices  $\mathbf{g}$  can always be taken as real symmetric, to describe measured data, and it follows that then there exists a special spatial Cartesian coordinate system, the principal axis system (determined by the local symmetry, if any). Here  $\mathbf{g}$  is diagonal, exhibiting its principal values (e.g. in EPR, see [Ref. 7](#), Chapter 4). However, from theory, the ‘true’ matrix  $\mathbf{g}$  can turn out in some situations to be non-symmetric.<sup>10</sup>

The same considerations hold true for the exchange parameter matrices  $\mathbf{J}$ , as well as for the hyperfine matrices  $\mathbf{A}$  encountered in EPR. An example of a measurement of parameter sets  $\mathbf{J}$  can be found in [Ref. 11](#).

- 1.10 For nuclei with spin  $> 1/2$ , there is the whole field of nuclear quadrupole spectroscopy, basically zero-field NMR, measuring local electric-field gradients and arriving at quadrupole parameter matrices  $\mathbf{P}$ . Here too the equivalence or not of nuclei is important.
- 1.11 The reader can find a discussion of the relationship of magnetic resonance parameter matrices and symmetry-related sites to the possible crystal symmetries in an available review article.<sup>12</sup>
- 1.12 One way of dealing with the symmetry of the molecular species considered is to realize that, within any interval of time, there never is anything but a trivial symmetry (identity operation only). In other words, every part of every molecular species is continuously moving, and there is exact zero probability of catching it to the last decimal place in its ‘equilibrium’ position.

Furthermore, this seemingly suicidal viewpoint is valid not only if any motion of sub-particles is occurring but also when all the interactions with the rest of the universe are brought in. Also, in every sample containing numerous molecules, there are impurities and other defects, and of course the finite size of the sample yields surface effects—observable in some approximation.

Perhaps, it will be useful to the reader to realize that the perversions and predilections found in the present chapter arise since the author is not a typical NMR guru, but rather has primarily practiced solid-state EPR spectroscopy. On the other hand, he has accumulated appreciable liquid-solution NMR experience. The author, together with S.M. Nokhrin and D.F. Howarth, has teamed on some studies of equivalence of nuclei as implying certain subtle phenomena in EPR.<sup>13,14</sup>

## 2. INTRODUCTION

Despite the presence of the above-cited limitations, one can make excellent progress in understanding magnetic resonance phenomena when one ignores some of those realities.

- 2.1 We shall safely consider certain chemical species as composed of particles: electrons and nuclides.
- 2.2 We may or may not explicitly consider motions of the species and their components. Thus the 3D symmetry of the set of particles located in certain spatial positions will be used.
- 2.3 Classical viewpoints ignoring quantum-mechanical aspects are often fruitful, for example the idea of precession of the particles and/or their spins.
- 2.4 Motional magnetism, caused by rotation, vibration or translation of charged particles will be ignored. Thus all diamagnetism aspects will enter only implicitly. Thus we will not focus on static magnetic susceptibility theory (e.g. magnetizability) or measurements.
- 2.5 We shall herein be dealing with magnetic resonance spectroscopy. When unpaired-electron spins and nuclear spins both are present, one cannot always distinguish between EPR and NMR; for example, see atomic hydrogen at sufficiently low applied magnetic fields.<sup>15</sup>
- 2.6 Presumably it will be clear to the reader than in 21st century NMR, computerology has so advanced and is readily available, so that most parameters can be adequately estimated from theory.
- 2.7 We shall not be shy in citing classical works going back to the early decades of magnetic resonance spectroscopy.

## 3. EXCHANGE ACTIONS AND INTERACTIONS

The term 'exchange' so frequently used in quantum mechanics and magnetic resonance spectroscopy is often allowed to be ill-defined. We will attempt to rectify this situation. For instance, the question lingers for 'exchange of particles': exchange for what? Clearly the word 'interchange' is more apt. With quantum-mechanical identical particles, interchange in fact means interchange of the labels that the observer has attached to the particles, and not actual interchange of the particles themselves: See [Ref. 16](#), Chapter 18.

### 3.1. Electrons

The individual electrons in any pair (labelled  $i$  and  $j$ ) are completely indistinguishable. A good description of the interchange phenomenon and theory may be found in [Ref. 17](#) (Chapter 4, and beyond), as well as in [Ref. 16](#). The so-called exchange interaction energy is merely a part of the total coulomb repulsion energy between the electrons, and involves the spatial orbitals.



In addition, the electron spin system also exhibits an exchange energy, often called the Heisenberg exchange, denoted by  $J_o \text{ } ^\text{op}\mathbf{S}_i \bullet \text{ } ^\text{op}\mathbf{S}_j$  where  $J_o$  represents a coulombic repulsion term (Ref. 7, Section 6.2.1) not to be confused with the primary angular momentum quantum number  $J$ . In general, the scalar  $J_o$  can be anisotropic, that is generated via a  $3 \times 3$  matrix.

Higher terms, biquadratic in the spin operators  $^\text{op}\mathbf{S}$ , also can occur.<sup>18</sup> Spin–spin anisotropic interactions of the type  $\mathbf{D} \bullet [\mathbf{S}_1 \otimes \mathbf{S}_2]$  are known for electrons,<sup>19</sup> where  $\mathbf{D}$  is a parameter vector; this expression is the antisymmetric part of the most general bilinear spin–spin interaction. Observation of a field-induced magnetization in  $\text{SrCu}_2(\text{BO}_3)_2$  via  $^{11}\text{B}$  NMR has revealed the presence of such an interaction therein.<sup>20</sup>

### 3.2. Nuclei

Nuclei are of course more compact in space and more massive than electrons are, and slower in typical speeds, and hence do not approach each other as readily. While individual nuclides of the same isotopic species are indistinguishable, this aspect is not as important with regard to actual physical approach and interchange.

However, indirect magnetic exchange interactions between nuclear spins occur readily, and yield much information. This type of nuclear spin–spin interaction is mediated by the intervening electrons (Ref. 3, Chapter 5), via magnetic hyperfine interactions with the members of the electron pairs. The interaction parameter  $J$  generally used is called the spin–spin coupling parameter. It does not depend significantly on any applied field  $\mathbf{B}$ . This ‘indirect’ spin–spin interaction is generally taken to be isotropic, unlike the direct magnetic dipolar interaction between the nuclear spins—which most often is negligibly small, especially since it is effectively diminished by any molecular motions present. Generally,  $J$  does depend on the temperature of the medium.

Of course, as is well known, the indirect nuclear interaction is the cause of the multiplet structure observed in most NMR spectra.

## 4. EQUIVALENT NUCLIDES WITHIN A MOLECULAR SPECIES

Just as with the concept of molecular symmetry discussed above, the reality is that no two nuclei in any molecule can ever be caught as being exactly equivalent. However, at usable time scales, the concept of equivalence is useful and powerful. A modest list of some molecules containing ‘equivalent’ nuclei can be found in Appendix 1, together with references.

### 4.1. NMR in gases

Studies of atomic and molecular species in the gas-phase are not uncommon, and this research field has been quite widely reviewed.<sup>21–24</sup> One attractive feature is that extrapolation to zero pressure yields information about isolated species. Of course

anisotropic properties tend to be averaged out, but isotropic spin–spin interactions are detected and can give information about equivalence (or not) of nuclides. For the latter, the  $^1\text{H}$  DNMR example of NN-diethylacetamide is edifying [Ref. 24, Figure 7]. Other good examples, for which all shift and spin–spin parameters have been measured as a function of gas density, are  $\text{CH}_2\text{F}_2$ <sup>25</sup> as well as  $\text{BF}_3$ .<sup>26</sup>

## 4.2. NMR in non-viscous liquids

Here then, the molecular species can be deemed to be tumbling rapidly enough so that we need consider only the time average value of the shift matrix  $\sigma$ , that is its isotropic component. Usually the systems are so dilute that the molecules can be considered not to ‘see’ each other.

Following Abragam,<sup>1</sup> let us consider nuclides all of the same isotopic variety and let us demand in NMR that they have identical chemical shifts, presumably over a very appreciably wide temperature range. These nuclei will be called ‘isochronous’, since they will all have the same Larmor frequency.

The chemical shift (in Hz) of any particular nuclide is proportional to its  $g_n$  value. Thus, different isotopes, such as  $^1\text{H}$  and  $^2\text{H}$ , cannot be isochronous. Also, it is worth noting that replacing one isotopic species by another at some distance from a given nuclide can affect the location of the latter’s NMR line.<sup>27</sup>

Now consider any set of isochronous spins within a molecule. These will be called ‘equivalent’ if and only if (iff) each member of the set has the same sets of coupling parameters  $J$  (conceivably with different values: see example below) with all the other spins. Abragam gives examples: In difluoromethane  $\text{CH}_2\text{F}_2$  (equilibrium molecular point symmetry group  $G=\text{C}_{2v}$ ), the protons are equivalent (and so are the fluorine nuclides). In 1,1-difluoroethylene  $\text{C}_2\text{H}_2\text{F}_2$  ( $G=\text{C}_{2v}$ ), there are no equivalent nuclides since each  $^{19}\text{F}$  has different couplings with the two protons, and vice versa. In bromine pentafluoride  $\text{BrF}_5$  ( $G=\text{C}_{4v}$ ), there are two types of fluoride: four F anions form a square base and the other is at the apex of a pyramid occupied by the Br. The four are equivalent, even though the  $J$  linking to adjacent F differs from the  $J$  to F across the square.

In other later works (e.g. Ref. 5), the terms ‘isochronous’ and ‘anisochronous’ are often replaced by the usage ‘chemically equivalent’ and ‘chemically non-equivalent’. The above-cited conditions on the  $J$  interactions have led to the nomenclature ‘magnetically equivalent’ and ‘magnetically non-equivalent’. Note that isochronous nuclei are not necessarily chemically equivalent.

Nuclei are chemically equivalent if they can be interchanged by a non-trivial symmetry operation. Nuclei interchangeable by a pure rotation ( $C_n$ ,  $n=2, 3, 4, \dots$ ) are called ‘homotopic’. Nuclei related only by a centre (i) of inversion or by a plane ( $\sigma$ ) of symmetry are said to be ‘enantiotopic’ (also ‘prochiral’).

A great deal of work has been done in measuring chemically equivalent and inequivalent nuclei, using complex and sophisticated pulse techniques, often while rotating the samples (e.g. MAS: magic angle spinning, a technique developed ca. 50 years ago). We shall not herein pay attention to the details of the actual instrumental techniques.

### 4.3. NMR in crystalline solids

For experiments on molecular crystals, [Ref. 28](#) distinguished the following three cases. ‘exchange’ between:

- (a) magnetically equivalent nuclei, that is between members of pairs of nuclei inter-related by lattice translation and/or spatial inversion.
- (b) congruent nuclei, that is nuclei related by other than the operations cited in category (a).
- (c) inequivalent nuclei.

An interesting example is available of inequivalent nuclei becoming equivalent on raising the temperature and going through a phase transition, reversibly. This occurs in squaric acid  $C_4(O)_2(OH)_2$ , studied by single-crystal  $^{13}C$  NMR,<sup>29</sup> and later (2004) also by  $^{17}O$  NMR. Here, MAS was used to narrow the lines sufficiently to observe the changes in the isotropic parts of the chemical-shift matrices. The phase transition occurs at 373 K.

## 5. THE EFFECTS OF MOTIONS

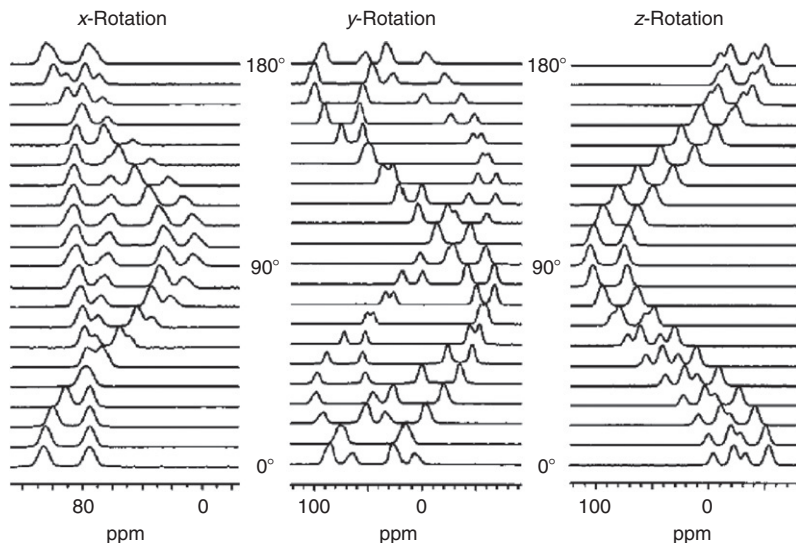
Of course, all multi-atomic species are actively vibrating, usually at frequencies much higher than those of nuclear magnetic effects. Thus NMR generally measures parameters time-averaged over vibrations. We shall not deal with this aspect herein.

### 5.1. Internal molecular rotations and interchanges

In molecular species, whether individual or embedded in a liquid or solid, internal motions can occur. For instance, entities such as phenyl or methyl groups or of course hydrogens, can go on and off the main frame and possibly interchange. Furthermore, even if they stay bonded in place, their environment can change. For example, consider the picryl protons in molecule 2,2'-diphenyl-1-(2,4,6-trinitrophenyl)hydrazine, in liquid solution, which at low temperatures yields an AB spectrum (two pairs of NMR lines).<sup>30</sup> At sufficiently high temperatures, hindered internal rotations within the molecule occur sufficiently frequently (i.e. cause the environment of the A and B protons to interchange sufficiently frequently) that A and B appear to be chemically equivalent—yielding a single  $^1H$  line. Thus equivalence of nuclei can be a time-average phenomenon. Other examples are readily available: for example see [Ref. 3](#), Chapter 6.

### 5.2. Intermittent crystal rotations

Single-crystal EPR and NMR measurements involve spectral measurement at fixed orientations relative to the applied magnetic field **B**, and rotating the crystal (about some selected axis by set angles) between such measurements. Then ‘road maps’ can be constructed of line positions (or intensities) versus the positional



**Figure 1** Three line-position and line intensity roadmaps as a function of rotation angle (deg), for rotations about three orthogonal rotation axes, obtained from solid-state  $^{31}\text{P}$  cross-polarization (CP) NMR spectra at fixed magnetic fields of 4.7 T, for single-crystals (space group  $C2/m$ ) of TMPS (tetramethyldiphosphine sulfide). One sees the spectra from two site types occurring in abundance ratio 1:2, each with a spin-spin doublet structure. Taken from Ref. 31.

angles. Figure 1 gives an example of such experimental measurements. It is from such data that the parameter matrices can be obtained.

### 5.3. Random molecular rotations

In liquid samples (and in gases), the individual molecules rotate randomly (above cryogenic temperatures) with frequencies large compared to those of nuclear magnetic effects. Then each parameter matrix present can be taken as reduced to a single parameter (times the  $3 \times 3$  unit matrix), and of course the sample becomes effectively isotropic.

### 5.4. Sample rotations

Often, in liquid-phase as well as in single-crystal NMR work, the samples are deliberately spun, often at special orientations (magic angle) relative to **B**. This will average out dipolar interactions, often narrowing the observed lines by substantial amounts. For example, see Ref. 3, Section 7.10 and Ref. 4, Chapter 8. Under some circumstances, additional lines (spinning sidebands) are generated by the MAS technique.<sup>32–34</sup>

The paper by Jeschke et al.<sup>32</sup> deals with single-crystal NMR of  $^{31}\text{P}$  ( $I=1/2$ , 100% natural abundance) of  $\text{P}_4\text{O}_{10}$ , following on the earlier polycrystalline

study.<sup>35</sup> This oxide has space group R3c, proper rotation group  $D_3$ , and hence is trigonal with six molecules per standard unit cell. The local equilibrium symmetry of each molecule turns out to be  $T_d$  (providing an overall  $A_3B$  NMR system). Thus one can visualize a basis of three  $P(5+)$  equivalent atoms with another slightly different  $P(5+)$  on the three-fold axis above that plane. The word ‘equivalent’ here implies identical sets of principal values of the chemical-shift parameter matrix  $g_n$ , which in fact are uniaxial. However, the unique principal axes point in three different directions, along P–O bonds. Each P is bonded to four oxygen anions, one being a terminal double bond. There are no P–P bonds. The major contribution of this chapter is the careful examination of the MAS frequency, relative to the chemical-shift magnitude(s), and the effects of the spinning on the NMR lineshape. There is no evidence of fluxional motions interchanging the P cations, unlike the situation in  $PF_5$  cited below (see [Section 8.6](#)).

## 6. EXCHANGE DEGENERACY

The concept of ‘exchange degeneracy’ is of appreciable import herein (see [Section 7.1](#) below). Baym ([Ref. 16](#), p. 391) defines it by considering the permutations  $P$  among a set of identical particles as applied to a Hamiltonian operator  ${}^{\text{op}}H$  symmetric in these. Various of the different energy eigenstates of  ${}^{\text{op}}P {}^{\text{op}}H$  will be degenerate, with such superpositions not affected by Zeeman interactions.<sup>13</sup>

## 7. SPIN–SPIN INTERACTIONS OF SETS OF DISTINCT PARTICLES

### 7.1. Basics 1

In EPR spectroscopy, the isotropic part of the hyperfine spectrum arising from the interaction between an unpaired electron and a set of  $n$  equivalent nuclei is given by spin-Hamiltonian term  $A {}^{\text{op}}\mathbf{S} \cdot ({}^{\text{op}}\mathbf{I}_1 + {}^{\text{op}}\mathbf{I}_2 + \cdots + {}^{\text{op}}\mathbf{I}_n)$ . This yields line positions of the multiplet and relative intensities to first approximation following the multinomial scheme (Pascal triangle), as depicted in [Table 1](#), taken from [Ref. 7](#), p. 61; Also note our [Appendix 2](#).

In complete analogy with this, for a nucleus with spin  $I_0$ , interacting with a set of  $n$  equivalent other nuclei, the spin-Hamiltonian term is  $J {}^{\text{op}}\mathbf{I}_0 \cdot ({}^{\text{op}}\mathbf{I}_1 + {}^{\text{op}}\mathbf{I}_2 + \cdots + {}^{\text{op}}\mathbf{I}_n)$ , and the same table applies to yield the spin–spin multiplet (see [Ref. 36](#), p. 247, and [Ref. 5](#), p. 26) for nuclear spins  $I = 1/2$ .

The extension to higher spin is known.<sup>37</sup>

The above widely accepted notions using the Pascal triangle turn out to be not quite quantitative, as will now be discussed.

The situation has been elucidated in a series of recent papers: ‘Magnetic resonance in systems with equivalent spin-1/2 nuclides’.<sup>13,14,38,39</sup> These works deal with EPR examples, that is each with an unpaired electron exposed to a set of  $n$  equivalent  $I = 1/2$  nuclei. For our present purpose, we can deem the electron to have been replaced by some spin-bearing nucleus to be examined by NMR.

**TABLE 1** Relative line positions and relative intensities of first-order multiplets arising from indirect coupling between a spin-bearing nucleus and a set of  $n$  equivalent other nuclei having spin  $I$

A		$I_i = 1/2 \ (i = 1, 2, \dots, n)$									
No. of nuclei $n$	No. of lines $2I + 1$	First-order line positions/ $s_0$ $M_I$							Binomial intensity ratios		
0	1	0							1		
1	2	$\overline{1/2} \ 1/2$							1 \ 1		
2	3	$\overline{1} \ 0 \ 1$							1 \ 2 \ 1		
3	4	$\overline{3/2} \ \overline{1/2} \ 1/2 \ 3/2$							1 \ 3 \ 3 \ 1		
4	5	$\overline{2} \ \overline{1} \ 0 \ 1 \ 2$							1 \ 4 \ 6 \ 4 \ 1		
5	6	$\overline{5/2} \ \overline{3/2} \ \overline{1/2} \ 1/2 \ 3/2 \ 5/2$							1 \ 5 \ 10 \ 10 \ 5 \ 1		
6	7	$\overline{3} \ \overline{2} \ \overline{1} \ 0 \ 1 \ 2 \ 3$							1 \ 6 \ 15 \ 20 \ 15 \ 6 \ 1		
⋮	⋮	⋮							⋮		
⋮	⋮	⋮							⋮		
⋮	⋮	⋮							⋮		

B		$I_i = 1 \ (i = 1, 2, \dots, n)$									
No. of nuclei $n$	No. of lines $2I + 1$	First-order line positions/ $s_0$ $M_I$							Multinomial intensity ratios		
0	1	0							1		
1	3	$\overline{1} \ 0 \ 1$							1 \ 1 \ 1		
2	5	$\overline{2} \ \overline{1} \ 0 \ 1 \ 2$							1 \ 2 \ 3 \ 2 \ 1		
3	7	$\overline{3} \ \overline{2} \ \overline{1} \ 0 \ 1 \ 2 \ 3$							1 \ 3 \ 6 \ 7 \ 6 \ 3 \ 1		
4	9	$\overline{4} \ \overline{3} \ \overline{2} \ \overline{1} \ 0 \ 1 \ 2 \ 3 \ 4$							1 \ 4 \ 10 \ 16 \ 19 \ 16 \ 10 \ 4 \ 1		
⋮	⋮	⋮							⋮		
⋮	⋮	⋮							⋮		
⋮	⋮	⋮							⋮		

Triangles displaying the relative EPR line positions and intensities arising from the interaction of an electron-spin moment with the spin moments from  $n$  equivalent nuclei, each with spin  $I_i$ . The composite spin  $I$  is a sum over all the individual spins  $I_i$ . (a)  $I_i = 1/2$ ; (b)  $I_i = 1$ . The right-hand triangles represent the coefficients in the expansion of  $[1 + x + x^2 + \dots + x^{2I_i}]^n$ . The triangle for  $I_i = 1/2$  is usually attributed to Blaise Pascal. Note that the sum across any row is  $(2I_i + 1)^n$  and that every non-peripheral integer is the sum of the  $2I_i + 1$  integer closest above it. From Ref. 7.

The above papers tackle the problem by use of group theory, that is the permutation groups  $P_n$  associated with interchanging the equivalent nuclei. It turns out that certain energy degeneracies are in place for  $n > 2$ , fewer than at first expected, which are not lifted by any external magnetic field. Thus not all states assumed as being degenerate in the Pascal view actually are so. Thus certain splittings of the

magnetic resonance spectra are present, although these may be small and difficult to discern. This too is so for the NMR situation.

## 7.2. Basics 2

It has been shown from theory, in a classic pioneering paper by Gutowsky, McCall and Slichter,<sup>40</sup> that NMR multiplets are unaffected by the interactions between structurally equivalent nuclides within any molecule. Such homonuclear couplings of course are present, but their contributions to the spectrum cancel. The proof of this theorem is given for orthogonal conditions  $\mathbf{B}$  along  $\mathbf{z}$  and  $\mathbf{B}_1$  along  $\mathbf{x}$ , with interaction Hamiltonian for the coupling of form  $J_{ij}\mathbf{I}_i \cdot \mathbf{I}_j$ , under rapid tumbling circumstances (i.e. liquid-solution NMR). It may pay to examine this result under more stringent conditions. [Appendix 2](#) presents a computer-based example of equivalence in NMR spectroscopy.

## 8. SELECTED MOLECULES WITH EQUIVALENCES

We now turn to consideration of certain ‘simple’ molecules, to serve as examples of ideas and applications of NMR spectroscopy.

### 8.1. Molecular hydrogen

In a sense, when considering equivalence between atoms in a molecule, diatomic hydrogen is the simplest situation. However, in reality, just the opposite is found to be true.

The magnetic properties of the  $\text{H}_2$  molecule as arising from its two electrons are well known, both experimentally and from basic theory. Thus accurate calculations of its magnetic shielding and its dipole magnetizability (susceptibility) tensors are available (e.g. see [Refs. 41 and 42](#)).

For  $^1\text{H}_2$ , the electrons are paired in the ground state, and the nuclei each have spin-1/2 and thus are fermions. Hence, the molecule must obey rigid quantum-statistical laws, consistent with the Pauli exclusion principle.<sup>43</sup> This causes  $\text{H}_2$  molecules to occur in nature in either of two quite inequivalent forms, called *ortho* and *para* hydrogen, which are hardly interconvertible.

The total angular momentum  $^o\mathbf{P}_I$  of each molecule is the sum of the rotational and the two nuclear spin vector operators. The coupling between these is sufficiently weak that one can safely make use of the individual quantum numbers of the two. Details of the situation have been discussed by Bloom.<sup>44</sup>

In *o*- $\text{H}_2$ , the two nuclear spins appear as coupled to form an  $I(\text{total}) = 1$  species, with three states having  $M_I = -1, 0, +1$  respectively. Thus it is NMR-active.<sup>45</sup> Furthermore, only rotational states with odd quantum numbers can be occupied. Thus the rotational ground state has  $N = 1$ : a triplet of states. In other words, *o*- $\text{H}_2$  can never stop rotating, about any axis perpendicular to its molecular axis  $n$ .

On the other hand, in *p*- $\text{H}_2$ , the two nuclear spins appear as coupled to form an  $I(\text{total}) = 0$  species, with a single state having  $M_I = 0$ . Thus it is NMR-inactive.

Only rotational states with even quantum numbers  $N$  can be occupied. Thus the rotational ground state has  $N=0$ : a singlet. It follows that hydrogen gas is a mixture of components in a 3:1 ratio of abundance, and that  $o$ -H<sub>2</sub> molecules continue to rotate even when cooled, when unimpeded.

Consider isolated molecules of H<sub>2</sub>. Within each rotating molecule, the electron cloud distorts due to the rotation and thereby creates a local magnetic field  $\mathbf{B}_r$  acting on the two nuclei. In the absence of external fields, the Hamiltonian is

$${}^{\text{op}}H = E_r {}^{\text{op}}\mathbf{N}^T \bullet {}^{\text{op}}\mathbf{N} + u_{\text{NI}} {}^{\text{op}}\mathbf{N}^T \bullet {}^{\text{op}}\mathbf{I} + E_e {}^{\text{op}}\mathbf{L}^T \bullet {}^{\text{op}}\mathbf{I} + D_1 ({}^{\text{op}}I_z^2 - {}^{\text{op}}I^2/3).$$

On the right-hand side, the terms represent:

- (1) The pure rotation energy of a diatomic molecule [Ref. 46, e.g. Chapter 2], which is not in fact rigid (the inter-nuclear distance depends on quantum number  $N$ , which is often denoted by symbol  $J$ ).
- (2) The energy is that of the magnetic field  $\mathbf{B}_r$  set up by the rotation, acting on each nuclear magnetic moment. Field  $\mathbf{B}_r$  points along the axis of rotation, and for  $N=1$  has a magnitude of 2.7 mT.<sup>47</sup>
- (3) The coupling between the electronic orbital angular momentum and the nuclear spin moment. Here symbol  $L$  denotes the electron orbital angular momentum. Electronic currents are caused by the non-spherical electronic orbital motions, affecting the bond length ( $r_{\text{HH}} \approx 0.075$  nm) and causing a magnetic field acting on the nuclei.
- (4) The direct through-space magnetic coupling between the two nuclear magnetic moments. The magnetic field at one proton due to the other is 3.4 mT.<sup>47</sup> Also, the first nucleus perturbs the nearby electrons, which effect is carried by them to the second nucleus, yielding an indirect nuclear spin-spin coupling.

To supplement the above, in the presence of an external magnetic field  $\mathbf{B}$ , one must add the Zeeman Hamiltonian

$${}^{\text{op}}H_Z = -\beta_n \mathbf{B}^T \bullet [\mathbf{g}_n \bullet {}^{\text{op}}\mathbf{I} + \mathbf{g}_R \bullet {}^{\text{op}}\mathbf{N}],$$

where  $\beta_n$  is the nuclear magneton, and  $3 \times 3$  matrix  $\mathbf{g}_n$  contains the chemical shift correction and here is deemed to be the same for both protons.

Dihydrogen can be cooled into a liquid and then a solid phase. Thus solid-state proton NMR is feasible, including single-crystal work. The gas-phase (200 torr, room T) <sup>1</sup>H FT-NMR spectrum at 200 MHz exhibits a single line.<sup>24</sup>

At sufficiently high applied magnetic fields, the frequency-swept NMR spectrum, for solid H<sub>2</sub> at ca. 1 K, consists basically of transitions  $M_I \rightarrow M_I - 1$  for  $M_I = +1$  and 0.<sup>43</sup> These two lines are split somewhat by the dipole-dipole term set out above.

One activity of lively interest has been the development of understanding the mechanism(s) of the nuclear paramagnetic to diamagnetic transition, that is the *ortho*  $\rightarrow$  *para* phase transformation.<sup>48</sup> Such conversion in solid dihydrogen at ambient pressure is mainly due to magnetic dipole-dipole interaction between the nuclei of pairs of neighbouring *ortho* molecules, with the energy released being carried away by phonons.<sup>49</sup> The dominant quantized lattice excitations invoked are called rotons and librons.<sup>50</sup>



Further and later NMR studies revealed the presence of peaks from *o*-H<sub>2</sub> dimers and trimers.<sup>51–53</sup> Such clustering increased as the temperature was lowered beyond ca. 0.1 K. The interaction between pairs can be thought of as being of the electric quadrupole–quadrupole type. In the single-crystal work, one can discern pairs differing in being either in or out of the basal plane of the crystal. A typical distance between them is 0.4 nm. The energy diagrams for any one *o*-H<sub>2</sub> molecule showing the splitting for the nine states can be found in Ref. 53, Figure 2. It is to be noted that the two protons become inequivalent at most relative orientations and positions of the two members of the dimer. Thus here, were it not for likely rapid rotations, direct spin–spin interaction between the proton moments within an *o*-H<sub>2</sub> molecule could become observable.

## 8.2. Methane

The CH<sub>4</sub> molecule is of course highly symmetrical on the time average, its equilibrium configuration being tetrahedral. Thus a single <sup>1</sup>H NMR line is to be seen, in the gas-phase, since molecular rotation too is not a factor there.

However, the NMR properties of solid-phase methane are very complex, due to subtle effects associated with the permutation symmetry of the nuclear spin set and molecular rotational tunnelling.<sup>55</sup> Nuclear spin states  $I_{\text{total}} = 0$  (irred. repr. E), 1 (T) and 2 (A) are observed. The situation is made more complicated since, as the solids are cooled and the individual molecules go from rotation to oscillation, several crystal phases become available, and slow transitions between them take place. Much work has been done in the last century on this problem, including use of deuterated versions of methane; for example see Refs. 56–59. Much detail has emerged from NMR lineshape analysis and relaxation time measurements, and kinetic studies. For example, the second moment of the <sup>13</sup>C resonance is found to be caused by intermolecular proton–carbon spin–spin interaction.<sup>60</sup> Thus proton inequivalence within the methane molecules is created.

Comparisons have been made between the two analogous molecules CH<sub>4</sub> and CF<sub>4</sub>. In the latter, clusters of molecules are seen via <sup>19</sup>F NMR, at various temperatures and pressures,<sup>61</sup> in various phases. Intermolecular potentials have been derived and compared for the two molecular species, as a result of gas-phase NMR studies.<sup>62</sup>

## 8.3. The hydrazines

An obvious example of nuclear equivalence is evident in hydrazine, H<sub>2</sub>N–NH<sub>2</sub>, for both types of nuclides therein. This molecule's capability to take on protons and form various cations leads to interesting NMR (and EPR) phenomena. An excellent summary of the NMR aspects of hydrazine and its alkyl/aryl derivatives is available, to be found in the two-volume tome by Eckart Schmidt.<sup>63</sup>

The proton NMR spectrum of highly purified N<sub>2</sub>H<sub>4</sub> (anhydrous liquid, at 298 K) consists of a single line, its width (ca. 36 Hz) presumably being due to quadrupolar relaxation of the neighbouring <sup>14</sup>N nuclei.<sup>64</sup>

Removing one electron produces the planar  $S=1/2$  free-radical ion  $(\bullet\text{N}_2\text{H}_4)^+$ , which has three  $\pi$  electrons, a spin population of ca. 0.5 on each nitrogen, and equilibrium symmetry  $D_{2h}$ .<sup>65</sup> The single-crystal EPR reveals that matrix  $\mathbf{A}(^{14}\text{N})$  is uniaxial along an axis  $\mathbf{II}$ , for both nitrogens.  $\mathbf{II}$  is a principal axis of the rhombic  $g$  matrix. The four hyperfine matrices  $\mathbf{A}(^1\text{H})$  portray an unusually large anisotropy (principal values  $A_i/(g_e\beta_e)=+0.2, -1.3, -2.1$  mT). The crystal structure of the hydrogen-oxalate host  $\text{N}_2\text{H}_5(\text{HC}_2\text{O}_4)$  is monoclinic (point group  $C_{2h}$ , and thus containing two symmetry-related molecules 1 and 2 per standard unit cell: Ref. 12). The structure is described using Cartesian axes  $a, b, c^*$ , with  $\mathbf{b}$  the monoclinic axis. In plane  $ac^*$ , external field  $\mathbf{B}$  yields EPR spectra in which  $\underline{1}$  and  $\underline{2}$  appear as equivalent, as expected. Crystal rotation such that  $\mathbf{B} \perp \mathbf{b}$  causes all four protons of the molecule to appear equivalent. In the plane  $\mathbf{B} \perp \mathbf{II}$ , these protons act as equivalent in pairs. More details may be found in the fine paper: Ref. 65. Also, the  $^{14}\text{N}$  hyperfine and the nuclear quadrupole couplings of  $(\bullet\text{N}_2^2\text{H}_4)^+$  were obtained from single-crystal rotations, using ENDOR.<sup>66</sup> Thermal EPR studies (ca. 283–333 K) of the  $^{14}\text{N}$  hyperfine splitting revealed torsional vibrations of the N–N bond,<sup>67</sup> and electron spin echo (ESEEM) explored the  $T$  dependence of the phase-memory relaxation time<sup>68</sup>; also note Ref. 69.

Graduating now to the diamagnetic cation  $[\text{H}_2\text{N}-\text{NH}_3]^+$ , one finds much of interest. NMR (of  $^1\text{H}$ ,  $^2\text{H}$ ,  $^7\text{Li}$ ,  $^{14}\text{N}$ ,  $^{15}\text{N}$ ) and other measurements of  $(\text{H}_2\text{N}-\text{NH}_3)(\text{HSO}_4)$  and similar salts, and especially of  $\text{Li}(\text{H}_2\text{N}-\text{NH}_3)(\text{SO}_4)$ , reveal ferroelectric behaviour and substantial capability of proton conductivity/diffusion through the crystals (e.g. Refs. 70 and 71).

Finally, we touch upon the hydrazinium cation  $[\text{H}_3\text{N}-\text{NH}_3]^{++}$ , which has been much studied by NMR, for some 50 years now. In aqueous solution, it acts as a weak acid. Internal rotations of the molecules exist, and it is known that the two  $\text{NH}_3$  groups within the molecule generally are not equivalent when in a solid phase such as in the sulfates.<sup>72–74</sup>

## 8.4. Benzene and the $\text{C}_6\text{H}_6$ isomers

This aromatic time-honoured species, first prepared by Faraday in 1825, is of course a highly symmetric stable molecule,  $\text{C}_6\text{H}_6$ , featuring six equivalent protons, yielding an ‘uninteresting’ single NMR line. The term ‘aromatic’ implies presence of enhanced diamagnetic currents provided by electrons in the species.<sup>75,76</sup>

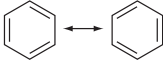



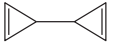
In the gas-phase, benzene shows a single line.<sup>77,78</sup> and can yield useful information regarding the diffusion/transport properties. Benzene trapped within pores in glasses and silica gels too yields results, about pore size and adsorbed versus liquid-phase conditions.<sup>79</sup> Chemisorption on alumina-supported platinum catalysts leads to disclosure as to how and where the benzene molecules are located, via  $^1\text{H}$  NMR.<sup>80</sup>

Benzene was the first molecule studied by NMR within liquid crystals, that is oriented in nematic liquids.<sup>81</sup> This opened up much research, using benzene,<sup>82</sup> leading to information about the chemical-shift anisotropy and selected spin–spin couplings. Isotope substitution too played a major role; for example see Ref. 83. The  $^1\text{H}$  NMR powder spectrum at ca. 225 K gave principal values of the proton-shift parameter matrix.<sup>84</sup> Various isotopically labelled versions of benzene

dissolved in liquid crystals, using  $^1\text{H}$  and  $^{13}\text{C}$  NMR, have led to quantitative information about the indirect spin–spin parameter matrices  $\text{J}_{\text{CH}}$  and  $\text{J}_{\text{CC}}$ , which were theoretically modelled.<sup>11</sup>

Things become complex indeed when we consider all possible combinations  $6\text{C} + 6\text{H}$  featuring covalent bonds: four per carbon and one per hydrogen. There are 217 of these,<sup>54</sup> becoming 328 if diastereomers and enantiomers are taken into account, nearly all unknown and likely highly unstable. We list the four valence isomers of benzene (see for example: Ref. 85), all of which appear fairly prominently in the literature (note Figure 2):

- (1) Tectadiene = Dewar benzene = bicyclo[2.2.0]hex-2,5-diene, featuring 1 pair ( $^1\text{H}$  quintet) and 1 quartet ( $^1\text{H}$  triplet) of equivalent protons. Not planar; time-average symmetry  $\text{C}_{2v}$ .<sup>86,87</sup>
- (2) Benzvalene = tricyclo[3.1.0.0<sup>2,6</sup>]hex-3-ene, featuring three pairs of equivalent protons (two  $^1\text{H}$  triplets and one quintet). Not planar; time-average symmetry  $\text{C}_{2v}$ .<sup>88–91</sup>
- (3) Prismane = Ladenburg benzene = tetracyclo[2.0.0.0<sup>2,6</sup>.0<sup>3,5</sup>], featuring two pairs of equivalent protons (single  $^1\text{H}$ , single  $^{13}\text{C}$  line). Time-average symmetry  $\text{D}_{3h}$ .<sup>92</sup>
- (4) Bicyclopropenyl (2,2) = (3'-cycloprop-1-enyl)-3-cycloprop-1-en, featuring two pairs of equivalent protons ( $^1\text{H}$ : one singlet and one doublet). Time-average symmetry  $\text{D}_{2h}$ .<sup>93</sup>

In the table below are given the valence isomers of benzene (for definition and explanation see the article, benzene and its isomers, resonance, vol. 6, no. 5, pp. 74–78, 2001). A few properties that are listed here give an idea of how different and interesting such isomers could be. These structures can be found among the 217 structures given in this poster.			
Structure	Name	Source	Properties
	Benzene	Petroleum, coal tar, trimerization of acetylene, natural products, etc.	Colourless liquid, b.p. 80 °C; m.p. 5.5 °C. Stable. Has relatively pleasant odour. (carcinogenic). Industrially a very important compound).
	Dewar benzene; Bicyclo[2.2.0]hex-2,5-diene	Van Tamelen and Pappas <sup>86</sup>	Unstable, $t_{1/2} = 2$ days. Rearranges to benzene. (stable in pyridine soln).
	Benzvalene; Tricyclo[3.1.0.0 <sup>2,6</sup> ]hex-3-ene	Wilzbach et al. <sup>91</sup> Katz et al. <sup>90</sup>	Stable in solution. Explosive in pure state. Foul smelling.
	Prismane; Tetracyclo[3.1.0.0 <sup>2,4</sup> .0 <sup>3,6</sup> ]hexane	Katz and Acton <sup>92</sup>	Odourless liquid. Explosive. Stable at RT in toluene, at 90 °C isomerizes to benzene, $t_{1/2} = 11$ h.
	Bicyclopropenyl (2,2); (3'-cycloprop-1-enyl)-3-cycloprop-1-ene	Billups and Haley <sup>93</sup>	Stable below 10 °C, above that, decomposes to an unknown solid.

**Figure 2** The valence isomers of benzene, as taken from the poster associated with Ref. 54. Courtesy of the Indian Academy of Sciences.

All of these isomers of benzene have been prepared, and their  $^1\text{H}$  and  $^{13}\text{C}$  NMR spectra have been observed. We see that in going from benzene itself to the four valence isomers, the breakdown in atom equivalence leads to four very different  $^1\text{H}$  NMR spectra (and also four very different  $^{13}\text{C}$  spectra), allowing structure proof for each isomer. In principle, interconversion studies and rate studies thereof could be accomplished by NMR spectroscopy.

We can next consider, as an annulene other than benzene, the very unstable enigmatic cyclobutadiene, see Refs. 94 and 95, which was first prepared some 40 years ago.<sup>96</sup> The  $^{13}\text{C}$  NMR spectra from doubly labelled  $^{13}\text{C}$  molecules<sup>97</sup> suggest that the two valence isomeric forms: square and rectangular, interconvert rapidly even at ca. 25 K. The energies and some NMR parameters of the two forms have been estimated recently from theory,<sup>98</sup> as have those of benzene in its ground state—for comparison. More work is needed to establish exactly where the electron singlet and triplet states occur.

## 8.5. Cyclopropane

Perhaps, it is appropriate to remind the reader that sophisticated analytical papers using NMR appeared already 40+ years ago. Thus  $^1\text{H}$  (60 MHz) NMR spectra of cyclopropane molecules containing a single  $^{13}\text{C}$  in natural abundance were analyzed quantitatively,<sup>99</sup> for the solute in a nematic solvent at 348 K, revealing the several direct  $D_{\text{HH}}$  and indirect  $J_{\text{HH}}$  spin–spin interactions, as well as  $J_{\text{CH}}$  on the labelled carbon. The presence of the  $^{13}\text{C}$  atom of course causes inequivalence of the protons, yielding 2 of one type and 4 of another. Work on  $(\text{CH}_2)_3$  continues; for example see Ref. 100.

## 8.6. Fluxional molecules

We now turn to some fluxional molecules: these feature dynamics in which atoms interchange between symmetry-equivalent positions, without bond breaking necessarily occurring.

The  $\text{CH}_5^+$  cation has been prepared, but is quite unstable. It is of great interest, especially to theorists, since it is a fluxional species which features a potential energy surface with many minima of more or less the same total energy. In this quintessential carbonium ion, the barriers to proton exchange are so low that transfers persist to lowest cryogenic temperatures, that is there is no rigid molecular structure. Recent theory suggests that the molecule can be thought of as basically a pyramidal  $\text{CH}_3^+$  species bearing a  $\text{H}_2$  molecule bonded to its fourth vertex, with all four vertices equivalent.<sup>101</sup> The result is that all five protons appear to be equivalent. No definitive  $^1\text{H}$  or  $^{13}\text{C}$  NMR spectra have yet been obtained.

The  $\text{CH}_5^+$  cation is isoelectronic and isostructural with the neutral molecule  $\text{BH}_5$ . Both have equilibrium point group  $\text{C}_s$ . Comparisons between various relevant compounds yielded prediction of some NMR parameters of the methonium ion.<sup>102</sup>

As a second example, we can cite a relatively simple molecule:  $\text{PF}_5$ , which was first measured by  $^{19}\text{F}$  NMR in the early days, in the gas phase.<sup>40</sup> There was no

splitting besides the  $^{31}\text{P}$  contribution, despite the known asymmetric structure. It was Berry who suggested the explanation: presence of a rapid 'pseudorotation' taking place in the trigonal bipyramid.<sup>103</sup> Thus relatively small movements of the fluorine atoms can interchange two identical but differently oriented molecular configurations. On the measured time scale, all five fluorine atoms act as equivalent. A similar phenomenon occurs in the square pyramidal molecule  $\text{IF}_5$ .

Similar effects may occur in molecule  $\text{ClF}_3$ , which has an equilibrium T-shaped structure ( $G=C_{2v}$ ). Both gas and liquid-phase  $^{19}\text{F}$  NMR measurements have been reported (yielding an  $\text{AB}_2$ -type spectrum),<sup>104</sup> and some theoretical analyses exist.<sup>105,106</sup>

Next, cyclohexane: If it had a planar  $^{12}\text{C}$  carbon skeleton, it would exhibit but a single  $^1\text{H}$  NMR peak. This is not the case, and it is well known that this species has a set of possible configurations, which can and do interconvert.<sup>107</sup> The puckered ring can occur in the ground state 'boat' form, in the 'twist-boat' form and the high-energy 'chair' form. NMR spectroscopy has contributed more than a little to our knowledge of the energetics and interchange kinetics. In the chair form, the protons occur in axial and equatorial positions, and are thus inequivalent with respect to the two sets. Interchange between the two sets occurs, via flipping of the carbon atoms, so that dynamic NMR is very apt: See Ref. 108, pp. 102–107 for NMR in liquid  $\text{CS}_2$ , Ref. 109 in the gas-phase,<sup>110</sup> for the neat plastic crystalline phase. NMR shielding of many different cycloalkanes have been reported.<sup>111</sup> The twist-boat conformation has been observed fairly recently<sup>112</sup> in a substituted cyclohexane.

Perhaps the ultimate example of fluxional molecules is bullvalene ( $\text{C}_{10}\text{H}_{10}$ : tricyclo[3.3.2.0<sup>4,6</sup>]deca-2,7,9-triene), a multi-ring hydrocarbon containing three double bonds. Equilibrium point group  $=C_{3v}$ . The number of interchanging isomers is huge:  $10!/3 = 1,209,600$ . Early studies of the interchanges (Cope rearrangements) were done in liquid tetrachloroethylene, with spin-echo NMR at 26.85 MHz,<sup>113</sup> yielding rearrangement rates and activation energies (also see Ref. 114, where presence of but a single  $^1\text{H}$  peak was reported). Thereafter, the valence-bond isomerization rates were studied by  $^1\text{H}$  NMR of bullvalene in a nematic crystal solvent at 143 K.<sup>115</sup> A single-crystal deuterium NMR study of bullvalene too is available,<sup>116</sup> demonstrating simultaneous occurrence of molecular re-orientations and the fluxional behaviour.

Finally, site jumping of the three bulky ligands ( $\text{Si}_5\text{C}_{15}\text{H}_{14}$ ) among the four equivalent Si atoms of a central tetrahedral  $\text{Si}_4$  cage bearing a  $-1$  charge number has been seen with  $^{29}\text{Si}$  NMR, i.e., the four Si cage atoms act as equivalent.<sup>117</sup>

## 9. SPIN-HAMILTONIAN PARAMETERS

We now wish to discuss the topic of what parameters are in fact measurable with magnetic resonance spectroscopy.

The spin-Hamiltonian operator can be written as the sum of a large number of terms: for example, see Equation (A3) in Appendix 3. As may be seen therein, the convention for the two Zeeman terms (electron spin and nuclear spin) is that their signs differ, due to the difference in charge of the two most basic particles to be dealt with: the electron and the proton. Hence the  $g$  values of these particles are taken to be both positive.

The sub-structure varies sufficiently from nuclide to nuclide that the bare-nuclear  $g$  factors  $^0g_n$  occur frequently with either sign. The chemical shifts are relatively minor, so that  $^0g_n$  sets the sign for matrix  $\mathbf{g}_n$ . With electrons,  $g$  is generally positive in all unpaired-electron species except for a few cases of heavy atoms in which the magnetic levels occur in reverse order.

## 9.1. Zeeman term

For simplicity in this complex topic, let us begin by considering only a single Zeeman term of the spin-Hamiltonian. For notation, consult app. 3.

### 9.1.1. Two conventional choices for $^{\text{op}}H$

$$\text{Choice 1 } ^{\text{op}}H = \beta \mathbf{B}^T \bullet \mathbf{g} \bullet ^{\text{op}}\mathbf{J} \text{ (see Ref. 7, Equation 4.4c)}$$

in the case of a single spin-bearing particle exposed to a constant externally applied magnetic field  $\mathbf{B}$ , aligning the magnetic moment (angular momentum operator  $^{\text{op}}\mathbf{J}$ ). The magneton  $\beta$  is a positive scalar, by definition.

We shall consider a spin  $J=1/2$ .

Then there are two spin states, labelled by eigenvalue  $^{\text{op}}J_z = M_{\pm} = \pm 1/2$ .

The above is derived from quantum mechanics, via a definition of the anisotropic magnetic moment operator. What are the conditions this imposes on  $3 \times 3$  matrix  $\mathbf{g}$ ?

However, first of all, consider what difference would arise if we had picked

$$\text{Choice 2 } ^{\text{op}}H = \beta ^{\text{op}}\mathbf{J}^T \bullet \mathbf{g}' \bullet \mathbf{B}$$

instead. How are matrices  $\mathbf{g}$  and  $\mathbf{g}'$  related?

The non-negative<sup>a</sup> difference  $\Delta U$  in energy eigenvalues of the system  $= g\beta B$ , where  $B = \mathbf{B}^T \bullet \mathbf{n} = \mathbf{n}^T \bullet \mathbf{B} \geq 0$ , and

$$g = [\mathbf{n}^T \bullet (\mathbf{g} \bullet \mathbf{g}^T) \bullet \mathbf{n}]^{1/2} \text{ for Choice 1 (see Ref. 7, Equation 4.12),}$$

whereas  $\Delta U = g'\beta B$  with

$$g' = [\mathbf{n}^T \bullet (\mathbf{g}' \bullet \mathbf{g}'^T) \bullet \mathbf{n}]^{1/2} \text{ for Choice 2.}$$

How are  $g$  and  $g'$  related? Since we deal with the same data set, they must be equal.

<sup>a</sup> The difference  $\Delta U$  is by definition that of the energy of the upper state minus that of the lower state. This positive energy difference is set equal to  $h\nu$ , where the frequency  $\nu$  of the excitation magnetic field is taken to be positive. The latter is usually linearly polarized.

Hence

$$\mathbf{g} \bullet \mathbf{g}^T = \mathbf{g}' \bullet \mathbf{g}'^T.$$

Thus  $\mathbf{g} = \pm \mathbf{g}'$ . We can choose the plus sign, with impunity. Thus Choices 1 and 2 are completely equivalent. We will select Choice 1.

The question of sign of  $\mathbf{g}$  is another matter. The convention  $\Delta U = g\beta B$  makes  $g$  non-negative, at least for usual spectroscopic purposes. Thus it might be better to write  $|g|$  in this equation.

### 9.1.2. 'Squared' parameter matrix

Since it is scalars  $g(\mathbf{n})$  that are the measurable quantities, from line positions, we can obtain the 'squared' matrix  $\mathbf{G} \equiv \mathbf{g} \bullet \mathbf{g}^T$ . Basically it is a set of magnetization components  $\mathbf{M} \bullet \mathbf{n}$  that are measured. The matrix  $\mathbf{G}$  is necessarily symmetric.<sup>b</sup> Note that  $\mathbf{G}$  must be real, and is a true second-rank tensor.

Since  $\mathbf{G}$  is real symmetric, it is a normal matrix.<sup>c</sup> This guarantees that it can be transformed into diagonal form by a unitary transformation, in fact by a real orthogonal transformation. Thus it has a principal axis system, and a set of three principal values which are all non-negative.

Strictly speaking, as we will see, it is matrix  $\mathbf{G}$  which should be reported in the literature, along with its principal properties.

Note that we cannot access  $\mathbf{g}$  directly! Can one achieve this at all?

Obviously there are two approaches: One from basic quantum-mechanical theory of the chemical species at hand, and the other from EPR experimental data!

The choice of matrices  $\mathbf{g}$  that yield a given  $\mathbf{G}$  is far from unique.<sup>d</sup>

Note also that matrix  $\mathbf{g}$  is not necessarily real or symmetric.

However, one can always find a real symmetric  $\mathbf{g}$  that will suit, and will reproduce the data set  $g(\mathbf{n})$ , but it may not be the one arising from basic quantum theory describing the chemical species being dealt with.

Since one can attain the diagonal form  $\mathbf{G}_d$  from an appropriate real orthogonal transformation  $\mathbf{R} \bullet \mathbf{G} \bullet \mathbf{R}^{-1}$ , one can then take the square roots of its principal values to attain a diagonal matrix  $\mathbf{g}_d$  (with signs arbitrary!), and return the latter to the original coordinate system using the 'backward' transformation  $\mathbf{R}^{-1} \bullet \mathbf{g}_d \bullet \mathbf{R}$  to yield a matrix  $\mathbf{g}$ .

<sup>b</sup> Even if it were not, the relation to the experimental value  $g(\mathbf{n})$  filters out its antisymmetric part, so that the latter can be ignored [Ref. 12, footnote 5]. Note also that, in general:  $\mathbf{A} \bullet \mathbf{B} \neq \mathbf{B} \bullet \mathbf{A}$ . Thus the inequality in  $\mathbf{Y}^T \bullet \mathbf{Y} = (\mathbf{Y}^T \bullet \mathbf{Y})^T \neq (\mathbf{Y} \bullet \mathbf{Y}^T)^T = \mathbf{Y} \bullet \mathbf{Y}^T$  occurs for most arbitrary matrices  $\mathbf{Y}$ .

<sup>c</sup> Normal matrix: By definition, any complex square matrix  $\mathbf{A}$  is a normal matrix iff

$$\mathbf{A}^\dagger \bullet \mathbf{A} = \mathbf{A} \bullet \mathbf{A}^\dagger,$$

where  $\mathbf{A}^\dagger$  is the conjugate transpose of  $\mathbf{A}$ . That is, a matrix is normal if it commutes with its conjugate transpose. It is Hermitian by definition if  $\mathbf{A} = \mathbf{A}^\dagger$ . Thus  $\mathbf{A}^\dagger \bullet \mathbf{A}$  is Hermitian. If  $\mathbf{A}$  is a real matrix, then  $\mathbf{A}^\dagger = \mathbf{A}^T$ ; thus it is normal if  $\mathbf{A}^T \bullet \mathbf{A} = \mathbf{A} \bullet \mathbf{A}^T$ .

Normality is a convenient test for diagonalizability: every normal matrix can be converted to a diagonal matrix by a unitary transform, and every matrix which can be made diagonal by a unitary transform is also normal (but finding the desired transform requires much more work than simply testing to see whether the matrix is normal).

<sup>d</sup> Changing the signs simultaneously of certain trios (e.g.  $\{g_{xy}, g_{yz}, g_{zx}\}$ ) of elements of  $\mathbf{g}$  will leave  $\mathbf{G}$  untouched. Our own investigation, making the arbitrary simplifying condition  $\mathbf{g} \bullet \mathbf{g} = \mathbf{g} \bullet \mathbf{g}^T$ , discloses that possible matrices  $\mathbf{g}$  can be asymmetric and also complex, for any given real symmetric  $\mathbf{G}$ .

Is there any other physical measurement, other than the one cited above, that could give more info about the matrix  $\mathbf{g}$ ? Yes,  $\det(\mathbf{g})$  is in principle available, yielding a product combination within  $\mathbf{g}$  unless of course  $\det(\mathbf{g})=0$  (i.e.  $\mathbf{g}$  singular). It can be obtained by comparing the spectral intensities using the two possible circularly polarized excitation fields; this yields the sense (sign) of precession of  $\mathbf{M}$  about  $\mathbf{B}$ ; see Refs. 118–121. Since the spectral intensity in our case is not zero for one of the polarizations, we can take  $\det(\mathbf{g}) \neq 0$ .

If  $\mathbf{g}$  can be diagonalized, then we can say that  $\det(\mathbf{g})$  is the product of its three principal values, and we can say that this product defines the sign of  $\mathbf{g}$ . The sign of course gets lost when one takes the product  $\mathbf{g} \bullet \mathbf{g}^T = \mathbf{G}$ .

### 9.1.3. Situation $\mathbf{g}$ isotropic

If the scalar  $g$  is isotropic (i.e. not a function of  $\mathbf{n}$ ), then  $\mathbf{G} = g^2 \mathbf{U}_3$ , where  $\mathbf{U}_3$  is the  $3 \times 3$  identity matrix. It follows that  $g^2$  must be real. Hence  $g$  must be either pure real or pure imaginary. We can insist that  $g$  be pure real.

In NMR, the shift parameters  $g$  tend to be much closer to being isotropic than they are in EPR.

### 9.1.4. Asymmetry of $\mathbf{g}$

By asymmetry of any  $3 \times 3$  real matrix  $\mathbf{Y}$ , we mean that in general at least one set of its off-diagonal paired elements  $Y_{ij} \neq Y_{ji}$ , in some coordinate system. This is not to be confused with its situation regarding principal values: If all three are identical, we call this the isotropic case; if only two are equal, we call that the uniaxial case, and if all three are distinct, that is the rhombic case.

As it turns out, matrix  $\mathbf{g}$  must be real but is not necessarily symmetric,<sup>122–126</sup> as discussed in terms of EPR. The asymmetry exists if the local symmetry is low enough: triclinic or monoclinic (see Ref. 12, Table I). The same concepts are valid in NMR.<sup>126–128</sup>

Matrix asymmetry is linked to the existence of anisotropic spin-orbit coupling,<sup>123</sup> and the presence of sufficiently low-symmetry electric fields (static and dynamic).

We do want to emphasize that the nuclear shift matrix too is generally asymmetric.<sup>127</sup> Such effects would show up with nuclei which exhibit very large chemical shifts.<sup>126</sup>

## 9.2. Coupling parameters

We now address the question of how to attain from experimental data the coupling parameter matrices, denoted here by symbol  $\mathbf{Y}$ , existing in spin-Hamiltonian terms.

### 9.2.1. Entanglement

If one or more spin-coupling terms also occur (e.g. hyperfine or nuclear spin-spin), then each such spin-Hamiltonian parameter matrix  $\mathbf{Y}$  occurs in the transition energy and intensity expressions within combinations of type



$$[\{\mathbf{n}^T \bullet (\mathbf{g} \bullet \mathbf{Y} \bullet \mathbf{Y}^T \bullet \mathbf{g}^T) \bullet \mathbf{n}\} / g^2]^{1/2},$$

that is  $\mathbf{Y}$  is entangled with matrix  $\mathbf{g}$ ; see Refs. 129, [12, Footnote 4], [130, Equations (27) and (28)], and also [7, Equation 6.55]. The set of matrices  $\mathbf{Y}$  includes the hyperfine coupling parameter matrices  $\mathbf{A}$ , and the nuclear–nuclear spin interaction matrices  $\mathbf{J}$ . The latter of course can portray interaction between identical nuclides, or different nuclides.

We see that even if  $g$  were isotropic, we would still have somehow to extract  $\mathbf{Y}$  from its square combination, in analogy with the above pure  $g$  case. This is made problematic since there is good reason to believe that  $\mathbf{Y}$  is asymmetric in some physical (hyperfine) situations.

In some physical situations, namely when the hyperfine energy is small compared to the nuclear Zeeman energy, then the hyperfine splitting is linear in (the projection magnitude of) matrix  $\mathbf{A}$ ; for example, see Ref. 131. Then, provided that  $g$  is anisotropic (note Ref. 128 on this point), one can detect asymmetry of  $\mathbf{A}$  directly from EPR line-position measurement: see below.

### 9.2.2. Asymmetric matrices $\mathbf{Y}$

Thus it has been well established in the literature that these matrices are in general asymmetric.

**9.2.2.1. Hyperfine matrix ( $\mathbf{A}$ ) asymmetry** There are numerous (20–30) papers dealing with this topic in some manner. These include Refs. 131–135, as well as 128 and 129.

As a fine example of the actual measurement of a parameter matrix asymmetry, we cite the collaborative effort,<sup>132</sup> which reported the quantitative measurement via ENDOR of superhyperfine splittings attributed to neighbours of oxygen  $\text{O}^-$  contaminative defects (with  $S=1/2$ ) in  $x$ -irradiated BaFBr single-crystals. Here  $g$  is anisotropic, and the local symmetry is  $C_{2h}$ . While  $g$  was taken to be symmetric, the matrix  $A(^{19}\text{F})$  required to fit the line-position data was found to be highly asymmetric. ENDOR of course measures NMR transitions by using EPR spectroscopy.

**9.2.2.2. Nuclear spin–spin matrix ( $\mathbf{J}$ ) asymmetry** Discussions of the theory of asymmetric nuclear spin–spin coupling matrices and their relation to local symmetry exist.<sup>136,137</sup> However, experimental evidence dealing with this topic seems to be non-existent or else very sparse.

## 9.3. Reported NMR measurements of matrix $\mathbf{g}_n$ and/or $\mathbf{J}$ properties

There are various publications reporting measurement from single-crystal or liquid-crystal NMR of parameter ‘tensor’ properties. They all assume these matrices to be symmetric. These works include Refs. 11,31,138,139.

In closing this section, it is fair to point out that much more work on parameter matrix analysis and asymmetry is needed, that is better experimental evidence

and first-class *ab initio* simulations. It will be interesting to establish how relevant matrix asymmetry actually is in the NMR field.

## 10. SPECTRAL DEGENERACY

We now wish to outline the situations in which nuclei can appear as equivalent for certain magnetic-field ( $\mathbf{B}$ ) orientations chosen relative to single-crystal orientations in magnetic resonance (NMR and EPR) spectroscopic work. This topic has been covered in considerable detail in an earlier publication.<sup>12</sup>

For adequate simplicity, we return to consider the case when there is only a single Zeeman splitting term in the spin-Hamiltonian. For a given matrix  $\mathbf{g}$ , much depends on the relations of its principal values. If all three such values are identical, then of course only one spectral line is observed, at all orientations of  $\mathbf{n} = \mathbf{B}/B$ , where  $B > 0$ . Except in that isotropic case, it becomes important what crystal symmetry is at hand: there are 11 distinct cases (Laue groups).<sup>12</sup>

Besides the crossing of lines from different symmetry-related species (for examples, see [Figure 1](#)), (i.e. points where two species act as equivalent), there are also cases in which pairs of  $\mathbf{g}$  matrices are equivalent at all orientations of  $\mathbf{B}$ ; these are discussed/listed in [Ref. 12](#). Furthermore, there are ‘planes of degeneracy’, in which  $\mathbf{B}$  can be rotated without separation of lines from sets of such species; these too are discussed in excruciating detail.

As discussed above, the parameter matrices are usually measured using line-position data from rotations of  $\mathbf{B}$  in three orthogonal planes. However, with various crystal symmetries, it is possible to attain the same goal using multiple-site data obtained from  $\mathbf{B}$  rotated in a *single* plane.<sup>12</sup> This can be very useful.

Finally, one can ask the question regarding magnetic species in a crystal of unknown symmetry: What can be learned about the symmetry from the rotational magnetic resonance data? This too is explicated in [Ref. 12](#), as well as in [Ref. 140](#).

## ACKNOWLEDGEMENT

The present author wish to thank Drs. S. Arimoto, J. R. Pilbrow and C. Rangacharyulu for their helpful comments.

## APPENDIX 1. SOME MOLECULAR SPECIES CONTAINING EQUIVALENT NUCLEI

$\text{H}_2\text{C}=\text{CF}_2$  Ref. 2

$\text{CH}_3\text{Br}$  Ref. 2

$\text{CH}_3\text{FX}$  Ref. 2

$\text{CH}_2\text{F}_2$  Refs. 1,25  
 $\text{C}_2\text{H}_2\text{F}_2$  Ref. 1  
 $\text{ClF}_3$  Ref. 104  
 $\text{BrF}_5$  Ref. 1  
 Dichloroacetaldehyde  $\text{Cl}_2\text{CHCHO}$  Ref. 1  
 2-Bromo-5-chlorothiophene  $\text{BrClH}_2\text{C}_4\text{S}$  Ref. 1  
 1-Fluoro-3,4,5-trichlorobenzene  $\text{C}_6\text{H}_2\text{Cl}_3\text{F}$  Ref. 5  
 1,4-Difluoro-2,3-dichlorobenzene  $\text{C}_6\text{H}_2\text{Cl}_2\text{F}_2$  Ref. 5  
 Tropolone  $\text{C}_6\text{H}_5\text{O}_2$  Ref. 26  
 1-Chloro-4-fluorobenzene  $\text{C}_6\text{H}_4\text{ClF}$  Ref. 6  
 Tricyclo(3.3.2.0<sup>4,6</sup>)deca-2,7,9-triene  $\equiv$  Bullvalene  $\text{C}_{10}\text{H}_{10}$  Ref. 113  
 Tetraphosphorus decaoxide  $\text{P}_4\text{O}_{10}$  Refs. 29,33  
 Dimethyl sulfone (DMS)  $(\text{CH}_3)_2\text{SO}_2$  Ref. 141

### Free radicals

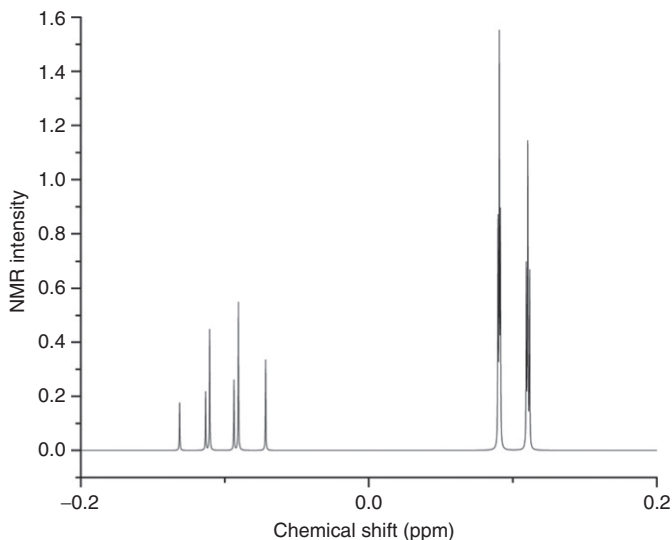
$\bullet\text{CH}_3$  Ref. 39  
 $\bullet\text{C}_6\text{H}_6^-$  Ref. 7  
 $\bullet\text{CH}_2\text{OH}$  Ref. 7  
 Glycolic acid radical  $\bullet\text{C}(\text{OH})\text{HCO}_2\text{H}$  Ref. 7  
 Hydrazine cation radical  $\bullet\text{NH}_2\text{-NH}_2^+$  Refs. 65,67

## APPENDIX 2. A COMPUTER-BASED EXAMPLE OF EQUIVALENCE IN NMR

It seems incumbent to produce an NMR example of the equivalence theorem (see Section 7.2), using our in-house quantitative computer program EPR-NMR.<sup>142</sup> For this purpose, we have ‘generated’ the chemical proton (+1) species  $^1\text{H}_\text{A}(^1\text{H}_\text{X})_3$ , where the latter three nuclides were taken to be equivalent. Thus there will be 16 spin states. To begin with, we considered an isotropic system. The 500.0... MHz spectrum (external field  $B=11.74334$  T) illustrating the example is shown in Figure 3. The primary line positions were taken arbitrarily to occur at chemical-shift positions  $-0.10...$ , and  $0.10...$  ppm (three times). This is identical to the statements for the nuclear  $g$  values:  $g_\text{A}=-5.5856904166$  and  $g_\text{X}=-5.5856915338$ . The coupling parameters  $J_{\text{Ai}}$  for nucleus  $A$  to the other nuclei ( $i=2, 3, 4$ ) were taken arbitrarily to each be 10.0... Hz. It turns out that indeed, the spectrum is independent of the various ‘tested’ (from 0 to 10,000 Hz) numerical values of the other three coupling parameters  $J_{ij}$  (existing among the equivalent protons  $\text{H}_\text{X}$ ).

Note the deviations (Figure 3) of the spectrum from simplest first-order behaviour (deviations from Pascal triangle estimation).

Next, we can take species  $^1\text{H}_\text{A}(^1\text{H}_\text{X})_3$  to be anisotropic. First, let all eight parameter matrices  $\mathbf{Y}$  be simultaneously diagonal (principal-axis system  $x, y, z$ ), with their third diagonal elements  $g_{\text{Az}}=-5.5856904166$ ,  $g_{\text{Xz}}=-5.5856915338$ ,  $J_{12z}=J_{13z}=J_{14z}=10.0...$  Hz, then we obtain the same line positions as in Figure 3 for all sets of three identical  $J_{ij}$  (and arbitrary diagonal elements  $\text{Y}_\text{x}$  and  $\text{Y}_\text{y}$ ), when external magnetic field  $\mathbf{B}||\mathbf{z}$ .



**Figure 3** A simulated  $^1\text{H}$  pulsed NMR spectrum of an idealized chemical species  $^1\text{H}_\text{A}(^1\text{H}_\text{X})_3$ , nominally taken at fixed carrier frequency  $\nu_0 = 500.0 \dots \text{MHz}$ . Here the Zeeman field  $B$  is deemed to be kept fixed at 11.74334 T, and Fourier transformation yields the spectrum. There are 6 (A) and 6 (X) distinct lines of appreciable intensity (12 and 14 transitions, respectively), with each individual line depicted as a Lorentzian with half-width 0.1 Hz.

For any arbitrary coordinate system used to express matrices  $\mathbf{Y}$ , spectrum [Figure 3](#) is again obtained as long as the matrix projections along the applied field direction obey the correct equivalence conditions.

If we return to the case of the diagonal matrix set, we can consider the isotopic species  $^2\text{H}_\text{A}(^2\text{H}_\text{X})_3$  (spins 1) and add a set of four nuclear quadrupole parameter matrices (traceless, say with  $P_{\text{Az}} = 1.0 \text{ Hz}$ ). It is found that here too, the NMR spectrum is independent of the coupling constants between the equivalent nuclei.

Finally, clearly, if instead of the above we were to consider the unpaired-electron chemical species  $^1\text{H}^0_\text{A}(^1\text{H}^0_\text{X})_3$ , the same equivalence properties would show up in the simulated fixed-field or fixed-frequency EPR spectra.

### APPENDIX 3. TENSORS IN MAGNETIC RESONANCE SPECTROSCOPY

Not all members of the magnetic resonance community have the realization that the common generally angle-dependent properties (scalars  $g$ ,  $g_\text{n}$ ,  $D$ ,  $A$ ,  $P$ , ...) are not obviously related to *tensors* as carefully defined by mathematicians. Thus, despite the frequent usage by some scientists of the word ‘tensor’, it is far from obvious that there is such a thing as for example a  $g$  tensor (Zeeman splitting for electron), a  $g_\text{n}$  tensor (Zeeman splitting for nucleus and chemical-shift tensor), or

an  $A$  (hyperfine) tensor, as is stated in some of the literature. Herein, the ‘ins and outs’ of the concepts involved will be explored.

Consider any real  $3 \times 3$  matrix

$$\mathbf{M} = \begin{pmatrix} M_{11} & M_{12} & M_{13} \\ M_{21} & M_{22} & M_{23} \\ M_{31} & M_{32} & M_{33} \end{pmatrix}, \quad (\text{A1})$$

that is a set of nine scalars (18 if the elements were allowed to be complex). The set may be merely a ‘simple’ array of numbers with no other mathematical properties. Usually however, other aspects are specified (Footnote <sup>e</sup>). For our purposes, we differentiate between parameter matrices and transformation matrices (see below):

When the matrix  $\mathbf{M}$  is a parameter matrix  $\mathbf{Y}$  (i.e. describing some physical property of the system considered) then the sub-indices of its elements  $Y_{\alpha\beta}$  (range  $\alpha, \beta = 1, 2, 3$ ) may indicate action on the physical system of two different physical ‘agents’ (e.g.  $\mathbf{E}^T \bullet \mathbf{Y} \bullet \mathbf{F}$ ) described using the same three-space coordinate axis set. Here symbol  $\bullet$  denotes matrix multiplication. However, alternatively, it is legitimate and possible to describe the two agents  $\mathbf{E}$  and  $\mathbf{F}$  by using two *different* sets of coordinate axes.

Often in science, one associates transformation properties under coordinate transformations with the sub-index labels of a matrix  $\mathbf{M} = \mathbf{R}$ . And, one can associate such behaviour *separately* for each member of the index pair. Thus, the human in charge has the freedom to construct relationships between two different coordinate systems, each linked to one of the indices. Generally,  $\mathbf{R}$  is real orthogonal but not symmetric.

When both indices are *linked* to the *same* coordinate system, we can (and formal mathematicians do) call  $\mathbf{Y}$  a second-rank tensor, providing that  $\mathbf{Y}$  describes some physico-chemical property of a natural system and obeys the relation (Footnote <sup>f</sup>):

$$Y'_{ab} = (\mathbf{R} \bullet \mathbf{Y} \bullet \mathbf{R}^T)_{ab} = \sum_{\alpha\beta} R_{a\alpha} R_{b\beta} Y_{\alpha\beta} \quad \text{integers } \alpha, \beta, a, b \text{ all range from 1 to 3} \quad (\text{A2})$$

(for instance, see Ref. 143, Equation (3.19)) when the coordinate system is changed via one or more proper (or improper) rotations ( $R$ ) of the coordinate axes. Superscript  $T$  denotes transposition, of a matrix [or of a vector (column  $\Leftrightarrow$  row)]. However, if the indices are linked to *different* coordinate systems, then  $Y$  is *not* a true tensor. Thus a second-rank tensor is a  $3 \times 3$  matrix, but a  $3 \times 3$  matrix is not necessarily a second-rank tensor.

The relationships between the concepts ‘matrix’ and ‘tensor’ are also discussed by Goldstein et al. [Ref. 144, pp. 188ff]. The term ‘tensor’ (most important in our case above: the ‘second-rank’ tensor) is rigorously defined in the text book by

<sup>e</sup> An important consideration is whether the matrix (tensor)  $\mathbf{Y}$  is a symmetric one. If so, its principal axis system is an orthogonal set, and otherwise not. In the symmetric case, the principal axis system is Cartesian. Also, here, one need not consider the difference between covariant and contravariant indices [Ref. 144, pp. 289ff]. With skew-symmetric tensors, the principal axes are not orthogonal. When one can restrict oneself to coordinate transformations between orthogonal-axis sets, one can limit oneself to ‘Cartesian’ tensors [Ref. 153, pp. 127–136].

<sup>f</sup> Valid for axial tensors and also for polar tensors (see the text). Note also that, for the sake of simplicity, we will ignore translations of the origins of the axis sets.

Nye.<sup>145</sup> Nye carefully defines the terms ‘matrix’ and ‘tensor’, and also points out (p. 35) that all tensors can be represented by matrices, but that the converse is not true. For similar information, also see the books by Arfken and Weber,<sup>146</sup> Brand,<sup>147</sup> Lovett,<sup>148</sup> Sands,<sup>149</sup> and by Wooster.<sup>150</sup>

It will now be useful to consider pseudo-tensors. Pseudo-vectors, alias axial vectors (unlike polar vectors), are invariant under the spatial inversion operation on the coordinate system, which changes a Cartesian set between left and right. Polar vectors change sign upon inversion. On the other hand, pseudo-scalars are numbers which change sign under such transformation, while ordinary scalars do not. A pseudo-tensor is a quantity which transforms like a true tensor under spatial rotations, but which transforms like a true tensor *plus* a change of sign of all its components under spatial inversion. Note the major difference between the above three definitions of ‘pseudo’.

We shall now consider various examples of matrices  $\mathbf{Y}$  as they occur in a routine spin-Hamiltonian, such as is set out below (Equation (A3)). Matrices  $\mathbf{g}$ ,  $\mathbf{g}_n$  and  $\mathbf{A}$  are not necessarily symmetric (however, in practice this effect is usually ignored).

A basic reason for existence of the above-stated problem is that the parameters cited are linked to quantum-mechanical angular-momentum (spin) operators, for instance via the ‘usual’ spin-Hamiltonian operator

$${}^{\text{op}}H_s = \beta_e \mathbf{B}^T \bullet \mathbf{g} \bullet {}^{\text{op}}\mathbf{S} - \beta_n \mathbf{B}^T \bullet \mathbf{g}_n \bullet {}^{\text{op}}\mathbf{I} + {}^{\text{op}}\mathbf{S}^T \bullet \mathbf{D} \bullet {}^{\text{op}}\mathbf{S} + {}^{\text{op}}\mathbf{I}^T \bullet \mathbf{P} \bullet {}^{\text{op}}\mathbf{I} + {}^{\text{op}}\mathbf{S}^T \bullet \mathbf{A} \bullet {}^{\text{op}}\mathbf{I} + \dots, \quad (\text{A3})$$

appropriate for presence of a single electron paramagnetic system (spin  $S$ ) and one nuclear spin ( $I$ ). Here (as indicated)  ${}^{\text{op}}H_s$ ,  ${}^{\text{op}}\mathbf{S}$  and  ${}^{\text{op}}\mathbf{I}$  (but not applied magnetic field  $\mathbf{B}$ ) are operator matrices ( $n \times n$ ) in the  $n$ -dimensional spin space, symbols  $\mathbf{B}$ ,  ${}^{\text{op}}\mathbf{S}$  and  ${}^{\text{op}}\mathbf{I}$  denote pseudo-vectors (and represented by column vectors  $= 3 \times 1$  matrices) in our usual three-space (Euclid et al.), while  $\mathbf{g}$ ,  $\mathbf{g}_n$ ,  $\mathbf{D}$ ,  $\mathbf{P}$  and  $\mathbf{A}$  are  $3 \times 3$  matrices expressed in that three-space (see Footnote <sup>8</sup>). Each such parameter matrix generally has its own principal axis system. We note that the  $\mathbf{g}$ ,  $\mathbf{g}_n$  and  $\mathbf{A}$  terms in Equation (A3) contain two *different* spin operators, while the  $\mathbf{D}$  and  $\mathbf{P}$  terms contain the same such operator twice. Hence the two indices in the matrices  $\mathbf{D}$  and  $\mathbf{P}$  necessarily refer to the same coordinate system.

We can call the terms shown explicitly in Equation (A3) ‘quadratic’ terms; other (higher-order) terms can exist [Ref. 7, Section 6.7]. The above spin-Hamiltonian is used to obtain the energies (and hence also transition energies) of the spin system considered. Another, similar spin-Hamiltonian (with the excitation magnetic-field amplitude vector  $\mathbf{B}_\mu$  replacing  $\mathbf{B}$  in Equation (A3)), yields the transition relative intensities. The line positions and intensities obtained are expressed in terms of the scalar (‘tensors’ of zeroth rank) parameters  $g$ ,  $g_n$ ,  $D$ ,  $P$ ,  $A$ ,  $\dots$ , derived as projections from the matrices  $\mathbf{g}$ ,  $\mathbf{g}_n$ ,  $\mathbf{D}$ ,  $\mathbf{P}$  and  $\mathbf{A}$ .<sup>12</sup>

<sup>8</sup> Also see papers by Skinner and Weil,<sup>130,154</sup> wherein some of the same problems are discussed in terms of polyadics. Thus the physical parameters are contained in the polyadics, with for example dyadics represented by  $3 \times 3$  matrices.

See Abragam and Bleaney's book [see Ref. 151, pp. 651ff] for some discussion of the situation for matrix  $\mathbf{g}$ , wherein it is stated that  $\mathbf{g}$  is not a true tensor. The essence here is the difference between the concepts of actual spins and fictitious spins.

One question to be settled is how the formal definition of 'tensor' involves the quality of the vectors projecting onto  $\mathbf{Y}$ , that is how are products of type  $\mathbf{E}^T \bullet \mathbf{Y} \bullet \mathbf{F}$  affected by whether vectors  $\mathbf{E}$  and  $\mathbf{F}$  are axial or polar [see Ref. 152, p. 98]. The latter authors, Pake and Estle, make the statement that for example  $\mathbf{g}$  is not a true tensor due to this characteristic. Our thought is that both axial and polar tensors are tensors as defined by mathematicians. Then too, the question arises: if  $\mathbf{Y}$  is a tensor, how does one decide in practice whether it is an axial tensor or a pseudo-tensor?

It appears that the three-space basis associated with each spin vector operator is 'arbitrary'. Thus operator  ${}^{\text{op}}\mathbf{S}$  (and/or  ${}^{\text{op}}\mathbf{I}$ ) need not necessarily be taken as quantized along some obvious physical direction, such as that of an applied magnetic field  $\mathbf{B}$ . In other words, spin operators  ${}^{\text{op}}\mathbf{S}$  and  ${}^{\text{op}}\mathbf{I}$  need *not* be expressed in the same space, that is to be quantized along the same spatial directions (i.e. the spin projection quantum numbers may be measured along different selected directions in our three-space). The most general case, which occurs when the two quantization axes are not aligned, prevents the parameter matrices from being tensors.

One can explore what functions of each parameter matrix are actually obtainable by scientists using the above spin-Hamiltonian, via the measurable line positions and relative line intensities of magnetic-resonance spectra; see publications by Skinner and Weil<sup>130,154</sup> for some aspects of this. The question as to which parameter matrices occurring in Equation (A3) are directly available from experimental data is far from trivial<sup>7,26</sup>; matrices  $\mathbf{g}$ ,  $\mathbf{g}_n$  and  $\mathbf{A}$  are not, while their squares (see below) are.

The  $3 \times 3$  matrices  $\mathbf{g}^T \bullet \mathbf{g}$ ,  $\mathbf{g} \bullet \mathbf{g}^T$ ,  $\mathbf{g}_n^T \bullet \mathbf{g}_n$ ,  $\mathbf{g}_n \bullet \mathbf{g}_n^T$ ,  $\mathbf{A}^T \bullet \mathbf{A}$ ,  $\mathbf{A} \bullet \mathbf{A}^T$ ,  $\mathbf{D}$  and  $\mathbf{P}$  are all true second-rank tensors, whereas  $\mathbf{g}$ ,  $\mathbf{g}_n$  and  $\mathbf{A}$  are not necessarily so (note Ref. 7, Section 4.4). Note that the task of deconvoluting (say)  $\mathbf{g}^T \bullet \mathbf{g}$  to arrive at  $\mathbf{g}$  is a vexing one; for instance, the 'sign' of  $\mathbf{g}$  is not readily available (i.e. all of the nine elements of  $\mathbf{g}$  can be multiplied by  $-1$  with no change to  $\mathbf{g}^T \bullet \mathbf{g}$ ). However, the sign is available from  $\det(\mathbf{g})$ , which is measurable, if  $\mathbf{g}$  is not singular: see Refs. [7, Section 4.4], 135 and 154. Attaining matrix  $\mathbf{A}^T \bullet \mathbf{A}$  or  $\mathbf{A} \bullet \mathbf{A}^T$  has its own problems: see Ref. 7, Section 6.8.

The question of whether matrix  $\mathbf{g}$  can be singular, symmetric, or even complex must be left for another discussion. Similarly, the relationship between the matrices occurring in quadratic terms in  ${}^{\text{op}}H_s$  of the form  $\mathbf{E}^T \bullet \mathbf{Y} \bullet \mathbf{F}$  and the 'opposite' form  $\mathbf{E} \bullet \mathbf{Y}' \bullet \mathbf{F}^T$ , when  $\mathbf{E} \neq \mathbf{F}$ , also deserves some discussion.

Much of the above is predicated on the major question, still to be completely and formally settled, as to whether, in quantum mechanics, specification of the quantization axis  $\mathbf{Z}_1$  for one spin leaves the quantization axes for all other spins in the system arbitrary, rather than compelling all of these to be identical to  $\mathbf{Z}_1$ .

The above appendix material is a slightly updated copy of the 'tirade' published in Ref. 8.

## REFERENCES

1. A. Abragam, *The Principles of Nuclear Magnetism*. Clarendon Press, Oxford, UK, 1961.
2. J. A. Pople, W. G. Schneider and H. J. Bernstein, *High-Resolution Nuclear Magnetic Resonance*. McGraw-Hill, New York, USA, 1959.
3. E. D. Becker, *High-Resolution NMR*. 3rd ed. Academic, San Diego, CA, USA, 2000.
4. F. A. Bovey, *Nuclear Magnetic Resonance Spectroscopy*. 2nd ed. Academic, San Diego, CA, USA, 1988.
5. R. K. Harris, *Nuclear Magnetic Resonance Spectroscopy*. Pitman, London, UK, 1983.
6. Y.-C. Ning, *Structural Identification of Organic Compounds with Spectroscopic Techniques*. Wiley-VCH, Weinheim, Germany, 2005.
7. J. A. Weil and J. R. Bolton, *Electron Paramagnetic Resonance*. 2nd ed. Wiley, New York, NY, USA, 2007.
8. J. A. Weil, Tensors in magnetic resonance spectroscopy. *Int. EPR Soc. Newslett*, 2007, **17**(1), 13–14.
9. C. J. Jameson, Reply to ‘conventions for tensor quantities used in nuclear magnetic resonance, nuclear quadrupole resonance and electron spin resonance spectroscopy’. *Solid State Magn. Reson.*, 1998, **11**, 265–268.
10. F. K. Kneubühl, Symmetrie und mikrowellenspektren mehratomiger paramagnetischen zentren. *Phys. Kondens. Materie*, 1963, **1**(5), 410–447.
11. J. Kaski, J. Vaara and J. Jokisaari,  $^{13}\text{C}$ – $^{13}\text{C}$  spin–spin coupling tensors in benzene as determined experimentally by liquid crystal NMR and theoretically by *ab initio* calculations. *J. Am. Chem. Soc.*, 1996, **118**, 8879–8886.
12. J. A. Weil, T. Buch and J. E. Clapp, Crystal point group symmetry and microscopic tensor properties in magnetic resonance spectroscopy. *Adv. Magn. Reson.*, 1973, **6**, 183–257.
13. S. M. Nokhrin, J. A. Weil and D. F. Howarth, Magnetic resonance in systems with equivalent spin-1/2 nuclides. Part 1. *J. Magn. Reson.*, 2005, **174**, 209–218.
14. S. M. Nokhrin, D. F. Howarth and J. A. Weil, Magnetic resonance in systems with equivalent spin-1/2 nuclides. Part 2. *J. Magn. Reson.*, 2008, **193**, 1–9.
15. J. A. Weil, The hydrogen atom, revisited: parallel-field magnetic resonance. *Concepts Magn. Reson. Part A*, 2006, **28**, 331–336.
16. G. Baym, *Lectures on Quantum Mechanics*. New York, NY, USA, 1969.
17. M. Karplus and R. N. Porter, *Atoms & Molecules*. New York, NY, USA, 1970.
18. E. A. Harris and J. Owen, Bi-quadratic exchange between  $\text{Mn}^{2+}$  ions in  $\text{MgO}$ . *Phys. Rev. Lett.*, 1963, **11**(1), 9–10, Erratum **11**(2), 104.
19. T. Moriya, Anisotropic superexchange interaction and weak ferromagnetism. *Phys. Rev.*, 1960, **120**(1), 91–98.
20. K. Kodama, S. Miyahara, M. Takigawa, M. Horvatić, C. Berthier, F. Mila, H. Kageyama and Y. Ueda, Field-induced effects of anisotropic magnetic interactions in  $\text{SrCu}_2(\text{BO}_3)_2$ . *J. Phys.: Condens. Matter*, 2005, **17**(4), L61–L68.
21. G. Govil, Nuclear magnetic resonance studies in gases. *Appl. Spectr. Rev.*, 1973, **7**(1), 47–78.
22. C. J. Jameson, Gas-phase NMR spectroscopy. *Chem. Rev.*, 1991, **91**(7), 1375–1395.
23. C. B. LeMaster, Nuclear magnetic resonance spectroscopy of molecules in the gas phase. *J. Progr. NMR Spectr.*, 1997, **31**, 119–154.
24. C. Suarez, Gas-phase NMR spectroscopy. *Chem. Educator*, 1998, **3**(2), 1–18.
25. M. Kubiszewski, W. Makulski and K. Jackowski, Intermolecular effects on spin–spin coupling and magnetic shielding constants in gaseous difluoromethane. *J. Mol. Struct.*, 2004, **704**, 211–214.
26. K. Jackowski, W. Makulski, A. Szyprowska, A. Antušek, M. Jaszuński and J. Jusélius, NMR shielding constants in  $\text{BF}_3$  and magnetic dipole moments of  $^{11}\text{B}$  and  $^{10}\text{B}$  nuclei. *J. Chem. Phys.*, 2009, **130**, 044309, (1–5).
27. F. A. L. Anet and A. H. Dekmejian, Intrinsic steric deuterium isotope effects on proton and carbon-13 shifts. *J. Am. Chem. Soc.*, 1979, **101**(18), 5449–5451.
28. P. Tekely, D. Reichert, H. Zimmerman and Z. Luz, Initial conditions for carbon-13 MAS NMR 1D exchange involving chemically equivalent and inequivalent nuclei. *J. Magn. Reson.*, 2000, **145**, 173–183.



29. A. N. Klymachyov and N. S. Dalal, Magic angle spinning NMR on single crystals as a new aid in characterizing phase transitions: application to squaric acid. *Z. Phys. B*, 1997, **104**, 651–656.
30. K. C. Brown, R. L. Tyson and J. A. Weil, Conformation interchange in nuclear magnetic resonance spectroscopy. *J. Chem. Ed.*, 1998, **75**, 1632–1635.
31. M. Gee, R. E. Wasylishen, K. Eichele and J. F. Britten, Phosphorus chemical shift tensors for tetramethyldiphosphine: a  $^{31}\text{P}$  single-crystal NMR, dipolar-chemical shift NMR and *ab initio* molecular orbital study. *J. Phys. Chem. A*, 2000, **104**, 4598–4605.
32. G. Jeschke, W. Hoffbauer and M. Jansen, Survival of dipolar splitting between equivalent nuclei in high-speed MAS-NMR—Interpretation of the  $^{31}\text{P}$  coupling patterns for tetraphosphorus deca-oxide. *Chem. Eur. J.*, 1998, **4**(9), 1755–1761.
33. G. Wu, B. Sun, R. E. Wasylishen and R. G. Griffin, Spinning sidebands in slow-magic-angle-spinning NMR spectra arising from tightly J-coupled spin pairs. *J. Magn. Reson.*, 1997, **124**(2), 366–371.
34. G. Wu, D. Rovnyak, M. J. A. Johnson, N. C. Zanetti, D. G. Musaev, K. Morokuma, R. R. Schrock, R. G. Griffin and C. C. Cummins, Unusual  $^{31}\text{P}$  chemical shielding tensors in terminal phosphide complexes containing a phosphorus-metal triple bond. *J. Am. Chem. Soc.*, 1996, **118**, 10654–10655.
35. A.-R. Grimmer and G.-U. Wolf,  $^{31}\text{P}$ -MAS-NMR studies on crystalline and vitreous polymorphs of phosphorous pentoxide  $\text{P}_2\text{O}_5$ . *Eur. J. Solid State Inorg. Chem.*, 1991, **28**, 221–232.
36. M. D. Bruch (ed.) (1996). *NMR Spectroscopy Techniques*. 2nd ed. Marcel Dekker, New York, NY, USA, 1996.
37. E. Kuss and U. Brehm, Intensitätsformel für hyperfeinstruktur-linien bei *n* äquivalenten kernen mit beliebigem spinmoment I. *Org. Magn. Reson.*, 1971, **3**(3), 325–330.
38. J. A. Weil and D. F. Howarth, Magnetic resonance in systems with equivalent spin-1/2 nuclides. Part 3: ket analysis and spectral intensities. *J. Magn. Reson.*, 2009, **197**, 28–35.
39. J. A. Weil and D. F. Howarth, Magnetic resonance spectroscopy of extra-terrestrial methyl radical. *Can. J. Phys.*, 2009, **87**, 709–719.
40. H. S. Gutowsky, D. W. McCall and C. P. Slichter, Nuclear magnetic resonance multiplets in liquids. *J. Chem. Phys.*, 1953, **21**(2), 279–292.
41. G. W. Parker, Gauge-invariant calculation of the magnetic properties of the hydrogen molecule. *Mol. Phys.*, 1982, **46**(1), 183–192.
42. G. W. Parker and J. D. Memory, Gauge-invariant calculation of the magnetic susceptibility of the hydrogen molecule. *Phys. Rev. A*, 1981, **23**(5), 2099–2105.
43. F. Reif and E. M. Purcell, Nuclear magnetic resonance in solid hydrogen. *Phys. Rev.*, 1953, **91**(3), 631–642.
44. M. Bloom, Nuclear magnetic resonance and nuclear spin symmetry in molecular solids. *Pure Appl. Chem.*, 1972, **32**(1–4), 99–109.
45. J. Hatton and B. V. Rollin, Nuclear magnetic resonance at low temperatures. *Proc. Roy. Soc. (Lond.) A*, 1949, **199**, 222–237.
46. J. M. Brown and A. Carrington, *Rotational Spectroscopy of Diatomic Molecules*. Cambridge Press, Cambridge, UK, 2003.
47. J. M. B. Kellogg, I. I. Rabi, N. F. Ramsey, Jr. and J. R. Zacharias, The magnetic moments of the proton and the deuteron—The radiofrequency spectrum of  $\text{H}_2$  in various magnetic fields. *Phys. Rev.*, 1939, **56**, 728–743.
48. M. A. Strahemechny and R. J. Hemley, New *ortho*–*para* conversion mechanism in dense solid hydrogen. *Phys. Rev. Lett.*, 2000, **85**(26), 5595–5598.
49. K. Motizuki and T. Nagamiya, Theory of the *ortho*–*para* conversion in solid hydrogen. *J. Phys. Soc. Jpn.*, 1956, **11**, 93–104.
50. M. Fujio, J. Igarashi and T. Nakamura, Roton-dragging librions in the ordered solid hydrogen. *Prog. Theor. Phys.*, 1978, **59**(2), 329–350.
51. A. B. Harris, L. I. Amstutz, H. Meyer and S. M. Myers, Observation of pair interaction between *ortho* molecules in solid  $\text{H}_2$ . *Phys. Rev.*, 1968, **175**(2), 603–609.
52. R. Schweizer, S. Washburn and H. Meyer, NMR of dilute *o*- $\text{H}_2$  in solid *p*- $\text{H}_2$  at temperatures below 1 K. *Phys. Rev. Lett.*, 1978, **40**(15), 1035–1038, Erratum, 1978, **41**(13), 913.

53. R. Schweizer, S. Washburn, H. Meyer and A. B. Harris, NMR studies of single crystals of  $H_2$ : I–III. The spectrum of isolated *ortho*- $H_2$  pairs. *J. Low Temp. Phys.*, 1979, **37**(3/4), 289–308, and 309–341; 1980, **40**(1–2) 187–205.
54. G. Nagendrappa, Benzene and its isomers. *Resonance*, 2001, **6**(5), 74–78, Also, 2001, **6**(6).
55. P. A. Beckmann, M. Bloom and E. E. Burnell, Deuteron Zeeman relaxation of  $CD_4$  in the isotropic liquid, the liquid crystalline, and the solid state of several substances. *J. Chem. Phys.*, 1986, **54**(10), 5898–5905.
56. L. Pauling, The rotational motion of molecules in crystals. *Phys. Rev.*, 1930, **36**, 430–443.
57. Y. Kataoka, Theory of phase transitions in solid methanes. VI. *Prog. Theor. Phys.*, 1970, **43**(5), 1132–1147.
58. R. F. Code, Nuclear magnetism in solid methane. *Bull. Magn. Reson.*, 1982, **4**((3/4), 91–98.
59. A. Hüller, M. Prager, W. Press and T. Seidel, Phase III of solid methane: the orientational potential and rotational tunneling. *J. Chem. Phys.*, 2008, **128**, 034503, 1–9.
60. J. Higinbotham, B. M. Wood and R. F. Code, Time dependence of spin conversion in solid  $^{13}CH_3D$  by nuclear magnetic resonance. *Can. J. Phys.*, 1979, **57**, 1752–1757.
61. D. van der Putten, K. O. Prins, P. J. Kortbeek and N. J. Trappeniers, A high-pressure study of solid carbon tetrafluoride. *J. Phys. C: Solid State Phys.*, 1987, **20**, 3161–3173.
62. S. Rajan, K. Lalita and S. V. Babu, Intermolecular potentials from NMR data. II.  $CH_4$ ,  $CF_4$  and  $SiF_4$ . *Can. J. Phys.*, 1975, **53**, 1631–1634.
63. E. W. Schmidt, Hydrazine and its Derivatives. 2nd ed. New York, NY, USA, 2001.
64. N. G. Yunda, G. V. Lagodzinskaya and G. B. Manelis, The slowdown of fast proton exchanges and the  $^1H\{^{14}N\}$  NMR spectra of hydrazine and its methyl derivatives. *Russ. Chem. Bull.*, 1975, **24**(11), 2330–2333.
65. O. Edlund, A. Lund and A. Nillson, Hydrazine cation radical formation in  $\gamma$ -irradiated single crystals of hydrazinium hydrogen oxalate. *J. Chem. Phys.*, 1968, **49**(2), 749–755.
66. Y. Itagaki, A. Sanderuk, E. Sagstuen and A. Lund, ENDOR study of  $^{14}N$  hyperfine and quadrupole couplings of  $N_2D_4^{+\bullet}$  formed in deuterated  $Li(N_2H_5)SO_4$  single crystal. *J. Phys. Chem. A*, 2002, **106**, 2512–2622.
67. H. R. Falle, Temperature dependence of the electron resonance spectrum of the hydrazine positive ion. *Can. J. Chem.*, 1968, **46**, 1703–1706.
68. J. Goslar, W. Hilczer and P. Morawski, Low-temperature dynamics of hydrazinium ions in lithium hydrazinium sulfate (LHS) studied by electron spin echo (ESE) technique. *Solid State Ionics*, 2000, **127**, 67–72.
69. P. Morawski, S. K. Hoffmann, W. Hilczer and J. Goslar, ESR and electron spin echo studies of spin–lattice relaxation of hydrazinium radical in  $Li(N_2H_5)SO_4$  single crystal. *Acta Phys. Polon. A*, 1997, **91**, 1121–1129.
70. C. M. Deeley, P. Lewis and R. E. Richards, Proton magnetic resonance spectra of hydrazine salts. *Trans. Farad. Soc.*, 1954, **50**, 536–560.
71. R. R. Knispel and H. E. Petch, Proton rotating frame relaxation in lithium hydrazinium sulfate,  $Li(N_2H_5)SO_4$ . *Can. J. Phys.*, 1971, **49**, 870–875.
72. C.-F. Hoelger, E. Rössler, B. Wehrle, F. Aguilar-Parrilla and H.-H. Limbach, Self-decoupling of  $^{15}N$ – $^{14}N$  dipole–quadrupole couplings in  $^{15}N$  CPMAS NMR spectra and molecular motions in crystalline hydrazine sulfate, *p*-(diethylamino)benzaldehyde, and its solid solution in polycarbonate. *J. Phys. Chem.*, 1995, **99**, 14271–14276.
73. S. Chandra and N. Singh, Fast-proton transport in hydrazine sulphate: II. NMR linewidth and relaxation studies. *J. Phys. C: Solid State Phys.*, 1983, **16**, 3099–3103.
74. L. Pratt and R. E. Richards, Proton magnetic resonance spectra of hydrazine salts. *Trans. Farad. Soc.*, 1953, **49**, 744–751.
75. P.v.R. Schleyer, What is aromaticity? *Pure Appl. Chem.*, 1996, **68**(2), 209–218.
76. A. T. Balaban and Z. Simon, Aromaticity. Part V. Stability of monocyclic aromatic compounds. *Rev. Roumaine Chim.*, 1965, **10**, 1059–1092.
77. M. M. Folkendt, B. E. Weiss-Lopez and N. S. True,  $^1H$  and  $^{13}C$  spin–lattice relaxation on gaseous benzene. *J. Phys. Chem.*, 1988, **92**(17), 4859–4863.
78. T. Saitoh, Y. Nakamura and S. Shimokawa, Diffusion coefficient of benzene around the gas–liquid critical temperature. *Bull. Chem. Soc. Jpn.*, 1992, **65**, 3480–3481.

79. D. W. Aksnes and L. Kimtys,  $^1\text{H}$  and  $^2\text{H}$  NMR studies of benzene confined in porous solids: melting point depression and pore size distribution. *Solid State NMR*, 2004, **25**, 146–152.
80. C. F. Trendl, G. A. Mills and C. Dybowski, Platinum–proton coupling in the NMR spectrum of benzene on an alumina-supported platinum catalyst. *J. Phys. Chem.*, 1992, **96**(12), 5045–5048.
81. A. Saue and G. Englert, High-resolution nuclear magnetic resonance spectra of orientated molecules. *Phys. Rev. Lett.*, 1963, **11**(10), 462–464.
82. G. Englert, P. Diehl and W. Niederberger, Proton magnetic resonance spectra of benzene and benzene- $1\text{-}^{13}\text{C}$  in isotropic and in nematic solution. *Z. Naturforsch.*, 1971, **26a**, 1829–1836.
83. H. Günther, H. Seel and M. E. Günther, Carbon-13,  $^1\text{H}$  coupling constants for benzene and the tropylium ion. *Org. Magn. Reson.*, 1978, **11**(2), 97–102.
84. L. M. Ryan, R. C. Wilson and B. C. Gerstein, The proton magnetic shielding anisotropy in benzene. *J. Chem. Phys.*, 1977, **67**(9), 4310–4311.
85. A. T. Balaban, Valence isomerism of cyclopolyenes. *Rev. Roumaine Chim.*, 1966, **11**(9), 1097–1116, Erratum, 1967, 12(1), 101.
86. E. E. van Tamelen and S. P. Pappas, Bicyclo[2.2.0]hexa-2,5-diene. *J. Am. Chem. Soc.*, 1963, **85**(20), 3297–3298.
87. D. Bryce-Smith, A. Gilbert and D. A. Robinson, Direct transformation of the second excited singlet state of benzene into Dewar benzene. *Ang. Chem. Int. Ed.*, 1971, **10**(10), 745–746.
88. M. Christl, Benzvalene—properties and synthetic potential. *Angew. Chem. Int. Ed. Engl.*, 1981, **20**, 529–546.
89. P. J. Harman, J. E. Kent, M. F. O'Dwyer and D. W. T. Griffith, Photochemistry of benzene isomers. 2. Benzvalene and Dewar benzene. *J. Phys. Chem.*, 1981, **85**, 2731–2733.
90. T. J. Katz, E. J. Wang and N. Acton, A benzvalene synthesis. *J. Am. Chem. Soc.*, 1971, **93**(15), 3782–3783.
91. K. E. Wilzbach, J. E. Ritscher and L. Kaplan, Benzvalene, the tricyclic isomer of benzene. *J. Am. Chem. Soc.*, 1967, **89**(4), 1031–1032.
92. T. J. Katz and N. Acton, Synthesis of prismane. *J. Am. Chem. Soc.*, 1973, **95**(8), 2738–2739.
93. W. E. Billups and M. M. Haley, Bicycloprop-2-enyl ( $\text{C}_6\text{H}_6$ ). *Angew. Chem. Int. Ed. Engl.*, 1989, **28**, 1711–1712, *Angew. Chem.*, 1989, 101, 1735–1736.
94. T. Bally, Cyclobutadiene: the antiaromatic paradigm? *Angew. Chem. Int. Ed.*, 2006, **45**(40), 1–4.
95. G. Maier, Tetrahedrane and cyclobutadiene. *Angew. Chem.*, 1988, **27**(3), 309–332.
96. L. Watts, J. D. Fitzpatrick and R. Pettit, Cyclobutadiene. *J. Am. Chem. Soc.*, 1965, **87**(14), 3253–3254.
97. A. M. Orendt, B. R. Arnold, J. G. Radziszewski, J. C. Facelli, K. D. Malsch, H. Strub, D. M. Grant and J. Michl,  $^{13}\text{C}$  NMR and polarized IR spectra of vicinally labeled [ $^{13}\text{C}_2$ ]cyclobutadiene in an argon matrix: interconversions of valence isomers. *J. Am. Chem. Soc.*, 1988, **110**(8), 2648–2650.
98. P. B. Karadkov, Ground- and excited-state aromaticity and antiaromaticity in benzene and cyclobutadiene. *J. Phys. Chem. A*, 2008, **112**(31), 7303–7309.
99. L. C. Snyder and S. Meiboom, Molecular structure of cyclopropane from its proton NMR in a nematic solvent. *J. Chem. Phys.*, 1967, **47**(4), 1480–1487.
100. W. Makulski and M. Wilczek, Nuclear magnetic shielding and indirect spin–spin coupling constants in cyclopropane. Gaseous and liquid NMR measurements. *Polish J. Chem.*, 2006, **80**(7), 1055–1060.
101. K. C. Thompson, D. L. Crittenden and M. J. T. Jordan,  $\text{CH}_5^+$ : chemistry's chameleon unmasked. *J. Am. Chem. Soc.*, 2005, **127**, 4954–4958.
102. G. Rasul, G. K. S. Prakash and G. A. Olah, Calculated  $^{11}\text{B}$ – $^{13}\text{C}$  NMR chemical shift relationship in hypercoordinate methonium and boronium ions. *Proc. Natl. Acad. Sci. USA*, 1998, **95**, 7257–7259.
103. R. S. Berry, Correlation of rates of intramolecular tunneling processes, with application to some group-V compounds. *J. Chem. Phys.*, 1960, **32**(3), 933–938.
104. L. G. Alexander and D. Cornwell, NMR spectra of  $\text{ClF}_3$  and  $\text{ClF}$ : gaseous spectra and gas-to-liquid shifts. *J. Chem. Phys.*, 1964, **41**(7), 2098–2107.
105. J. J. Lehmann and E. Goldstein, The potential energy surface of  $\text{ClF}_3$ . *J. Chem. Ed.*, 1996, **73**(11), 1096–1098.
106. D. L. Bryce and R. E. Wasylshen, Symmetry properties of indirect nuclear spin–spin coupling tensors: first-principles results for  $\text{ClF}_3$  and  $\text{OF}_2$ . *J. Am. Chem. Soc.*, 2000, **122**, 11236–11237.

107. E. V. Anslyn and D. A. Dougherty, *Modern Physical Organic Chemistry*. University Science Books, Sausalito, CA, USA, 2006.
108. A. Allerhand, F.-M. Chen and H. S. Gutowsky, Spin-echo NMR studies of chemical exchange. III. Conformational isomerization of cyclohexane and  $d_{11}$ -cyclohexane. *J. Chem. Phys.*, 1965, **42**(9), 3040–3047.
109. B. D. Ross and N. S. True, NMR spectroscopy of cyclohexane. Gas-phase conformational kinetics. *J. Am. Chem. Soc.*, 1983, **105**(15), 4871–4875.
110. K. J. McGrath and R. G. Weiss, Rate of chair-to-chair interconversion of cyclohexane- $d_{12}$  in the neat plastic crystalline phase. *J. Phys. Chem.*, 1993, **97**(11), 2497–2499.
111. P. C. Lauterbur,  $^{13}\text{C}$  and  $^1\text{H}$  Nuclear magnetic resonance spectra of cycloalkanes. *J. Am. Chem. Soc.*, 1964, **86**, 1870–1871.
112. G. Gill, D. M. Pawar and E. A. Noe, Conformational study of *cis*-1,4-di-*tert*-butylcyclohexane by dynamic NMR spectroscopy and computational methods. Observation of chair and twist-boat conformations. *J. Org. Chem.*, 2005, **26**, 10726–10731.
113. A. Allerhand and H. S. Gutowsky, Spin-echo NMR studies of chemical exchange. VI. Rearrangement of bullvalene and of its silver nitrate complex. *J. Am. Chem. Soc.*, 1965, **87**(18), 4092–4096.
114. M. Saunders, Measurement of the rate of rearrangement of bullvalene. *Tetrahedron Lett.*, 1963, **4**, 1699–1702.
115. C. S. Yannoni, Nuclear magnetic resonance spectrum of oriented bullvalene. *J. Am. Chem. Soc.*, 1970, **92**(17), 5237–5238.
116. S. Schlick, Z. Luz, R. Poupko and H. Zimmerman, Cope rearrangement and molecular reorientation in solid bullvalene: a single-crystal deuterium NMR study. *J. Am. Chem. Soc.*, 1992, **114**(11), 4315–4320.
117. M. Ichinohe, M. Toyoshima, R. Kinjo and A. Sekiguchi, Tetrasilatetrahedranide: a silicon cage anion. *J. Am. Chem. Soc.*, 2003, **125**(44), 13328–13329.
118. L. D. Barron, C. Meehan and J. Vrbancich, Experimental confirmation that the isotropic  $g$ -factor of  $\text{IrCl}_4^{2-}$  is negative. *Mol. Phys.*, 1980, **41**(4), 945–947.
119. B. Bleaney, Electron spin resonance intensity in anisotropic substances. *Proc. Phys. Soc. (Lond.)*, 1960, **75**, 621–623.
120. M. H. L. Pryce, Sign of  $g$  in magnetic resonance, and the sign of the quadrupole moment of  $^{237}\text{Np}$ . *Phys. Rev. Lett.*, 1959, **3**(8), 375.
121. M. E. Foglio, The determination of the sign of the spin-Hamiltonian parameters. *Il Nuovo Cimento B*, 1967, **50**(1), Erratum, 1967, 51(2), 570.
122. J. E. Geusic and L. C. Brown, Computation of the principal components of an asymmetric  $g$  tensor from paramagnetic resonance data. *Phys. Rev.*, 1958, **112**(1), 64–65.
123. F. K. Kneubühl, Anisotropic spin-orbit interactions in paramagnetic resonance. *Phys. Lett.*, 1962, **2**, 163–164, Erratum, 1963, 4(3), 208.
124. F. S. Ham, Anisotropic spin-orbit interactions in paramagnetic resonance. *J. Phys. Chem. Solids*, 1963, **24**, 1165–1174.
125. A. Rockenbauer and P. Simon, Ambiguity problems of the spin-Hamiltonian. *J. Magn. Reson.*, 1976, **22**, 243–263.
126. R. F. Schneider, Asymmetry in magnetic second-rank tensor quantities. *J. Chem. Phys.*, 1968, **48** (11), 4905–4909.
127. A. D. Buckingham and S. M. Malm, Asymmetry in the nuclear magnetic shielding tensor. *Mol. Phys.*, 1971, **22**(6), 117–1130.
128. H. M. McConnell, A pseudo-vector nuclear hyperfine interaction. *Proc. Natl. Acad. Sci. USA*, 1958, **44**, 766–767.
129. A. Rockenbauer and P. Simon, Second-order perturbation treatment of spin Hamiltonian for low symmetry. *J. Magn. Reson.*, 1973, **11**, 217–218.
130. R. Skinner and J. A. Weil, Spin-Hamiltonian energies. *J. Magn. Reson.*, 1976, **21**, 271–283.
131. J. A. Weil, Germanium-hydrogen-lithium center in  $\alpha$ -quartz. *J. Chem. Phys.*, 1971, **55**(10), 4685–4698.
132. R. S. Eachus, R. H. D. Nuttall, M. T. Olm, W. G. McDugle, F. K. Koschnick, Th. Tangleiter and J.-M. Spaeth, Oxygen defects in BaFBr and BaFCl. *Phys. Rev. B*, 1995, **52**(6), 3941–3950.

133. M. Rudin, A. Schweiger and Hs. H. Günthard, On the electronic structure of  $N,N'$ -ethylenebis (acetylacetonatiminato)Co(II), Co(II)acacen II. ENDOR and DOUBLE ENDOR of ligand nuclei. *Mol. Phys.*, 1982, **46**(5), 1027–1044.
134. A. Rockenbauer and P. Simon, Perturbation solution of the spin Hamiltonian of low symmetry using the projector technique. *Mol. Phys.*, 1974, **28**(5), 1113–1126.
135. R. L. Belford and J. R. Pilbrow, Motionally averaged hyperfine structure and asymmetries in low-symmetry EPR. *J. Magn. Reson.*, 1973, **11**, 381–387.
136. A. D. Buckingham, P. Pyykkö, J. B. Robert and L. Wiesenfeld, Symmetry rules for the indirect nuclear spin–spin coupling tensor, revisited. *Mol. Phys.*, 1982, **46**(1), 177–182.
137. A. D. Buckingham and I. Love, Theory of the anisotropy of nuclear spin coupling. *J. Magn. Reson.*, 1970, **2**, 338–351.
138. R. G. Griffin, J. D. Ellett, M. Mehring, J. G. Bullitt and J. S. Waugh, Single crystal study of the  $^{19}\text{F}$  shielding tensors of a trifluoromethyl group. *J. Chem. Phys.*, 1972, **57**(5), 2147–2155.
139. D. R. Spearing and J. F. Stebbins, The  $^{29}\text{Si}$  NMR shielding tensor in low quartz. *Am. Miner.*, 1989, **74**(7–8), 956–959.
140. J. A. Weil, Use of symmetry-related crystal sites for measuring tensor properties in magnetic resonance. *J. Magn. Reson.*, 1973, **10**, 391–393, *Erratum*: Note that the last 4 rows of Table I are tainted. Please see the correct version in Table V of Ref. 12.
141. V. Gérardy-Montouillout, C. Malveau, P. Tekely, Z. Olender and Z. Luz, ODESSA, a new 1D NMR exchange experiment for chemically equivalent nuclei in rotating solids. *J. Magn. Reson. A*, 1996, **123**, 7–15.
142. J. A. Weil and M. J. Mombourquette, Fortran Program EPR–NMR, Version 6.5.3 (New version forthcoming), Department of Chemistry, University of Saskatchewan, Saskatoon, SK, S7N 5C9 Canada 2007.
143. H. J. Juretschke, Crystal Physics. W. A. Benjamin, Reading, MA, USA, 1974.
144. H. Goldstein, C. P. Poole, Jr. and J. L. Safko, Classical Mechanics. 3rd ed. New York, NY, USA, 2002.
145. J. F. Nye, Physical Properties of Crystals—Their Representation by Tensors and Matrices. Clarendon Press, Oxford, UK, 1957.
146. G. Arfken and H. J. Weber, Mathematical Methods for Physicists. 6th ed. Elsevier/Academic Press, San Diego, CA, USA, 2005, pp. 133ff.
147. L. Brand, Vector and Tensor Analysis. New York, NY, USA, 1947.
148. D. R. Lovett, Tensor Properties of Crystals. Institute of Physics Publishing, Bristol, UK, 1989, 1994.
149. D. E. Sands, Vectors and Tensors in Crystallography. Addison-Wesley, Reading, MA, USA, 1982.
150. W. A. Wooster, Tensors and Group Theory for the Physical Properties of Crystals. Oxford University Press, London, UK, 1973.
151. A. Abragam and B. Bleaney, Electron Paramagnetic Resonance of Transition Ions. Clarendon Press, Oxford, UK, 1970.
152. G. E. Pake and T. L. Estle, The Physical Principles of Electron Paramagnetic Resonance. 2nd ed. W. A. Benjamin, Reading, MA, USA, 1973.
153. J. L. Synge and A. Schild, Tensor Calculus. University of Toronto Press, Toronto, ON, Canada, 1949.
154. R. Skinner and J. A. Weil, Spin-Hamiltonian energies and state vectors II. *J. Magn. Reson.*, 1978, **29**, 223–241.

# CHAPTER 2

## Protein Dynamics as Reported by NMR

Zoltán Gáspári\* and András Perczel\*,†

---

Contents		
	1. Introduction	36
	2. Motions and Time Scales in Proteins	38
	3. Representation of Protein Structure and Dynamics	39
	4. Exploring Protein Structure and Dynamics: A Brief Overview of Techniques	42
	4.1. Electron microscopy	43
	4.2. ECD and VCD spectroscopy	43
	4.3. UV fluorescence	43
	4.4. Hydrogen–deuterium exchange mass spectroscopy (HXMS)	44
	4.5. X-ray diffraction	44
	4.6. Molecular modelling	45
	5. NMR Spectroscopy for Determining Protein Structure and Dynamics	46
	5.1. Basics of biomolecular NMR	46
	5.2. Dynamical information from NMR	47
	5.3. Chemical shifts	48
	5.4. Nuclear Overhauser effect	49
	5.5. Scalar couplings	50
	5.6. Residual dipolar couplings (RDCs)	51
	5.7. Heteronuclear relaxation experiments and analysis	52
	5.8. Paramagnetic relaxation enhancement	55
	5.9. H–D exchange followed by NMR	56
	6. Examples Highlighting the Role of Protein Internal Dynamics in Biological Processes	58
	6.1. Characterization of systems with supra- $\tau_c$ motions	58
	6.2. Characterization of systems with sub- $\tau_c$ motions	63

\* Laboratory of Structural Chemistry and Biology, Institute of Chemistry, Eötvös Loránd University, Pázmány Péter sétány 1/A, Budapest, Hungary

† Protein Modeling Group HAS-ELTE, Institute of Chemistry, Eötvös Loránd University, Budapest, Hungary

7. Concluding Remarks	69
Acknowledgements	72
References	72

---

**Abstract**

Among biomolecules, proteins fulfil the most diverse roles. Recent advances in NMR-spectroscopy demonstrate that these molecules can be characterized by motions on a wide range of time scales, and besides their three-dimensional (3D) structures, dynamics is also fundamental to truly understand their biological activity. The present review focuses on NMR techniques suitable to assess the internal dynamics of proteins from picoseconds to minutes. After a brief introduction of protein motions and different techniques used to capture them, we describe the dynamical aspects of a diverse set of NMR observables in detail. We also present some examples of investigations on various systems aimed to understand Dynamics–Structure–Activity Relationships (DSARs) of proteins.

**Key Words:** Protein structure, Internal dynamics, Conformational ensemble, Conformational averaging, NMR observables, Dynamics–Structure–Activity Relationship.

---

## 1. INTRODUCTION

Human perception is poised to treat objects as entities with a defined shape in the 3D space. The fourth dimension, time, is usually considered as a separate coordinate and is traditionally not linked inherently to object properties even though, for example in the case of living “objects”, birth and deterioration are typically accompanied by drastic changes in shape. Moreover, the temporal aspects of objects are approached conceptually differently for both ends of the size scale of our known world: physicists describe the universe in terms of the space–time concept, considering a set of four interdependent coordinates, and for elemental particles “location and velocity” notions—according to Heisenberg’s uncertainty principle—are not plausible to separate. Biomolecules—like proteins—are nanoparticles and belong close to the regime where both quantum mechanical and classical physical phenomena are relevant. However, we are tempted to picture them as entities with a well-defined 3D shape which is used to explain their biochemical function. This otherwise tremendously useful description dates back to the early days of structural biology (*E. Fischer*) and was supported by the basically static structures determined by X-ray crystallography for over half a century. However, it is now clear that proteins are highly dynamic over a wide range of time scales and their description cannot be complete without understanding the nature of their internal motion(s).

Before describing the protein world, let us reflect on motion and time scales in general. When we consider human life on Earth, we observe a very wide range of different motions, naturally distinct from—but not completely dissimilar to—

those relevant for macromolecules. Taking the example of a car race on a circuit, each car is speeding over the course of the race according to its own instantaneous speed. Over the full race, the average speed of the car can be calculated, but this figure will tell us nothing about its actual instantaneous speed “distribution”, since the car may not have held any particular speed for longer than seconds. When zooming out of the track for an aerial view for example as seen from a helicopter above, many cars on different positions of the circuit will be seen. In the middle of the race, at a significant time after its start, the overall picture at different snapshots will be very similar with cars scattered over the full track. This is a vague analogue of the ergodic hypothesis, that is the states assumed by a single entity over time are similar to the states assumed by many entities at a single moment. If a fly is buzzing around in the cockpit of a racing car, its movement can be described in two ways. First, we might attach our reference coordinate system to the car and we will observe the familiar random pattern of insect flight. However, if we observe the motion from the circuit (grandstand), we will see the superposition of the motions of the car and the fly within. If we draw the trajectory of the fly over several circles of the race, we will be able to separate the two motions because of their different and characteristic contributions to the trajectory and time scale. However, this would be a far more complicated problem if we were to observe only a few seconds of the race. In the latter case, only the different speeds and nature of motions could be of help and we would most probably need sophisticated mathematical methods to complete such a separation. Having a slow camera taking pictures at every minute only, it would also hinder the identification of the contributions from different movements. Finally, all these motions considered are superposed to Earth’s own orbiting and spinning. It is important to note that events on Earth cannot only be quicker (occur on shorter time scales) than its geological motions as for example plate tectonics occurs on a time-scale orders of magnitudes slower. Thus, a complete description of the flight of the fly in the cockpit would require the use of time scales from seconds to millions of years,<sup>a</sup> spanning over 13 orders of magnitude. This is not unlike in proteins, where in solution state both much slower and faster motions than their diffusion occur regularly, spanning also more than 10 orders of magnitude of time scales, ranging from picoseconds to seconds/minutes/hours.

In proteins, all these different motions are localized within one macromolecule or a few molecules bound to each other. Thus, the space of motions is limited compared to the car race picture, just as if we were to explore the motions of selected parts of the engine and the cockpit during the race. Clearly, movements of the pistons and the crankshaft occur on a different time scale than that of the wheels or the full car, not to mention the driver-controlled steering wheel and transmission. In summary, molecular motions cover a wide range of time scales, occur in a spatially limited manner and, unlike cars and racing events, are not even directly observable. That is why we need sophisticated experimental techniques to characterize dynamics in biomacromolecules.

<sup>a</sup> Provided the fly lives long enough.

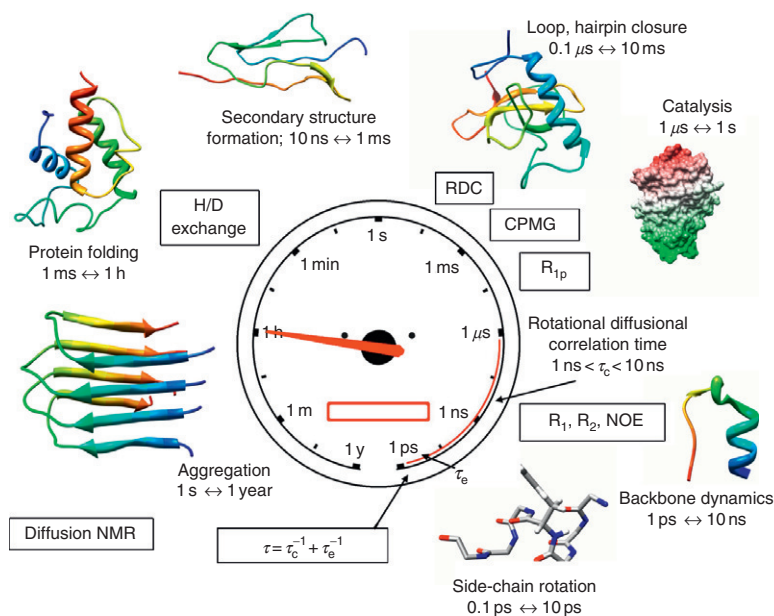


In this review, we present NMR spectroscopic techniques currently used to study protein dynamics at various time scales. Instead scrutinizing each technique, we put emphasis on their fundamentals. On the other hand, we enumerate a number of NMR-derived parameters and discuss their relation and relevance to macromolecular motions. As a complement, we briefly describe several other techniques capable of capturing protein dynamics, as synthesis of different methods is the most fruitful way to understand biomolecular processes.

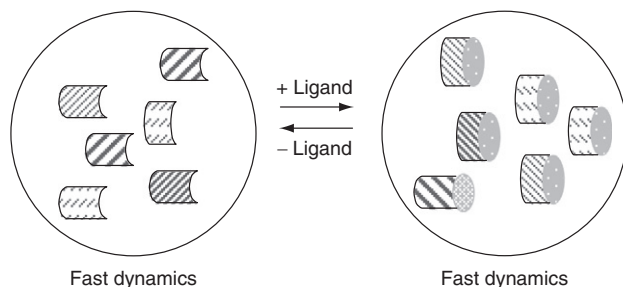
## 2. MOTIONS AND TIME SCALES IN PROTEINS

Conformational motions in proteins span at least 14 orders of magnitude in terms of time scales, from picoseconds to minutes/hours (Scheme 1).

An important reference point is the rotational correlation time of the protein molecule itself, denoted  $\tau_c$ , (also the notation  $\tau_m$  is used) corresponding to the time required for the molecule to rotate one radian (Scheme 1). The rotational motion/diffusion of the molecule can be isotropic or anisotropic and depends on the size and shape of the molecule as well as on solvent viscosity. Thus, in aqueous



**Scheme 1** The motional time scale of proteins covers over 14 orders of magnitude, starting from the slowest one (formation of aggregates requires typically minutes to hours) up to the fastest event; side-chain rotation (<ps). NMR-based techniques capable of capturing dynamics at different time scales are shown boxed and positioned approximately at their relevant range of time scales.



**Scheme 2** Protein dynamics and ligand recognition. Fast motions are indicated by different shadings, slow motions by different (narrow vs. elongated) shape. Ligand binding shifts the population and is associated by changes in the fast dynamics.

solutions, motion is influenced by temperature and, to a lesser extent, the pH and viscosity. In proteins,  $\tau_c$  is usually on the order of nanoseconds. Internal motions can be slower or faster than this overall rotation. If molecular motion is characterized by a slow and a fast time scale with the respective correlation times  $\tau_c$  and  $\tau_e$ , then the resulting characteristic time  $\tau$  can be expressed as<sup>1</sup>

$$\tau^{-1} = \tau_c^{-1} + \tau_e^{-1} \quad (1)$$

where  $\tau_e$  is the internal correlation time. Protein function is always connected to partner recognition, the latter being either another protein, nucleic acid, a small ligand, water or just a single electron. Proteins in general exist in multiple conformational states in solution, which is perturbed upon interaction. The mechanism and the time scale of this perturbation vary for different proteins. The currently emerging view is that most proteins work, at least to some extent, via the mechanism called conformer selection.<sup>2</sup> This means that the conformational diversity of the free proteins in solution covers those in the bound form, in other words, the states with high affinity towards the ligand are present in free form. Ligand binding modifies the energy of the different states and thus shifts the population towards the bound forms just like in any other chemical equilibrium (Scheme 2).

### 3. REPRESENTATION OF PROTEIN STRUCTURE AND DYNAMICS

All representations of proteins are models of the actual structures themselves. These models can be built for different purposes, thus may or may not contain information about specific aspects of interest.<sup>3</sup> The most common representations of proteins are based on 3D atomic coordinates, constituting the basis of the Protein Data Bank (PDB) format used to store as many as 63,000 macromolecular structures in the PDB<sup>4</sup> as of February, 2010. These models, the majority of them determined by X-ray crystallography, are generally static in nature and give the impression that proteins adopt a single or just a few well-defined conformations

in their native state. NMR-derived structures are more often represented by multiple conformers (multiple models in the PDB file), mostly because the NMR-derived structural parameters are compatible with all of them. The other reason is that these ensembles are sometimes believed to represent some of the internal dynamics of the proteins investigated. However, this is not necessarily the case, given that another important aspect of selecting models to be deposited in the PDB is the high similarity between the models to demonstrate that the experimental parameters correspond to a well-defined structure. Thus, these structures can be regarded as over-refined ones with the aim of approaching the precision of X-ray crystallography (see below). Another way of representing molecular structures is to use internal coordinates such as bond lengths, bond angles and torsion angles. Although not used in current databases, such internal representations are used by several programs used for structure calculations (e.g. CYANA<sup>5</sup>).

A common approach to describe protein motions is the use of (auto)correlation functions. An autocorrelation function  $C(t)$  can be defined as:

$$C(t) = \frac{1}{5} e^{-t/\tau_c} \quad (2)$$

Such a function characterizes the “memory” of the arrangement of a set of vectors within the sample (for more see Ref. 6). This form is valid for a vector (e.g. bond vector defined by two atoms) fixed to the molecule, thus its motion is completely determined by the isotropic molecular tumbling of the protein (characterized by  $\tau_c$ ). If the vector motion has an additional, fast and spatially restricted component characterized by  $\tau_e$ , the correlation function becomes somewhat more complicated:

$$C(t) = \frac{1}{5} S^2 e^{-t/\tau_c} + \frac{1}{5} (1 - S^2) e^{-t/\tau_e} \quad (3)$$

where  $0 \leq S^2 \leq 1$  reflects the extent of the spatial restriction and is denoted as generalized order parameter. Order parameters related to motions on different time scales are widely used in describing protein motions and are discussed in more detail below. For different forms of the correlation function see Ref. 1, a comprehensive review on protein dynamics in the ps–ns time scale and heteronuclear relaxation.

In practice, the Fourier transform of the correlation function, denoted as spectral density function,  $J(\omega)$ , is more often used to express the interrelationships of parameters<sup>b</sup>:

$$J(\omega) = 2 \int_0^\infty C(t) \cos(\omega t) dt \quad (4)$$

<sup>b</sup> The relation between the correlation function and the spectral density function is analogous to that of between the FID and the (FT)-NMR spectrum, a Fourier pair well-known for NMR spectroscopists.

For example, in the above case (Equations (2) and (3)), the corresponding spectral density functions are as follows:

$$J(\omega) = \frac{2}{5} \left( \frac{\tau_c}{1 + (\omega\tau_c)^2} \right) \quad \text{and} \quad J(\omega) = \frac{2}{5} \left( \frac{S^2\tau_c}{1 + (\omega\tau_c)^2} + \frac{(1 - S^2)\tau}{1 + (\omega\tau)^2} \right) \quad (5)$$

For the relationship between  $\tau$ ,  $\tau_c$  and  $\tau_e$ , the last of which is not explicit above, refer to Equation (1).

In all of the above descriptions and equations, it was assumed that molecular tumbling is isotropic in the solution. This is an idealized case that can be approximated by real proteins only in fortunate instances. In general, proteins exhibit totally anisotropic tumbling<sup>7</sup>; but in special cases, the simplification of only an axially symmetric motion is used, for which two of the molecular axes are assumed to be identical and thus the corresponding rotational diffusion tensor can be simplified.

Adding dynamical information to the static conformers can be achieved in several ways. In crystallography, *B*-factors (see below) are assigned to each atom representing the uncertainty in its coordinates caused primarily by thermal fluctuations. In exceptionally high-resolution structures even the anisotropy of these fluctuations can be depicted. In NMR, it is not possible to obtain information about the fluctuations of all atoms but only of selected motions of certain atom types (see below). Therefore, it is much more common to define order parameters reflecting the extent of the conformational space occupied by the bonds involved in the detected motions.<sup>8</sup> The general form of the order parameters can be written as:

$$S_i^2 = \frac{4\pi}{5} \sum_{k=-2}^2 \langle Y_{2k}^i(\Theta, \Phi) \rangle \langle Y_{2k}^{i*}(\Theta, \Phi) \rangle \quad (6)$$

where  $i$  is the locus investigated,  $Y_{2k}^i(\Theta, \Phi)$  is the spherical harmonics of the degree  $2k$  for the vector direction given by the polar coordinates  $\Theta$  and  $\Phi$ . Angular brackets denote integration over the vector directions. Equation adapted from Ref. 9.

The value of the general order parameter  $S^2$  is between 0 and 1. Value 0 corresponds to totally unrestricted motion, while value 1 to fully restricted motion. As these parameters are commonly interpreted within the internal molecular reference frame,<sup>c</sup> the value of 1 means that the bond is constrained to a fixed orientation and all of its motions correspond to the overall tumbling of the molecule.

Such parameters can be derived from a number of NMR measurements and can be treated similarly to *B*-factors although with lower resolution (e.g. an order parameter obtained for backbone NH bond vector is assigned to all bonds of the

<sup>c</sup> The internal molecular reference frame, although commonly used, is far from being defined unambiguously. The reason of this is that due to the dynamics of the molecule there is no "fix part" which could be objectively chosen for reference. In practical applications, measurement of geometric parameters relative to the reference frame is often implemented by using least-squares fitting of the backbone atoms of the conformers investigated before obtaining the values.

residue in question). Such  $B$ -factors can be used in representations where the colours or thickness of the lines corresponding to the residues are proportional to these parameters.

Order parameters can also be calculated from an ensemble of structures given in Cartesian coordinates:

$$S_{ab}^2 = \frac{3}{2} \left( \langle \hat{x}_{ab}^2 \rangle^2 + \langle \hat{y}_{ab}^2 \rangle^2 + \langle \hat{z}_{ab}^2 \rangle^2 + 2\langle \hat{x}_{ab}\hat{y}_{ab} \rangle^2 + 2\langle \hat{x}_{ab}\hat{z}_{ab} \rangle^2 + 2\langle \hat{y}_{ab}\hat{z}_{ab} \rangle^2 \right) - \frac{1}{2} \quad (7)$$

where  $S_{ab}^2$  is the order parameter for the bond between atoms  $a$  and  $b$ , and  $\hat{x}_{ab}$  are the normalized components of the bond vector. Equation adapted from Ref. 10.

Consequently, there are approaches to convert NMR-derived order parameters into structural information in the form of conformational ensembles of proteins.<sup>10,11</sup> Such ensembles, in contrast to those obtained by “conventional” NMR calculations, reflect directly the experimentally observed dynamics at the time scale probed by the parameter actually used. The latter set of structures, often denoted “dynamic conformational ensembles”, have the advantage of direct visualization of the conformations available for the protein and can be compared to other conformers of the same protein obtained under different conditions (most prominently binding partners) in a straightforward manner. Structural ensembles can of course be “back-transformed” to residue-specific numbers such as local RMSD values which can be used to generate the representations described above.

## 4. EXPLORING PROTEIN STRUCTURE AND DYNAMICS: A BRIEF OVERVIEW OF TECHNIQUES

In contrast to macroscopic objects, molecules cannot be observed directly: we cannot see them and thus cannot acquire information on objects smaller than  $0.2\ \mu\text{m}$  (diffraction limits). We have to rely on different techniques yielding different types of information about proteins. Each technique probing the structure will be sensitive to dynamics on different time scales, and no single technique can be expected to give (and no known technique is indeed capable of giving) information relevant to all time scales applicable to internal motions of macromolecules. Thus, it is important to stress that we are only able to build models of biomolecular structure and dynamics<sup>d</sup> which might be appropriate to the description and understanding of selected but by far not all existing aspects of protein dynamics and function. In the following section, we will overview techniques that can be used to get structural and dynamic information on proteins.

<sup>d</sup> In natural sciences, it is common to have models to understand entities and phenomena. In structural biology, all known protein structures are models in that sense. However, for a structural biologist the word “model” usually means a purely theoretical set of coordinates of proteins most often built without any experimental structural data on the modelled system (e.g. a “homology model”) and therefore the word has a slightly negative overtone.

## 4.1. Electron microscopy

Different variants of electron microscopy (EM) can be used to visualize the shape of proteins and their complexes over the size of several nanometers. The basic principle of EM is to take 2D pictures of the particles immobilized on a surface. 3D reconstruction of the particle shape is possible if the pictures represent a sufficient range of the possible aspects corresponding to different orientations of the particles on the surface. Due to its relatively low resolution and static nature of imaging, EM is not capable of discriminating subtle structural changes associated with fast motions. However, cryo-EM is a leading technique today in studying the shape of different functional states of supramolecular complexes such as the ribosome.<sup>12</sup> This requires that the distinct molecular states should be available for isolation and stabilization for the course of the investigation—a hardly achievable condition in practice. Shape contours obtained by EM can be “filled” with higher (e.g. atomic) resolution details obtained using other techniques, resulting in approximate models for the conformations and interactions of protein components within complexes.<sup>13</sup>

## 4.2. ECD and VCD spectroscopy

UV or Electronic (ECD) and Vibrational Circular Dichroism spectroscopy is commonly used for rapid, non-atomic level structural analysis of proteins. The secondary structure content of proteins adopting a well defined and single conformer can be analyzed and the induced structural shifts can be monitored via CD. Well-established post-experimental data analyzing methods are used for the interpretation of a variety of global structural information. For the more dynamical systems, as peptides and protein fragments are, such a “simple” CD based structure elucidation suffers severe inherent limitations. Unlike for globular proteins, mobile parts and fragments less frequently adopt a single 3D-fold in a time average manner. These units can exhibit an ensemble of conformers composed of a multitude of substantially different structures, picked up in principle, both by ECD- and VCD-spectroscopy. The interpretation of these raw spectral data of highly dynamic molecular systems can be awkward. *In situ* deconvolution algorithms (singular value decomposition,<sup>14</sup> variable selection,<sup>15</sup> locally linearized model,<sup>16</sup> self-consistent method,<sup>17</sup> principal component factor analysis,<sup>18</sup> neural network,<sup>19</sup> matrix descriptor,<sup>20</sup> convex constraint analysis<sup>21</sup>) could be of great help.

## 4.3. UV fluorescence

A variety of experimental setups were developed for structure analysis of proteins, based on the excitation of the tryptophan moiety (the most brightly fluorescent proteogenic amino acid residue), that produces an intrinsic fluorescence emission of a folded protein. Tryptophane residues excited at wavelength values around 280–290 nm emit at a characteristic wavelength range (330–350 nm) thus reporting on how much this residue is buried within the protein. Techniques such

as fluorescence quenching (FQ), fluorescence resonance energy transfer (FRET), fluorescence correlation spectroscopy (FCS), etc. were successfully applied for studying folding propensities of globular proteins as well as their re- and unfolding processes. There are additional nice FRET measurements on the internal dynamics of intrinsically disordered proteins (IDPs), such as Sup35 prion, in [Ref. 22](#). As sensitive as CD-spectroscopy on folding and dynamics this method also lacks atomic resolution. By presenting an environment sensitive picture on structure and dynamics it has its merits, but it is unsuitable to monitor site and residue-specific changes over time.<sup>23</sup>

#### 4.4. Hydrogen–deuterium exchange mass spectroscopy (HXMS)

FT-IR spectroscopy can detect various exchange phenomena but unless the protein is selectively isotope-labelled it is unsuitable to do so in a primary sequence-specific manner. On the contrary, sequence-specific information can be pulled out not only by NMR spectroscopy (*see below*) but also by hydrogen/deuterium exchange MS; HXMS.<sup>24</sup> This method has its merits especially for studying folded proteins with regions where H/D exchange is of limited velocity; time scale of exchange not below the MS-range can be detected. This method has a higher sensitive compared to NMR and can be used for larger macromolecules as well.<sup>25</sup> When combined with limited protease digestion, regions of the protein can be characterized in term of internal dynamics and flexibility. This method was found effective for detecting slow time-scale protein motions related to allostery, and enzyme functions. Furthermore, a brief review related to IDPs is available in [Ref. 23](#).

#### 4.5. X-ray diffraction

Real crystals do not fulfill the perfect repetition of the unit cell in three dimensions. While at larger scale crystal dislocations and twinning deteriorate periodicity, at the atomic level static and dynamic disorder take effect. Dynamic disorder is caused by the thermal motion of atoms around their equilibrium positions, which can be larger scale motion as well. Co-existence of different atoms at the same spots of different unit cells (e.g. molecules adopting different conformations) causes static disorder. Classical crystallographic methods cannot discriminate between static and dynamic disorder because the resulting electron density maps are averages of molecular conformations over the volume of the crystal and over the whole period of the diffraction data collection. Disorder can be described at different levels depending on the quality of the experimental data (i.e. resolution) using the atomic displacement parameter (ADP) ( $U$  or  $B$ -factor:  $B = 8\pi^2 U$ ).<sup>26</sup> Assuming the thermal motion of the atom is spherically symmetric,  $U$  is isotropic, and it is the square mean shift of the atom with respect to its average position during vibration ( $U_{eq} = \langle d^2 \rangle$ ). Anisotropic ADPs are better description of atomic scale disorder in the crystal, typically used with atomic resolution data. Macromolecular crystals, even though they usually diffract weaker, allow only isotropic description of ADPs, or even averaged values only. An intermediate and effective

description of anisotropy in macromolecular crystals is to model isotropic ADPs and anisotropic motion (translation, libration and screw motion<sup>27</sup>) for more rigid domains within the same macromolecule.

As a result of static disorder, often alternate positions of atoms can be resolved in electron density maps. In macromolecular crystals, some of the flexible regions possess variable conformers and as a consequence none of the individual ones can be detected in electron density maps. Thus, dynamics between several energetically similar states and/or larger amplitude makes to vanish more mobile sequential subunits. In practice, more than two or three conformer makes detection and/or assignment impossible. In other words lower than 25–33% of relative population of conformers is unseen by diffraction methods.

Using modern synchrotron X-ray sources from the late 1990s, it has been possible to study complex dynamic behaviour of proteins using Laue techniques. The structures of the intermediates and transient states of enzymes involved in their catalytic cycles can be identified and the respective time scale 100 ps to 100 ms can be assigned. The analysis of the bacterial photoreceptor photoactive yellow protein revealed that by taking snapshots at every 150 ps throughout the photocycle of 10 ns to 100 ms, five distinct intermediate structures could be identified and used to establish a reasonable chemical kinetic mechanism.<sup>28</sup> Consequently the chemical mechanism of the process can be formulated.<sup>29</sup> Recent advances made possible sampling picosecond dynamics of the protein by 100–150 ps time resolution of measurement.<sup>30–33</sup> New frontiers include 5D time and temperature dependent studies<sup>34</sup> as well as developing new techniques to further shorten time scale of the experiments.<sup>35</sup> Time-resolved Laue studies require photoreaction-initiated systems for triggering the reaction uniformly in the whole crystal volume rapidly with respect to the process under study to explore dynamics of the sub-ns–ms range in these systems. For systems presenting a significantly slower motion of *s–h* time scales initiation is not restricted to *fs* photo reactions, but it can be carried out by for example substrate diffusion. Intermediates of these systems can be freeze-trapped, so there is no need for using Laue techniques.<sup>36,37</sup>

In conclusion, common diffraction techniques are typically unable to refer to subunits and sequences of significant dynamics, but are usually able to identify the dominant conformers/conformations. More specific approaches can report on events (e.g. series of reaction(s) and allosteric conformational changes) happening in the crystal state at slower (*s–h*) or even faster (*ms–μs*) time scale of motion. However, even the latter approaches are “blind” to highly flexible regions of proteins structures with many conformation possibilities appearing at *ms–ns* time scale of motion.

## 4.6. Molecular modelling

Molecular modelling is a technique that is used both with and without incorporating experimental data. Carefully performed “pure” simulations can be quite useful as guides for experiment design and interpretation leading to new insights of macromolecular dynamics and function.<sup>38</sup> Here, we focus only on techniques



which use experimentally determined distance-type or dynamics-related restraints incorporated as extra energy terms in addition to the force field used. Approaches combining theory and experimentally derived data are regarded as efficient and reliable tools for the “conversion” of measurements to molecular structure(s) even though atoms as well as their interactions are treated classically instead of using a more adequate quantum mechanical description.<sup>e</sup>

Current trends involve the computation of structurally heterogeneous conformer ensembles whose diversity is aimed to reflect the observed dynamics of the molecule at a specific time scale. This is in contrast with the traditional structure determination/representation, where a single static conformer is both expected to correspond to experimental data and be sufficient to explain biological function.<sup>f</sup> Thus, the recently emerging “dynamical ensembles” of proteins represent new kinds of protein structural models. We will discuss the impact of this paradigm shift in detail below.

## 5. NMR SPECTROSCOPY FOR DETERMINING PROTEIN STRUCTURE AND DYNAMICS

X-ray crystallography keeps its role as the leading method for determining protein structures at the atomic level. Until recently, the role of NMR in structure elucidation was almost exclusively confined to small and medium-sized proteins not suitable for the production of well-diffracting crystals. Therefore, a fruitful complementary role-casting emerged where the static structures obtained from crystallography were “dressed up” with solution-state dynamical information, the field where NMR shows its real strength. In the last decade, intrinsically unstructured proteins of all sizes, also not amenable to crystallization, joined the popular NMR targets. Moreover, sophisticated structure determination techniques emerged recently that are capable of generating structural ensembles directly showing the observed mobility of proteins. In the following sections, we will briefly overview the basics of biomolecular NMR, then give a detailed account of the observation of dynamical features observed by NMR, and finally present examples that highlight the role of protein internal dynamics in biological processes.

### 5.1. Basics of biomolecular NMR

The present suitability and versatility of NMR to study macromolecules has been made available, among others, by the pioneering work of Nobel laureates Richard R. Ernst and Kurt Wüthrich (Nobel Prize in Chemistry, 1991 and 2002). The established protocol of structure determination by NMR consists of the

<sup>e</sup> Macromolecular structure determination uses much less experimental information per atom than small molecule NMR or crystallography, thus all commonly used structure calculation methods rely heavily on different force fields using parameters derived from studies of small molecules.<sup>3</sup>

<sup>f</sup> Recognition of slow motions during for example enzyme catalysis (closure of the binding site, etc.) have been of course recognized and represented by 2 (sometimes 3) separate conformers, but as seen as different states, they were not put together in a single ensemble.

following steps: (i) preparation of the sample by chemical synthesis or biotechnology, including thorough purification, (ii) spectrum acquisition and processing, (iii) resonance assignment manually or automatically, (iv) evaluation of spectral information to obtain restraints for (v) structure calculation, refinement and validation.

Samples from natural sources contain only protons as NMR active nuclei, other observable isotopes (most commonly  $^{13}\text{C}$  and  $^{15}\text{N}$  at 1.1% and 0.36% natural abundance, respectively) have to be incorporated chemically or biochemically. On the technical details of isotope labelling of proteins there are exhaustive reviews and some perspectives available.<sup>39–41</sup>

Most NMR experiments in biomolecular spectroscopy are either used for resonance assignment or to obtain specific structural and/or dynamical information. Notable exceptions are homonuclear  $^1\text{H}$ – $^1\text{H}$  nuclear Overhauser effect (NOE)-based measurements used for both purposes. Resonance assignment requires prior knowledge of the amino acid sequence of the protein, corresponding to the complete chemical structure of the molecule. The two main steps of the assignment process are spin system identification where information on the possible type of the corresponding amino acid residue is obtained and sequential assignment, where the spin systems are ordered and thus specifically assigned to residues at given positions of the polypeptide chain.<sup>42</sup> While the former step always relies on experiments based on chemical connectivity (magnetization transfer using scalar couplings), the latter might also utilize direct spin–spin couplings (2D NOESY, 3D HSQC–NOESY). In general, sequential assignment is more straightforward and reliable when multi-dimensional (3D or even higher) heteronuclear experiments (HNCA, HNCOC, HNCACB, CBCACONH, etc.) are recorded and through-bond connections are used for sequential assignment. Consequently, so-called triple-resonance experiments (containing information about  $^1\text{H}$ ,  $^{13}\text{C}$  and  $^{15}\text{N}$  nuclei) are the most common subjects of modern automatic assignment protocols.<sup>43,44</sup> A new direction in resonance assignment is to reduce the measurement time, ranging from 1–2 days to 1–2 weeks for widely used 3D experiments by using experiments where signal-less spectral regions are not (extensively) sampled.<sup>45</sup> These and other fast NMR techniques require suitably adjusted spectral processing and/or assignment tools.

## 5.2. Dynamical information from NMR

Practically all NMR observables bear information on the dynamics of the investigated molecules. This is a quite inherent feature of solution-state NMR measurements as there are  $10^{16}$ – $10^{17}$  solute molecules in the sample tube, and all of them are interconverting from one conformer to another on a range of time scales. Thus, all parameters obtained are essentially time- and ensemble averages of a high number of conformers and their proper interpretation should take this into account. In other words, in a general case no single conformer can be expected to fulfill all measured parameters simultaneously.<sup>46</sup> Apparently, this is in contrast with the considerations above for “conventional” structural calculations where multiple structures were compatible with the data used. This problem can be referred to as

the underfitting/overfitting problem, where the actual number of NMR parameters and calculated conformers determine the balance between the two cases. This will be discussed in more detail below.

### 5.3. Chemical shifts

Chemical shifts (CSs) are the most common NMR parameters obtained as the result of the assignment process as a prerequisite of all subsequent analyses. As a consequence, large data sets of CSs and their analyses are available; therefore, their relation to protein structure and dynamics is well documented. The basic observation is that CSs, especially  $H\alpha$  and  $C\alpha$  values depend heavily on the local conformation of the peptide chain. This relationship can be further refined by additional factors such as the spatial environment of these atoms. Currently, applications such as SHIFTX<sup>47</sup> are capable of calculating CSs from 3D protein structures and, as a reversal, protein folds can be reconstructed solely on the basis of CS information.<sup>48,49</sup> Moreover, internal dynamics of proteins can be estimated solely on the basis of CSs.<sup>50,51</sup>

To use CSs as indicators of local structure, a reference CS set is needed. There are many attempts in the literature to generate such a set, many involving highly flexible short peptides.<sup>52,53</sup> Other approaches involve careful analysis of database-deposited shifts from globular proteins.<sup>54,55</sup> In practice, it is advisable to use sequence-dependent correction factors for these shifts, especially for intrinsically unfolded proteins.<sup>56</sup> Another important practical aspect is the accurate determination of the CS values which requires correct spectral referencing, an issue well documented in literature but still not always easily followed in practice.

CSs are also sensitive indicators of molecular motions. A well-known basic NMR phenomenon is coalescence, that is that separate signals corresponding to distinct conformational states merge at higher temperatures indicating that the energy barrier separating them can be easily passed by molecules with higher internal energy. In other words, NMR is able to discriminate between slow and fast molecular motions on the relevant time scales. This is also true for molecular interactions, as exemplified by monitoring ligand binding to protein at various concentrations of the interacting partners. Depending on the binding constant, the exchange between the free and bound form of the molecules can be slow or fast relative to the NMR CS time scale. When the exchange is slow, two separate signal sets will be observed for the two states, whereas for fast exchange, each signal will gradually shift its position according to the protein:ligand molar ratio. In both cases, a rough estimate of the binding constant can be calculated based on the peak volume ratios (slow exchange) or CSs at different titration points. In the so-called intermediate exchange regime, the extreme line broadening may result in the loss of identifiable signals.

In accordance with these considerations, a number of dynamic features can be observed in proteins as early as in the resonance assignment stage. Several residues might give rise to duplicate signals indicating slow interconversion between distinct conformations. The most prominent example of this is the

*cis-trans* isomerization of peptide bonds before proline residues. On the other hand, as CSs are sensitive to local conformation, their actual value manifests as an average of rapidly interconverting conformations.

Signal dispersion, that is the CSs and their ranges occupied by the signals are commonly used to assess the folded/unfolded nature of a polypeptide chain and is one of the most straightforward ways to identify IDPs.<sup>23</sup> More sophisticated methods define the extent of foldedness, the fraction of molecules or even its segments adopting compact conformation, by comparing CSs to those observed in a well-folded species.<sup>57</sup> CSs calculated for invisible states of proteins, that is low-populated conformations with slow exchange with the dominant one(s), are used in characterizing these states and comparing them to the observable ones (see below).

## 5.4. Nuclear Overhauser effect

The nuclear Overhauser effect (NOE, nOe) is the traditional basis of biomolecular structure determination in NMR.<sup>42</sup> Homonuclear (<sup>1</sup>H-<sup>1</sup>H) NOEs can be obtained from 2D NOESY or 3D HSQC-NOESY type experiments. However, as homonuclear 2D NOESY spectra contain a vast amount of information about all <sup>1</sup>H-<sup>1</sup>H interactions, only those involving <sup>1</sup>Hs attached to isotopically labelled heteroatoms are accessible with heteronuclear 3D experiments. Bearing information on spatial relationships regardless of chemical connectivity, NOE peaks can conveniently be converted to <sup>1</sup>H-<sup>1</sup>H distance restraints used in structure calculations. The volume of the NOE cross-peak is approximately proportional to  $d_{H \leftrightarrow H}^{-6}$  and thus, in principle, (assuming the same dynamics for the <sup>1</sup>H-<sup>1</sup>H spin pairs) can be converted to a more or less exact internuclear distance. This requires the use of a reference distance, for example the fixed distance between geminal or aromatic ring protons. In practice, NOE-derived distances are more often categorized into distinct ranges such as 1.8–2.5, 1.8–3.5 and 1.8–5.0 Å where 1.8 Å is the distance of two close but non-overlapping protons. This latter procedure acknowledges that exact distances are practically impossible to be obtained due to the internal flexibility of proteins, spin diffusion, relaxation and conformational exchange phenomena. Moreover, the Overhauser effect itself takes time to build up requiring that the two protons remain spatially close for several milliseconds. Thus, only a small fraction of close <sup>1</sup>H-<sup>1</sup>H distances is observed as NOEs and the volumes of the corresponding signals are heavily influenced by conformational variability and dynamics. In highly flexible molecules, only intraresidual and sequential NOEs can be typically observed in spite of that long/range transient interactions might be present in the polypeptide chain.

The ensemble-averaged NOE distances can be obtained as<sup>58</sup>:

$$r_{\text{ens}} = \langle r^{-6} \rangle^{-1/6} \quad (8)$$

where  $r$  is the interproton distance in the selected conformer.

## 5.5. Scalar couplings

In proteins, three-bond scalar couplings are an important source on backbone and side-chain conformation. The conformation dependence of scalar couplings can be quantitatively described with the Karplus equation<sup>59</sup> ( $^3J = A \cos^2 \theta + B \cos \theta + C$ , where  $\theta$  is the dihedral angle between the two vicinal nuclei for which the coupling is measured and  $A$ ,  $B$  and  $C$  are constants). In protein structure determination, adequately selected couplings are often used to set up dihedral angle restraints in the form of ranges within which the backbone or side-chain dihedral angles are restricted. There are several types of couplings measured routinely, for example  $^3J_{\text{H}\alpha\text{HN}}$  for  $\varphi$ ,  $^3J_{\text{H}\alpha\text{HB}1/\beta 2}$  and  $^3J_{\text{NH}\beta 1/\beta 2}$  for  $\chi_1$ , etc. using different 2D and 3D experiments (e.g.  $\beta$ -COSY, z-COSY, E-COSY, HNCA-J, HNHA).

The Karplus equation refers to a rigid molecule or to the case of a single conformation in a flexible one. However, in proteins, a number of conformations contribute to the observed couplings arising as a time and ensemble average. Considering a conformational ensemble, scalar coupling can be calculated for each conformer using available Karplus parameters (e.g. from quantum chemical calculations) or, oppositely, “dynamic” Karplus parameters can be computed using experimentally derived restraints.<sup>60</sup> The former case is an important tool for validating structural ensembles representing the dynamical heterogeneity of proteins (see below). For the averaged coupling affected by the protein backbone dihedral angle  $\varphi$ , the following Karplus relationship can be formulated<sup>61</sup>:

$$^3J_{\text{ens}} = A \langle \cos^2(\varphi + \theta) \rangle + B \langle \cos(\varphi + \theta) \rangle + C \quad (9)$$

where  $\theta$  is a correction angle needed because of the usage of  $\varphi$  instead of the dihedral angle defined by the NH and H $\alpha$  hydrogens. Angular brackets represent conformational and across-ensemble averaging. Note that not the dihedral angles themselves but the derived quantities are averaged because of the effect of couplings on the magnetization is instantaneous (Ref. 6). More recently, techniques for measuring scalar couplings through H-bonds have emerged. These can be used to directly probe H-bond networks and their dynamics in biomolecules. Moreover, in contrast to NOEs couplings through H-bond arise instantaneously, requiring no build-up time. An optimized equation for calculating the  $J$ -coupling across the H-bond from geometrical parameters is<sup>62</sup>:

$$^{\text{h}3}J_{\text{NC}'}(\theta_2, \rho, r_{\text{HO}'}) = \{ -1.31 \cos^2 \theta_2 + [0.62 \cos^2 \rho + 0.92 \cos \rho + 0.14] \sin^2 \theta_2 \} \exp[-3.2(r_{\text{HO}'} - r_{\text{HO}'}^0)] \quad (10)$$

where  $r_{\text{HO}'}$  is the H–O' atomic distance with a reference value  $r_{\text{HO}'}^0 = 1.76 \text{ \AA}$ ,  $\theta_2$  is the H–O'–C' angle and  $\rho$  is the H–O'–C'–N dihedral angle.

Recently, correlations between  $^2J$  couplings and protein secondary structure have been described, opening new ways for structure determination and validation.<sup>63,64</sup>

## 5.6. Residual dipolar couplings (RDCs)

Dipolar couplings constitute the second largest term of the Hamiltonian but are effectively averaged out by isotropic molecular tumbling in solution.<sup>65</sup> Hence, they are not observable in the majority of standard NMR experiments. Detection of RDCs requires that the orientation of the molecule with respect to the external magnetic field should be non-random, thus rendering the vector between the specified pair of nuclei (for which the RDC is measured) partially aligned. This is usually achieved by the use of dilute liquid crystalline media such as bicelles or filamentous bacteriophages which, in lucky circumstances, do not adversely affect the structure and dynamics of the protein to be studied. RDCs are measured analogously to scalar couplings which also means that the acquisition of two spectra is always necessary, a measurement in isotropic solution to determine  $J$ -couplings and another in oriented media yielding the sum of RDC +  $J$ -coupling values for each nuclei. Nowadays, RDCs are one of the most powerful NMR parameters in describing the structure and dynamics of both folded and unfolded proteins.<sup>66</sup> RDCs contain information about relative orientation of internuclear vectors, and, in addition, also their dynamics up to the millisecond time scale. The use of RDCs is greatly facilitated by the fact that they can be calculated from atomic coordinates and thus can be used for structure refinement<sup>67</sup> and validation.<sup>68</sup> If multiple sets of RDCs are available for a given system (e.g. from different media or for different pairs of nuclei), cross-validations between different RDC sets can also be performed increasing the reliability of the obtained structures. In general, observed RDCs represent an average over all conformations and their alignments present in the sample<sup>69</sup>:

$$D_{\text{ens}} = \frac{1}{N} \sum_{k=1}^N \int w_k(\Omega) P_2(c_z^k) d\Omega \quad (11)$$

where  $N$  is the number of conformers,  $\Omega$  is the orientation of the molecule in the liquid crystal,  $P_2$  is the second-order Legendre polynomial,  $w_k$  is the orientation-dependent weight of the  $k$ th conformer and  $c_z^k$  is the projection of the internuclear vector  $c$  in conformer  $k$  along the external magnetic field ( $z$  axis). The orientation of the protein is governed by multiple factors including shape and electrostatics, thus if these are different for distinct conformers, the alignment will be conformer-specific, hence the conformer-dependent weighting factor  $w$  is taken into account.

In practice, calculation of RDCs from structure can be basically done in two ways: either a common alignment tensor can be used for all molecules, or the alignment of each molecule can be taken into account separately. The former approach is suitable for molecular dynamics calculations of well-folded proteins,<sup>67</sup> where the conformation-dependence of the alignment can be ignored. However, the latter is necessary for treating molecules with highly diverse conformations, such as IDPs.

## 5.7. Heteronuclear relaxation experiments and analysis

One of the most widely used tools to assess protein dynamics are different heteronuclear relaxation parameters. These are in intimate connection with internal dynamics on time scales ranging from picoseconds to milliseconds and there are many approaches to extract dynamical information from a wide range of relaxation data (for a thorough review see Ref. 1). Most commonly  $^{15}\text{N}$  relaxation is studied, but  $^{13}\text{C}$  and  $^2\text{H}$  relaxation are the prominent tools to characterize side-chain dynamics.<sup>70</sup> Earliest applications utilized  $^{15}\text{N}$   $T_1$ ,  $T_2$  relaxation as well as heteronuclear ( $^1\text{H}$ – $^{15}\text{N}$ ) NOE experiments to characterize N–H bond motions in the protein backbone.<sup>71</sup> The vast majority of studies applied the so-called model-free approach to translate relaxation parameters into overall and internal mobility. Its name contrasts earlier methods where explicit motional models of the N–H vector were used, for example diffusion-in-a-cone or two- or three-site jump, etc. Unfortunately, we cannot obtain information about the actual type of motion of the bond. As reconciliation, the model-free approach yields motional parameters that can be interpreted in each of these motional models. There is a well-established protocol to determine the exact combination of parameters to invoke for each bond, starting from the simplest set to the most complex one until the one yielding satisfactory description is reached. The scheme, a manifestation of the principle of Occam's razor is shown in Table 1.<sup>72</sup>

In Table 1,  $S^2$  is the general order parameter describing bond motions at the ps–ns time scale,  $\tau_e$  is the characteristic correlation time for these motions and  $R_{\text{ex}}$  is the conformational exchange term representing motions on the  $\mu\text{s}$ –ms time scale. Internal motions on the ps–ns time scale are considered as the superposition of fast and slow motions characterized by  $S_f^2$  and  $\tau_f$  as well as  $S_s^2$  and  $\tau_s$ . Here,  $S^2 = S_s^2 S_f^2$  and  $\tau_f < \tau_s < \tau_e$ .<sup>72</sup> In models 1–4,  $S^2 = S_f^2$  (i.e.  $S_s^2 = 1$ ) and  $\tau_e = \tau_s$ .

In practice, relaxation parameters are measured as a series of HSQC-type spectra as a function of a variable time delay, and peak heights (or volumes) are used to fit relaxation rates.<sup>73</sup> The next step is the determination of the overall rotational correlation time of the molecule, typically from the  $T_1/T_2$  ratio obtained for the residues. In such calculations, outliers are generally excluded, that is those residues for which  $R_{\text{ex}}$  or  $\tau_e$  is significant (residues with  $T_1/T_2$  ratio well above and below the average, respectively, Ref. 71). The second step is to determine the best fit between the relaxation parameters  $R_1$ ,  $R_2$  and heteronuclear NOE and the motional parameter sets. The correspondence between these can be expressed

**TABLE 1** Parameter sets commonly used in the model-free formalism

Set	Parameters	Notes
1	$S^2$	$\tau_f \rightarrow 0$ ( $\tau_f < 20$ ps), slow internal motions negligible
2	$S^2, \tau_e$	“Original” model-free parameter set, $\tau_e = \tau_f$
3	$S^2, R_{\text{ex}}$	Conformational exchange term is considered
4	$S^2, \tau_e, R_{\text{ex}}$	Original set + conformational exchange term, $\tau_e = \tau_f$
5	$S^2, S_f^2, \tau_e, R_{\text{ex}}$	$\tau_f \rightarrow 0$ , $\tau_e = \tau_s$ . Fast and slow internal motions are considered

with the spectral density function: the form shown in Equation (3) corresponds to the original model-free parameter set (set 2 in Table 1). The interrelationships of relaxation parameters and the spectral density function are given as (if both  $^1\text{H}$ - $^{15}\text{N}$  dipole-dipole (DD) and  $^{15}\text{N}$  CSA relaxation contribute to the relaxation processes):

$$\begin{aligned}
 R_1 &= (d^2/4)[J(\omega_{\text{H}} - \omega_{\text{N}}) + 3J(\omega_{\text{N}}) + 6J(\omega_{\text{H}} + \omega_{\text{N}})] + c^2J(\omega_{\text{N}}) \\
 R_2 &= (d^2/8)[4J(0) + J(\omega_{\text{H}} - \omega_{\text{N}}) + 3J(\omega_{\text{N}}) + 6J(\omega_{\text{H}}) + 6J(\omega_{\text{H}} + \omega_{\text{N}})] \\
 &\quad + (c^2/6)[4J(0) + 3J(\omega_{\text{N}})] + R_{\text{ex}} \\
 \text{NOE} &= 1 + (d^2/4R_1)(\gamma_{\text{H}}/\gamma_{\text{N}})[6J(\omega_{\text{H}} + \omega_{\text{N}}) - J(\omega_{\text{H}} - \omega_{\text{N}})] \\
 d &= (\mu_0 h \gamma_{\text{N}} \gamma_{\text{H}} / 8\pi^2) \langle r_{\text{NH}}^{-3} \rangle \\
 c &= \omega_{\text{N}} \Delta\sigma / \sqrt{3}
 \end{aligned} \tag{12}$$

where  $\mu_0$  is the permeability of vacuum,  $h$  is Planck's constant,  $\gamma_{\text{H}}$  and  $\gamma_{\text{N}}$  are the gyromagnetic ratios of  $^1\text{H}$  and  $^{15}\text{N}$  nuclei, respectively. The N-H bond length is given by  $r_{\text{NH}}$  and its value is commonly taken as 1.02 Å and  $\Delta\sigma$  is the CS anisotropy of  $^{15}\text{N}$  nuclei, usually taken as -160 ppm.<sup>74</sup> The equations are shown as in Ref. 72.

There are several programs capable of performing the calculation of model-free parameters from relaxation data, such as Modelfree<sup>75</sup> and Tensor2.<sup>7</sup>

Although the model-free formalism is very popular and offers a good pictorial representation of protein motions, it is not always straightforward to perform. For example, there might be cases when the isotropic model for the overall rotational motion is not sufficient but no reliable anisotropic solution can be obtained. Furthermore, several bond motions cannot be described sufficiently with any of the five parameter sets listed above. Last but not least, only the generalized order parameter can be directly assigned to a physical picture of the motions, neither  $\tau_{\text{e}}$  nor  $R_{\text{ex}}$  offers a straightforward interpretation. Hence the growing popularity of spectral density mapping approaches, where the values of the spectral density function  $J(\omega)$  are determined at specific frequencies. From these, we discuss reduced spectral density mapping<sup>76</sup> in brief below.

Reduced spectral density mapping aims at determining the values of  $J(\omega)$  at three frequencies:

$$\begin{pmatrix} J(0) \\ J(\omega_{\text{N}}) \\ J(0.87\omega_{\text{H}}) \end{pmatrix} = \begin{pmatrix} \frac{-3}{4(3d^2 + c^2)} & \frac{3}{2(3d^2 + c^2)} & \frac{-9}{10(3d^2 + c^2)} \\ \frac{1}{(3d^2 + c^2)} & 0 & \frac{-7}{5(3d^2 + c^2)} \\ 0 & 0 & \frac{1}{5d^2} \end{pmatrix} \begin{pmatrix} R_1 \\ R_2 \\ \frac{\gamma_{\text{N}}}{\gamma_{\text{H}}}(\text{NOE} - 1)R_1 \end{pmatrix} \tag{13}$$

where  $d$  and  $c$  are defined as for Equation (12). Equation is adapted from Ref. 77. The advantage of this approach is that at a single magnetic field the three values of  $J(\omega)$  can be obtained from the three commonly measured relaxation parameters in



a straightforward manner applying only a linear relationship. Thus, in contrast to the model-free approach this analysis is always feasible at the cost of resulting parameters with no direct links to physical motions. Nevertheless, reduced spectral density mapping can be extremely useful especially in assessing differences in dynamics of two or more protein states, for example at different temperatures or free/ligand-bound forms.<sup>77</sup>

For motions on slower time scales, relaxation dispersion methods are the most powerful ones to characterize distinct states adopted by a protein during its dynamical fluctuations. These methods are applicable when there is substantial CS difference between the states studied. The two approaches for quantitative measurements of protein motions in the  $\mu\text{s}$ – $\text{ms}$  regime are the relaxation-compensated Carr-Purcell-Meiboom-Gill (rcCPMG) and the off-resonance rotating-frame measurements denoted  $R_{1\rho}$ .<sup>78</sup> Both measurements aim at the separation of  $R_2^0$ , the intrinsic transverse relaxation rate and additional terms in the observed  $R_2$  that originate from the exchange processes broadening related to the transition between two (or more) conformational states of interest.

The rcCPMG approach relies on a series of experiments with different  $\tau_{\text{cp}}$  delays between the  $180^\circ$  pulses in the CPMG pulse trains used to measure  $R_2$  relaxation rates. For two-state kinetics in the fast exchange limit, the dependence of  $R_2$  on  $\tau_{\text{cp}}$  can be formulated as<sup>78</sup>:

$$\begin{aligned} R_2(1/\tau_{\text{cp}}) &= R_2^0 + \phi_{\text{ex}}/k_{\text{ex}}[1 - 2 \tanh(k_{\text{ex}}\tau_{\text{cp}}/2)/(k_{\text{ex}}\tau_{\text{cp}})] \\ \phi_{\text{ex}} &= p_A p_B \Delta\omega^2 \\ \omega_e &= \sqrt{12}/\tau_{\text{cp}} \end{aligned} \quad (14)$$

where  $p_A$  and  $p_B$  are the relative populations of conformational states A and B, respectively, separated by the CS difference  $\Delta\omega$  and  $\omega_e$  is the effective magnetic field.

The rotating-frame  $R_{1\rho}$  relaxation can be expressed as<sup>78,79</sup>:

$$\begin{aligned} R_{1\rho} &= R_1 \cos^2\theta + R_2^0 \sin^2\theta + \frac{\phi_{\text{ex}} k_{\text{ex}}}{k_{\text{ex}}^2 \omega_e^2} \sin^2\theta \\ \omega_e &= \left(\omega_1^2 + \bar{\Omega}^2\right)^{1/2} \\ \theta &= \arctan(\omega_1/\bar{\Omega}) \end{aligned} \quad (15)$$

where  $\theta$  denotes the tilt angle and  $\omega_1$  is the amplitude of the effective spin-locking field and  $\bar{\Omega}$  is the average resonance offset.<sup>79</sup> In both rcCPMG and  $R_{1\rho}$  experiments,  $R_2$  is measured as a function of the effective magnetic field  $\omega_e$  because  $R_2$  dephasing at distinct  $\omega_e$  values is influenced by the conformational exchange process differently. The obtained data can be used to fit a number of parameters of the conformational exchange process such as the CS difference between the states,  $\Delta\omega$  and rate constants. In practice, measurements at different external magnetic fields are required to eliminate ambiguities in parameter fitting.<sup>78</sup> The real power of such analyses is that not only the magnitude but also the sign of  $\Delta\omega$  values can be obtained,<sup>80</sup> thus, having the CSs for the dominant conformer—that is that gives rise to the signals in the measured spectra such as HSQCs—at hand,

CS values of the lowly populated, “invisible” state can be obtained. Naturally, when the kinetics is not two-state, more complicated models should be invoked.<sup>79</sup>

## 5.8. Paramagnetic relaxation enhancement

The principle of paramagnetic relaxation enhancement (PRE) is the increase in relaxation rates due to dipolar interaction between a nucleus and the unpaired electron in a paramagnetic probe.<sup>81</sup> The PRE effect is considerably large, thus, distances up to 20–35 Å can be mapped depending on the probe used. Intramolecular probes comprise metal ions, the use of which is evidently limited to several metalloproteins, whereas spin probes, such as nitroxide stable radicals or chelators binding a paramagnetic metal ion, can be linked chemically to virtually all proteins for example to cysteines occurring naturally or introduced artificially into the sequence. In practice, probes are preferred that can be conveniently switched from the paramagnetic to the diamagnetic state by reduction with for example ascorbic acid. These probes, for example *N*-(1-oxyl-2,2,5,5-tetramethyl-3-pyrrolidiny) iodoacetamide or PROXYL in short ensure that the only difference between the two states is the presence or absence of the unpaired electron.

The transverse PRE  $\Gamma_2$  is the difference between the  $R_2$  rates in the paramagnetic and diamagnetic states of the system and can be calculated from peak intensities in  $R_2$  experiments at two time points without the need for relaxation rate fitting<sup>81</sup>:

$$\Gamma_2 = R_{2,\text{para}} - R_{2,\text{dia}} = \frac{1}{T_b - T_a} \ln \frac{I_{\text{dia}}(T_b)I_{\text{para}}(T_a)}{I_{\text{dia}}(T_a)I_{\text{para}}(T_b)} \quad (16)$$

where the two time points  $T_a$  and  $T_b$  can be  $T=0$  and  $T=\Delta T$  chosen to minimize the error in  $\Gamma_2$ . Accurate measurements require specific pulse sequences for obtaining  $^1\text{H}$  relaxation in N–H groups.<sup>82</sup>

The distance dependence of the PRE is  $\langle r^{-6} \rangle$ , but its actual interpretation is complicated due to the fact that most paramagnetic probes contain flexible linkers between the attachment site to the protein and the actual paramagnetic centre. Thus, in structure calculations the different conformers of the probe should be taken into account.<sup>81</sup>

Because of the strength and long-range nature of PRE, it is particularly useful in detecting and characterizing low-populated species occurring during protein dynamics. The requirements for this are that the distance between the paramagnetic centre and particular protons investigated should be shorter in the minor than in the major species and the exchange rate between the two species A and B should be fast relative to the  $\Gamma_2$  time scale:  $k_{\text{ex}} \gg \Gamma_{2B} - \Gamma_{2A}$ . When these apply, the observed PRE is the weighted average of the two populations<sup>81</sup>:

$$\Gamma_2^{\text{obs}} \approx p_A \Gamma_{2,A} + p_B \Gamma_{2,B} \quad (17)$$

If the distance in the minor state is considerably shorter than in the major one, the observed PRE will be dominated by the minor conformer even when its

population is around 1%. The distance of the paramagnetic centre and the observed proton can be calculated as<sup>83</sup>:

$$r = \left[ \frac{K_{ep}}{\Gamma_2} \left( 4\tau_{ep} + \frac{3\tau_{ep}}{1 + \omega_H^2 \tau_{ep}^2} \right) \right] \quad (18)$$

where  $K_{ep}$  is  $1.23 \times 10^{-32} \text{ cm}^6 \text{ s}^{-2}$  for the interaction between a free electron and a proton,  $\omega_H$  is the proton Larmor frequency and  $\tau_{ep}$  is the correlation time for the electron–nucleus dipole–dipole interaction which is in the range of  $10^{-9}$ – $10^{-8}$  s and can be estimated from the  $\Gamma_1$  and  $\Gamma_2$  relaxation rates.<sup>84</sup> In random coil conformation, the theoretical range of the PRE effect is  $\sim 15$  residues from the attachment site. In denatured or IDPs, any further effect indicates deviations from a completely random chain meaning transient long-range interactions within the protein.

## 5.9. H–D exchange followed by NMR

Proton–deuteron exchange experiments correspond to a direct probe of the environment and dynamics of N–H amide groups in proteins.<sup>85</sup> In one of the simplest setup, measurements are taken at regular intervals after dissolving the freeze-dried sample in  $\text{D}_2\text{O}$ . Naturally, exchange can also be monitored in the D–H direction. H–D exchange can be followed by multiple techniques (e.g. IR spectroscopy) but only NMR yields resolution at the atomic level. The basis of the NMR experiments is that deuterons do not give rise to a signal in  $^1\text{H}$ -based experiments and thus the decrease in the peak volumes in subsequent spectra yields direct information about the amount of still proton-bearing sites. Besides temperature and pH, H–D exchange rates depend on the conformation of the protein and the exact position of the observed residue within as exposed groups exchange faster. Conformational motions that “open” buried groups to the solvent also influence the exchange rates and can be characterized by suitable experiments.

One way of enhancing the precision of the measured exchange times even for proteins with fast H–D exchange is the use of interrupted H–D exchange where the exchange process is quenched at a given time point typically by lowering the pH or the temperature of the protein solution. In a common pulse-labelling experiment, the unfolded protein is incubated in  $\text{D}_2\text{O}$  environment where folding can be initiated and exchange is slow. At a given time point, the protein is transferred to aqueous environment at basic pH where exchange rapidly occurs. After slowing down the exchange at acidic pH, and leaving the folding process to finish, groups buried early during folding will remain deuterated and can be identified. For several proteins, quenching of the exchange can also be achieved by inducing the quick adoption of a tightly packed native conformation for example by adding a cofactor such as heme for myoglobin<sup>86</sup> or flavin adenine mononucleotide (FMN) for flavodoxin.<sup>87</sup> Subsequent NMR measurements might even be made in aprotic organic solvents

with careful corrections to the additional exchange caused by the residual water in the lyophilized sample.<sup>88</sup>

Assuming that the closed state is dominant ( $k_o \ll k_c$ ), the observed exchange rate  $k_{ex}$  can be expressed as:

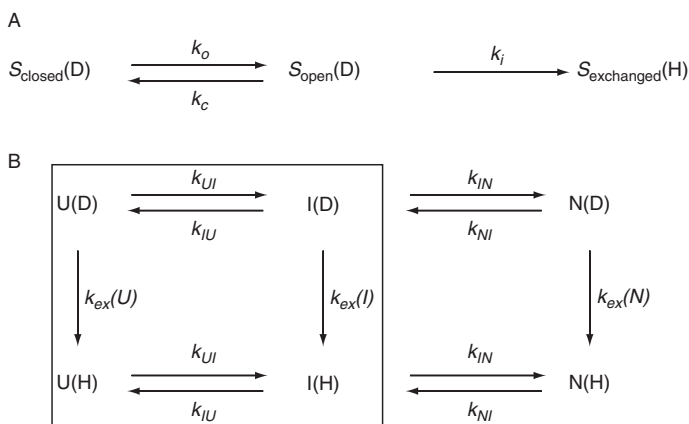
$$k_{ex} = \frac{k_o k_i}{k_c + k_i} \quad (19)$$

This equation simplifies to  $k_{ex} = k_o$  if  $k_c \ll k_i$  and to  $k_{ex} = k_o k_i / k_c$  if  $k_i \ll k_c$ . The former condition is called EX1, where the conformational openings are the rate-limiting step of the exchange and the latter condition is referred to as EX2, where the equilibrium constant for local opening together with the intrinsic exchange rate determine the H-D exchange process.

A useful concept is the introduction of H-D exchange protection factors, which can be defined using the exchange rates of unfolded, folded or partially folded intermediate species:

$$\begin{aligned} P(N) &= k_{ex}(U) / k_{ex}(N) \\ P_{struc}(I) &= k_{ex}(U) / k_{ex}(I) \end{aligned} \quad (20)$$

where  $P_{struc}(I)$  is the structural protection factor for a given site in the folding intermediate. In practice, when the  $k_{ex}(I)$  cannot be measured directly, the apparent protection factor  $P_{app}(I)$ , can be used.  $P_{app}(I)$  can be derived from the boxed part of Scheme 3, contains contributions to the exchange rate from unfolding events, and is always smaller than  $P_{struc}(I)$ . Scheme and equation are adapted from Ref. 89.  $P_{struc}(I)$  is related to the structure of the intermediate whereas  $P_{app}(I)$  yields information primarily about its stability.<sup>89</sup>



**Scheme 3** (A) General scheme of HD-exchange in structure S. The D and H in brackets refers to the deuterated and protonated species, respectively. (B) A simplified folding scheme with unfolded (U), folded (N for native) and one intermediate (I) state with H-D exchange considered. Adapted from Ref. 89.

## 6. EXAMPLES HIGHLIGHTING THE ROLE OF PROTEIN INTERNAL DYNAMICS IN BIOLOGICAL PROCESSES

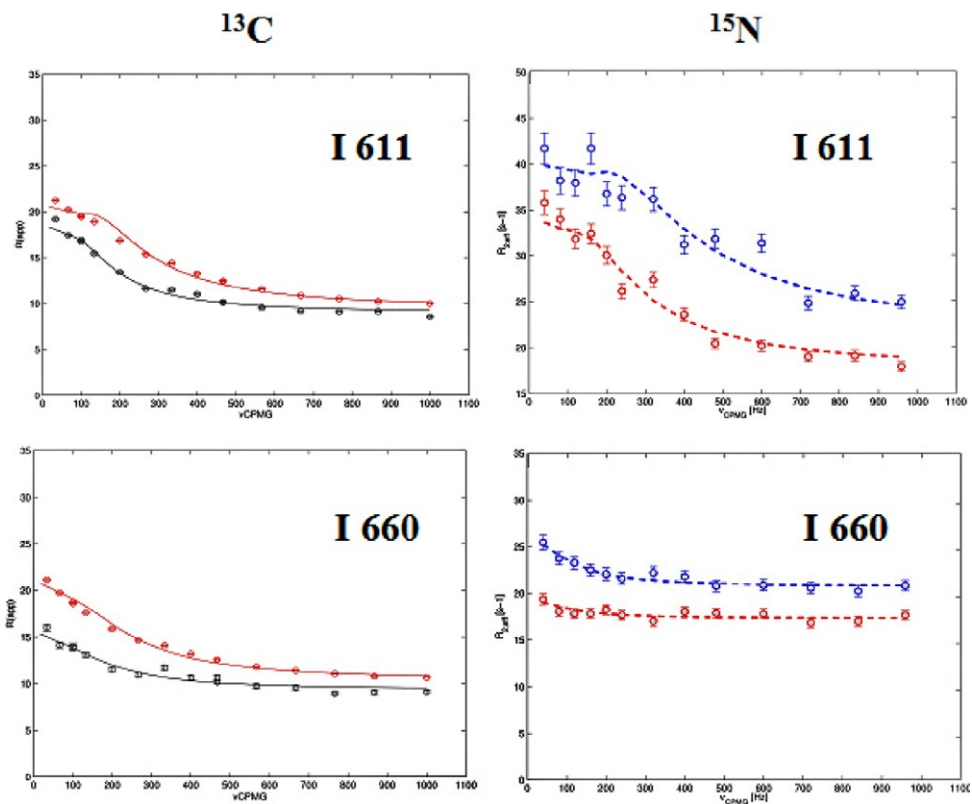
In the followings, using the parameters outlined above we present several detailed examples of biological and biochemical applications of these methods. The previewed examples are divided into two groups: the first one contains studies about motions slower than the overall rotational correlation time of the molecule ( $\tau_c$ ); while the second group enumerates faster internal motions. Although all proteins exhibit both types of motions, studies generally focus only either on one or on the other.

### 6.1. Characterization of systems with supra- $\tau_c$ motions

Motions slower than the overall correlation time of the molecule are effectively probed by relaxation dispersion methods. Examples of biological applications include demonstration of correlation between the intrinsic dynamics of an enzyme and its catalytic rate<sup>90</sup> as well as contributing to the mapping of the activation pathway of a signalling protein.<sup>38</sup> Below we select only a few cases with the intention of highlighting the versatility of the method on its own and in combination with other NMR-derived data. We conclude with a different technique, RDC-based determination of a structural ensemble yielding details of molecular recognition processes at the atomic level.

The KIX domain of the CBP (CREB-binding protein) transcriptional coactivator protein binds to a number of interaction partners. The KIX domain structure is composed of three densely packed helices. To investigate the presence of excited states in this domain,  $^{15}\text{N}$  backbone and  $^{13}\text{C}$  methyl relaxation dispersion methods were applied on suitably labelled samples.<sup>91</sup> For all residues, the relaxation dispersion profiles obtained for both methyl  $^{13}\text{C}$  and backbone  $^{15}\text{N}$  nuclei were consistent with a two-state exchange process between states G (ground) and E (excited state). For all  $^{13}\text{C}$  shifts and  $^{15}\text{N}$  shifts in the first two  $\alpha$ -helices of KIX, the magnitude of the CS differences  $|\Delta\omega|$  agrees well with the difference between the observed native state and sequence-corrected random coil shifts, suggesting a folding–unfolding event as the source of the chemical exchange observed. In contrast, the third helix exhibits considerably smaller  $^{15}\text{N}$  CS changes (Figure 1.). This suggests that although all sites probed the same partial unfolding event, the third helix largely retains its conformation in the high-energy state as its backbone  $^{15}\text{N}$  shifts are only moderately affected but changes in  $^{13}\text{C}$  methyl shifts are consistent with the disruption of tertiary contacts.

H–D exchange experiments corroborated these findings as slow exchange rates could be measured only for residues in the third helix while all other residues exhibited very fast exchange. The rates measured in the third helix correspond to  $(K_{\text{GE}}K_{\text{HEL}})k_{\text{int}}$ , where  $K_{\text{GE}}$  is the equilibrium constant for the G–E transition,  $K_{\text{HEL}}$  is that for the unfolding of the helix and  $k_{\text{int}}$  is the intrinsic H–D exchange rate. Thermodynamic parameters calculated from denaturation experiments and the obtained value of  $K_{\text{HEL}}$  indicate that about 25% of molecules in the

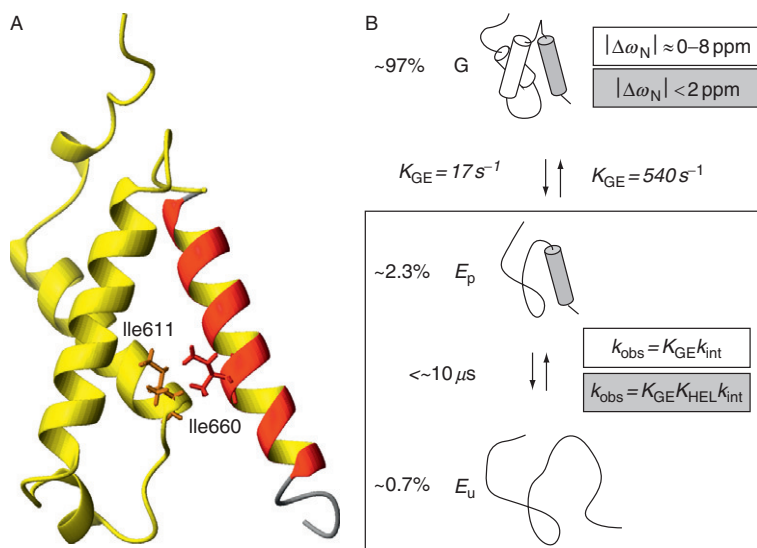


**Figure 1** Relaxation dispersion profiles for two selected residues in KIX. Residue numbering corresponds to that of PDB file 2AGH.<sup>92</sup> The two isoleucines pack against each other, I611 is in helix 2 while I660 resides in helix 3. Images courtesy of Bianka Szalaién Ágoston.

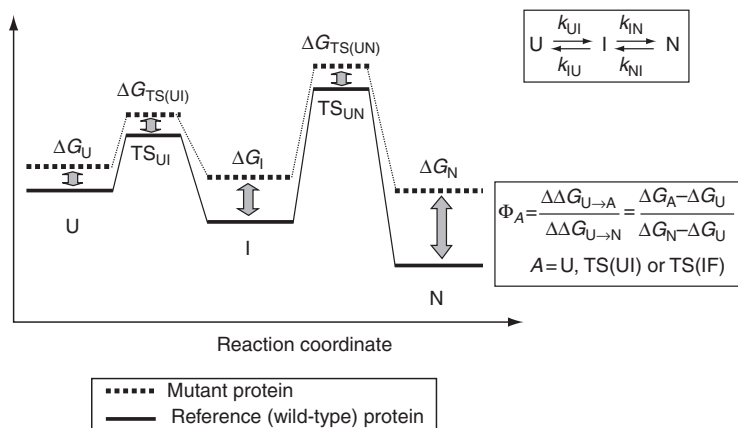
excited state are largely unfolded. The overall picture is summarized in [Figure 2](#). The helix unfolding event cannot be observed directly in NMR as it is too fast ( $<10\ \mu\text{s}$ ) to give rise to a measurable CPMG dispersion effect.

A more detailed picture of the folding of the SH3 (Src homology 3) domain of the Fyn protein kinase has been obtained by relaxation dispersion experiments.<sup>93,94</sup> SH3 domains bind proline-rich sequences and are key components of proteins involved in protein tyrosine kinase signalling pathways. The folding of the SH3 domain of the Fyn protein kinase has been extensively characterized by stopped-flow and NMR experiments. CPMG relaxation dispersion analysis revealed that the Fyn SH3 domain is essentially a three-state folder with an intermediate state.

$\Phi$  values correspond to the ratio of relative destabilizations between the native folded state (N) and a chosen TS or intermediate calculated for a mutant and the wild-type protein,<sup>95</sup> yielding information about the environment of the mutated residue in the state of interest ([Scheme 4](#)).  $\Phi$  values of 1 indicate that the neighborhood of the mutated residue is native-like in the TS or intermediate whereas a  $\Phi$  value of 0 indicates that its environment is not formed. Values between 0 and 1 may reflect partially folded structures or multiple folding pathways so their interpretation requires caution.



**Figure 2** (A) Ribbon representation of the structure of the KIX domain (PDB 2AGH). The third helix is colored red/yellow, Ile611 is highlighted in orange and Ile660 in red. (B) Schematic representation of the interconverting KIX species. The third helix is shown in grey.  $E_p$  is the partially folded sub-state in the excited state and  $E_u$  is the unfolded sub-state.  $^{15}\text{N}$   $|\Delta\omega|$  values as well as the derivation of the observed H–D exchange rates for residues outside (white background) and within (grey background) the third helix are shown. Image adapted from [Ref. 91](#).



**Scheme 4** Derivation of  $\Phi$  values in a three-state folder protein. Outline of the folding process and the folding rates are shown in the upper right inset. U denotes the unfolded state; N, the folded native state; and I, the folding intermediate. The respective transition states between them are denoted  $TS_{UI}$  and  $TS_{UN}$ . The extent of relative destabilization ( $\Delta G$ ) for a particular mutant is shown above the states. Calculation of  $\Phi$  values is shown in the lower right inset. Adapted from Ref. 94.

In the case of a variant of Fyn SH3 (A39V/N53P/V55L), CPMG relaxation data obtained at 15–20 °C can be fit to two-state kinetics corresponding to the  $I \leftrightarrow N$  transition, allowing the determination of CSs in state I. At higher temperatures, using a three-state model  $U \leftrightarrow I \leftrightarrow N$  was appropriate. From these data, all the thermodynamic parameters needed for the calculation of  $\Phi$  values shown in Scheme 4 could be extracted. The results obtained indicate that there are non-native contacts in the intermediate state involving  $\beta$  strand 1, which adopts its native conformation only in the folded state, whereas strands  $\beta 3$  and  $\beta 4$  are already formed in the first transition state  $TS_{UI}$ .

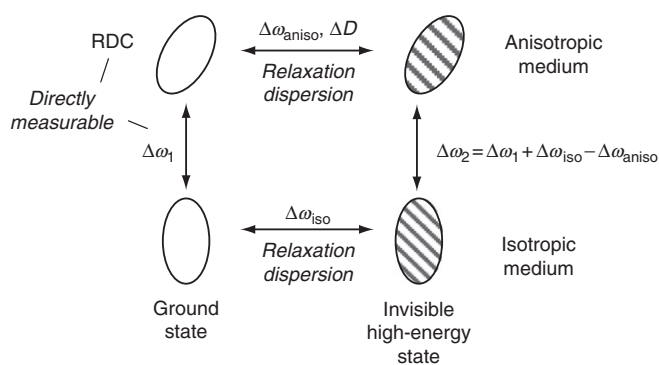
Recent developments in relaxation dispersion experiments allow the determination of atomic-detail 3D structures of low-population excited states. This is based on experiments capable of extracting not only CSs but also RDCs of the excited state (Scheme 5). CS changes upon alignment can be derived for the high-energy “invisible” state according to a suitably designed measurement cycle where the  $\Delta\omega$  values for the excited state are obtained both in isotropic and anisotropic medium.<sup>96,97</sup> RDC values for the excited state can be obtained by recording spin-state selective CPMG relaxation dispersion experiments yielding frequency differences between the TROSY components corresponding to  $|\Delta\nu - \Delta D/2|$  and between anti-TROSY components to  $|\Delta\nu + \Delta D/2|$ .<sup>98</sup>

Such measurements have been applied to a model system exchanging between free and ligand-bound form of an SH3 domain where the low-populated state could either be the free or the ligand-bound form according to the concentrations applied. This setup allowed explicit testing of the methodology as measurements yielding information on the excited state could be verified by direct measurements

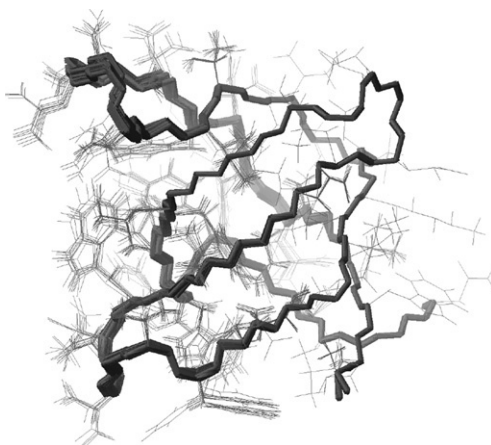


under different sample conditions. Moreover, a high-quality atomic resolution structure of the excited state could be calculated from the data obtained<sup>99</sup> (Figure 3).

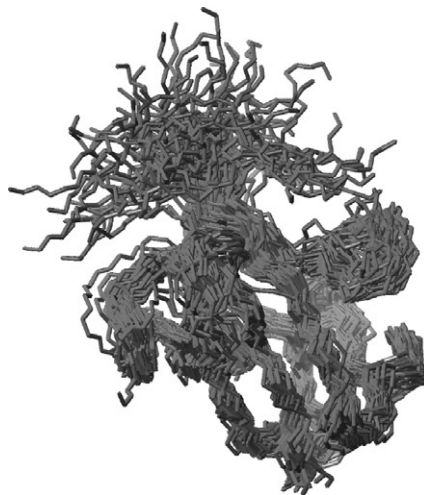
Conformationally heterogeneous states of proteins can be determined using NMR-derived structural data and suitable molecular dynamics techniques.<sup>100</sup> Residual dipolar couplings have been shown to represent motions in ubiquitin slower than its correlation time.<sup>101</sup> Using an extensive set of residual dipolar couplings, namely, 36 sets of amide NH, 6 sets of  $\text{H}^{\text{N}}\text{C}'$  and  $\text{NC}'$  as well as 11



**Scheme 5** Interrelation and measurement scheme of chemical shift and RDC values in a two-state system where the high-energy state is scarcely populated. Adapted from Ref. 96.



**Figure 3** Ten lowest-energy conformers of the excited (Ark1p peptide-bound) state of the Abp1p SH3 domain determined using restraints from residual anisotropic interactions. Note the remarkable fit of the conformers demonstrating the precision of the restraints used. Drawn from PDB structure 2K3B.<sup>99</sup>



**Figure 4** EROS ensemble of human ubiquitin determined using NOE and orientational restraints. Drawn from structure 2K39.<sup>102</sup>

sets of methyl group RDCs, a 116-membered conformer ensemble of human ubiquitin has been calculated.<sup>102</sup> The simulation was done using ensemble-averaged NOE and orientation restraints implemented in the GROMACS molecular dynamics package,<sup>67,103</sup> using a protocol designated EROS for “ensemble refinement with orientational restraints” by the authors. The resulting ensemble reflects the internal dynamics of ubiquitin up to the microsecond time scale (Figure 4). Intriguingly, the structural diversity of the ensemble covers the range of known conformational changes occurring during partner binding observed in ubiquitin-containing molecular complexes by X-ray crystallography. This observation suggests that binding partners select from the existing conformational equilibrium in solution, thus not induced fit, rather conformer selection accompanied by a population shift explains partner recognition for ubiquitin (see above). The prevalent pincer-like motion observed for the molecule affecting the binding interface suggests that functionally relevant motions dominate the internal dynamics of ubiquitin. Moreover, these motions ensure that the entropic cost for high-affinity binding remains low even when allowing the recognition of a number of different partners.

## 6.2. Characterization of systems with sub- $\tau_c$ motions

Studies focusing on fast internal motions generally use heteronuclear relaxation experiments most commonly interpreted within the model-free framework. In this section, we start with proteins with well-defined structure and after describing more flexible systems arrive to the class of IDPs.

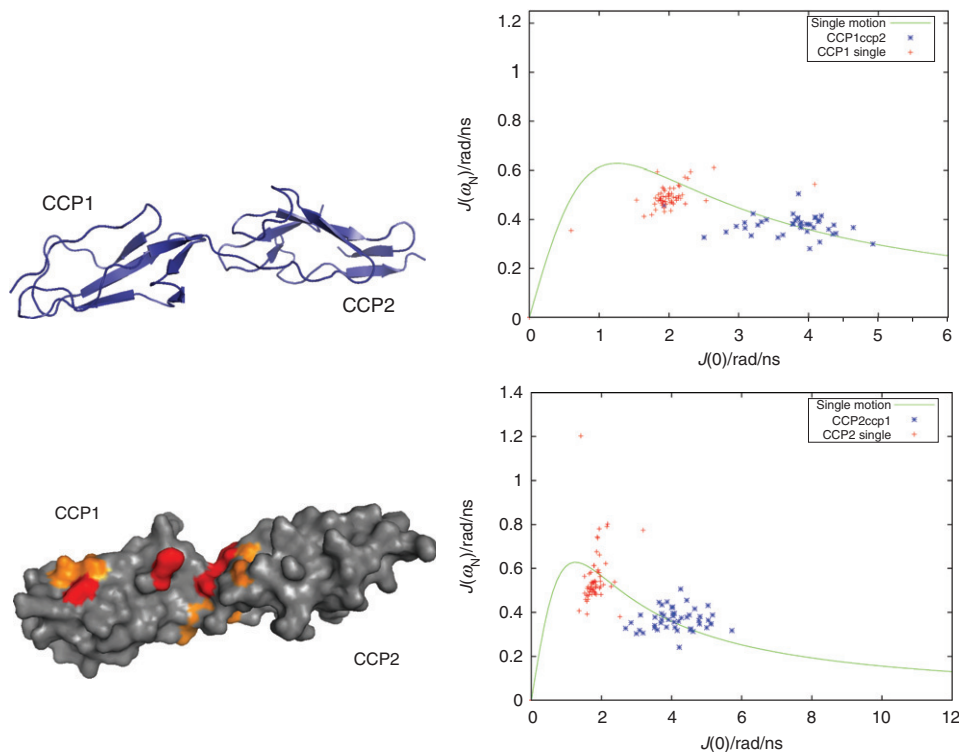
### 6.2.1. Proteins with considerable rigidity

Complement control modules (CCPs) occur frequently in modular proteins of the immune system and are thought to modulate both intra- and inter-molecular interactions ultimately regulating the activation of specific proteases. Internal dynamics of the CCP1–CCP2 module pair of the complement protease has been mapped by  $^{15}\text{N}$  relaxation experiments in order to localize its possible interaction sites and regions of enhanced flexibility. Although model-free parameters could be extracted for the isolated CCP1 and CCP2 modules, no diffusion tensor could be reliably obtained for their covalently linked construct CCP1CCP2. Thus, the mobility of the free and tandem occurring domains could be compared using reduced spectral density mapping.<sup>104</sup>

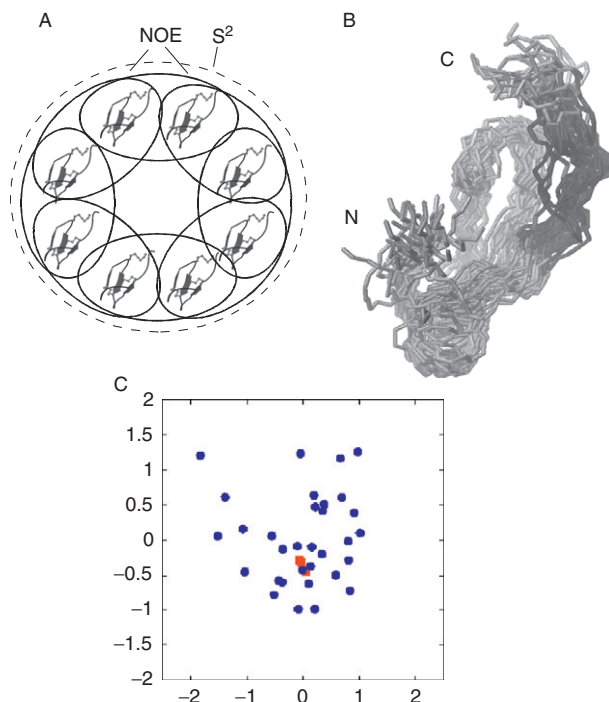
In the graphical form of the reduced spectral density mapping analysis depicted in Figure 5, the solid line represents the single motion limit, thus dots near the line represent amide N–Hs with motion following the overall tumbling of the full molecule. The overall correlation time can be estimated by the average position of the dots relative to the single-motion line as its intersection with a line fitted to the dots yields  $0.4 \cdot \tau_c$ .<sup>77</sup> Thus, the increase in molecular size of the tandem construct relative to the free modules can clearly be deduced. In general, residues with high  $J(\omega_N)$  and low  $J(0)$  values exhibit largely unrestricted motion whereas those with increased  $J(0)$  are affected by chemical exchange. The internal mobility of the CCP modules investigated, especially that of CCP1, shows remarkable changes upon linking to the C-terminal CCP2 domain. This notion is corroborated by the observed CS changes in the tandem construct relative to the free modules calculated as the weighted average of  $^{15}\text{N}$  and  $^1\text{H}$  amide shifts for each residue<sup>105</sup> (Figure 5). Largest changes are observed on surface loops corresponding to putative protein:protein interaction sites in the modules.

Smaller proteins are generally more flexible even when stabilized by disulfide bridges. This is indeed the case for the 35-residue canonical serine protease inhibitor SGCI (*Shistosoma gregaria* chymotrypsin inhibitor), for which model-free analysis of  $^{15}\text{N}$  relaxation data yielded general order parameters around 0.7 throughout the molecule.<sup>106</sup> The relatively high flexibility of these molecules contrasts the still accepted rigid lock-and-key theory for canonical serine protease inhibition stating that no conformational changes occur in the rigid protease binding loop upon interaction with the target enzyme. To analyze the role of dynamics in molecular recognition at atomic detail, dynamically restrained conformer ensembles<sup>107</sup> were generated using  $S^2$  and NOE data. To avoid both over- and under-fitting, the MUMO (Minimal Under-restraining Minimal Over-restraining)<sup>108</sup> procedure was applied where NOE restraints are applied in a pairwise manner over the simultaneously refined conformer replicas whereas all replicas are restrained by the amide NH  $S^2$  values.

The resulting ensemble reflects the ps–ns time-scale internal dynamics of the inhibitor (Figure 6) and is superior to that determined by “conventional” structure calculation methods aimed at refining each replica for best agreement with NOE data. Improvements are observed both in terms of conforming to ideal geometry and correspondence to observed H $\alpha$  CSs. Moreover, specific interactions are more restricted in the dynamical ensemble than in the conventional one,



**Figure 5** *Upper left panel:* Ribbon representation of the linked CCP1-CCP2 domains of Clr. *Lower left panel:* combined chemical shift changes in the tandem construct relative to the free modules mapped onto the surface of the molecule, red  $> 1.00$  ppm; orange  $> 0.60$  ppm. See text for details. *Right panel:* graphical representation of the reduced spectral density mapping analysis (300 K, 500 MHz) of the free (red dots) and linked (blue dots) modules,  $J(\omega_N)$  plotted as a function of  $J(0)$ . The solid line represents the single motion limit.



**Figure 6** (A) Scheme of the MUMO calculations used for calculating the dynamic conformation ensemble of SGCI. (B) Dynamic conformational ensemble of SGCI with the protease binding loop shown in dark grey. (C) Result of the principal component analysis on the inhibitor structures depicting that the dynamic conformational ensemble (blue circles) contains the conformers of corresponding to the enzyme-bound state (red boxes).

clearly indicating that the resulting high conformational diversity is not a non-specific feature stemming from relaxing the restraints by applying them to the ensemble rather to individual conformers. The dynamic conformational ensemble contains conformers highly similar to the protease-bound form of the inhibitor, suggesting that not a rigid lock-and-key interaction rather conformer selection is appropriate to describe the process of enzyme binding. However, as the conformational motions are faster than the intermolecular association rate, they are not a limiting factor in the recognition process, which in fact yields a scenario consistent with the rigid-body model neglecting conformational fluctuations.<sup>109</sup>

### 6.2.2. Dynamics of intrinsically disordered and unfolded proteins

Unlike for globular proteins, internal motions of IDPs can hardly be interpreted within the framework of the Lipari-Szabo model-free formalism. IDPs are dominated by segmental motions with low or negligible cooperativity between

subunits, the approach fails as the global rotational diffusional correlation time as a single reference measure cannot be defined in a meaningful way. Instead, reduced spectral density mapping can be applied, where  $J(0)$ ,  $J(\omega_N)$  and  $J(0.87\omega_H)$  frequencies are of significance. Tracing dynamical properties along the primary sequence is of primary interest for IDPs revealing local and residual structural preferences, such as hydrophobic clusters, residual secondary structural elements and transient long-range contacts. Recently, various types of relaxation measurements have been successfully applied for a number of IDPs; the transcription factor specific for the expression of bacterial flagella and chemotaxis genes. FlgM,<sup>110</sup> the 393-residue long tumour suppressor p53,<sup>111</sup>  $\alpha$ -synuclein, the major protein component of amyloid-like deposits in Parkinson's disease,<sup>112</sup> etc. as collected and meticulously reviewed in [Ref. 23](#).

**6.2.2.1. Residual structural elements holding functionality** The identification and characterization of minor populations of residual structural elements within a highly mobile and unfolded or intrinsically disordered structure is a continuous challenge. For the urea and acid unfolded state of apomyoglobin not only the kinetic folding process was proposed<sup>113</sup> but also PRE measurements uncovered the presence of a collapsed state populated as low as 5%.<sup>114</sup> In fact, multiple distinct hydrophobic clusters of differing thermodynamic stability could be identified. Interestingly enough, these sparsely populated states can have some native-like character.

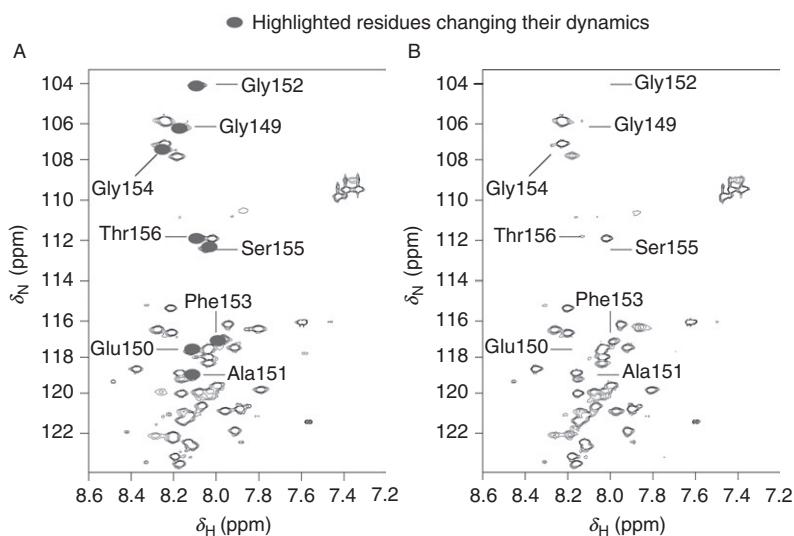
Calpastatin is a specific inhibitor of calpain, a calcium-activated intracellular cysteine protease made responsible of several physiological and pathological phenomena.<sup>115</sup> The complete sequence-specific assignment of the 121 non-Pro residues (out of the 126) enabled the detailed characterization of its backbone dynamics in solution.<sup>116</sup> Both CSI data and  $^{15}\text{N}$  relaxation rates in conjunction with heteronuclear NOE values demonstrate that two out of the three conserved subdomains A (Ser12–Gly30) and C (Ser87–Cys105) present low (5–10%) but significant amount of helical backbone conformations. In addition, subdomain B (Met50–Arg70), the primary determinant of inhibition, also has non-random backbone fold. Binding to calpain takes place through a few specificity-determinant residues connected by variable flexible linkers separating subdomains A from B and B from C. The exact binding mode of calpastatin to the enzyme has been recently revealed by X-ray crystallography.<sup>117</sup> This atomic resolution picture agrees perfectly with the independent NMR study: a tripartite binding mode was revealed, in which the disordered inhibitor wraps around, and contacts, the enzyme at three points clearly facilitated by flexible linkers. The residual helical elements of subdomains A, B and C of specific dynamics determine target enzyme binding. The preformed structural elements together with their flexibility on the ps–ns time scale permit a unique combination of specificity, speed and binding strength governing the regulation of calpain.<sup>118</sup>

**6.2.2.2. Turning disorder to order can hold functionality** SecA is a helicase-like motor coupling ATP hydrolysis with the translocation of extracytoplasmic substrates.<sup>119</sup> It was shown that SecA takes advantages of such a mechanism, namely

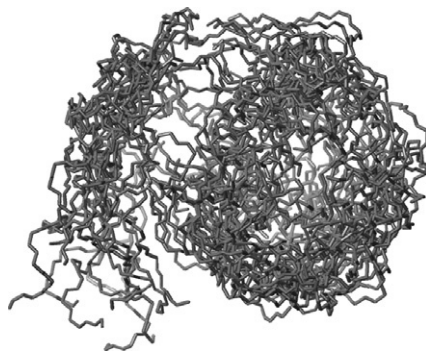
its conserved domains close to the nucleotide cleft undergo cycles of disorder-order transitions which is coupled to functional catalytic states. These state transitions are controlled by Arg-fingers acting between the domains. The disorder-order interconversions are coupled to ligand binding and yield the basis of not only the catalytic activity but also that of allosteric regulation.

The catalytic action of dUTP hydrolase (dUTPase), an enzyme preventing uracil incorporation into DNA by lowering the amount of dUTP in the cell, involves ordering of its flexible C terminal tail region. The disorder-to-order transitional shift detected by NMR is obvious as the sharp resonances of the disordered tail of the homotrimer (total MW over 60 kDa) get broadened and became undetectable (Figure 7) by  $^1\text{H}$ - $^{15}\text{N}$  heteronuclear correlation spectroscopy.<sup>120</sup> This can be observed as the “disappearance” of eight sharp resonances corresponding to eight residues of the C-terminus upon ligand binding. Such a conformational shift and fundamental alterations in backbone dynamics put light on the kinetics of the enzymatic mechanism and suggest allostereism in the eukaryotic dUTPase.

Detailed atomic-level characterization of IDPs can result in the generation of highly diverse conformational ensembles which can be analyzed analogously to those generated for folded proteins. One approach is highly similar to conventional structure calculations involving restrained molecular dynamics while an alternative way is to generate a high number of conformers with varying degree of randomization and validating the resulting ensemble against experimental data.<sup>121</sup>



**Figure 7** Heteronuclear correlation spectra ( $^1\text{H}$ - $^{15}\text{N}$  HSQC at 500 MHz) of *D. melanogaster* dUTPase without substrate (A) and with  $\alpha,\beta$ -imino-dUTP. The indicated peaks that change their internal dynamics and diminish, Gly149-Thr156 of the C-terminus, are those involved in substrate binding.



**Figure 8** First 20 members of the structural ensemble of PDE $\gamma$  Drawn from structure PDB ID 2JU4<sup>83</sup> with the program MOLMOL.<sup>122</sup>

The first approach was used for calculating a structural ensemble for the  $\gamma$  subunit of phosphodiesterase 6 (PDE $\gamma$ ), a key protein in signal transduction during vision (Figure 8). Restraints used for the calculation comprise NOE data, backbone dihedral angles estimated from CSs and PRE values defining long-range interactions in the molecule. Analysis of the ensemble revealed that partner binding of PDE $\gamma$  is achieved by conformer selection, as preformed structural elements characteristic for the complex are clearly present in solution.<sup>83</sup>

The intrinsically disordered tau protein, a regulator of microtubule organization in neurons, is a major component of amyloid-like aggregations in a number of neurodegenerative diseases. Its atomic-level structure was examined by generating 50,000 conformers and validating them against NOE, scalar coupling and RDC data. Conformers generated using a structural library-based approach termed flexible-meccano<sup>123</sup> did not yield satisfactory agreement with experimental parameters, thus, specially setup molecular dynamics simulations allowing higher conformational freedom at four sites in the protein were performed. The results revealed that type I  $\beta$ -turn conformational elements are prevalent in the solution structure of tau, whose significance as enhancers or inhibitors of aggregation remains elusive.<sup>124</sup>

## 7. CONCLUDING REMARKS

From the simpler resonance line-shape and H/D-exchange analysis to the more complex studies of inherent dynamics, occurring on various time scale of motion, NMR remains a good choice to investigate protein flexibility and plasticity. If line-broadening due to exchange and inhomogeneity is minimized (or completely eliminated), then half-width,  $\Delta\nu_{1/2}$ , of a line becomes proportional to  $R_2^*$ , the transverse relaxation rate constant.

$$R_2^* = R_2 + R_{\text{inhomo}} + R_{\text{exchange}}, \quad \Delta\nu_{1/2} = R_2^* / \pi \quad (21)$$



In other words, by simply looking at a resonance signal its shape can refer to its relaxation, more precisely to its  $R_2^*$ .

Based on random fields, relaxation theory  $R_2$  decreases as molecular tumbling gets faster and more effectively averages the residual dipolar broadening. Both in the fast and slow motion limits,  $R_2$  is proportional to  $\tau_c$ <sup>6</sup>:

$$R_2 = 2\gamma^2 \overline{B_{\text{loc}}^2} \tau_c \quad \text{and} \quad R_2 = \gamma^2 \overline{B_{\text{loc}}^2} \tau_c \quad (22)$$

Thus, the line shape determining  $R_2$  correlates with the rotational diffusional correlation time;  $\tau_c$ .

$$\Delta\nu_{1/2} \approx R_2 \approx \tau_c \quad (23)$$

Therefore a larger molecule of spherical shape “wanders around” more slowly and thus produces a broader signal, a phenomenon primarily responsible for the size limit of proteins accessible by NMR methods.

For a globular protein of approximately spherical shape, the isotropic tumbling rate can be characterized by the rotational diffusional correlation time,  $\tau_c$ , as described above. Assuming that the protein fits in a sphere of radius  $r$ , then the viscosity ( $\eta$ ) and temperature ( $T$ ) of the sample determines  $\tau_c$ .

$$\tau_c = \frac{4\pi\eta r^3}{3k_B T} \quad (24)$$

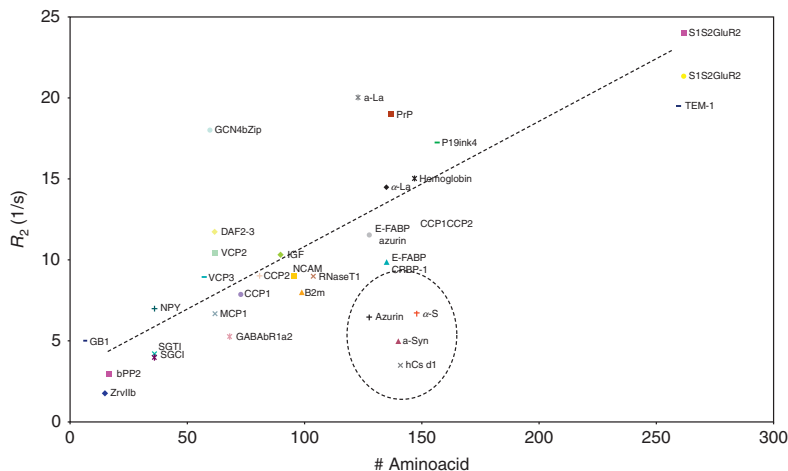
Alternatively, the number of the amino acid residues,  $N$ , forming a globular protein is proportional with  $\tau_c$ .<sup>125</sup>

$$\tau_c = \frac{9.148 \times 10^{-3}}{T} \exp\left(\frac{2416}{T}\right) N^{0.93} \quad (25)$$

However, if the time averaged structure of the polypeptide or protein is less spherical, or if it contains disordered or loosely folded parts, or if it is an IDP, than the “characteristic”  $\tau_c$  will not reflect its global motion any more. In case of asynchronized and fragmental backbone motion  $R_2$  drops. For example, the above mentioned quasi spherical CCP1 protein composed of some 60 residues presents an  $\langle R_2 \rangle$  of about 7 Hz when  $^{15}\text{N}$  relaxation is completed. The twice as long calpastatin (hCSd1)<sup>116</sup> also described above contains over 120 amino acid residues, nevertheless its  $\langle R_2 \rangle$  is around 3.5 Hz rather than the “expected” 14 Hz. Furthermore, the dimer of CCP1–CCP2 composed of about the same number of amino acid residues has an  $\langle R_2 \rangle$  of about 13.5 Hz (Figure 9). Interestingly enough, the calpastatin dimer (hCSd1–hCSd2), approximately 250 residues long, has about the same  $\langle R_2 \rangle$  value.

Thus, globular proteins above a certain size are largely inaccessible to NMR methods, whereas IDPs can be characterized regardless of their size.

The major paradigm of structural biology is that the amino acid sequence determines protein structure and function. Recent advances in understanding protein dynamics calls for an extension of this picture by including that protein dynamics, essentially coupled to function, is also encoded in the primary



**Figure 9** For quasi spherical proteins, the molecular size (measured here by  $N$ , the number of amino acid residues) is proportional to  $R_2$ . However, IDPs (circled), dominated by asynchronized and fragmented motions exhibit lower  $R_2$  values than expected based on their length.

sequence. This extension is consistent with the observation that proteins with similar 3D structure exhibit characteristic differences in their internal dynamics at a given time scale, with possible connection to their specific function.<sup>106</sup> Also, comparison of mesophilic and thermophilic enzymes revealed that the dynamics of homologous counterparts are different at any given temperature but are similar at conditions optimal for catalysis.<sup>126</sup> Thus, functionally relevant dynamics, like structure, could be optimized during evolution to perfection catalysis/ligand binding/partner regulation and other functions. As highlighted with the examples above, dynamics at various time scales can be relevant for function, from nanoseconds in highly flexible systems like IDPs or small proteins to microseconds in typical globular proteins usually described by a single structure implicitly suggesting a well-defined, relatively rigid conformation.

To understand the links between dynamics and function, direct representation of the conformational space sampled during dynamics is needed, for example by using dynamically relevant structural ensembles. This represents a paradigm shift compared to the use of single or highly similar “representative structures” aimed at approaching the precision provided by X-ray crystallography. Moreover, the standard tools of assessing the quality of NMR structures are not necessarily applicable: for example high RMSD is no longer a sign of low precision and the structures should be evaluated against NMR parameters as an ensemble, not as individual conformers.

Although in the past years, significant progress has been made in generating dynamically relevant ensembles, these methods are still not widely used. Such calculations require efforts beyond the current routine of protein structure determination by NMR both from the experimental side, as heteronuclear relaxation and/or

RDC data should be collected, as well as by means of computational analysis. The problem is even less tractable for IDPs where the size of the ensemble covering all relevant motions and reproducing the measured NMR parameters is a key issue. Furthermore, the diversity of such structural ensembles poses difficulties in their analysis by structural bioinformatics tools.<sup>127</sup>

Further consequences of internal dynamics are functional analyses like *in silico* docking methods for which proper representation of protein flexibility is a major challenge.<sup>128</sup> For studies incorporating molecular flexibility to understand and predict biological processes, we propose the term *DSAR* for *Dynamic-Structure-Activity Relationship* analysis. Incorporating the internal dynamics of binding partners into drug development might open new avenues to the development of more potent and selective inhibitors. Although the classic lock-and-key view on protein-ligand interactions proved extremely fruitful in the past decades, should be extended into the fourth, time dimension to allow for the representation, analysis and design of dynamic locks with flexible keys.

## ACKNOWLEDGEMENTS

This work was supported by grants from ICGB (CRP/HUN08-03), the Hungarian Scientific Research Fund (OTKA K72973, F68079 and NI-68466). Z. G. is also supported by a János Bolyai Research Fellowship. The authors would like to thank Veronika Harmat, Bianka Ágoston, Andrea Bodor, Andras Láng and Róbert Kiss for they help in improving the manuscript.

## REFERENCES

1. V. A. Jarymowycz and M. J. Stone, *Chem. Rev.*, 2006, **106**, 1624–1671.
2. D. D. Boehr, R. Nussinov and P. E. Wright, *Nat. Chem. Biol.*, 2009, **5**, 789–796.
3. P. Bourne, and H. Weissig (eds.), (2003). *In Structural Bioinformatics*. John Wiley & Sons, Hoboken, NJ.
4. H. M. Berman, *Found. Cryst.*, 2008, **64**, 88–95.
5. P. Güntert, *Methods Mol. Biol.*, 2004, **278**, 353–378.
6. J. Keeler, *Understanding NMR Spectroscopy*. Wiley, 2002.
7. P. Dosset, J.-C. Hus, M. Blackledge and D. Marion, *J. Biomol. NMR*, 2000, **16**, 23–28.
8. R. Brüschweiler and P. E. Wright, *J. Am. Chem. Soc.*, 1994, **116**, 8426–8427.
9. K. Fredriksson, M. Louhivuori, P. Permi and A. Annala, *J. Am. Chem. Soc.*, 2004, **126**, 12646–12650.
10. R. B. Best and M. Vendruscolo, *J. Am. Chem. Soc.*, 2004, **126**, 8090–8091.
11. C. D. Schwieters, J. D. Kuszewski and G. M. Clore, *Prog. Nucl. Magn. Reson. Spect.*, 47–62.
12. W. Baumeister and A. C. Steven, *Trends Biochem. Sci.*, 2000, **25**, 624–631.
13. K. Mitra, *Annu. Rev. Biophys. Biomol. Struct.*, 2006, **35**, 299–317.
14. J. P. Hennessey and W. C. Johnson, *Biochemistry*, 1981, **20**, 1085–1094.
15. P. Manavalan and W. C. Johnson, Jr., *Anal. Biochem.*, 1987, **167**, 76–85.
16. I. H. M. Van Stokkum, H. J. W. Spoelder, M. Bloemendal, R. Van Grondelle and F. C. A. Groen, *Anal. Biochem.*, 1990, **191**, 110–118.
17. N. Sreerema and R. W. Woody, *Anal. Biochem.*, 1993, **209**, 32–44.
18. P. Pancoska, S. C. Yasui and T. A. Keiderling, *Biochemistry*, 1991, **30**, 5089–5103.
19. B. Dalmas, G. J. Hunter and W. H. Bannister, *Biochem. and Mol. Biol. Int.*, 1994, **34**, 17–26.
20. P. Pancoska, V. Janota and T. A. Kiederling, *Anal. Biochem.*, 1999, **267**, 72–83.
21. I. Jákli and A. Perczel, *J. Pept. Sci.*, 2009, **15**, 738–752.

22. S. Mukhopahyay, R. Krishnan, E. A. Lemke, S. Lindquist and A. A. Deniz, *Proc. Natl. Acad. Sci. USA*, 2007, **104**, 2649–2654.
23. P. Tompa, *Structure and Function of Intrinsically Disordered Proteins*. CRC Press, 2009.
24. D. M. Ferraro, N. D. Lazo and A. D. Robertson, *Biochemistry*, 2004, **43**, 587–594.
25. A. N. Hoofnagle, K. A. Resing and N. G. Ahn, *Annu. Rev. Biophys. Biomol. Struct.*, 2003, **32**, 1–25.
26. K. N. Trueblood, H.-B. Bürgi, H. Burzlaff, J. D. Dunitz, C. M. Gramaccioli, H. H. Schulz, U. Shmueli and S. C. Abrahams, *Acta Cryst. A*, 1996, **52**, 770–781.
27. M. D. Winn, G. N. Murshudov and M. Z. Papiz, *Methods Enzymol.*, 2003, **374**, 300–321.
28. S. Rajagopal, S. Anderson, V. Srajer, M. Schmidt, R. Pahl and K. Moffat, *Structure*, 2005, **13**, 55–63.
29. K. Moffat, *Chem. Rev.*, 2001, **101**, 1569–1581.
30. D. Bourgeois, F. Schotte, M. Brunori and B. Vallone, *Photochem. Photobiol. Sci.*, 2007, **6**, 1047–1056.
31. V. Srajer and W. E. Royer, Jr., *Methods Enzymol.*, 2008, **437**, 379–395.
32. H. Ihee, S. Rajagopal, V. Srajer, R. Pahl, S. Anderson, M. Schmidt, F. Schotte, P. A. Anfinsen, M. Wulff and K. Moffat, *Proc. Natl. Acad. Sci. USA*, 2005, **102**, 7145–7150.
33. M. Schmidt, H. Ihee, R. Pahl and V. Srajer, *Methods Mol. Biol.*, 2005, **305**, 115–154.
34. M. Schmidt, T. Graber, R. Henning and V. Srajer, *Acta Crystallogr. A*, 2010, **66**, 198–206.
35. K. Moffat, *Faraday Discuss.*, 2003, **122**, 65–77, discussion 79–88.
36. B. L. Stoddard, *Methods*, 2001, **24**, 125–138.
37. J. Hajdu, R. Neutze, T. Sjögren, K. Edman, A. Szöke, R. C. Wilmouth and C. M. Wilmot, *Nat. Struct. Biol.*, 2000, **7**, 1006–1012.
38. A. K. Gardino, J. Villali, A. Kivenson, M. Lei, C. F. Liu, P. Steindel, E. Z. Eisenmesser, W. Labeikovsky, M. Wolf-Watz, M. W. Clarkson and D. Kern, *Cell*, 2009, **139**, 1109–1118.
39. D. Staunton, R. Schlinkert, G. Zanetti, S. A. Coelbrook and I. D. Campbell, *Magn. Reson. Chem.*, 2006, **44**, S2–S9.
40. M. Kainosho, T. Torizawa, Y. Iwashita, T. Terauchi and A. M. Ono, *Nature*, 2006, **440**, 52–57.
41. Z. Gáspári, G. Pál and A. Perczel, *BioEssays*, 2008, **30**, 772–780.
42. K. Wüthrich, *NMR of Proteins and Nucleic Acids*. Wiley, 1986.
43. H. N. Moseley, D. Monleon and G. T. Montelione, *Methods Enzymol.*, 2001, **339**, 91–108.
44. Y. S. Jung and M. Zweckstetter, *J. Biomol. NMR*, 2004, **30**, 11–23.
45. S. Hiller, G. Wider and K. Wüthrich, *J. Biomol. NMR*, 2008, **42**, 179–195.
46. R. B. Best and M. Vendruscolo, *Structure*, 2006, **14**, 97–106.
47. S. Neal, A. M. Nip, N. Zhang and D. S. Wishart, *J. Biomol. NMR*, 2003, **26**, 215–240.
48. A. Cavalli, X. Salvatella, C. M. Dobson and M. Vendruscolo, *Proc. Natl. Acad. Sci. USA*, 2007, **104**, 9615–9620.
49. D. S. Wishart, D. Arndt, M. Berjanskii, P. Tang, J. Zhou and G. Lin, *Nucleic Acids Res.*, 2008, **36**, W496–W502.
50. M. V. Berjanskii and D. S. Wishart, *J. Am. Chem. Soc.*, 2005, **127**, 14970–14971.
51. M. V. Berjanskii and D. S. Wishart, *J. Biomol. NMR*, 2008, **40**, 31–48.
52. D. S. Wishart, C. G. Bigam, A. Holm, R. S. Hodges and B. D. Sykes, *J. Biomol. NMR*, 1995, **5**, 67–81.
53. S. Schwarzingier, G. J. A. Kroon, T. R. Foss, P. Wright and H. J. Dyson, *J. Biomol. NMR*, 2000, **18**, 43–48.
54. G. Cornilescu, F. Delaglio and A. Bax, *J. Biomol. NMR*, 1999, **13**, 289–302.
55. A. De Simone, A. Cavalli, S. T. Hsu, W. Vranken and M. Vendruscolo, *J. Am. Chem. Soc.*, 2009, **131**, 16332–16333.
56. S. Schwarzingier, G. J. A. Kroon, T. R. Foss, J. Chung, P. Wright and H. J. Dyson, *J. Am. Chem. Soc.*, 2001, **123**, 2970–2978.
57. B. Barua, J. C. Lin, V. D. Williams, P. Kummier, J. W. Neidigh and N. H. Andersen, *Protein Eng. Des. Sel.*, 2008, **21**, 171–185.
58. A. M. Bonvin and A. T. Brünger, *J. Biomol. NMR*, 1996, **7**, 72–76.
59. M. Karplus, *J. Chem. Phys.*, 1959, **30**, 11–15.
60. K. Lindorff-Larsen, R. B. Best and M. Vendruscolo, *J. Biomol. NMR*, 2005, **32**, 273–280.
61. P. R. L. Markwick, S. A. Showalter, G. Bouvignies, R. Brüschweiler and M. Blackledge, *J. Biomol. NMR*, 2009, **45**, 17–21.
62. M. Barfield, *J. Am. Chem. Soc.*, 2002, **124**, 4158–4168.

63. J. M. Schmidt, M. J. Howard, M. Maestre-Martínez, C. S. Pérez and F. Löhr, *Magn. Reson. Chem.*, 2009, **47**, 16–30.
64. J. M. Schmidt, Y. Hua and F. Löhr, *Proteins*, 2010, **78**, 1544–1562.
65. A. Annila and P. Permi, *Concept Magn. Reson. A*, 2004, **23A**, 22–37.
66. A. Bax, *Protein Sci.*, 2003, **12**, 1–16.
67. B. Hess and R. M. Scheek, *J. Magn. Reson.*, 2003, **164**, 19–27.
68. M. Zweckstetter, *Nat. Protoc.*, 2008, **3**, 679–690.
69. M. Louhivuori, R. Otten, K. Lindorff-Larsen and A. Annila, *J. Am. Chem. Soc.*, 2006, **128**, 4371–4376.
70. T. I. Igumenova, K. K. Frederick and A. J. Wand, *Chem. Rev.*, 2006, **106**, 1672–1699.
71. G. M. Clore, P. C. Driscoll, P. Wingfield and A. M. Gronenborn, *Biochemistry*, 1990, **29**, 7387–7401.
72. A. M. Mandel, M. Akke and A. G. Palmer, 3rd, *J. Mol. Biol.*, 1995, **246**, 144–163.
73. N. A. Farrow, R. Muhandiram, A. U. Singer, S. M. Pascal, C. M. Kay, G. Grish, S. E. Shoelson, T. Pawson, J. D. Forman-Kay and L. E. Kay, *Biochemistry*, 1994, **33**, 5984–6003.
74. Y. Hiyama, C. H. Niu, J. V. Silverton, A. Bavoso and D. A. Torchia, *J. Am. Chem. Soc.*, 1988, **110**, 2378–2383.
75. A. G. Palmer, 3rd, M. Rance and P. E. Wright, *J. Am. Chem. Soc.*, 1991, **113**, 4371–4380.
76. J. F. Lefèvre, K. T. Dayie, J. W. Peng and G. Wagner, *Biochemistry*, 1996, **35**, 2674–2686.
77. H. Křížová, L. Židek, M. J. Stone, M. V. Novotny and V. Sklenář, *J. Biomol. NMR*, 2004, **28**, 369–384.
78. J. P. Loria, R. P. Berlow and E. D. Watt, *Acc. Chem. Res.*, 2008, **41**, 214–221.
79. A. G. Palmer, 3rd and F. Massi, *Chem. Rev.*, 2006, **106**, 1700–1719.
80. N. R. Skrynnikov, W. Dahlquist and L. E. Kay, *J. Am. Chem. Soc.*, 2002, **124**, 12352–12360.
81. G. M. Clore and J. Iwahara, *Chem. Rev.*, 2006, **109**, 4108–4139.
82. J. Iwahara, C. Tang and G. M. Clore, *J. Magn. Reson.*, 2007, **184**, 185–195.
83. J. Song, L.-W. Guo, H. Muradov, N. O. Artemyev, A. E. Ruoho and J. L. Markley, *Proc. Natl. Acad. Sci. USA*, 2008, **105**, 1505–1510.
84. J. R. Gillespie and D. Shortle, *J. Mol. Biol.*, 1997, **268**, 158–169.
85. T. M. Raschke and S. Marqusee, *Curr. Opin. Biotechnol.*, 1998, **9**, 80–86.
86. F. M. Hughson, P. E. Wrigth and R. L. Baldwin, *Science*, 1990, **249**, 1544–1548.
87. S. M. Nabuurs and C. P. M. van Mierlo, *J. Biol. Chem.*, 2010, **285**, 4165–4172.
88. C. Nishimiura, H. J. Dyson and P. E. Wright, *Proc. Natl. Acad. Sci. USA*, 2005, **102**, 4765–4770.
89. W. A. Houry, J. M. Sauder, H. Roder and H. A. Scheraga, *Proc. Natl. Acad. Sci. USA*, 1998, **95**, 4299–4302.
90. E. Z. Eisenmesser, O. Millet, W. Labeikovsky, D. M. Korzhnev, M. Wolf-Watz, D. A. Bosco, J. J. Skalicky, L. E. Kay and D. Kern, *Nature*, 2005, **438**, 117–121.
91. M. Tollinger, K. Klobner, B. Ágoston, C. Dorigoni, R. Lichtenecker, W. Schmid and R. Konrat, *Biochemistry*, 2006, **45**, 8885–8893.
92. R. N. DeGuzman, N. K. Goto, H. J. Dyson and P. E. Wright, *J. Mol. Biol.*, 2006, **355**, 1005–1013.
93. D. M. Korzhnev, X. Salvatella, M. Vendruscolo, A. A. Di Nardo, A. R. Davidson, C. M. Dobson and L. E. Kay, *Nature*, 2004, **430**, 586–590.
94. P. Neudecker, A. Zarrine-Afsar, A. R. Davidson and L. E. Kay, *Proc. Natl. Acad. Sci. USA*, 2007, **104**, 15717–15722.
95. A. R. Fersht and V. Daggett, *Cell*, 2002, **108**, 573–582.
96. D. F. Hansen, P. Vallurupalli and L. E. Kay, *J. Biomol. NMR*, 2008, **41**, 113–120.
97. P. Vallurupalli, D. F. Hansen and L. E. Kay, *J. Am. Chem. Soc.*, 2008, **130**, 2734–2735.
98. P. Vallurupalli, D. F. Hansen, E. Stollar, E. Meirovich and L. E. Kay, *Proc. Natl. Acad. Sci. USA*, 2007, **104**, 18473–18477.
99. P. Vallurupalli, D. F. Hansen, E. Stollar, E. Meirovich and L. E. Kay, *Proc. Natl. Acad. Sci. USA*, 2008, **105**, 11766–11771.
100. M. Vendruscolo, *Curr. Opin. Struct. Biol.*, 2007, **17**, 15–20.
101. N. A. Lakomek, T. Carlomagno, S. Becker, C. Griesinger and J. Meiler, *J. Biomol. NMR*, 2006, **34**, 101–115.
102. O. F. Lange, N. A. Lakomek, C. Farès, G. F. Schröder, K. F. A. Walter, S. Becker, J. Meiler, H. Grubmüller, C. Griesinger and B. L. de Groot, *Science*, 2008, **320**, 1471–1475.
103. D. Van der Spoel, E. Lindahl, B. Hess, G. Groenhof, A. E. Mark and H. J. C. Berendsen, *J. Comput. Chem.*, 2005, **26**, 1701–1718.

104. A. Láng, K. Szilágyi, B. Major, P. Gál, P. Závodszy and A. Perczel, *FEBS J.*, doi:10.1111/j.1742-4658.2010.07790.x
105. F. A. Mulder, D. Schipper, R. Bott and R. Boelens, *J. Mol. Biol.*, 1999, **292**, 111–123.
106. B. Szenthe, Z. Gáspári, A. Nagy, A. Perczel and L. Gráf, *Biochemistry*, 2004, **43**, 3376–3384.
107. K. Lindorff-Larsen, R. B. Best, M. A. DePristo, C. M. Dobson and M. Vendruscolo, *Nature*, 2005, **433**, 128–132.
108. B. Richter, J. Gsponer, P. Várnai, X. Salvatella and M. Vendruscolo, *J. Biomol. NMR*, 2007, **37**, 117–135.
109. Z. Gáspári, P. Várnai, B. Szappanos and A. Perczel, *FEBS Lett.*, 2010, **584**, 203–206.
110. G. W. Daughdrill, L. J. Hanely and F. W. Dahlquist, *Biochemistry*, 1998, **37**, 1076–1082.
111. D. B. Veprintsev, S. M. Freund, A. Andreeva, S. E. Rutledge, H. Tidow, J. M. P. Canadillas, C. M. Blair and A. R. Fersht, *Proc. Natl. Acad. Sci. USA*, 2006, **103**, 2115–2119.
112. C. W. Bertoncini, Y. S. Yung, C. O. Fernandez, W. Hoyer, C. Griesinger, T. M. Jovin and M. Zweckstetter, *Proc. Natl. Acad. Sci. USA*, 2005, **102**, 1430–1435.
113. C. Nishimura, M. A. Lietzow, J. H. Dyson and P. E. Wright, *J. Mol. Biol.*, 2005, **351**, 383–392.
114. D. J. Felitsky, M. A. Lietzow, H. J. Dyson and P. E. Wright, *Proc. Natl. Acad. Sci. USA*, 2008, **29**, 6278.
115. A. Wendt, V. F. Thompson and D. E. Goll, *Biol. Chem.*, 2004, **385**, 465–472.
116. R. Kiss, D. Kovács, P. Tompa and A. Perczel, *Biochemistry*, 2008, **47**, 6936–69345.
117. T. Moldoveanu, K. Gehring and D. R. Green, *Nature*, 2008, **456**, 404–408.
118. R. Kiss, Z. Bozoky, D. Kovács, G. Róna, P. Friedrich, P. Dvortsák, R. Weisemann, P. Tompa and A. Perczel, *FEBS Lett.*, 2008, **582**, 2149–2154.
119. D. Keramisanou, N. Biris, I. Gelis, G. Sianidis, S. Karamanou, A. Economou and C. G. Kalodimos, *Nat. Struct. Mol. Biol.*, 2006, **13**, 594–602.
120. Z. Dubrovay, Z. Gáspári, É. Hunyadi-Gulyás, K. F. Medzihradsky, A. Perczel and B. G. Vértessy, *J. Biol. Chem.*, 2004, **279**, 17945–17950.
121. M. Louhivuori, K. Pääkönen, K. Fredriksson, P. Permi, J. Lounila and A. Annala, *J. Am. Chem. Soc.*, 2003, **125**, 15647–15650.
122. R. Koradi, M. Billeter and K. Wüthrich, *J. Mol. Graph.*, 1996, **14**, 51–55.
123. P. Bernadó, L. Blanchard, L. P. Timmins, D. Marion, R. W. H. Ruigrok and M. Blackledge, *Proc. Natl. Acad. Sci. USA*, 2005, **102**, 17002–17007.
124. M. D. Mukrasch, P. Markwick, J. Biernat, M. von Bergen, P. Bernadó, C. Griesinger, E. Mandelkow, M. Zweckstetter and M. Blackledge, *J. Am. Chem. Soc.*, 2007, **129**, 5235–5243.
125. V. A. Daragan and K. Mayo, *Prog. Nucl. Magn. Reson. Spectroscopy*, 1997, **31**, 63–105.
126. K. A. Henzler-Wildman, M. Lei, V. Thai, S. J. Kerns, M. Karplus and D. Kern, *Nature*, 2007, **450**, 913–916.
127. Z. Gáspári, A. F. Ángyán, S. Dhir, D. Franklin, A. Perczel, A. Pintar and S. Pongor, *Curr. Prot. Pept. Sci.*, in press
128. C. B-Rao, J. Subramanian and S. D. Sharma, *Drug Disc. Today*, 2009, **14**, 394–400.

# CHAPTER 3

## Virtual MRS: Spectral Simulation and its Applications

Brian J. Soher,<sup>\*</sup> Karl Young,<sup>†</sup> and Lana Kaiser<sup>‡</sup>

---

Contents	1. Introduction and Background	78
	1.1. Technology improvements	78
	1.2. The power of “what if?”	79
	1.3. Spectral simulation software overview	80
	1.4. The GAMMA spectral simulation library	81
	2. From Physics to Object-Oriented Programming	83
	2.1. NMR physics basics	83
	2.2. Mapping physics operators to computational objects	85
	2.3. Examples of simulated pulse sequence coding	85
	2.4. Spectral simulation design considerations	88
	3. Practical Applications and Implications	89
	3.1. Case 1—Prior metabolite information for improved spectral analysis	89
	3.2. Case 2—Pulse sequence optimization for specific metabolites	92
	3.3. Case 3—Real-world RF pulses and spatially varying artefacts	92
	3.4. Case 4—Real-world pulse sequence development by spectral simulation	94
	4. Conclusions	99
	References	101

---

**Abstract** There has been a significant increase in the use of spectral simulation in many areas of clinical research in the past decade, due greatly to improved access to more powerful mainstream computers and open source simulation software packages. Spectral simulation software is available in both software

<sup>\*</sup> Department of Radiology, Duke University Medical Center, Durham, North Carolina, USA

<sup>†</sup> Department of Radiology, University of California San Francisco/VAMC San Francisco, USA

<sup>‡</sup> Agilent Technologies, Walnut Creek, California, USA

library and simulation application formats. They may be command line driven or have a graphical user interface. Regardless of the top level “wrapper”, the underlying elements typically make use of object-oriented programming techniques to map NMR operators and elements directly to software objects. This simplifies the learning curve for researchers by allowing them to create simulations with terminology closely matched with either NMR physics notation or pulse sequence program language style. The design and implementation of spectral simulations depends greatly on the level of complexity needed to achieve the desired specificity in results, tempered by the computational time required. Spectral simulation methods provide fruitful opportunities for pulse sequence development. They can be used to optimize existing pulse sequence settings for the observation of specific metabolite structures. They can also be applied towards shortening the development time for new sequences. Also, the spectral estimation output from a simulation can serve as the input to a model driven spectral analysis algorithm for estimating the content of both *in vitro* and *in vivo* MRS signals. Specific case studies for each of these areas, and observations on their design and results, are given.

**Key Words:** Spectral simulation, Clinical MRS, Pulse sequence simulation, Virtual spectrometry.

---

## 1. INTRODUCTION AND BACKGROUND

Methods for acquisition and analysis of magnetic resonance spectroscopy (MRS) in biomedical applications have undergone significant evolution over the past decade. The developments of improved MR instruments for both animal and human studies; improved spatial localization techniques; and enhanced computational capabilities that power increasingly sophisticated spectral analysis algorithms are just a few examples. For *in vivo* measurements, MR spectroscopic data is complicated by the resonance group overlap and complex shapes for metabolite signals of interest. Methods to improve detection of specific spectral contributions include: spectral editing,<sup>1–7</sup> spectral fitting using constrained parametric model optimization and incorporating *a priori* metabolic information,<sup>8–16</sup> and use of multi-dimensional spectral acquisition methods.<sup>17–19</sup> In all of these areas of research, spectral simulation methods are becoming increasingly important sources for *a priori* information to improve and extend these techniques.

### 1.1. Technology improvements

Simulation techniques have been used in scientific studies for decades, but only the advent of open source tools, increases in desktop computational power and broad access to commodity super-computers have made these techniques readily available to individual investigators. So, what is “spectral simulation”? For the purpose of this chapter we will define it as “The estimation of the results of an



MRS experiment based on known physical principles”, and in particular for clinical applications, the estimation of *in vivo* or *in vitro* experiments.

The technological improvements that have facilitated spectral simulation include both CPU speed and computer memory size. In 1978, the Intel 8086 processor ran at 5 MHz. In 1993, the typical high-end CPU was the Pentium Pro 60 which ran at 60 MHz. By comparison, in 2005, a typical Pentium 4 was running at 3.8 GHz, a 760 and 63-fold increase in speed, respectively. Since then, power dissipation issues have begun to drive CPU design leading to multi-core approaches on a single CPU die. This makes a direct comparison more difficult but still serves to improve the usability of spectral simulation which often can easily incorporate distributed processing methods.

In a similar fashion, computer memory and data transfer rates have also increased since 1993. Intel introduced the first ever RAM chip in 1970 with 1024 bits of storage space and a transfer rate of 500 Hz. In 1994, a typical PC had 16 MB of RAM with a transfer rate of 66 MHz. And in 2010, typical PC memory can be up to 64 GB in 8 GB modules with 1033 MHz transfer rate. It is the access to this level of technology today that enables spectral simulation calculations to take place on a single user workstation that would previously have required mainframe or even super-computer performance.

The adoption and spread of modular programming techniques and open source software philosophies have also advanced the growth of spectral simulation. In particular, object-oriented programming methods and the push for easily reusable code has greatly facilitated the development of user friendly libraries and applications for MRS researchers. The use of object representations of the physics underlying spectral acquisition enables a researcher with little experience in computer programming to more quickly become a proficient user of a given library. Equivalently, it enables programmers to design more flexible graphical user interfaces that resemble the software interface a researcher might actually use at an MR spectrometer. Another important consideration is the growing trend by the computing community to encourage open source software projects. This philosophy simplifies access to spectral simulation software for users at many technical and economic levels and creates communities that are constantly improving or extending a given project.

## 1.2. The power of “what if?”

The foremost benefit of spectral simulation tools is to simplify the exploration of various “what if?” scenarios in MRS experimentation. Spectral simulation is much like the first “killer app” for the personal computer, VisiCalc. That program enabled users, originally in business but eventually in a wide variety of fields, to model and ask “what if” questions about a range of mathematical and business trends. It simplified laborious pencil and paper calculations that took hours or days into electronic operations that took seconds. As a PC application, no longer was it just large corporations with specialized software and mainframes who could afford to mathematically model business trends. The introduction of a

simple, low cost and generalized tool for mathematical manipulation brought about a major shift in how the business community approached its field.

Spectral simulation tools provide a similar opportunity for MR researchers. In its simplest form, spectral simulation allows changes in a data acquisition to be observed without having to program an MR pulse sequence and scan a volunteer on an actual MR scanner. This is particularly convenient in a clinical research setting where scanner time costs are high and access can be scarce. However, simulation methods additionally provide researchers with the ability to run “experiments” on instruments that are not available at their institution. Variations in the “samples” can also be part of a simulation and the effects of their variability on the MR results calculated. Properly characterized, a spectral simulation can incorporate the effects of any physical equipment or environment on a given sample.<sup>20,21</sup>

Spectral simulation methods provide fruitful opportunities for pulse sequence development. They can be used to optimize existing pulse sequence settings for the observation of specific metabolite structures.<sup>22,23</sup> They can also be applied towards shortening the development time for new sequences. Finally, the spectral estimation output from a simulation can serve as the input to a model driven spectral analysis algorithm for estimating the content of both *in vitro* and *in vivo* MRS signals.<sup>11,13,24</sup> This is most typically useful in clinical research where localized data acquisitions result in signal to noise (SNR) and line shape constraints as well as in complex overlapping metabolite resonance groups.

These benefits for spectral simulation do come with limitations and/or challenges as well. Most have to do with trading-off inclusion of prior information sufficient to describe the environment against the amount of computational power or computation duration needed for a simulation. These topics will be discussed in more specific detail in later sections.

### 1.3. Spectral simulation software overview

As described previously, the growth of open source programming projects and increases in computational power have contributed greatly towards making spectral simulation techniques available to individual investigators. Since the early 1990s, there have been a number of reports of NMR simulation libraries<sup>25–28</sup> and applications<sup>24,29–36</sup> which have sought to provide the functionality for spectral simulation in either a more optimized or user friendly fashion. The growth in available tools reflects the consensus among MR scientists that simulation methods are a necessary step in the development of increasingly sophisticated data acquisition/analysis methods for the study of complex molecular systems.

A brief (and incomplete) list of publications describing a variety of MRS and MRI simulation packages is given in [Appendix A](#). These packages contain a range of claims for mathematical completeness and computational speed. They are implemented on a variety of hardware and software platforms including: C++, Mathematica, Java, Windows/Intel, MacOS and Linux/Unix. Only a few claim to be completely cross-platform compatible, though many have unofficial implementations on unsupported platforms. There are many levels of sophistication

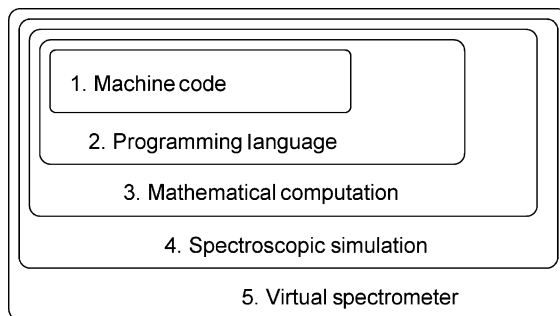
in terms of whether the packages are code libraries or GUI-based applications. Some packages are slanted more towards traditional high field liquid and/or solid state NMR experiments while others are organized to support localized, clinical MRS experiments. Despite their outward differences, all are based on similar underlying principles. To simplify the discussions of and examples for spectral simulation, the remainder of this chapter will focus on just one of these packages, the GAMMA C++ spectral simulation package<sup>25</sup> as it is a well designed and frequently used package that served as the basis for many of the packages that came later and its authors were pioneers in the field of spectral simulation.

#### 1.4. The GAMMA spectral simulation library

Introduced in 1994, the GAMMA C++ library is a flexible and efficient tool for describing and simulating MR experiments. Despite the increase in available tools, GAMMA has maintained a strong presence in the field due to its flexibility, performance, straightforward elegant design and standard C++ implementation. There have been over 300 reports in the literature that include spectral simulations making use of the GAMMA library.<sup>14,28,37–56</sup> While many of these are reports for high field NMR experiments, a growing number of more recent reports are for uses in clinical MRS investigations including both pulse sequence design and spectral data analysis applications.

Speaking practically, the development of GAMMA embodies a straightforward design. It uses multiple levels to separate the user from the complexity of the MR physics while conserving the inherent physics-based structures familiar to an MR experimenter as shown in [Figure 1](#). It also embodied good programming practices that consider short/long term usability and expansion, namely:

1. A mathematics layer to deal with computational issues independent from the physics.
2. An MR spectroscopy layer to provide the user with familiar physics operations.
3. A spectrometer console layer to ease the transition from experiment to simulation.



**Figure 1** Virtual spectrometer application layers.

4. Leverages latest generation computer language features to simplify the above.
5. Allows for easy expansion of the tools.
6. Considers overall computational load.
7. Granular code for ease of reuse.
8. Cross-platform support.

GAMMA is a good example of many of the benefits and compromises listed previously. The bulk of the library was the doctoral work of Dr. Scott Smith at the Eidgenössische Technische Hochschule (ETH) in Zurich, Switzerland. Subsequently, Dr. Smith took a job at the National High Field Magnetic Laboratory in Florida. Both sites shared in hosting a web site to provide open access to the source code, examples, documentation and compiled binaries for many platforms and compilers. As a code library, many of the obstacles to cross-platform support go away, especially the need to support an application across different graphical user interfaces.

As an object-oriented implementation, code to implement a typical simulation often is similar to the code format used on actual NMR consoles. Most of the underlying code to implement the MR physics is hidden within a given object, leaving the user only to learn how to piece together GAMMA objects to create desired “pulse sequence” and “data acquisition” steps. An ongoing drawback to packages like GAMMA is a requirement for at least a minimal knowledge of object-oriented programming, C++ in the case of GAMMA. Also, many provide only rudimentary tools for the display, storage and analysis of simulation results. This requires a certain level of programming expertise among users and likely is one of the more significant obstacles to adoption of spectral simulation techniques in the clinical MRS arena. Some recent efforts, such as GAVA (GAMMA Visualization and Analysis) a graphical interface for plotting and storing GAMMA simulation results,<sup>13,57</sup> have attempted to further reduce the required programming knowledge for scientific end users by providing interfaces to packages like GAMMA in “simpler” languages such as IDL and Python. By wrapping GAMMA in a fourth generation language, such as Python, rather than creating a new package in Python, programming is made more straightforward via the Python interface while the computational efficiency of C++ is generally maintained. And maintaining computational efficiency is generally very important, particularly in simulations of current high field experiments that can require simulation at a large number of spatial points.

The current status of GAMMA exemplifies the robustness of the open source software philosophy. GAMMA has had an active user community for over 15 years, although it has waned somewhat with the development of other simulation libraries and applications with less programming intensive interfaces. In 2008, ETH partnered with groups at Duke University and UC San Francisco, and with the support of the High Field Magnet Laboratory at Florida State University, to give GAMMA a “makeover”. With the funding of the NIH, GAMMA was refactored to utilize existing optimized math libraries to speed up its internal calculations. It was also “wrapped” to make its objects available within the Python programming language. The upshot of the “PyGAMMA” module for Python is

that GAMMA spectral simulations can now be written and run without needing to be compiled. And the learning curve for a fourth generation programming language is much lower than that for C++, thus positioning it well for a new generation of MR researchers to integrate into their workflow.

In this report, we use the GAMMA library as a primary example of NMR simulation development and usage. It encompasses specific implementations of the Mathematical Computation and Spectroscopic Simulation sections via a specific programming language, API. At the same time, it serves to compare and contrast the issues surrounding specific platform implementations and how these underpinnings can be wedded to a full virtual spectrometer simulation and analysis environment where multiple spectral simulations can be compared or optimized.

## 2. FROM PHYSICS TO OBJECT-ORIENTED PROGRAMMING

### 2.1. NMR physics basics

As described above, simulation is playing an increasingly critical role in both the acquisition and processing of the complex spectra produced in modern spectroscopic imaging protocols. For acquisition, simulation plays a key role in the design of the types of pulses and pulse sequences required for detecting the extremely weak signals produced by a number of biologically important metabolites such as *N*-acetylaspartate (NAA), choline containing compounds (Cho), creatine (Cr), glutamate (Glu), glutamine (Gln), GABA, myo-inositol (myo-Ins) and lactate (Lac) to name a few. For processing, accurate modelling of metabolite signals is required. These signals are a product of both the intrinsic metabolite characteristics such as chemical shift and spin coupling as well pulse and pulse sequence characteristics. In the case of the metabolites mentioned previously and which produce weak signals, simulations for both acquisition and processing typically require use of the full quantum mechanical formalism for producing sufficiently accurate approximations to the experimentally observed spectra. There are special cases for which the classical Bloch formulation is adequate and more efficient<sup>58,59</sup> but this chapter focuses on the more typical and complex cases that require a full quantum treatment.

The original GAMMA paper contains an excellent description of what is required of a simulation package that implements a reasonably complete model of the quantum mechanical evolution of a spin system under the influence of a pulse sequence. For anyone seriously interested in the implementation details required for NMR simulation consultation of that paper is highly recommended. Here an overview is provided for completeness.

A complete description of the quantum mechanical wavefunction for any given spin system in an ensemble of spin systems is both infeasible and unnecessary, given that in NMR spectroscopy it is the properties of the nuclear spins that are of primary interest. And as NMR experiments deal with a large ensemble of spin systems the basic element required for a complete description of the system is

the density matrix (density operator), the quantum statistical mechanical equivalent of the wavefunction. The traditional NMR treatment divides the full quantum system into two components, the spin system and its surroundings, which for historical reasons is referred to as the lattice. As a result, the wavefunctions for the different molecules in the sample depend on the lattice variables and together form an ensemble of wavefunctions referred to collectively as a *mixed state*. Each subensemble of the mixed state is described by a wavefunction  $\Psi$  and a probability density  $P(\Psi)$  that quantifies the contribution of the subensemble to the full mixed state.

To provide a definition of the density matrix in terms of fundamental wavefunctions first consider the generalization of the expectation value from quantum mechanics to quantum statistical mechanics. In the quantum statistical case, an additional average over the probability density needs to be considered in the calculation of the expectation value:

$$\langle \bar{A} \rangle = \int P(\Psi) \langle \Psi | A | \Psi \rangle d\tau = \sum_{ij} \int P(\Psi) c_i c_j^* d\tau \langle i | A | j \rangle = \sum_{ij} \int \overline{c_i c_j^*} \langle i | A | j \rangle \quad (1)$$

The matrix elements  $c_i c_j^*$  vary between particular systems but the matrix elements  $A_{ij}$  do not. The ensemble average of the matrix elements:

$$\sigma_{ij} = \overline{c_i c_j^*} \quad (2)$$

form the *density matrix*  $\sigma_{ij}$ . Then the expectation value of property A in a mixed state is obtained as follows:

$$\langle \bar{A} \rangle = \text{Tr}\{\sigma A\} \quad (3)$$

So to obtain expectation values relevant to any particular experiment one needs an estimate of the density matrix at the time of measurement. For an NMR experiment, this typically requires the ability to estimate the time evolution of the density matrix for the pulse sequence used for the experiment. The time dependent differential equation that describes the time evolution of the density matrix, known as the Liouville–von Neumann equation is given by

$$\frac{d}{dt} \sigma(t) = -i2\pi[H, \sigma(t)] - \Gamma\{\sigma(t) - \sigma_{\text{inf}}\} \quad (4)$$

where  $H$  denotes the Hamiltonian of the spin system, and  $\Gamma$  denotes the relaxation superoperator. For example, a typical Hamiltonian used in simulations is the free-precession laboratory-frame Hamiltonian for  $N$  scalar coupled spins:

$$H = H_z + H_J = \sum_{i=1}^N \omega_i I_{iz} + 2\pi \sum_{i=2}^N \sum_{j=1}^{i-1} J_{ij} \vec{I}_i \bullet \vec{I}_j \quad (5)$$

When considering relaxation, a Liouville space representation is typically used in which the Hamiltonian and density matrix are represented as superoperators in addition to the relaxation operator being represented as a superoperator. Once a

solution for the Liouville–von Neumann equation has been found the resulting density matrix, transformed to a suitable representation, can be used for calculation of expectation values of interest.

Simulation packages such as GAMMA take advantage of the fact that evolution of the density matrix under the Liouville–von Neumann equation is well approximated by a small number of easily applied transformations of the density matrix, namely free evolution can be represented by a simple unitary transformation and application of ideal RF pulses can be represented by a simple rotation. Real RF pulses can be effectively modelled as a succession of ideal RF pulses. The beauty of this method is that fairly complex, realistic effects, such as evolution of coupled spin systems through complex pulses, can be modelled by a straightforward combination of these simple building blocks.

## 2.2. Mapping physics operators to computational objects

Many packages utilize the power of objected-oriented languages, C++ in the case of GAMMA, to extend the language to include NMR specific objects. Given the above list of elements required for simulation of NMR experiments, a fairly straightforward mapping from abstract objects such as the Hamiltonian to computational objects can be made. Table 1 shows a short exemplary list of object mappings from GAMMA, but for an in depth, detailed description of such mappings, see the original GAMMA manuscript.

Much of the simplicity of use for the GAMMA library lies in the general operator class defined to provides a mapping for spin systems, Hamiltonians, density matrices and a number of other NMR specific elements (e.g. Table 1, lines 1–4). This hides much of the unnecessary detail from users and in effect creates an easy to use, NMR specific language. These operators are specifically set to evaluable operations by grouping one or more GAMMA objects (Table 1, lines 5–7). In the case of the Hamiltonian, line 7, this can be done by specifying very specific low level objects or through the use of intermediate object (e.g. *Hcs()* and *HJ()*) which pre-group specific assignments.

Simulated “pulse sequences” are built line-by-line similarly to operator assignments. Typical operations on a spin system’s density matrix, such as the application of a pulse or evolution over time  $t$ , can be applied explicitly in an operator by operator manner (Table 1, lines 8–9) or through the use of built-in grouped operators (Table 1, lines 8–9 alternative coding). Either way, the user has complete control to structure the object-oriented code in a manner which reads almost as naturally as the original physics notation itself. Two examples of spectral simulation pulse sequences coding are shown in the next section.

## 2.3. Examples of simulated pulse sequence coding

In Figures 2 and 3 are shown the GAMMA C++ code for a simulated spin-echo pulse sequence using ideal RF pulses and a simulated PRESS pulse sequence that accounts for a non-ideal RF pulse envelope, crusher gradients and spatially varying RF refocusing due to resonance group chemical shift offset and

**TABLE 1** Sample mappings of physics operators to GAMMA library objects and code

Description	Analytic	GAMMA code
1. Declare a spin system	AB spin system	<i>spin_system</i> AB(2)
2. Declare density operators	$\sigma(0)$ , $\sigma(t)$	<i>gen_op</i> <i>sigma0</i> , <i>sigma1</i>
3. Declare a Hamiltonian	$H$	<i>gen_op</i> $H$
4. Declare an expectation value	$\langle \bar{A} \rangle$	<i>complex</i> $a$
5. Assign a density operator	$\sigma_0 = F_z$	<i>sigma</i> 0 = $F_z(AB)$
6. Assign a detection operator	$A = F^+$	$A = Fp(AB)$
7. Assign a Hamiltonian	$H = f_0 I_{0z} + f_1 I_{1z} + J [I_{0z} I_{1z} + I_{0x} I_{1x} + I_{0y} I_{0y}]$	$H = f0 \bullet Iz(AB,0) + f0 \bullet Iz(AB,0) + J \bullet [Iz(AB,0) \bullet Iz(AB,1) + Ix(AB,0) \bullet Ix(AB,1) + Iy(AB,0) \bullet Iy(AB,1)];$ OR $H = Hcs(AB) + HJ(AB)$
8. Apply $(\pi/2)_y$ pulse	$\sigma(0) = e^{-i(\pi/2)F_y} \sigma_0 e^{i(\pi/2)F_y}$	<i>sigma1</i> = $exp(-I \bullet (PI/2) \bullet Fy(AB)) \bullet sigma0 \bullet exp(I \bullet (PI/2) \bullet Fy(AB));$ OR <i>sigma1</i> = <i>Iypuls</i> (AB, <i>sigma0</i> , 90)
9. Evolve for time $t$	$\sigma(0) = e^{-2\pi i H t} \sigma_0 e^{2\pi i H t}$	<i>sigma1</i> = $exp(-2 \bullet PI \bullet I \bullet H \bullet t) \bullet sigma0 \bullet exp(2 \bullet PI \bullet I \bullet H \bullet t);$ OR <i>sigma1</i> = <i>evolve</i> ( <i>sigma0</i> , <i>prop</i> ( $H, t$ ))

bandwidth limited RF pulses. For brevity, the coding shown for the two examples are not complete C++ programs. Only the portion that demonstrates the initialization and organization of the GAMMA MR simulation is shown.

Figure 2 shows the code for the spin-echo pulse sequence. In lines 1–7, NMR object variables are declared. In lines 9–16, these objects are assigned values or specific NMR operations. A lactate spin system is read in from a file using a standard GAMMA text file format. Lines 20–24 are the code for the actual  $90^\circ_x$ -delay- $180^\circ_x$ -delay-acquire pulse sequence. In line 26, the density matrix is parsed into a transition table for the specified observation operator. And the “write\_results” function in line 27 converts the GAMMA transition table into three arrays of ppm, area and phase values; one value for each line found in the transition table. This is a fairly trivial example, and the use of ideal pulses is often not sufficient to account for real-world artefacts in a simulation, but it shows how the object-oriented style of coding results in short amounts of code that is easy to read and comprehend. When compiled with the Visual Studio C++ compiler on a



```

01 // Spin-Echo simulation - code initialization -----
02
03 spin_system      sys;
04 gen_op           H, D, Udelay, sigma0, signal;
05 acquire1D       ACQ;
06 TTable1D        mx;
07 double          te1=0.010;          // delay period in [sec]
08
09 sys.read('lactate.sys');             // spin system prior information
10 sigma0 = sigma_eq(sys);             // set equilibrium density matrix
11
12 H = Hcs(sys) + HJ(sys);             // define the Hamiltonian
13 D = Fm(sys);                       // define observation operator
14 acquire1D ac(D, H, 0.001);          // set acquisition parameters
15 ACQ = ac;
16 Udelay = prop(H, te1*0.5);          // set propagation parameter
17
18 // Pulse Sequence Code -----
19
20 signal = Ixpuls(sys, sigma0, 90);    // ideal 90 degree RF pulse
21
22 sigma0 = evolve(signal,Udelay);      // evolve system for time TE/2
23 signal = Ixpuls(sys, sigma0, 180);   // ideal 180 degree RF pulse
24 sigma0 = evolve(signal,Udelay);      // evolve system for time TE/2
25
26 mx = ACQ.table(sigma0);             // acquire transition table
27 write_results(mx,freq,amp1,phas);    // parse and output transitions

```

**Figure 2** A simple example of GAMMA C++ code that initializes objects and organizes them into a spin-echo pulse sequence simulation that uses ideal RF pulses.

Windows Core 2 Duo 2.6 GHz platform, the executable takes less than one second to complete.

Figure 3 shows the code for the PRESS pulse sequence that accounts for a non-ideal RF pulse envelope, crusher gradients and spatially varying RF refocusing due to resonance group chemical shift offset and bandwidth limited RF pulses. Code to initialize NMR object variables has been left out but would be similar to lines 1–7 in Figure 2. Also for brevity, the code to read in the RF pulse profiles from file to an array has been left out. In lines 6–8, the base template for a Hamiltonian is assigned and then Hamiltonian arrays in the X and Y direction are declared and calculated to determine spatial variations due to localization gradients. The simulation then loops over all X, Y voxels (typically a  $40 \times 40$  matrix depending on the variability of the RF pulse profile of interest) in lines 10–11. Lines 13–15 defines shaped RF pulses that depend on the X, Y location and the original RF pulse profile for the refocusing  $180^\circ$  pulses in the X and Y directions. Lines 17–19 excite the spin system with an ideal  $90^\circ$  pulse and evolve for a given time. Lines 21–25 simulate the effects of a localized (shaped)  $180^\circ$  pulse with crusher gradients on either side. Lines 27–28 remove higher order transitions and evolve the spin system. Lines 30–34 simulate the effects of the second localized  $180^\circ$  pulse with crusher gradients on either side. In line 39, a weighted sum of all spatially localized simulations is kept. In line 42, the summed density matrix is parsed into a transition table for the specified observation operator. And the “write\_results” function in line 27 converts the GAMMA transition table into three arrays of ppm, area and phase values. This is a more complete example of the care that must be taken to account for real-world variability in spectral simulations used in

```

01 // PRESS simulation - spatial dependencies and non-ideal RF pulses
02
03 // Code for simulation initialization and variable definition
04 // Code to read real pulses into GAMMA objects pulse1 and pulse2
05
06 H0 = Hcs(sys) + HJ(sys); // define Hamiltonian
07 Hzgrad(sys, H0, Hx); // modify base Hamiltonian to reflect
08 Hzgrad(sys, H0, Hy); // localization pulse offset in x,y
09
10 for (x=0; x<XVoxels; x++) // loop over all x,y locations
11 for (y=0; y<YVoxels; y++)
12 {
13 // create shaped pulses propagators for position x,y
14 U180x = Shxpuls_U(sys, pulse1, Hx[x], "1H", time1, 180);
15 U180y = Shxpuls_U(sys, pulse2, Hy[y], "1H", time2, 180);
16
17 // run PRESS sequence for position x,y
18 sigma = Iypuls( sys, sigma, 90.0); // ideal excitation
19 sigma = evolve( sigma, UDelay0); // propagation
20
21 // x localization 180 pulse and crusher gradients at x,y
22 for (n=0;n<4;n++) temp[n] = evolve( sigma, Rz(sys, n*90.0));
23 for (n=0;n<4;n++) temp[n] = evolve( temp[n], U180x );
24 for (n=0;n<4;n++) temp[n] = evolve( temp[n], Rz(sys, nd*90.0));
25 sigma = (temp[0]+temp[1]+temp[2]+temp[3])/4.0;
26
27 zero_mqc( sys, sigma, 2, 1 ); // filter for desired states
28 sigma = evolve(sigma, UDelay1); // propagation
29
30 // y localization 180 pulse and crusher gradients at x,y
31 for (n=0;n<4;n++) temp[n] = evolve( sigma, Rz(sys, n*90.0));
32 for (n=0;n<4;n++) temp[n] = evolve( temp[n], U180y );
33 for (n=0;n<4;n++) temp[n] = evolve( temp[n], Rz(sys, nd*90.0));
34 sigma = (temp[0]+temp[1]+temp[2]+temp[3])/4.0;
35
36 zero_mqc( sys, sigma, 2, 1 ); // filter for desired states
37 sigma = evolve( sigma, UDelay2); // propagation
38
39 sigma_total += (sigma/nvox); // final result = sum of x,y
40 }
41
42 mx = ACQ.table(sigma_total); // acquire transition table
43 write_results(mx,freq,ampl,phas); // parse and output transitions

```

**Figure 3** GAMMA C++ code to implement a PRESS pulse sequence simulation that accounts for the use of real RF pulses and the application of gradient crushers around refocusing pulses.

clinical MRS; however, the actual amount of code is still relatively short and also easy to read.

## 2.4. Spectral simulation design considerations

The implementation of spectral simulations benefits from a number of practical considerations. First, keep in mind that the amount of prior knowledge available versus that which is actually used in the simulation can result in calculations ranging from the very simple to very complex, with computational times that vary accordingly. Next, the results depend on the accuracy of the prior information (Garbage In = Garbage Out). Also, in the immortal words of Don Knuth, “Premature optimization is the root of all evil.” In other words, it is important to give sufficient thought towards including all necessary elements in simulations and in

improving the simulation code but do not forget to finish at some point and see if it works. And, finally, a simulation is only as good as the data to which it is compared. This is particularly true at the field, gradient strengths and shim homogeneities achieved by clinical and *in vivo* research MR scanners.

The GAMMA C++ style of spectral simulation is just one approach. Other libraries that make use of object-oriented languages (Java in PJNMR) will have a similar structure and natural programming style. Other libraries that are based on more traditional procedural languages (C, Fortran, IDL, Matlab) will have less of an NMR physics notation, and may require more familiarity with programming. Finally, a number of spectral simulation application options exist whose control inputs are styled more like the scripts (SIMPSON) or timing tables (SPINEVOLUTION) that are used on NMR consoles to describe the RF pulses and gradients in a pulse sequence. Some of these packages are more computationally powerful (relating to the size of spin systems that can be modelled) or have better optimized simulation algorithms leading to shorter processing times. On some, there are graphical user interfaces (PJNMR and VirtualNMR) to simplify simulation setup. There are benefits and trade-offs for all of these, but the underlying functionality in all of them is that demonstrated by the examples above. In the final analysis, pick a platform and package that is comfortable to program in, meets your performance requirements, and allows you to create the simulations and analysis of results that you are seeking.

### 3. PRACTICAL APPLICATIONS AND IMPLICATIONS

Some of the motivations to pursue spectral simulation in a clinical MRS setting include: providing metabolite prior information for use in parametric spectral analysis procedures, pulse sequence parameter optimization for observation of specific metabolite structures and shortening times for pulse sequence development. This section will describe, in some detail, examples of each with particular regard for the design and level of prior information inclusion of each simulation and the clinical use of the results.

#### 3.1. Case 1—Prior metabolite information for improved spectral analysis

One widely used application of clinical MRS spectral simulation is the creation of prior information for spectral analysis and fitting routines. Well-defined metabolite prior information results in more consistent and complete estimations of the actual data. One example of a parametric model used to fit clinical MRS data is shown below.

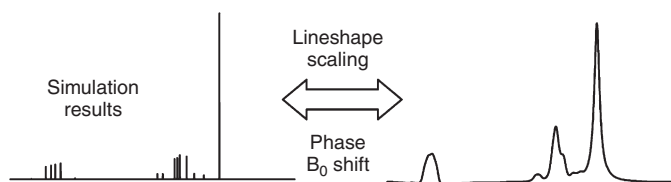
$$S(\omega) = \text{FFT} \left[ \sum_{m=1}^M \sum_{n=1}^{N(m)} A_m A_n^m e^{-i[(\omega_0 + \omega_n^m + \phi_1)t + \phi_n^m + \phi_0]} \times L_n^m(t) \right] \quad (6)$$

The terms subscripted in “ $n$ ” in this equation comprise the normalized set of resonance lines we extract from the transition table in our simulation. From the areas, frequencies and phases parsed from the GAMMA transition table object at the end of the spectral simulation, we can create either an idealized or fully parameterized spectrum such as shown in Figure 4.

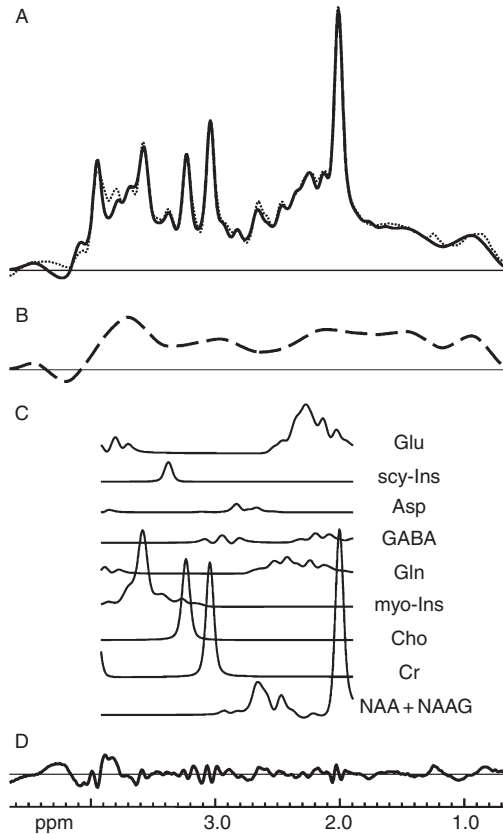
A major class of spectral fitting routines (including LCModel, MIDAS-FITT and jMRUI<sup>11,13,24</sup>) use combinations of expected metabolites basis functions to fit MRS data as shown in Figure 5. The spectral simulations that create these basis functions are typically set up to run a single pulse sequence with one set of parameters for multiple metabolites. The major consideration in these cases is over how much prior information needs to be included to achieve usable metabolite models. Often the expected SNR levels and typical data quality of clinical MRS data preclude the need for the use of more complicated simulations. Many of the spectral analysis models for clinical PRESS, STEAM<sup>60</sup> and spin-echo MRS metabolite data from 1.5 and 3 T MR scanners are created using simulations with ideal RF pulse objects and exact evolution timings. Some of the effects not accounted for in the simulation, such as relaxation (a.k.a. line shape), are subsequently accounted for in the analysis model in later programs, and others, like crusher gradients, simply are often not needed mathematically.

A benefit to simplifying simulations is that it becomes easier to modify simulation code to investigate pulse sequence parameter ranges or to troubleshoot mismatches with actual data. However, sometimes additional levels of physics or programming complexity are necessary to accurately simulate the MRS data. This is particularly true for high SNR single voxel data and metabolite edited MRS data at higher fields where more spectral detail can be seen.

Simulated basis spectra of the metabolites expected in a data set can also be used to improve estimates for starting parameter values. This can be important for both computational speed and fitting accuracy. A simulated basis spectrum has known phases and frequencies for an idealized absorption spectrum. An estimate of the zero and first order phases for the raw data can be made either by maximizing the integral under prominent metabolite singlet peaks or by maximizing the correlation of a basis function model to the raw data over a limited PPM range. Similarly,  $B_0$  shifts in the actual data can be corrected using peak



**Figure 4** Example of a spectral simulation result for NAA from a PRESS TE = 30 ms simulation reconstituted for use as a basis function. The ideal area, frequency and phase values of all transition lines in the simulation have global lineshape, phase and  $B_0$  shift applied and are summed to create the representation of a whole metabolite.



**Figure 5** Use of metabolite basis functions to fit clinical MRS data. (A) Final metabolite + baseline fit (black) overlaid on raw data (grey). (B) Non-parametric baseline signal estimation (based on wavelet filtering). (C) Metabolite basis functions modulated via scaling,  $B_0$  shift, lineshape and phase 0 and phase 1 to optimally fit raw data. (D) Residual spectrum of metabolite + baseline minus the raw data.

searches or correlation measures. Many clinical data acquisitions contain non-parameterized signal contributions (a.k.a. baseline signals), such as from residual water, lipids or macromolecules, that need to be estimated for an accurate optimization of the parameterized model. Metabolite simulations provide useful information for estimating these signals by suggesting regions where metabolites signal contributions are minimal. Finally, metabolite basis functions can also be used to set optimization parameter constraints. These can range from the trivial, such as allowing only positive metabolite peak areas, to the complex, such as constraining a multi-parameter lineshape model to be within a maximum and minimum overall line width based on a prominent metabolite peak's estimated line width.

### 3.2. Case 2—Pulse sequence optimization for specific metabolites

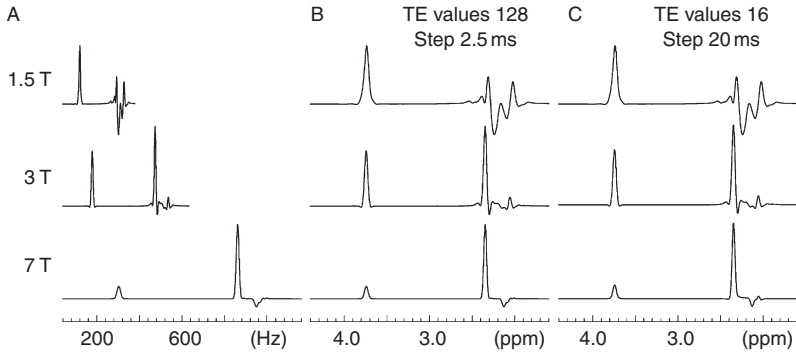
Pulse sequence optimization is another active area for clinical spectral simulation research. As opposed to the previous example that simulated a particular pulse sequence for one set of parameters and multiple metabolites, a given simulation can be coded to act as kernel for data acquisition parameter optimization for one particular metabolite. This might include calling the kernel for a variety of sequence timings to determine their affect on metabolites that is a STEAM sequence's TE/TM settings. Or, as in this example, summing a series of timing results such as for a TE-averaged PRESS sequence.

The 2004 paper by Hurd *et al.*<sup>61</sup> describes a pulse sequence that through TE averaging, allowed a typical PRESS sequence to yield the  $f_1=0$  slice of a 2D J-resolved spectrum. This method allows improved discrimination of Glu, Gln, *N*-acetyl compounds (NAA+NAAG), Cr and Cho peaks. Whereas a typical clinical PRESS MRS acquisition acquires multiple averages at one TE, TE-averaged PRESS acquires and sums multiple averages of data at multiple TE values. Two of the effects demonstrated in the Hurd paper were the effect of field strength on the Glu peak at 2.35 ppm, and the number of TE steps that were averaged. A partial recreation of their results is shown in [Figure 6](#). This figure shows that Glu discrimination improves as field strength increases. It also suggests that the results for 128 TE values with TE step size of 2.5 ms gives almost the same results as 16 TE values with TE step size of 20 ms, so long as the total number of averages are the same.

This example brings up an important consideration for staging simulations. While there are a number of ways to explore TE-averaged data acquisitions, it is typically more computationally efficient to output an array of results for various TE values and use a subsequent coding step (either in C++ or another language) to determine the best combination to achieve your goals, rather than re-computing sequence timings in GAMMA. This observation typically generalizes to any spectral optimization which depends on combinations of a limited number of metabolite results rather than on changes to the underlying NMR physics of the base spectral simulation.

### 3.3. Case 3—Real-world RF pulses and spatially varying artefacts

The code shown in [Figure 3](#) is an example of a spectral simulation that requires additional complexity to account for real-world artefacts that affect all metabolites' final forms. This code simulates a PRESS pulse sequence that (1) uses real-world (non-ideal) RF pulses and (2) accounts for the spatially varying chemical shift offset artefacts that they cause in J-coupled metabolites. The chemical shift offset artefact arises from variations in the spatial distributions of the excitation/refocusing pulses due to the chemical shift of each spin. For coupled spins, this can result in phase variations leading to signal cancellation. The magnitude of this effect is a function of the chemical shift difference between coupled partners and the bandwidth and shape of the localizing pulse, which is typically limited by the strength of the available gradients and RF power. Because the initial excitation

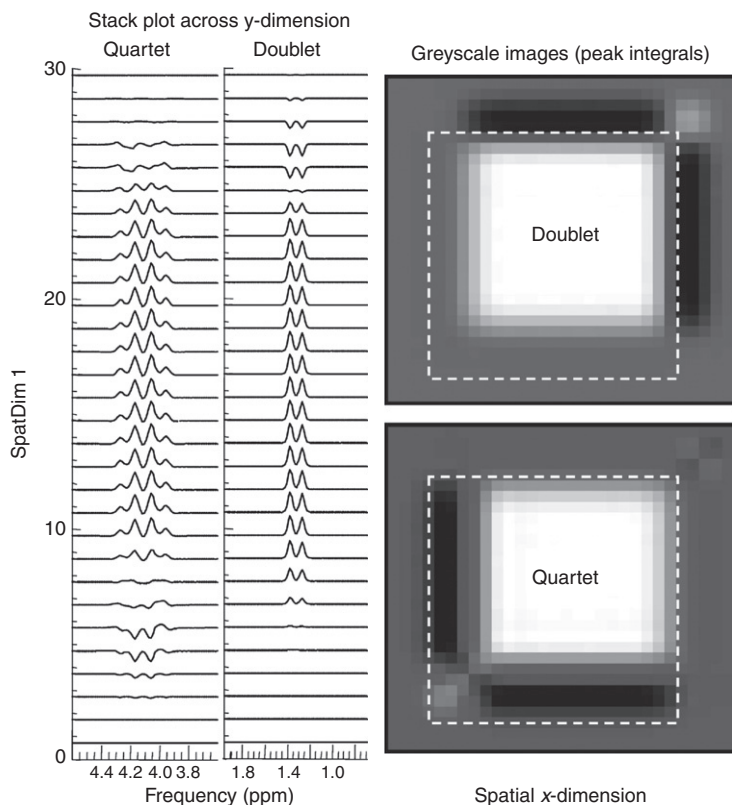


**Figure 6** Effects of field strength, step size and number of steps on glutamate in a TE-averaged PRESS data acquisition. Spectral simulation results have had a line broadening of 0.04 ppm applied. Spectral separation effects are shown in (A), and a comparison of 128 steps of 2.5 ms versus 16 steps of 20 ms (each ranging from TE = 35–355 ms) are shown in (B) and (C).

pulse requires less power than subsequent refocusing pulses, the chemical shift offset artefact in that localization direction is minimal and can be ignored in the spectral simulation. The use of an ideal  $90^\circ$  pulse in the simulation greatly reduces the computation time of the simulation. Because this effect is typically attributed to only the localized refocusing PRESS RF pulses, it is often referred to as the “4 compartment” artefact due to the distributions of spins that are affected by (1) both  $180^\circ$  pulses, (2)  $180^\circ$  X-direction pulse only, (3)  $180^\circ$  Y-direction pulse only, or (4) neither  $180^\circ$  pulses. This distribution of effects can be seen in the greyscale images in [Figure 7](#).

In this example, a  $30 \times 30$  spatial matrix was used to simulate the spatial variations inside and outside the nominal PRESS box prescription (shown as dotted white line in greyscale images) for the two refocusing RF pulses. Two arrays of 30 Hamiltonians each, calibrated for localization effects in the X and Y localization directions, were created. For each of the 900 X, Y values, a PRESS simulation was run using the appropriate Hamiltonian for each localization direction. [Figure 7](#) shows a plot of a lactate doublet and quartet for X=15 and all Y spatial locations. Also shown are greyscale maps of the quartet and doublet peak integrals for each X, Y location. Variations in phase and amplitude can be seen in regions that did not experience full  $180^\circ$  refocusing pulses in both directions, up to and including inverted spectra. The final lactate basis function for the specified data acquisition consists of the sum of all 900 X, Y locations. This step assumes coherence of the spin systems across the measured region which has been shown to be a reasonable assumption in various phantom studies.

The primary consideration for this experiment was to determine the spatial digitization needed to sufficiently capture the effects of the chemical shift offset artefact. To determine this, the actual RF pulses used for the clinical data acquisition needed to be available for use in the GAMMA simulation. Many spectral simulation packages can import this type of information for use in a simulation,



**Figure 7** Example of chemical shift offset artefact in a PRESS sequence lactate acquisition. The variations in scale and phase for both the quartet and doublet resonance groups (4.1 and 1.3 ppm) are shown for all  $Y$ -locations at the central  $X$ -location in the greyscale images shown. The nominal voxel prescription is shown as a dotted white line each greyscale image.

but it must also be available from the MR scanner manufacturer. A further description and discussion of these sorts of spatially varying artefacts and their affects on metabolite basis functions are given in Ref. 47.

### 3.4. Case 4—Real-world pulse sequence development by spectral simulation

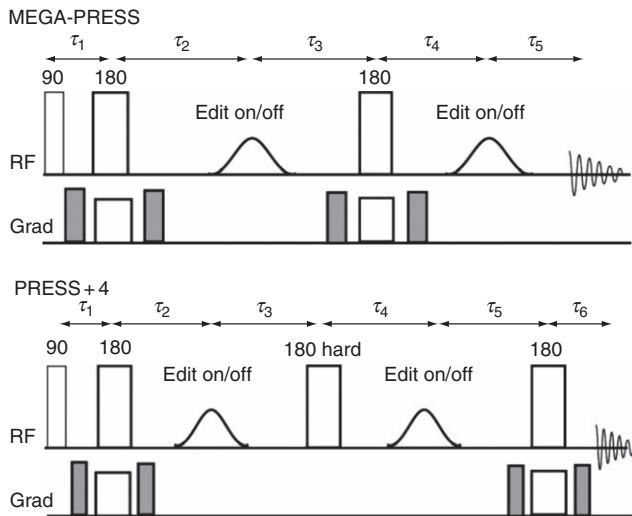
This final example showcases the development of the PRESS+4 pulse sequence, by Kaiser *et al.*,<sup>22</sup> to improve detection of the brain metabolite GABA using spectral editing. Here, a single pulse sequence and set of parameters were optimized to improve the accuracy and visibility of just one metabolite. The primary clinical issue was that detection of GABA in the human brain is compromised of



low *in vivo* concentration and spectral overlap with other metabolites. The standard of comparison for the PRESS+4 development was the widely used pulse sequence, MEGA-PRESS.<sup>62</sup> This sequence allows spectral separation of GABA from other metabolites but suffers from a significant SNR reduction due to the “4 compartment” artefact that results from chemical shift offset artefacts (described above), especially at higher field.

The primary consideration for PRESS+4 development was the fact that spectral editing sequences depend on highly optimized narrow band RF pulses to either excite (ON) or not excite (OFF) specific resonance groups of the metabolite of interest. For GABA, the multiplet at 1.9 ppm is used to create two states in the GABA multiplet at 3.0 ppm depending on whether the editing RF pulse is ON/OFF. By subtracting the two data states, unedited metabolites are nulled but edited metabolites are emphasized. Similarly, by adding the two states, the edited metabolites can be nulled, making the unedited metabolites easier to observe. The fact that GABA is a J-coupled metabolite makes the editing possible but also allows errors due to chemical shift offset to affect the results. For this reason, the PRESS+4 technique was developed primarily using spectral simulation techniques which both optimized and included real pulses and accounted for spatially varying artefacts within its design. The final PRESS+4 sequence was compared to spectral simulations of the MEGA-PRESS sequence. All simulations were demonstrated to agree extremely well with both phantom and clinical results.

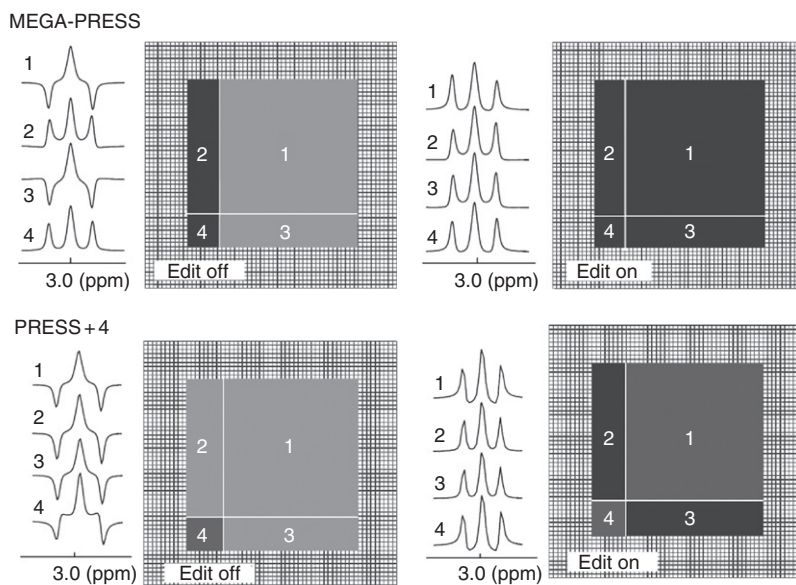
Figure 8 displays the cartoon representations of the MEGA-PRESS and PRESS+4 pulse sequences. The primary difference between the two is the addition of a non-localized refocusing  $180^\circ$  pulse between the two localized  $180^\circ$



**Figure 8** MEGA-PRESS and PRESS+4 pulse sequence timings, pulses and gradient representations.

refocusing pulses. Spectral simulations were carried out at 4 T for both MEGA-PRESS and PRESS+4 sequences using the GAMMA library. To reduce the complexity, the PRESS simulations assumed an ideal  $90^\circ$  excitation pulse without the volume selection gradient and identical localized spin echo  $180^\circ$  pulses in the other two directions. The simulation method used for the gradient volume selection with  $180^\circ$  pulses is described in detail elsewhere.<sup>56</sup> The RF editing pulse (duration = 19 ms) with SLR shape (bandwidth = 90 Hz) was initially generated in MATPULSE<sup>58</sup> and digitized to 190 points. The frequency shifts for the EDIT ON and OFF conditions of PRESS+4 were accomplished prior to importing into the GAMMA program by multiplying the time domain pulse shape by the appropriate exponential function containing the corresponding frequency. All experiments were carried out with TE = 72 ms (for MEGA-PRESS:  $\tau_1 = 6$  ms,  $\tau_2 = 36$  ms,  $\tau_3 = 30$  ms; for PRESS+4:  $\tau_1 = \tau_4 = 6$  ms,  $\tau_2 = \tau_3 = 30$  ms). It was shown by these simulations that while the MEGA-PRESS method suffers significant GABA signal loss ( $\sim 20\%$  for the difference spectrum), that the GABA signal intensity in PRESS+4 is reduced by only 2% compared to a non-localized condition at 4 T.

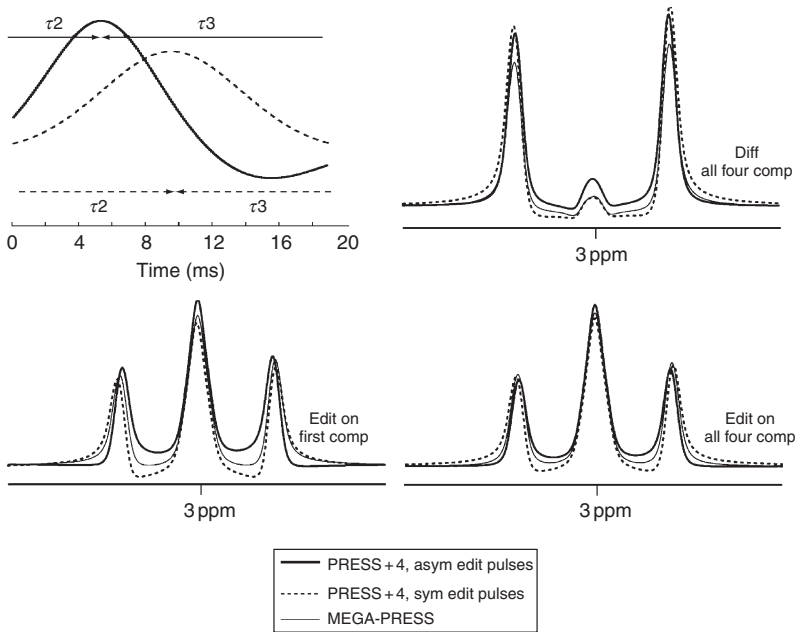
Results for each of the four compartments in MEGA-PRESS and PRESS+4 are shown in Figure 9 for the EDIT ON and EDIT OFF conditions. It shows the distribution of GABA outer peak intensity at 3 ppm for the area selected by the two ideal  $180^\circ$  pulses in both sequences. Representative GABA peaks at 3 ppm from each compartment of the simulated area are also shown in Figure 9. For the



**Figure 9** Four compartment results for GABA multiplet resonance group at 3.0 ppm for MEGA-PRESS and PRESS+4 in a  $64 \times 64$  spatially localized spectral simulation. Both edit ON and edit OFF states are shown.

EDIT OFF case in the MEGA-PRESS sequence, the GABA phases in compartments 2 and 4 added destructively with compartments 1 and 3. This spatial interference artefact in the MEGA-PRESS sequence induced signal loss of 40% in the EDIT OFF spectrum compared to non-localized conditions. In contrast, the PRESS+4 results in [Figure 9](#) show the GABA outer peak distributions where all four compartments contained spectra with similar phases. As a result, the GABA intensity loss in the EDIT OFF spectrum due to the four compartment artefact is negligible (less than 1% compared to non-localized simulation). The PRESS+4 edit ON GABA outer peaks in the total spectrum are slightly reduced ( $\sim 4\%$ ) compared to MEGA-PRESS, mainly due to the contribution from the first compartment.

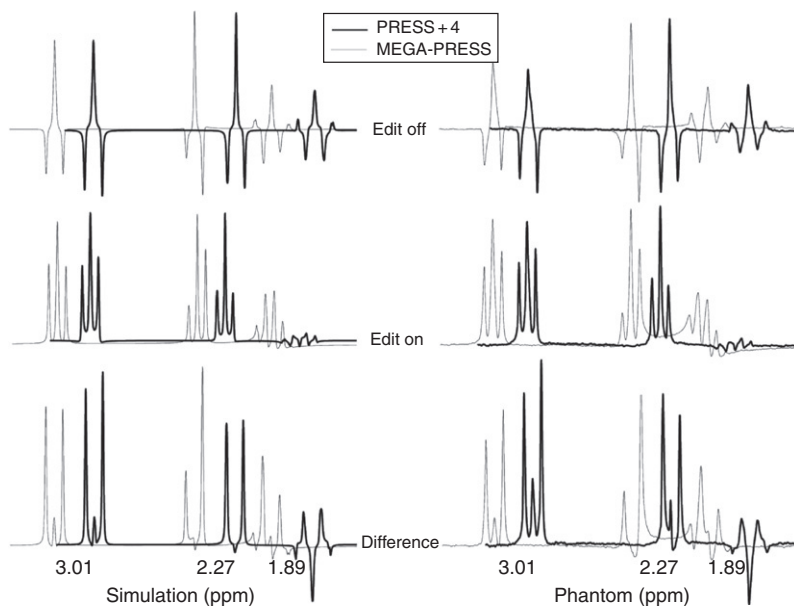
To further improve the performance of PRESS+4, asymmetrical RF editing pulses were investigated to reduce signal loss in compartment 1. Results are shown in [Figure 10](#). If symmetrical RF editing pulses are used, the PRESS+4 time of evolution in compartment 1 is  $\tau_1 + \tau_6$ , whereas for MEGA-PRESS the time of evolution in the same compartment is  $\tau_1$ . If asymmetrical editing pulses are used in PRESS+4, the total time of evolution for the GABA signal at 3 ppm can be reduced to 0 because maximum amplitudes of those pulses occur at different times compared to symmetrical excitation, resulting in different time evolution for GABA during the asymmetrical editing pulses.



**Figure 10** The effects of using symmetric (top left, dotted line) or asymmetric (top left, black) RF editing pulses in MEGA-PRESS and PRESS+4 experiments.

Figure 10 shows the maximum phase pulse shape that causes GABA to be refocused sooner compared to a symmetrical pulse (by  $\sim 5$  ms). This pulse asymmetry essentially negates the  $\tau_1$  evolution period and the second editing minimum phase pulse (not shown) negates the  $\tau_6$  evolution. As a result, the GABA signal in compartment 1 for the EDIT ON scan is at the maximum amplitude as shown (solid thick line). Also shown is the sum of all four compartments for the EDIT ON scan and the final difference spectra for all four compartments for the MEGA-PRESS and PRESS+4 with symmetrical and asymmetrical pulses. It is obvious that the contributions of other compartments are significant enough to make the outcome of symmetrical and asymmetrical pulses in PRESS+4 approximately the same (but still significantly better than MEGA-PRESS in the final difference spectrum). However, asymmetrical editing pulses were found to be superior to symmetrical editing only for volume selective RF pulse bandwidths  $> 1$  kHz because the contributions from compartments 2 and 3 become smaller for higher bandwidths. This form of spectral simulation can be applied in any PRESS-based experiments at higher field, where the “4 compartment” artefact is thought to be particularly detrimental.

Figure 11 compares GABA simulations (left) with 100 mM GABA phantom data (right) for the edit OFF (top), edit ON (middle) and difference (bottom) spectra collected by the MEGA-PRESS and PRESS+4 methods. Phantom and *in vivo* experiments were carried out on a Bruker MedSpec 4.0 Tesla system.



**Figure 11** Comparison of phantom data acquisition (right) with spectral simulation results (left) for the MEGA-PRESS (grey) and PRESS+4 (black) sequences.

RF pulses and timings were identical to those used in the spectral simulation. Overall, [Figure 11](#) demonstrated good agreement between simulations and experimental data. The small deviations between the simulation and the phantom data were likely caused by  $T_2$  differences between different GABA proton groups and line shape distortions from eddy currents (not accounted for in the simulations). The calculated increase in GABA intensity (18%) at 3.01 ppm in the difference spectrum for PRESS+4 compared well with observed a 17% increase in phantom spectrum.

## 4. CONCLUSIONS

As demonstrated by the previous examples, spectral simulation has become a well-defined tool for use by clinical MR researchers. It is available in many different forms, from libraries of NMR physics functions, to command line or GUI wrapped applications. Many of these are available for free through the adoption of open source software methodologies, which also fosters extended communities for each spectral simulation project. There are a number of significant roles for which spectral simulation tools have already proven to be important, including as a source for metabolite spectral analysis prior information and as a platform for improved RF pulse and MRS sequence design. With the advent of higher clinical field strengths, it can be expected to play an increasingly expanded and important role in all of these areas.

## APPENDIX A. A BRIEF LIST OF SIMULATION LIBRARIES AND PACKAGES

POMA: A complete mathematica implementation of the NMR product-operator formalism—Gunttert et al. *JMR*: **101A**, 103–105 (1993). POMA is a flexible implementation of the product operator formalism for spin-1/2 nuclei written for Mathematica. It provides analytical results for the time evolution of weakly coupled spin systems under the influence of free precession, selective and non-selective pulses, and phase cycling. As part of Mathematica, it requires a license, but the source code is free. Mathematica also provides a framework for visualizing and storing results.

Computer simulations in magnetic resonance: An object-oriented programming approach—Smith et al. *JMR*: **106A**, 75–105 (1994). This publication describes the GAMMA simulation library. This package is written in C++ and was one of the first open source packages to fully embrace an object-oriented programming approach to map NMR physics operators to C++ objects. It provides for both low and high level and manipulation of the density matrix, where high level operations are typically constructed from amalgams of low level objects. This provides great flexibility for constructing simulations at whatever level of complexity is needed. Both 1D and 2D NMR experiments can be performed on user defined metabolites. The original software was supported by two major laboratories but

required some knowledge of C++ programming. Binary installation packages are available for most major operating systems. Storage and visualization of results depends mainly on third party software programs for which GAMMA can create compatible output files. In more recent years, the C++ library has been wrapped by Python to provide compiler-free manipulation of the NMR objects.

**The virtual NMR spectrometer:** A computer program for efficient simulation of NMR experiments involving pulsed field gradients—Nicholas *et al.* *JMR*: **145**, 262–375 (2000). This is an application written in Matlab that provides an intuitive graphical user interface, similar to a real spectrometer, to assist in pulse sequence design. Both 1D and 2D NMR experiments can be performed on user defined metabolites. As part of Matlab, it requires a license, but the source code is free. The application itself provides a variety of ways of interacting with the data, and Matlab also provides a further framework for visualizing and storing results.

**SIMPSON:** A general simulation program for solid-state NMR spectroscopy—Bak *et al.* *JMR*: **147**, 296–330 (2000). This is “computer spectrometer” package written in Tcl which provides a scripting language, similar to a real spectrometer, to simplify the design of simulated “pulse sequences”. The simulations themselves are written as scripts, but the SIMPSON package provides graphical tools for post-processing, viewing and manipulating data. To speed up processing, some of the internal algorithms are written and compiled into C modules that are accessed by Tcl. Both 1D and 2D NMR experiments can be performed on user defined metabolites. The Tcl language does not require a license, and the package is free. Binary installation packages are available for most major operating systems.

**PJNMR:** A platform-independent graphical simulation tool for NMR spectroscopy—Letourneau *et al.* *JMR*: **161**, 154–167 (2003). This is a “Pure Java” simulation package that can simulate pulse sequences using a “spectrometer like” interface. Only spins systems of three or less spin 1/2 nuclei can be simulated which limits its general applicability. However, as a Java-based program it is easily cross-platform compatible. The program provides a graphical display of density matrix state and magnetization vectors for each nucleus.

**BlochLib:** A fast NMR C++ tool kit—Blanton, *JMR*: **162**, 269–2838 (2003). This simulation library is very similar to the GAMMA library. However, the author has taken advantage of other existing math and optimization libraries (ATLAS, MINUIT, FFTW) to considerably speed up the calculation of simulations containing larger spin systems. Users need some knowledge of C++ programming to use this package, and visualization and storage of results depend on third party packages. Both 1D and 2D NMR experiments can be performed on user defined metabolites. BlochLib contains functions to output to a number of standard formats, Matlab for example. The use of external math libraries adds additional dependencies to the installation of this package but can be very worthwhile if large or exceedingly complex simulations are required. Binary installation packages are available for most major operating systems.

**SPINEVOLUTION:** A powerful tool for the simulation of solid and liquid state NMR experiments—Veshtort *et al.* *JMR*: **178**, 248–282 (2006). SPINEVOLUTION is a command line driven spectral simulation application. It takes as an input a text

file that describes the simulation using language similar to many console pulse sequence programming languages. Both 1D and 2D NMR experiments can be performed on user defined metabolites. There are no facilities for graphical visualization or manipulation of results, but a number of functions for standard data format output are provided. A primary feature of SPINEVOLUTION is that it contains many optimized methods for speeding up calculation of spectral results. Users have great flexibility for selecting which methods to use. Binary installation packages are available for most major operating systems.

Development of an fMRI simulator for modeling realistic rigid-body motion artifacts—Drobnjak et al. *MRM*: 56, 364–380 (2006). This publication describes the FSL POSSUM (Physics-Oriented Simulated Scanner for Understanding MRI) package. This package allows users to produce realistic simulated MR images for fMRI and other MR imaging applications. It can account for a variety of input objects and acquisition artefacts. It creates accounts for these effects both across a “brain volume” as well as “through time”. It is listed here to demonstrate how researchers in other fields are using simulation techniques to anticipate and evaluate changes in MR data. While many of these simulations deal only with water, more and more are including contributions from both water and lipids to more effectively visualize changes due to off resonance artefacts.

## REFERENCES

1. A. Bax, P. G. De Jong, A. F. Mehlkopf and J. Smidt, *Chem. Phys. Lett.*, 1980, **69**, 567–570.
2. J. Hennig, T. Thiel and O. Speck, *Magn. Reson. Med.*, 1997, **37**, 816–820.
3. M. Mescher, H. Merkle, J. Kirsch, M. Garwood and R. Gruetter, *NMR Biomed.*, 1998, **11**, 266–272.
4. D. L. Rothman, F. Arias-Mendoza, G. I. Shulman and R. G. Shulman, *J. Magn. Reson.*, 1984, **60**, 430–436.
5. A. H. Trabesinger, D. Meier and P. Boesiger, *Magn. Reson. Imaging*, 2003, **21**, 1295–1302.
6. J. E. van Dijk, A. F. Mehlkopf and W. M. M. J. Bovee, *NMR Biomed.*, 1992, **5**, 75–86.
7. A. H. Trabesinger, D. Meier, U. Dydak, R. Lamerichs and P. Boesiger, *Magn. Reson. Med.*, 2005, **54**, 51–58.
8. C. Choi, N. J. Coupland, C. C. Hanstock, C. J. Ogilvie, A. C. Higgins, D. Gheorghiu and P. S. Allen, *Magn. Reson. Med.*, 2005, **54**, 272–279.
9. H. Kim, J. M. Wild and P. S. Allen, *Magn. Reson. Med.*, 2004, **51**(2), 263–272.
10. A. A. De Graaf and W. M. M. J. Bovee, *Magn. Reson. Med.*, 1990, **15**, 305–319.
11. S. W. Provencher, *Magn. Reson. Med.*, 1993, **30**(6), 672–679.
12. J. Slotboom, C. Boesch and R. Kreis, *Magn. Reson. Med.*, 1998, **39**, 899–911.
13. B. J. Soher, K. Young, V. Govindaraju and A. A. Maudsley, *Magn. Reson. Med.*, 1998, **40**, 822–831.
14. K. Young, V. Govindaraju, B. J. Soher and A. A. Maudsley, *Magn. Reson. Med.*, 1998, **40**, 812–815.
15. H. Kim, R. B. Thompson, C. C. Hanstock and P. S. Allen, *Magn. Reson. Med.*, 2005, **53**(4), 760–769.
16. R. B. Thompson and P. S. Allen, *Magn. Reson. Med.*, 2001, **45**, 955–965.
17. M. A. Thomas, N. Binesh, K. Yue and N. DeBruhl, *Magn. Reson. Imaging*, 2001, **14**, 181–186.
18. M. A. Thomas, L. N. Ryner, M. P. Mehta, P. A. Turski and J. A. Sorenson, *Magn. Reson. Imaging*, 1996, **6**, 453–459.
19. M. A. Thomas, K. Yue, N. Binesh, P. Davanzo, A. Kumar, B. Siegel, M. Frye, J. Curran, R. Lufkin, P. Martin and B. Guze, *Magn. Reson. Med.*, 2001, **46**, 58–67.
20. T. H. Jochimsen and M. von Mengershausen, *J. Magn. Reson.*, 2004, **170**, 67–78.
21. J. Magland and F. W. Wehrli, Pulse sequence programming in a dynamic visual environment, 2006, Seattle
22. L. G. Kaiser, K. Young and G. Matson, *Magn. Reson. Med.*, 2007, **58**(4), 813–818.

23. L. G. Kaiser, K. Young, D. Meyerhoff, S. G. Mueller and G. Matson, *NMR Biomed.*, 2008, **21**(1), 22–32.
24. A. Naressi, C. Couturier, J. M. Devos, M. Janssen, C. Mangeat, R. de Beer and D. Graveron-Demilly, *MAGMA*, 2001, **12**(2–3), 141–152.
25. S. A. Smith, T. O. Levante, B. H. Meier and R. R. Ernst, *J. Magn. Reson.*, 1994, **A106**, 75–105.
26. W. B. Blanton, *J. Magn. Reson.*, 2003, **162**(2), 269–283.
27. P. Guntert, N. Schaefer, G. Otting and K. Wuthrich, *J. Magn. Reson.*, 1993, **A 101**, 103–105.
28. R. P. F. Kanter, B. W. Char and A. W. Addison, *J. Magn. Reson.*, 1993, **A 101**, 23–29.
29. T. Allman, A. Bain and J. Garbow, *J. Magn. Reson.*, 1996, **A123**(1), 26–31.
30. M. Bak, J. T. Rasmusson and N. C. Nielsen, *J. Magn. Reson.*, 2000, **147**(2), 296–330.
31. M. Helgstrand and P. Allard, *J. Biomol. NMR*, 2004, **30**, 71–80.
32. G. H. Meresi, M. Cuperlovic, W. E. Palke and J. T. Gerig, *J. Magn. Reson.*, 1999, **137**(1), 186–195.
33. M. Veshtort and R. G. Griffin, *J. Magn. Reson.*, 2006, **178**, 248–282.
34. D. Graveron-Demilly, A. Diop, A. Briguet and B. Fenet, *J. Magn. Reson.*, 1993, **101**, 233–239.
35. H. Ratiney, M. Sdika, Y. Coenradie, S. Cavassila, D. van Ormondt and D. Graveron-Demilly, *NMR Biomed.*, 2005, **18**(1), 1–13.
36. P. Nicholas, D. Fushman, V. Ruchinsky and D. Cowburn, *J. Magn. Reson.*, 2000, **145**, 262–275.
37. M. Baldus, A. T. Petkova, J. Herzfeld and R. G. Griffin, *Mol. Phys.*, 1998, **95**, 1197–1207.
38. P. F. Devaux, G. L. Hoatson, E. Favre, P. Fellmann, B. Farren, A. L. McKay and M. Bloom, *Biochemistry*, 1986, **25**, 3804–3812.
39. S. Dusold, W. Milius and A. Sebald, *J. Magn. Reson.*, 1998, **135**(2), 500–513.
40. A. Ebel, B. J. Soher and A. A. Maudsley, *Magn. Reson. Med.*, 2001, **46**, 1072–1078.
41. T. R. Eykyn, R. Ghose and G. Bodenhausen, *J. Magn. Reson.*, 1999, **136**, 211–213.
42. C. Filip, S. Hafner, I. Schnell, D. E. Demco and H. W. Spiess, *J. Chem. Phys.*, 1999, **110**, 423–440.
43. V. Govindaraju, G. Gauger, G. Manley, A. Ebel, M. Meeker and A. A. Maudsley, *AJNR*, 2004, **25**, 730–737.
44. V. Govindaraju, D. J. Meyerhoff, A. A. Maudsley, M. Vermathen and M. W. Weiner, *Alcohol*, 1997, **32**, 671–681.
45. E. Hughes, E. B. Brouwer and R. K. Harris, *J. Magn. Reson.*, 1999, **138**, 256–267.
46. A. Kaikkonen, E. E. Ylinen and M. Punkkinen, *Appl. Magn. Reson.*, 1998, **15**, 509–518.
47. A. Maudsley, V. Govindaraju, K. Young, Z. Aygula, P. M. Pattany, B. J. Soher and G. Matson, *J. Magn. Reson.*, 2005, **173**(1), 54–63.
48. R. E. D. McClung, *Concepts Magn. Reson.*, 1999, **11**, 1–28.
49. P. Pelupessy, E. Chiarparin and G. Bodenhausen, *J. Magn. Reson.*, 1999, **138**, 178–181.
50. G. A. Sierra, M. A. Schuler and A. Schweiger, *Chem. Phys. Lett.*, 1999, **303**, 475–481.
51. S. A. Smith and N. Murali, *J. Magn. Reson.*, 1999, **136**, 211–213.
52. B. J. Soher and A. A. Maudsley, *Magn. Reson. Med.*, 2004, **52**(6), 1246–1254.
53. B. J. Soher, P. Vermathen, N. Schuff, D. Wiedermann, D. J. Meyerhoff, M. W. Weiner and A. A. Maudsley, *Magn. Reson. Imag.*, 2000, **18**(9), 1159–1165.
54. J. Suhy, K. D. Laxer, A. A. Capizzano, P. Vermathen, G. B. Matson, N. M. Barbaro and M. W. Weiner, *Neurology*, 2002, **58**(5), 821–823.
55. J. Suhy, R. G. Miller, R. Rule, N. Schuff, J. Licht, V. Dronskey, D. Gelinas, A. A. Maudsley and M. W. Weiner, *Neurology*, 2002, **58**(5), 773–779.
56. K. Young, G. B. Matson, V. Govindaraju and A. A. Maudsley, *J. Magn. Reson.*, 1999, **140**, 146–152.
57. K. Young, B. J. Soher and A. A. Maudsley, *Magn. Reson. Med.*, 1998, **40**, 816–821.
58. G. B. Matson, *Magn. Reson. Imag.*, 1994, **12**(8), 1205–1225.
59. G. B. Matson, D. J. Meyerhoff, T. J. Lawry, R. S. Lara, J. Duijn, R. F. Deicken and M. W. Weiner, *NMR Biomed.*, 1993, **6**, 215–224.
60. C. T. W. Moonen, M. von Kienlin, P. C. M. van Zijl, J. Cohen, J. Gillen, P. Daly and G. Wolf, *NMR Biomed.*, 1989, **2**, 201–208.
61. R. Hurd, N. Sailasuta, R. Srinivasan, D. B. Vigneron, D. Pelletier and S. J. Nelson, *Magn. Reson. Med.*, 2004, **51**(3), 435–440.
62. M. Terpstra, K. Ugurbil and R. Gruetter, *Magn. Reson. Med.*, 2002, **47**, 1009–1012.



## Simulation of Molecular Motion of Quadrupolar Nuclei in Solid-State NMR Spectra

**Flemming H. Larsen**

---

<b>Contents</b>		
	1. Introduction	104
	2. Theory	106
	2.1. Specifically for spin-1 nuclei	112
	2.2. Two-axis jump processes	114
	2.3. 2-by-2-site jump	114
	2.4. 2-by-3-site jump	115
	3. Numerical Simulations	117
	3.1. Spin-1 nuclei	118
	3.2. Half-integer quadrupolar nuclei	118
	4. Results and Discussion	119
	4.1. Spin-1 nuclei	119
	4.2. Dynamic effects in $^{14}\text{N}$ MAS spectra by SQ or DQ coherences	123
	4.3. Multi-axis jump processes	124
	4.4. Half-integer quadrupolar nuclei	129
	5. Conclusions	134
	Acknowledgements	135
	References	135

---

### Abstract

Simulations of QCPMG NMR type experiments have been used to explore dynamic processes of quadrupolar nuclei in solids. By setting up a theoretical approach that is well suited for efficient numerical simulations, the quadrupole-echo (QE), quadrupolar Carr-Purcell-Meiboom-Gill (QCPMG), single-pulse magic-angle-spinning (MAS) and QCPMG-MAS experiments (when appropriate) have been analysed regarding the effect of the magnitude

Department of Food Science, Quality and Technology, University of Copenhagen, Rolighedsvej 30, Frederiksberg, Denmark

Annual Reports on NMR Spectroscopy, Volume 71  
ISSN 0066-4103, DOI: 10.1016/S0066-4103(10)71004-8

© 2010 Elsevier Ltd.  
All rights reserved.

of the EFG-tensor, the spin-quantum number and different dynamical processes. This comparison enables determination of the most sensitive experiment for analysis of molecular dynamics of quadrupolar nuclei.

For spin-1 nuclei, both QCPMG and single-pulse MAS experiments were suitable for dynamics studies of nuclei having  $C_{QS}$  typical for  $^2\text{H}$  or  $^6\text{Li}$ . In case of  $^{14}\text{N}$ , the single-pulse MAS experiment was the method of choice for investigation of dynamics for  $C_{QS}$  larger than 750 kHz at 14.1 T.

For  $C_{QS}$  in the MHz range dynamical effects on the single-quantum (SQ) and double-quantum (DQ)  $^{14}\text{N}$  coherences were compared. Hereby it was demonstrated that the DQ lineshape was not broadened as much as the SQ lineshape as the DQ transition is not affected by the first-order quadrupolar Hamiltonian.

Dynamical effects of a two-axis 3-by-2-site jump process as can be observed in DMS- $d_6$  were investigated by both QCPMG and MAS simulations. Besides rather interesting line broadening effects when both rate constants were in the intermediate regime, it was observed that the QCPMG experiment is more sensitive towards motional effects than MAS if either of the two rate constants is in the fast regime.

For the half-integer nuclei, the effects of a two-site jump process was explored for a range of nuclei with different  $C_{QS}$ , spin-quantum numbers ( $I$ ) and Larmor frequencies ( $\omega_0$ ). As for spin-1 nuclei, significant line broadening of either sidebands and changes in the overall lineshape was observed in an intermediate dynamic regime. These effects and the range of the intermediate regime were shown to be highly dependent of the three parameters listed above. Comparing the four experiments (QE, QCPMG, MAS and QCPMG–MAS) on the central transition of a fictitious  $^{39}\text{K}$  site performing a two-site jump revealed that the QCPMG–MAS experiment is most sensitive towards dynamics as changes in both overall lineshape and spin-echo sidebands were observed. Higher order jump processes (3-, 4-, 6-site jumps) were also explored and by these it was noted that the width of the central transition in the fast limit decreases with the order of the jump process.

**Key Words:** QCPMG, MAS, Quadrupolar nuclei, Solid-state, Multiple-site jump, Molecular motion.

---

## 1. INTRODUCTION

Analysis of molecular motion in solids using NMR spectroscopy has been a developing field during the past decades. In this context,  $^2\text{H}$  NMR is the most used approach but recently a number of other quadrupolar nuclei have been studied. This includes spin-1 as well as half-integer quadrupolar nuclei such as  $^7\text{Li}$  and  $^{23}\text{Na}$ .

More specifically, determination of  $^2\text{H}$  dynamics by solid-state NMR has been used for a broad range of applications ranging from studies of glass formers,<sup>1</sup> small molecules in larger host matrices,<sup>2–4</sup> ionic rotors,<sup>5</sup> selectively deuterated sites<sup>6,7</sup> or functional groups in macromolecules.<sup>8,9</sup> Also the dynamics of selectively labelled amino acids<sup>10,11</sup> or nucleic acids in RNA<sup>12</sup> have recently been explored.

By far the most used experiment for such analysis has been the static quadrupolar echo (QE) experiment.<sup>13–15</sup> Using this experiment and subsequent lineshape analysis, detailed information about the dynamics may be extracted. The QE experiment has been shown to be more sensitive towards dynamic processes than the single-pulse experiment<sup>16</sup> and several approaches for lineshape analysis of jump processes up to N sites have been developed.<sup>17,18</sup> During the years, several improvements to the original QE experiment have been introduced. One of the experimental challenges has been excitation of the up to 350 kHz wide lineshape and therefore the effect of finite pulses has been explored. When no dynamics are present Bloom et al.<sup>19</sup> solved the problem analytically but in the presence of dynamics numerical simulations were required. To compensate for effects of finite rf-pulses, composite pulses<sup>20–22</sup> were introduced that minimize the pulse distortions when using low or intermediate rf-field strengths. Another improvement was the extension of the QE experiment to the Quadrupolar Carr-Purcell-Meiboom-Gill (QCPMG) experiment using a train of refocusing pulses during acquisition to obtain a sensitivity gain by an order of magnitude.<sup>23,24</sup> Furthermore, multi-dimensional homonuclear  $^2\text{H}$  experiments were developed and applied to obtain very accurate information about jump and diffusion processes.<sup>25–28</sup>

In addition to the previously mentioned experiments designed for static samples, single-pulse and QE magic-angle-spinning (MAS)<sup>29–31</sup> as well as off-MAS experiments<sup>32,33</sup> were used to explore  $^2\text{H}$  dynamics in detail. Even 2D  $^2\text{H}$  MAS experiments correlating double- and single-quantum coherences were suggested for samples with multiple  $^2\text{H}$  sites<sup>34</sup> but so far not employed for studies of dynamics.

Regarding  $^2\text{H}$  NMR, a number of studies were performed on compounds containing paramagnetic nuclei<sup>35–38</sup> where the paramagnetic effects of unpaired electrons must be taken into account. As this affects both lineshape and relaxation, the theoretical approach is somewhat different and this will not be dealt with any further in the present work.

In principle, all of the experiments mentioned above would be applicable for the other two NMR active spin-1 nuclei:  $^6\text{Li}$  and  $^{14}\text{N}$ . Solid-state  $^6\text{Li}$  NMR have so far been utilized in materials research<sup>39–42</sup> and even exchange experiments on  $^6\text{Li}$  enriched  $\text{Li}_2\text{SiO}_4$  have been performed.<sup>42</sup>

Solid-state spectroscopic studies of  $^{14}\text{N}$  are traditionally performed by Nuclear Quadrupole Resonance (NQR) spectroscopy due to the large quadrupolar coupling constants but recently a broad range of compounds have been investigated by single-pulse MAS NMR spectroscopy.<sup>43–45</sup> This included  $^{14}\text{N}$  MAS NMR applications in materials research<sup>43,44</sup> as well as amino acids<sup>45</sup> and model compounds for biological membranes.<sup>46</sup> Two-dimensional HMQC type experiments<sup>47–50</sup> were also used to correlate either  $^1\text{H}$  or  $^{13}\text{C}$  to  $^{14}\text{N}$  using evolution of either single- or double-quantum coherence for  $^{14}\text{N}$  in order to extract the parameters for the EFG-tensor. In this context, a particularly interesting result regarding dynamics is the motional effects of the NH- and  $\text{NH}_3^+$ -groups in the polypeptide AAG observed by  $^{14}\text{N}$ - $^1\text{H}$  HMQC spectra.<sup>49</sup>

Most of the studies mentioned above employ motional models using single-axis jump dynamics but multi-axis dynamics were also explored for  $^2\text{H}$  both experimentally<sup>30,33,51</sup> and purely theoretically.<sup>52</sup>

The motion of half-integer quadrupolar nuclei is so far less studied but they are of particular interest because of their structural significance in ion-exchange materials,<sup>53–55</sup> modifier ions in glasses,<sup>56</sup> or active sites in metallo-proteins.<sup>57–60</sup> Therefore, experimental analysis of the dynamic properties for these nuclei is a key issue in order to gain important insight into these classes of materials and molecules. Recently, the effects of molecular dynamics have been studied in detail for half-integer quadrupolar nuclei<sup>61–68</sup> with emphasis on applications within materials research. These studies have been performed using the either single-pulse, spin-echo or inversion recovery experiments under static or MAS conditions. Combined with lineshape simulations, this has provided information about the dynamics. Depending on the magnitude of the quadrupolar coupling constant, these types of experiments were conducted either on the central transition or when excitation of the satellite transitions were possible—using the full spinning sideband manifold.<sup>66</sup>

Most NMR-groups exploring effects of molecular motion tend to develop their own software to simulate these effects. Recently the simulation program EXPRESS developed by Vold and Hoatson<sup>69</sup> was presented. By this program, effects of dynamics can be simulated (see Table 1 in Ref. 69 for details) but so far effects of finite rf-pulses and the motional effects on satellite transitions in half-integer quadrupolar nuclei are not included.

In the present work, 1D QE, QCPMG, single-pulse MAS and QCPMG–MAS experiments for analysis of multi-site jump processes involving quadrupolar nuclei will be examined theoretically and by simulations. For this purpose, the Hamiltonian includes the first as well as secular second-order terms for both the CSA- and EFG-tensors, the second-order EFG–CSA mix-term and for spin-1 also the secular third-order term for the EFG-tensor. In addition effects of finite rf-pulses will be explored. Previously this has been presented for either half-integer quadrupolar nuclei<sup>70</sup> or spin-1 nuclei<sup>71</sup> only.

## 2. THEORY

The calculations presented here are based on the density operator formalism using the Liouville–von-Neumann equation and the theoretical approach is confined to quadrupolar nuclei subjected to EFG as well as CSA-interactions. Following the approach of Barbara et al.,<sup>20</sup> the Hamiltonian for an N-site jump may be written as

$$\dot{\rho} = i[\rho, H_{\text{tot}}] + k(\mathbf{P}\rho\mathbf{P} - \rho), \quad (1)$$

where  $\dot{\rho}$  is the density operator,  $H_{\text{tot}}$  is the effective Hamiltonian,  $k$  is the exchange rate and  $\mathbf{P}$  is a permutation operator. The density operator can be expressed as a linear combination of operators forming a complete basis set. For a spin-1 nucleus, a complete basis set consists of  $\dim = ((2I + 1)^2 - 1)$  basis operators for each of the

$N$  sites resulting in a total of  $R = N \cdot \dim$  operators. Therefore the density operator may be written as

$$\rho(t) = \sum_{i=1}^R m_i(t) \mathbf{O}_i, \quad (2)$$

where  $\{\mathbf{O}_i\}_{i=1}^R$  denotes a complete set of basis operators and  $m_i(t)$  denotes the time dependent coefficients  $m_i(t)$ ,  $i = 1, \dots, R$ . It is noted that

$$\rho(0) = \sum_{i=1}^N \text{pop}(i) \cdot I_{z,i}, \quad (3)$$

in which  $\text{pop}(i)$  denotes the population of site  $i$ . In the following  $\text{pop}(i) = 1/N$  corresponding to equally populated sites. Using the form of Equation (1), the coefficients  $m_i(t)$  in Equation (2) must fulfil

$$\dot{m}_i(t) = \sum_{j=1}^R L_{ij} m_j(t), \quad (4)$$

which has the general solution

$$\vec{m}(t_1) = T \exp \left( \int_{t_0}^{t_1} L(t) dt \right) \vec{m}(t_0), \quad (5)$$

where the Dyson time-ordering operator,<sup>72</sup>  $T$ , is used for evaluating the integral when  $L(t)$  is time dependent—for example, under MAS conditions. The exact expression for  $L(t)$  will be developed in the following.

An adequate basis set may be obtained from Bowden et al.<sup>73</sup> which was developed for multiple-quantum experiments. In this formalism, the irreducible spin operators  $T_q^n$ ,  $n = 0, \dots, 2I$ ;  $q = -n, \dots, n$ , of rank  $n$  and order  $q$  form an orthogonal basis set. The orthonormal operators,  $\hat{T}_q^n$ , derived from these form a complete basis set. These are defined as

$$\hat{T}_q^n = \frac{1}{n!} \sqrt{\frac{(2n+1)(2I-n)!2^n(2n!)}{(2I+n+1)!}} T_q^n = \hat{C}_I^n T_q^n. \quad (6)$$

The theoretical approach will take use of these operators. The effective Hamiltonian will be described for a single site, site  $v$ , but for simplicity the formalism omits the index  $v$  unless it is absolutely necessary as the expressions are equivalent for all sites in the  $N$ -site jump process. For a system including both CSA- and quadrupolar interactions, the effective Hamiltonian for a single site during a pulse is

$$H_{\text{tot}} = H_Q^{(1)} + H_Q^{(2)} + H_\sigma^{(1)} + H_\sigma^{(2)} + H_{Q,\sigma}^{(2)} + H_{\text{rf}} \quad (7)$$

in which  $H_Q^{(1)}$  and  $H_Q^{(2)}$  denote the first order and the secular parts of the second-order quadrupolar interaction, respectively,  $H_\sigma^{(1)}$  includes the isotropic as well as

the anisotropic part of the chemical shielding,  $H_\sigma^{(2)}$  is the secular part of the second-order CSA,  $H_{Q,\sigma}^{(2)}$  is the second-order EFG/CSA mix-term and  $H_{\text{rf}}$  represents the rf-operator for a pulse with phase  $\theta$ . The Hamiltonians operators corresponding to the various interactions are given both in the standard Zeeman basis and in the  $T_q^n$  basis:

$$H_Q^{(1)} = \omega_Q^{(1)} \frac{1}{\sqrt{6}} (3I_z^2 - I(I+1)) = \omega_Q^{(1)} T_0^2 \quad (8)$$

$$H_Q^{(2)} = \omega_Q^{(21)} (-8I_z^3 + 4I(I+1)I_z - I_z) + \omega_Q^{(22)} (-2I_z^3 + 2I(I+1)I_z - I_z) \\ = \begin{cases} \sqrt{\frac{2}{5}} (-8\omega_Q^{(21)} - 2\omega_Q^{(22)}) T_0^3 - \left( \frac{4}{5} I(I+1) - \frac{3}{5} \right) (\omega_Q^{(21)} - \omega_Q^{(22)}) T_0^1 & \text{when } I > 1, \\ (\omega_Q^{(22)} - \omega_Q^{(21)}) T_0^1, & \text{when } I = 1, \end{cases} \quad (9)$$

$$H_\sigma^{(1)} = - \left( \sqrt{\frac{2}{3}} \omega_\sigma + \omega_{\text{iso}} \right) I_z = - \left( \sqrt{\frac{2}{3}} \omega_\sigma + \omega_{\text{iso}} \right) T_0^1, \quad (10)$$

$$H_\sigma^{(2)} = -\frac{1}{2} \omega_0 (R_L^\sigma(1) R_L^\sigma(-1)) I_z = -\frac{1}{2} \omega_0 (R_L^\sigma(1) R_L^\sigma(-1)) T_0^1, \quad (11)$$

$$H_{Q,\sigma}^{(2)} = \frac{1}{2\omega_0} (R_L^Q(1) R_L^\sigma(-1) + R_L^Q(-1) R_L^\sigma(1)) (3I_z^2 - I(I+1)) \\ = \frac{\sqrt{3}}{\sqrt{2}\omega_0} (R_L^Q(1) R_L^\sigma(-1) + R_L^Q(-1) R_L^\sigma(1)) T_0^2, \quad (12)$$

$$H_{\text{rf}} = -\omega_{\text{rf}} (I_x \cos(\theta) + I_y \sin(\theta)) \\ = \frac{\omega_{\text{rf}}}{\sqrt{2}} (\cos(\theta) (T_1^1 - T_{-1}^1) - i \sin(\theta) (T_1^1 + T_{-1}^1)). \quad (13)$$

Schematically the effective Hamiltonian for a pulse having phase  $\theta$  may be written as

$$H_{\text{tot}} = a T_0^1 + b (\cos(\theta) (T_1^1 - T_{-1}^1) - i \sin(\theta) (T_1^1 + T_{-1}^1)) + c T_0^2 + d T_0^3 \\ = \frac{a}{\hat{C}_I^1} \hat{T}_0^1 + \frac{b}{\hat{C}_I^1} \left( \cos(\theta) (\hat{T}_1^1 - \hat{T}_{-1}^1) - i \sin(\theta) (\hat{T}_1^1 + \hat{T}_{-1}^1) \right) \\ + \frac{c}{\hat{C}_I^2} \hat{T}_0^2 + \frac{d}{\hat{C}_I^3} \hat{T}_0^3, \quad (14)$$

where  $a$ ,  $b$ ,  $c$  and  $d$  are given by

$$a = - \left( \omega_{\text{iso}} + \sqrt{\frac{2}{3}} \omega_\sigma \right) - \frac{1}{2} \omega_0 (R_L^\sigma(1) R_L^\sigma(-1)) \\ + \frac{4I(I+1) - 3}{5} (\omega_Q^{(22)} - \omega_Q^{(21)}), \quad (15)$$

$$b = \sqrt{\frac{1}{2}}\omega_{\text{rf}}, \quad (16)$$

$$c = \omega_Q^{(1)} + \frac{\sqrt{3}}{\sqrt{2}\omega_0} \left( R_L^Q(1)R_L^\sigma(-1) + R_L^Q(-1)R_L^\sigma(1) \right), \quad (17)$$

$$d = \begin{cases} -\frac{2\sqrt{2}}{\sqrt{5}} \left( 4\omega_Q^{(21)} + \omega_Q^{(22)} \right), & \text{when } I > 1, \\ 0, & \text{when } I = 1 \end{cases} \quad (18)$$

and

$$\omega_{\text{iso}} = \delta_{\text{iso}}\omega_0, \quad (19)$$

$$\omega_\sigma = \omega_0 R_L^\sigma(0), \quad (20)$$

$$\omega_q = \frac{2\pi C_Q}{2I(2I-1)}, \quad (21)$$

$$\omega_Q^{(1)} = \omega_q R_L^Q(0), \quad (22)$$

$$\omega_Q^{(2j)} = -\frac{\omega_q^2}{2\omega_0} R_L^Q(j)R_L^Q(-j) \quad (23)$$

and  $C_Q = e^2 q^Q / h$  denotes the quadrupolar coupling constant,  $\omega_{\text{rf}} = -\gamma \mathbf{B}_{\text{rf}}$  is the rf-field strength,  $\omega_0 = -\gamma \mathbf{B}_0$  the Larmor frequency and  $\delta_{\text{iso}}$  and  $\delta_\sigma$  the isotropic and anisotropic chemical shift (CSA), respectively. In their principal axis frames (P), the non-zero elements of the EFG (superscript  $Q$ )- and CSA (superscript  $\sigma$ )-tensors are given by  $R_P^Q(-2) = R_P^Q(2) = -\eta_Q/2$ ,  $R_P^Q(0) = \sqrt{3}/2$  and  $R_P^\sigma(-2) = R_P^\sigma(2) = -\delta_\sigma \eta_\sigma/2$ ,  $R_P^\sigma(0) = \sqrt{3}/2 \delta_\sigma$ , respectively. The spatial parts of the tensors in the laboratory frame (L) for the  $v$ th site are calculated as

$$R_L^Q(n) = \sum_{m=-2}^2 \sum_{k=-2}^2 \sum_{j=-2}^2 R_P^Q(j) \mathbf{D}_{j,k}^{(2)}(\alpha_{\text{PC},v}^Q, \beta_{\text{PC},v}^Q, \gamma_{\text{PC},v}^Q) \mathbf{D}_{k,m}^{(2)}(\alpha_{\text{CR}}, \beta_{\text{CR}}, \gamma_{\text{CR}}) \mathbf{D}_{m,n}^{(2)}(\omega_r t, \beta_{\text{RL}}, 0), \quad (24)$$

$$\begin{aligned} R_L^\sigma(n) = & \sum_{m=-2}^2 \sum_{k=-2}^2 \sum_{q=-2}^2 \sum_{j=-2}^2 R_P^\sigma(j) \mathbf{D}_{j,q}^{(2)}(\alpha_{\text{PP}}^\sigma, \beta_{\text{PP}}^\sigma, \gamma_{\text{PP}}^\sigma) \\ & \times \mathbf{D}_{q,k}^{(2)}(\alpha_{\text{PC},v}^Q, \beta_{\text{PC},v}^Q, \gamma_{\text{PC},v}^Q) \mathbf{D}_{k,m}^{(2)}(\alpha_{\text{CR}}, \beta_{\text{CR}}, \gamma_{\text{CR}}) \mathbf{D}_{m,n}^{(2)}(\omega_r t, \beta_{\text{RL}}, 0), \end{aligned} \quad (25)$$

where the Euler angles  $\Omega_{\text{PP}}^\sigma = (\alpha_{\text{PP}}^\sigma, \beta_{\text{PP}}^\sigma, \gamma_{\text{PP}}^\sigma)$  transform the CSA-tensor from its principal axis (P) system into the principal axis system of the EFG-tensor.  $\Omega_{\text{PC},v}^Q = (\alpha_{\text{PC},v}^Q, \beta_{\text{PC},v}^Q, \gamma_{\text{PC},v}^Q)$  are the angles describing the transformation from the principal axis frame (P) of the EFG-tensor into the crystal fixed frame (C) for site  $v$ . These may be given by<sup>18</sup>

$$\Omega_{\text{PC},v}^Q = \left( \theta, \phi, \frac{2\pi(v-1)}{N} \right), \quad v \in \{1, \dots, N\}, \theta \in [0 : 2\pi], \phi \in [0 : \pi]. \quad (26)$$

The angles for powder averaging  $\Omega_{\text{CR}} = (\alpha_{\text{CR}}, \beta_{\text{CR}}, \gamma_{\text{CR}})$  describe the transformation from the crystal (C) frame into the rotating frame (R) in case of MAS.  $\Omega_{\text{RL}} = (\omega_r t, \beta_{\text{RL}}, 0)$  are the Euler angles transforming from the rotating frame to the laboratory (L) frame, where  $\omega_r$  denotes the spin-rate and  $\beta_{\text{RL}}$  the rotor angle relative to the static magnetic field. It is important to note that the Hamiltonians are periodic with the rotor period and that the centerband ( $m=0$ ) is independent of the  $\gamma_{\text{CR}}$  angle. Taking the first point into account makes it computational favourable to make the rotor period an integral number of the dwell time and reuse the Hamiltonian after the first rotor period. The second point implies faster calculation of the centerband as integration only requires two powder angles. For static samples [Equations \(24\) and \(25\)](#) are reduced to

$$R_{\text{L}}^Q(n) = \sum_{k=-2}^2 \sum_{j=-2}^2 R_{\text{P}}^Q(j) \mathbf{D}_{j,k}^{(2)} \left( \Omega_{\text{PC},v}^Q \right) \mathbf{D}_{k,n}^{(2)} (\alpha_{\text{CL}}, \beta_{\text{CL}}, 0), \quad (27)$$

$$R_{\text{L}}^\sigma(n) = \sum_{k=-2}^2 \sum_{q=-2}^2 \sum_{j=-2}^2 R_{\text{P}}^Q(j) \mathbf{D}_{j,q}^{(2)} (\Omega_{\text{PP}}^\sigma) \mathbf{D}_{q,k}^{(2)} \left( \Omega_{\text{PC},v}^Q \right) \mathbf{D}_{k,n}^{(2)} (\alpha_{\text{CL}}, \beta_{\text{CL}}, 0). \quad (28)$$

Having expressed the Hamiltonian in an appropriate basis, the elements of the  $L$ -matrix in [Equation \(4\)](#) can be determined using the form of [Equation \(1\)](#). Arranging the basis operators according to their order and rank:

$$\left\{ \hat{T}_{-2I}^{2I}, \hat{T}_{-2I+1}^{2I}, \hat{T}_{2I-1}^{-2I+1}, \dots, \hat{T}_{2I}^{2I-1}, \hat{T}_{2I-1}^{2I-1}, \hat{T}_{2I}^{2I} \right\} \quad (29)$$

the  $L$ -matrix for an  $N$ -site jump must be of the form<sup>20</sup>

$$L = \begin{bmatrix} A_1 - (N-1)kE & kE & \dots & kE \\ kE & A_2 - (N-1)kE & \dots & kE \\ \vdots & \vdots & \dots & \vdots \\ kE & kE & kE & A_N - (N-1)kE \end{bmatrix}, \quad (30)$$

where  $E$  is the identity matrix and the entries of  $A_v$  may be calculated as

$$A_v(m, n) = i \langle [\mathbf{O}_{m,v}, H_{\text{tot},v}], \mathbf{O}_{n,v} \rangle, \quad v \in \{1, \dots, N\}; m, n \in \{1, \dots, \text{dim}\}, \quad (31)$$

where  $H_{\text{tot},v}$  denotes the effective Hamiltonian for site  $v$ . It is noted that the  $A_v$ -matrices and thereby the  $L$ -matrix during free precession are block-diagonal consisting of  $1 \times 1, \dots, 2I \times 2I$  matrices as different coherence orders do not mix when no rf-pulses are present. This means that the exponential of the  $L$ -matrix may be evaluated using  $N \times N, \dots, (2N)I \times (2N)I$  dimensional sub-spaces when dynamics is included for an  $N$ -site jump.



One specific sub-matrix,  $L_0$ , operating on the basis operators  $\hat{T}_0^{2I}, \dots, \hat{T}_0^1$  for an N-site jump during free precession can be evaluated analytically because of its high degree of symmetry. That is,

$$L_0 = \begin{bmatrix} -(N-1)kE & \dots & kE \\ kE & -(N-1)kE \dots & kE \\ \vdots & & \\ kE & kE & \dots - (N-1)kE \end{bmatrix}, \quad (32)$$

which means that

$$\exp(L_0 t) = \frac{1}{N} \begin{bmatrix} X_1 & X_2 & \dots & X_2 \\ X_2 & X_1 & \dots & X_2 \\ \vdots & & & \\ X_2 & \dots & X_2 & X_1 \end{bmatrix}, \quad (33)$$

in which

$$X_1 = (1 + (N-1)e^{-Nkt})E, \quad (34)$$

$$X_2 = (1 - e^{-Nkt})E. \quad (35)$$

The signal obtained for a single crystallite corresponding to the orientation  $\Omega_{\text{CR}} = (\alpha_{\text{CR}}, \beta_{\text{CR}}, \gamma_{\text{CR}})$  is calculated using

$$\text{sig}(t, \Omega_{\text{CR}}) = \text{Tr}(I_{+\rho}(t, \Omega_{\text{CR}})). \quad (36)$$

That is, only parts of the density operator containing terms with  $I_-$  contributes to the signal. Noting that  $I_+ = -\sqrt{10}\hat{T}_1^1$  and using that the  $\hat{T}_q^n$  operators form an orthonormal basis only  $\hat{T}_{-1}^1$  contribute to the signal. Taking into account that

$$\hat{T}_{-1}^1 = -(\hat{T}_1^1)^+ \quad (37)$$

$$\begin{aligned} \text{Tr}(I_+ \hat{T}_{-1}^1) &= -\sqrt{10} \text{Tr}(\hat{T}_1^1 \hat{T}_{-1}^1) \\ &= \sqrt{10} \text{Tr}(\hat{T}_1^1 (\hat{T}_1^1)^+) = \sqrt{10}, \end{aligned} \quad (38)$$

the total powder signal for an N-site jump process may be calculated as

$$\text{sig}(t) = \frac{\sqrt{10}}{8\pi^2} \int_0^{2\pi} \int_0^\pi \sum_{v=1}^N m_{-1,v}^1(t, \Omega_{\text{CR}}) d\alpha_{\text{CR}} \sin(\beta_{\text{CR}}) d\beta_{\text{CR}} d\gamma_{\text{CR}}, \quad (39)$$

where  $m_{-1,v}^1(t, \Omega_{\text{CR}})$  denotes the coefficient of  $\hat{T}_{-1}^1$  for the  $v$ th site.

## 2.1. Specifically for spin-1 nuclei

In the case of spin-1 nuclei, an extra term is added to the Hamiltonian: the third-order quadrupolar term,  $H_Q^{(3)}$ .

$$\tilde{H}_Q^{(3)}(t) = \frac{\omega_Q^3}{\omega_0^2} \left( 3R_L^Q(0)R_L^Q(1)R_L^Q(-1) - \sqrt{\frac{3}{8}}(R_L^Q(2)R_L^Q(-1)^2 + R_L^Q(-2)R_L^Q(1)^2) \right) T_0^2. \quad (40)$$

The spatial part of this will be added to  $c$  in Equation (17). For spin-1 nuclei, it is noted that  $\dim = 8$  and that the  $A_v$  matrix during an  $x$ -pulse ( $\theta = 0$ ) is given as

$$A_v = i \begin{bmatrix} 2a_v & b\sqrt{2} & 0 & 0 & 0 & 0 & 0 & 0 \\ b\sqrt{2} & a_v & c_v\sqrt{3/2} & b\sqrt{3} & 0 & 0 & 0 & 0 \\ 0 & c_v\sqrt{3/2} & a_v & 0 & b & 0 & 0 & 0 \\ 0 & b\sqrt{3} & 0 & 0 & 0 & 0 & b\sqrt{3} & 0 \\ 0 & 0 & b & 0 & 0 & b & 0 & 0 \\ 0 & 0 & 0 & 0 & b & -a_v & -c_v\sqrt{3/2} & 0 \\ 0 & 0 & 0 & b\sqrt{3} & 0 & -c_v\sqrt{3/2} & -a_v & b\sqrt{2} \\ 0 & 0 & 0 & 0 & 0 & 0 & b\sqrt{2} & -2a_v \end{bmatrix}. \quad (41)$$

Note that during delays (no rf-field strength) the matrix is block-diagonal consisting of  $1 \times 1$  and  $2 \times 2$  matrices. Therefore, during periods of free precession the corresponding  $L$ -matrix for an  $N$ -site jump process,  $L_d$ , is then readily block-diagonalized into two  $N \times N$  matrices ( $D_1$  having  $T_{-2,v}^2$  as basis operators and  $D_5$  having  $T_{2,v}^2$  as basis operators) and three  $2N \times 2N$  matrices ( $D_2$  having  $\{T_{-1,v}^2, T_{-1,v}^1\}$  as basis operators,  $D_3$  having  $T_{0,v}^k, k=1,2$ , as basis operators and  $D_4$  having  $\{T_{1,v}^2, T_{1,v}^1\}$  as basis operators). The effect of the  $D_3$  matrices is calculated as for general spin-1. Among the remaining matrices, the  $N \times N$  blocks  $D_1$  and  $D_5$  cannot be further block-diagonalized but the two  $2N \times 2N$  blocks,  $D_2, D_4$ , dealing with  $\pm 1Q$  operators can be further block-diagonalized using the following procedure. It is only demonstrated for  $-1Q$  operators but it is noted that

$$\exp(D_4 t) = \exp(D_2 t)^\dagger. \quad (42)$$

The form of the  $D_2$  matrix is

$$D_2 = \begin{bmatrix} B_1 - (N-1)kE & kE & \dots & kE \\ kE & B_2 - (N-1)kE & \dots & kE \\ \vdots & \vdots & \ddots & kE \\ kE & kE & kE & B_N - (N-1)kE \end{bmatrix} \quad (43)$$

in which  $B_v$  are  $2 \times 2$  matrices of the form:

$$B_v = \begin{bmatrix} ia_v & ic_v\sqrt{3/2} \\ ic_v\sqrt{3/2} & ia_v \end{bmatrix}. \quad (44)$$

<sup>†</sup> Complex conjugate.

This matrix may be diagonalized by the matrix:

$$U = U^{-1} = \frac{1}{\sqrt{2}} \begin{bmatrix} 1 & 1 \\ 1 & -1 \end{bmatrix}. \quad (45)$$

The effect of each  $U$  matrix is a change of basis from  $\{T_{-1,v}^2, T_{-1,v}^1\}$  to  $\left\{ (1/\sqrt{2}) (T_{-1,v}^2 + T_{-1,v}^1), (1/\sqrt{2}) (T_{-1,v}^2 - T_{-1,v}^1) \right\}$ . Introducing the block-diagonal  $2N \times 2N$  matrix,  $S_N$ :

$$S_N = \begin{bmatrix} U & 0 & \cdots & 0 \\ \vdots & & & \vdots \\ \vdots & & & \vdots \\ 0 & \cdots & 0 & U \end{bmatrix} \quad (46)$$

the matrix  $L_u = S_N D_2 S_N^{-1}$  can be obtained. Subsequent reordering of the matrix elements in even and odd numbered rows and columns performed by the matrix  $R_N$

$$R_N(i, j) = \begin{cases} 1, & i = 1, \dots, N \quad \text{and} \quad j = 2i - 1, \\ 1, & i = (N + 1), \dots, 2N \quad \text{and} \quad j = 2(i - N), \\ 0, & \text{elsewhere} \end{cases} \quad (47)$$

leads to

$$L_r = R_N S_N D_2 S_N^{-1} R_N^{-1} = \begin{bmatrix} L_p & 0 \\ 0 & L_m \end{bmatrix}, \quad (48)$$

in which

$$L_p = k \cdot \mathbf{1} + \text{diag} \left( i \left( a_v + \left( \sqrt{3/2} \right) c_v \right) - N \cdot k \right), \quad (49)$$

$$L_m = k \cdot \mathbf{1} + \text{diag} \left( i \left( a_v - \left( \sqrt{3/2} \right) c_v \right) - N \cdot k \right), \quad (50)$$

where  $\mathbf{1}$  denotes the  $N \times N$  matrix having 1 in each entry and  $\text{diag}(x_v)$  denotes a diagonal matrix having  $x_v$  in the  $v$ th entry. Hereby only  $N \times N$  matrices need to be diagonalized during delays.

The signal obtained for a single crystallite corresponding to the orientation  $\Omega_{\text{CR}} = (\alpha_{\text{CR}}, \beta_{\text{CR}}, \gamma_{\text{CR}})$  is calculated using:

$$\text{sig}(t, \Omega_{\text{CR}}) = \text{Tr}(I_{+\rho}(t, \Omega_{\text{CR}})). \quad (51)$$

That is, only parts of the density operator containing terms with  $L_-$  contributes to the signal. Noting that  $I_{+} = -\sqrt{10} \hat{T}_1^1$  and using that the  $\hat{T}_q^n$  operators form an orthonormal basis only  $\hat{T}_{-1}^1$  contribute to the signal. The total powder signal for an N-site jump process is therefore calculated as

$$\text{sig}(t) = \frac{\sqrt{10}}{8\pi^2} \int_0^{2\pi} \int_0^{\pi} \int_0^{2\pi} \sum_{v=1}^N m_{-1,v}^1(t, \Omega_{\text{CR}}) d\alpha_{\text{CR}} \sin(\beta_{\text{CR}}) d\beta_{\text{CR}} d\gamma_{\text{CR}}, \quad (52)$$

where  $m_{-1,v}^{-1}(t, \Omega_{\text{CR}})$  denotes the coefficient of  $\hat{T}_{-1}^1$  for the  $v$ th site. Focusing on the final signal, the coefficient vector  $\vec{m}$  may be transformed into the new basis and separated according to the  $L_p$  and  $L_m$  matrices. That is,

$$\vec{u} = \begin{pmatrix} \frac{1}{\sqrt{2}}(m_{-1,v}^2 + m_{-1,v}^1) \\ \frac{1}{\sqrt{2}}(m_{-1,v}^2 - m_{-1,v}^1) \end{pmatrix} = \begin{pmatrix} u_{p,v} \\ u_{m,v} \end{pmatrix}. \quad (53)$$

Hereby the signal,  $\text{sig}(t)$ , is defined as

$$\text{sig}(t) = \frac{\sqrt{5}}{8\pi^2} \int_0^{2\pi} \int_0^{2\pi} \int_0^{2\pi} \sum_{v=1}^N (u_{p,v}(t, \Omega_{\text{CR}}) - u_{m,v}(t, \Omega_{\text{CR}})) d\alpha_{\text{CR}} \sin(\beta_{\text{CR}}) d\beta_{\text{CR}} d\gamma_{\text{CR}}. \quad (54)$$

For detection of double quantum (DQ) coherence, it is the coefficients of  $\hat{T}_{-2}^2$  that are of interest.

## 2.2. Two-axis jump processes

The approach described above may be extended to 2-by-2-site jumps or 2-by-3-site jump as observed for  $^2\text{H}$  in, for example, thiourea- $d_4$  or DMS- $d_6$ . From a computational point of view, these two jump processes resembles the 4-site and 6-site jump processes, respectively, regarding matrix dimensions, but the presence of two rate constants  $k_1$  and  $k_2$  complicates matters. So far only single axis jump processes have been described. In order to generalize to multi-axis processes the following example may be useful. A more comprehensive description of such processes may be found in the work of Kristensen et al.<sup>30,52</sup>

## 2.3. 2-by-2-site jump

In this case a two-axis jump process is studied. The two-site jump around the first axis is characterized by a rate constant  $k$ , whereas the rate constant for the jump around the second axis is  $k'$ . During free precession only the  $+1Q$  coherence is of interest and therefore the matrix of interest is

$$L_d = \begin{bmatrix} ia_1 - k'' & ic_1\sqrt{3/2} & k' & 0 & k & 0 & 0 & 0 \\ ic_1\sqrt{3/2} & ia_1 - k'' & 0 & k' & 0 & k & 0 & 0 \\ k' & 0 & ia_2 - k'' & ic_2\sqrt{3/2} & 0 & 0 & k & 0 \\ 0 & k' & ic_2\sqrt{3/2} & ia_2 - k'' & 0 & 0 & 0 & k \\ k & 0 & 0 & 0 & ia_3 - k'' & ic_3\sqrt{3/2} & k' & 0 \\ 0 & k & 0 & 0 & ic_3\sqrt{3/2} & ia_3 - k'' & 0 & k' \\ 0 & 0 & k & 0 & k' & 0 & ia_4 - k'' & ic_4\sqrt{3/2} \\ 0 & 0 & 0 & k & 0 & k' & ic_4\sqrt{3/2} & ia_4 - k'' \end{bmatrix} \quad (55)$$

in which  $k'' = k + k'$  This matrix can be block-diagonalized using the  $S_4$  and  $R_4$ -matrices:

$$L_r = R_4 S_4 L_d S_4^{-1} R_4^{-1} = \begin{bmatrix} im_1^+ - k'' & k' & k & 0 & 0 & 0 & 0 & 0 & 0 \\ k' & im_2^+ - k'' & 0 & k & 0 & 0 & 0 & 0 & 0 \\ k & 0 & im_3^+ - k'' & k' & 0 & 0 & 0 & 0 & 0 \\ 0 & k & k' & im_4^+ - k'' & 0 & 0 & 0 & 0 & 0 \\ 0 & 0 & 0 & 0 & im_1^- - k'' & k' & k & 0 & 0 \\ 0 & 0 & 0 & 0 & k' & im_2^- - k'' & 0 & k & k \\ 0 & 0 & 0 & 0 & k & 0 & im_3^- - k'' & k' & k' \\ 0 & 0 & 0 & 0 & 0 & k & k' & im_4^- - k'' & 0 \end{bmatrix}, \quad (56)$$

where  $m_j^+ = a_j + c_j\sqrt{3/2}$  and  $m_j^- = a_j - c_j\sqrt{3/2}$ .

## 2.4. 2-by-3-site jump

Likewise the  $L$ -matrix for a two-axis jump process performing a three-site jump around one axis and followed by a two-site jump around the other axis having rate constants  $k_2$  and  $k_3$ , respectively, is then defined as

$$L = \begin{bmatrix} A_1 - (k_2 + 2k_3)E & k_3E & k_3E & k_2E & 0 & 0 \\ k_3E & A_2 - (k_2 + 2k_3)E & k_3E & 0 & k_2E & 0 \\ k_3E & k_3E & A_3 - (k_2 + 2k_3)E & 0 & 0 & k_2E \\ k_2E & 0 & 0 & A_4 - (k_2 + 2k_3)E & k_3E & k_3E \\ 0 & k_2E & 0 & k_3E & A_5 - (k_2 + 2k_3)E & k_3E \\ 0 & 0 & k_2E & k_3E & k_3E & A_6 - (k_2 + 2k_3)E \end{bmatrix}.$$

The example illustrates, for example, two rotating methyl groups undergoing a two-site jump—as in dimethyl sulfone. Grouping the six deuterons as 1, 2 and 3 on the first carbon and 4, 5, and 6 on the second carbon, the  $A_j$  matrices are calculated for the combined rotation in the three-site jump and the two-site jump.

As for the 2-by-2-site jump, the  $L_r$ -matrix for a 2-by-3-site jump process (such as for DMS- $d_6$ ) can be determined to be

$$L_r = \begin{bmatrix} im_1^+ - k_s & k_3 & k_3 & k_2 & 0 & 0 & 0 & 0 & 0 & 0 & 0 & 0 \\ k_3 & im_2^+ - k_s & k_3 & 0 & k_2 & 0 & 0 & 0 & 0 & 0 & 0 & 0 \\ k_3 & k_3 & im_3^+ - k_s & 0 & 0 & k_2 & 0 & 0 & 0 & 0 & 0 & 0 \\ k_2 & 0 & 0 & im_4^+ - k_s & k_3 & k_3 & 0 & 0 & 0 & 0 & 0 & 0 \\ 0 & k_2 & 0 & k_3 & im_5^+ - k_s & k_3 & 0 & 0 & 0 & 0 & 0 & 0 \\ 0 & 0 & k_2 & k_3 & k_3 & im_6^+ - k_s & 0 & 0 & 0 & 0 & 0 & 0 \\ 0 & 0 & 0 & 0 & 0 & 0 & im_1^- - k_s & k_3 & k_2 & 0 & 0 & 0 \\ 0 & 0 & 0 & 0 & 0 & 0 & k_3 & im_2^- - k_s & k_3 & 0 & k_2 & 0 \\ 0 & 0 & 0 & 0 & 0 & 0 & k_3 & k_3 & im_3^- - k_s & 0 & 0 & k_2 \\ 0 & 0 & 0 & 0 & 0 & 0 & k_2 & 0 & 0 & im_4^- - k_s & k_3 & k_3 \\ 0 & 0 & 0 & 0 & 0 & 0 & 0 & k_2 & k_3 & im_5^- - k_s & k_3 & k_3 \\ 0 & 0 & 0 & 0 & 0 & 0 & 0 & 0 & k_2 & k_3 & im_6^- - k_s & k_3 \end{bmatrix},$$

where  $k_s = k_2 + 2k_3$ ,  $m_j^+ = a_j + c_j\sqrt{3/2}$  and  $m_j^- = a_j - c_j\sqrt{3/2}$ .

### 2.4.1. Evolution of 0Q coherence

For jump processes around a single axis, a quite nice expression for the matrix associated with evolution of zero-quantum coherence is obtained. In the case of  $2 \times 3$ -site jump process, the corresponding  $L_0$  matrix is given by

$$L_0 = \begin{bmatrix} -k_s & 0 & k_3 & 0 & k_3 & 0 & k_2 & 0 & 0 & 0 & 0 & 0 \\ 0 & -k_s & 0 & k_3 & 0 & k_3 & 0 & k_2 & 0 & 0 & 0 & 0 \\ k_3 & 0 & -k_s & 0 & k_3 & 0 & 0 & 0 & k_2 & 0 & 0 & 0 \\ 0 & k_3 & 0 & -k_s & 0 & k_3 & 0 & 0 & 0 & k_2 & 0 & 0 \\ k_3 & 0 & k_3 & 0 & -k_s & 0 & 0 & 0 & 0 & 0 & k_2 & 0 \\ 0 & k_3 & 0 & k_3 & 0 & -k_s & 0 & 0 & 0 & 0 & 0 & k_2 \\ k_2 & 0 & 0 & 0 & 0 & 0 & -k_s & 0 & k_3 & 0 & k_3 & 0 \\ 0 & k_2 & 0 & 0 & 0 & 0 & 0 & -k_s & 0 & k_3 & 0 & k_3 \\ 0 & 0 & k_2 & 0 & 0 & 0 & k_3 & 0 & -k_s & 0 & k_3 & 0 \\ 0 & 0 & 0 & k_2 & 0 & 0 & 0 & k_3 & 0 & -k_s & 0 & k_3 \\ 0 & 0 & 0 & 0 & k_2 & 0 & k_3 & 0 & k_3 & 0 & -k_s & 0 \\ 0 & 0 & 0 & 0 & 0 & k_2 & 0 & k_3 & 0 & k_3 & 0 & -k_s \end{bmatrix}. \quad (57)$$

By rearranging elements corresponding to  $\{T_{0,v}^2 \text{ and } T_{0,v}^1\}, v \in \{1, \dots, 6\}$  respectively, leads to the following block-diagonal matrix:

$$L_{d0} = \begin{bmatrix} M_1 & 0 \\ 0 & M_1 \end{bmatrix}, \quad (58)$$

where

$$M_1 = \begin{bmatrix} -k_s & k_3 & k_3 & k_2 & 0 & 0 \\ k_3 & -k_s & k_3 & 0 & k_2 & 0 \\ k_3 & k_3 & -k_s & 0 & 0 & k_2 \\ k_2 & 0 & 0 & -k_s & k_3 & k_3 \\ 0 & k_2 & 0 & k_3 & -k_s & k_3 \\ 0 & 0 & k_2 & k_3 & k_3 & -k_s \end{bmatrix}. \quad (59)$$

It is noted that the  $M_1$ -matrix can be further diagonalized by the matrix

$$U_3 = \frac{1}{2} \begin{bmatrix} E & E \\ E & -E \end{bmatrix}. \quad (60)$$

Hereby

$$M_b = U_3 M_1 U_3^{-1} = \begin{bmatrix} -2k_3 & k_3 & k_3 & 0 & 0 & 0 \\ k_3 & -2k_3 & k_3 & 0 & 0 & 0 \\ k_3 & k_3 & -2k_3 & 0 & 0 & 0 \\ 0 & 0 & 0 & -2(k_2 + k_3) & k_3 & k_3 \\ 0 & 0 & 0 & k_3 & -2(k_2 + k_3) & k_3 \\ 0 & 0 & 0 & k_3 & k_3 & -2(k_2 + k_3) \end{bmatrix}. \quad (61)$$

Note that these two blocks are of the form  $k_3 \mathbf{1} + k_d E$ , where  $k_d$  denotes a linear combination of the rate constants. When calculating the exponential of such a matrix, it is worth noticing that  $\mathbf{1}$  and  $E$  commute and furthermore that

$$\exp(k_3 t \mathbf{1}) = E + \frac{1}{m} (\exp(m k_3 t) - 1) \mathbf{1}, \quad (62)$$

where  $m$  denotes the dimension of the  $\mathbf{1}$ - and  $E$ -matrices.

### 3. NUMERICAL SIMULATIONS

All calculations were performed on a Dell Inspiron 8200 (Laptop) equipped with a 2.0 GHz Pentium IV processor using homemade Fortran 77 programs. The programs employ the *zgeev*-routine from the LAPACK-package<sup>74</sup> for diagonalization and determination of eigenvalues and eigenvectors of matrices with complex entries.

All calculated spectra employ  $\delta_{\text{iso}} = 0.0$  ppm and the simulation parameters are displayed in Table 1. For an  $N$ -site jump around a single axis, the Euler angles for the  $v$ th site were defined by the orientations  $\Omega_{\text{PC},v}^Q = (0, \pi/3, v(2\pi/N))$ ,  $v = 0, \dots, (N-1)$ . In the maximum intensity plots, the intensities were normalized relative to a dynamic process corresponding to  $k = 10^6$  Hz.

**TABLE 1** Parameters for simulations

Data set	Nucleus	$C_Q$ (kHz)	$\eta_Q$	$\tau_2$ ( $\mu\text{s}$ )	$\tau_4$ ( $\mu\text{s}$ )	$\tau_d$ ( $\mu\text{s}$ )	$M^a$	dw ( $\mu\text{s}$ )	$\nu_{\text{rf}}$ (kHz)	$\Delta\nu^b$ (kHz)
P1	$^6\text{Li}$	30	0.1	32.5	32.5	400	100	2.0	50	2.0
P2	$^2\text{H}$	200	0.1	30.5	30.5	400	200	2.0	250	5.0
P2b	$^2\text{H}$	200	0.1	30.5	30.5	200	200	2.0	250	10.0
P3	$^{14}\text{N}$	500	0.1	30.4	30.0	100	200	0.5	250	10.0
P4	$^{14}\text{N}$	750	0.25					0.4		10.0
P5	$^{14}\text{N}$	1000	0.25					0.4	40	10.0
P6	$^{14}\text{N}$	1200	0.25					33.3		30.0
P7	$^{14}\text{N}$	2400	0.25					33.3		30.0
P8	$^{14}\text{N}$	3600	0.25					33.3		30.0
P9 <sup>c</sup>	$^{133}\text{Cs}$	225	0.47					5.0		2.0
P10	$^{23}\text{Na}$	337	0.10					1.0		4.0
P11a	$^{39}\text{K}$	2.0	0.50	100	100	1000	40	5.0	31.25	1.0
P11b	$^{39}\text{K}$	2.0	0.50					0.33		20.0
P11c	$^{39}\text{K}$	2.0	0.50	50	46	500	20	5.0	31.25	1.0 (20.0)

<sup>a</sup>  $M$  is the number of repeating units in the QCPMG experiment.

<sup>b</sup>  $\Delta\nu = \Delta\nu_a$  (spin-echo sideband separation in QCPMG)  $= \nu_r$  (MAS spin-rate). Except for parameter set P11c. In this case,  $\Delta\nu_a = 1.0$  kHz and  $\nu_r = 20.0$  kHz.

<sup>c</sup> CSA-parameters:  $\delta_{\text{iso}} = -225$  ppm,  $\delta_\sigma = -90$  ppm,  $\eta_\sigma = 0.44$ ,  $\Omega_{\text{PC}}^\sigma = (90, 23, 90)$ .

### 3.1. Spin-1 nuclei

The simulated spectra are calculated for three spin-1 nuclei having Larmor frequencies of 43.34, 73.580 and 76.753 MHz corresponding to  $^{14}\text{N}$  at 14.1 T and  $^6\text{Li}$  and  $^2\text{H}$  at 11.7 T, respectively.

Two experiments were explored: the single-pulse MAS and the QCPMG experiment. The latter may be presented as

$$(\pi/2)_0 - \tau_1 - (\pi/2)_{\pi/2} - \tau_2 - \text{Acq.}(\tau_a/2) - \left[ \tau_3 - (\pi/2)_{\pi/2} - \tau_4 - \text{Acq.}(\tau_a) \right]^M - \text{Acq.}(\tau_d),$$

where  $(\phi)_\theta$  denotes a  $\phi$ -pulse with phase  $\theta$ ,  $\tau_j$  a delay and  $\text{Acq.}(\tau)$  acquisition during a period  $\tau$ . It is noted that the spin-echo sideband separation is calculated as  $\Delta\nu_a = \tau_a^{-1}$ . All QCPMG spectra are calculated using  $\tau_1 = \tau_3 = 30.0 \mu\text{s}$  employing real pulses.

The  $^6\text{Li}$  and  $^2\text{H}$  single-pulse MAS FIDs have been calculated using ideal excitation and 20,250 data points whereas 32,800 data points were calculated for the  $^{14}\text{N}$  FIDs using parameter sets P3–P5 and 60,000 data points for parameter sets P6–P8. It should be noted that different dwell times have been used for different magnitudes of  $C_Q$  in order to comply with piecewise constant Hamiltonians during each time increment. For the same reason, the FIDs corresponding to rotor-synchronized acquisition are simply generated from the standard FIDs by extracting the rotor echoes only. Unless stated otherwise in the figure captions, the FIDs have been apodized by Gaussian line broadening of 50 Hz prior to Fourier transformation.

Powder averaging was obtained by using 6765  $(\alpha_{\text{CR}}, \beta_{\text{CR}})$  angle-pairs according to the Zaremba scheme<sup>75</sup> for the QCPMG and the rotor-synchronized  $^{14}\text{N}$  MAS FIDs using parameter set P6 whereas 28,657 (single quantum (SQ) coherences) or 75,025 (DQ coherences) Zaremba angle-pairs were utilized for calculation of rotor-synchronized FIDs for parameter sets P7 and P8. For the MAS spectra with full spinning sideband manifold, 610 Zaremba  $(\alpha_{\text{CR}}, \beta_{\text{CR}})$  angle-pairs and 19 equidistantly distributed  $\gamma_{\text{CR}}$ -angles were employed for the  $^2\text{H}$  and  $^6\text{Li}$  MAS calculations. The corresponding  $^{14}\text{N}$  MAS spectra used 987  $(\alpha_{\text{CR}}, \beta_{\text{CR}})$  angle-pairs and 37  $\gamma_{\text{CR}}$ -angles.

Computation times for  $^{14}\text{N}$  FIDs employing parameter set P3 and  $k=10^0$  Hz varied between 2.41 min (two-site jump, QCPMG) and 12.6 min (six-site jump, QCPMG) for the calculation of a static QCPMG FIDs. The computation time for an MAS FID with ideal excitation was 14 min for a two-site jump and 83 min for a six-site jump. In these calculations, the density operator was set to  $-I_y$  when acquisition begins. Calculations of the rotor-synchronized  $^{14}\text{N}$  SQ- and DQ-FIDs corresponding to parameter set P7 required 20 and 32 min, respectively.

### 3.2. Half-integer quadrupolar nuclei

Calculations were performed for nuclei having spins of 3/2, and 7/2. The Larmor frequencies were 23.325, 105.8 ( $I=3/2$ ), and 52.45 ( $I=7/2$ ) MHz. This corresponds to  $^{39}\text{K}$  at 11.74 T and  $^{23}\text{Na}$  and  $^{133}\text{Cs}$  at 9.4 T.



The QCPMG/QCPMG–MAS pulse sequence may be depicted as

$$(\pi/2)_0 - \tau_1 - (\pi)_{\pi/2} - \tau_2 - \text{Acq.}(\tau_a/2) - [\tau_3 - (\pi) - \tau_4 - \text{Acq.}(\tau_a)]^M - \text{Acq.}(\tau_d),$$

where  $(\phi)$  denotes a central transition selective  $\phi$ -pulse,  $\tau_j$  a delay and  $\text{Acq.}(\tau)$  acquisition during a period  $\tau$ . For QCPMG–MAS, the condition  $2pT_r = \tau_3 + \tau_4 + t_\pi + \tau_a$ , where  $p$  is an integer,  $t_\pi$  is the duration of a selective  $\pi$ -pulse, and  $T_r$  the rotor period, must be fulfilled.

Based on the previously observed significant effect of finite rf-pulses in QCPMG<sup>24</sup> and QCPMG–MAS<sup>71</sup> spectra, this effect is included in all calculations. The rf-field strengths were all in the central transition selective regime using the condition  $(2\pi C_Q)/(4I(2I-1)|\omega_{\text{rf}}|) > 3$ . This means that the nominal pulse widths were divided by  $(I+1/2)$ .

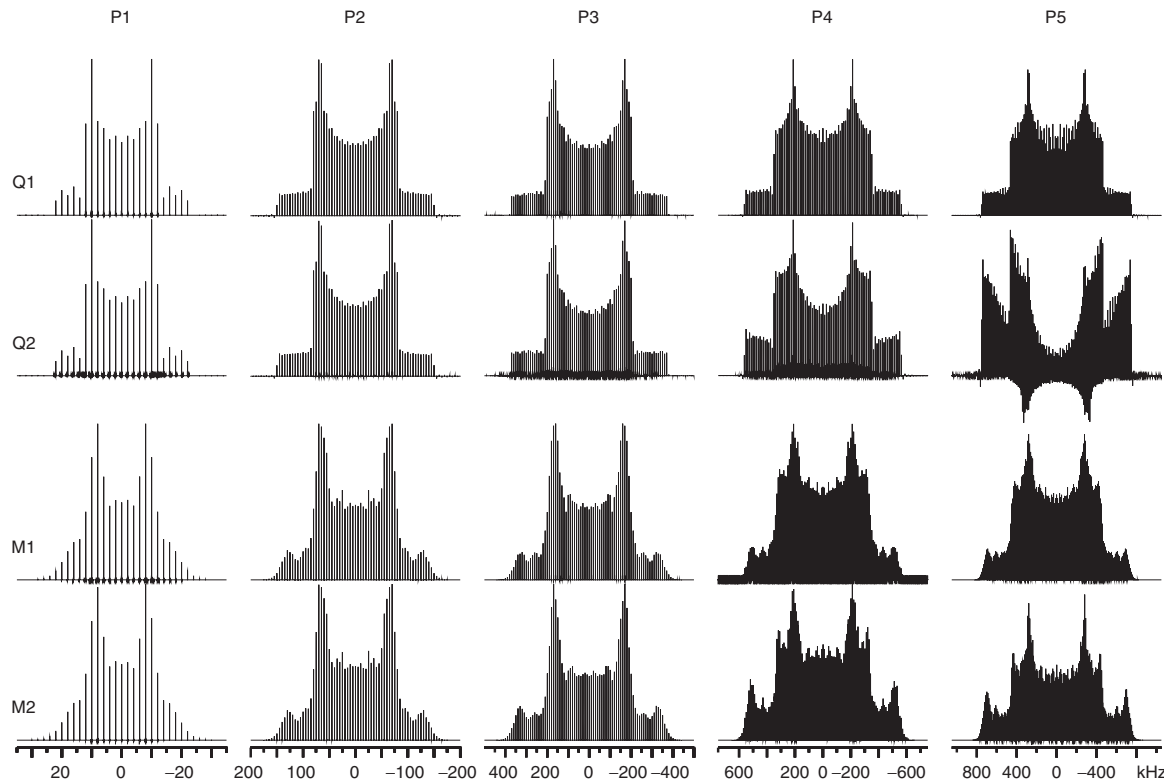
Powder averaging was obtained by using 6765  $(\alpha_{\text{CR}}, \beta_{\text{CR}})$  angle-pairs according to the Zaremba scheme<sup>75</sup> for the static spectra whereas 610 Zaremba  $(\alpha_{\text{CR}}, \beta_{\text{CR}})$  angle-pairs and 20 equidistantly distributed  $\gamma_{\text{CR}}$ -angles were employed for the QCPMG–MAS calculations. The single-pulse MAS (ideal excitation) spectra for <sup>23</sup>Na and <sup>133</sup>Cs were calculated using 610 Zaremba  $(\alpha_{\text{CR}}, \beta_{\text{CR}})$  angle-pairs and 19 equidistantly distributed  $\gamma_{\text{CR}}$ -angles whereas 4181 Zaremba  $(\alpha_{\text{CR}}, \beta_{\text{CR}})$  angle-pairs and 19  $\gamma_{\text{CR}}$ -angles were used for the <sup>39</sup>K spectra.

Processing times were 2.5 min (two-site jump,  $I=3/2$ ) for the calculation of a static QCPMG FID whereas 2119 min were required for a QCPMG–MAS FID (two-site jump,  $I=3/2$ ). For comparison, an ideal single-pulse MAS FID with 32,000 complex points using parameter set P10 required 19 min, an FID with 16,000 complex points employing parameter set P9 used 67 min and an FID with 32,000 complex points employing parameter set P11b required 103 min. The significantly longer processing time for the QCPMG–MAS calculation compared to a static QCPMG calculation is in part caused by the fact that the numerical integration needs to be performed for three Euler angles instead of two for a static. More importantly, the non-diagonal entries in the Hamiltonian during delays demand for time-ordered propagation in these periods which includes a diagonalization for each time increment whereas only one diagonalization is required for each delay in the static case.

## 4. RESULTS AND DISCUSSION

### 4.1. Spin-1 nuclei

In Figure 1, a series of calculated MAS (rows M1 and M2) and QCPMG (rows Q1 and Q2) spectra employing various magnitudes of  $C_Q$  corresponding to parameter sets P1–P5 in Table 1 and different effective Hamiltonians are displayed. In rows Q2 and M2, the EFG-interaction is included up to second order whereas only the first-order term is included for rows Q1 and M1. No differences are observed for typical <sup>6</sup>Li and <sup>2</sup>H parameters as displayed in the first two columns but in the third column representing a <sup>14</sup>N-site with a  $C_Q$  of 500 kHz minor intensity differences are observed between the MAS spectra beyond  $\pm 300$  kHz. Differences are



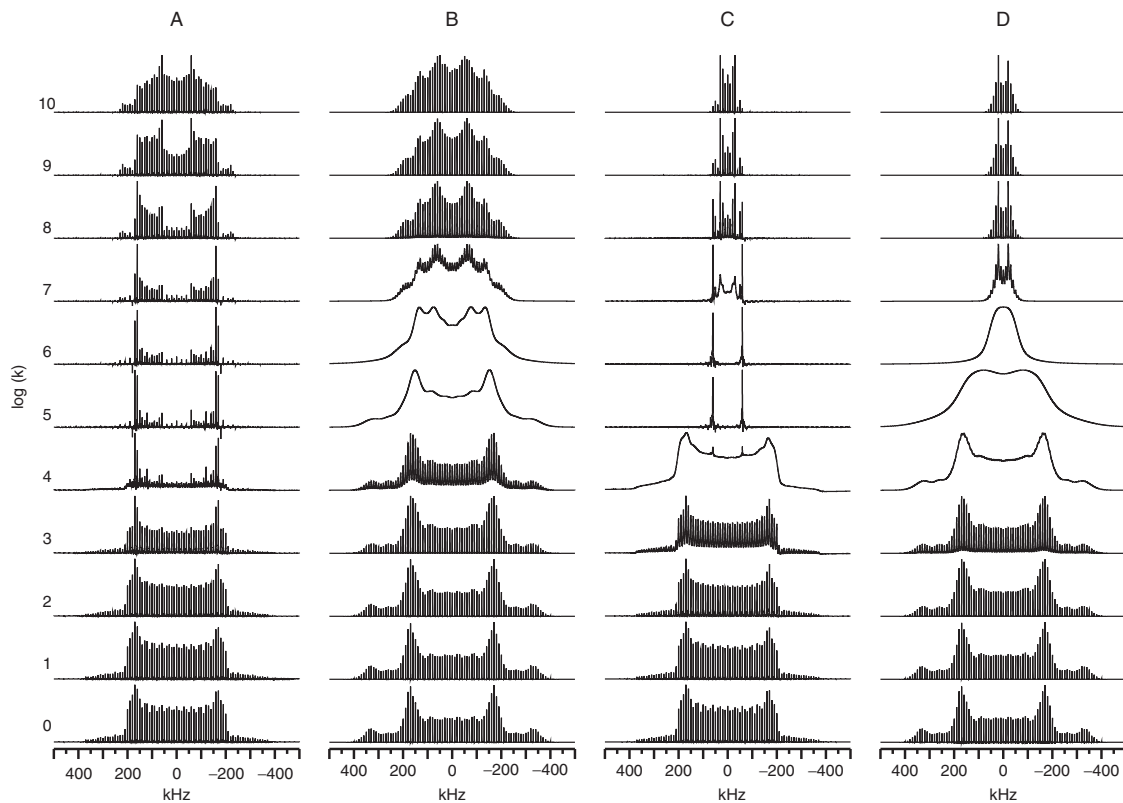
**Figure 1** Simulated MAS (rows M1 and M2) and QCPMG (rows Q1 and Q2) spectra corresponding to the static limit ( $k=10^{-9}$  Hz) of a two-site jump process corresponding to parameter sets P1–P5 in [Table 1](#). In rows Q1 and M1, the Hamiltonian includes the only  $H_Q^{(1)}$  whereas both  $H_Q^{(1)}$  and  $H_Q^{(2)}$  are included for the spectra in rows Q2 and M2. Gaussian line broadenings of 30 (A), 50 (B) or 75 (C–E) Hz were applied prior to Fourier transformation.

also observed in the QCPMG spectra. In between the real QCPMG peaks separated by integral multiples of  $1/\tau_a$  from the transmitter position some additional small peaks out-of-phase with the ordinary spin-echo sidebands are present. These effects become more pronounced for larger  $C_Q$ s and their intensity at higher frequencies increases in the QCPMG spectra. For  $C_Q$  of 1.0 MHz (column P5), it is still possible to phase the MAS spectra whereas the effect of the second-order quadrupolar Hamiltonian makes it impossible to produce in-phase QCPMG spectra. The reason for this is the lack of a common refocusing pulse for first and second-order terms in the Hamiltonian.

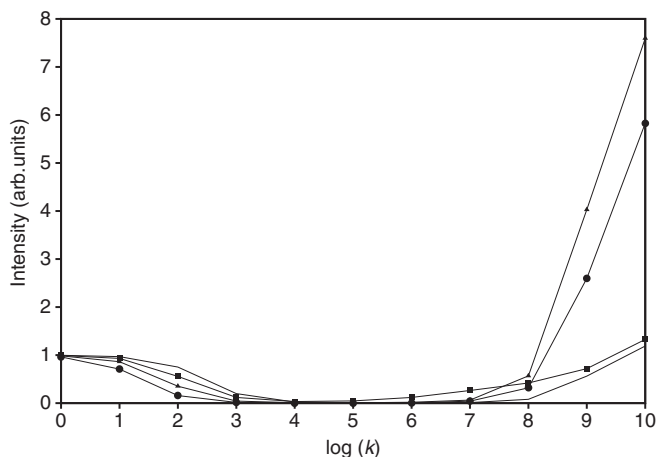
From these results, it is evident that QCPMG experiments may be performed when the second-order quadrupolar effect is adequately small. In the present calculations, the  $C_Q$ -limit for the QCPMG spectra is around 750 kHz at 14.1 T but this limit is of course higher at higher magnetic field strengths.

Recently, there has been a great interest in exploring  $^{14}\text{N}$  in inorganic, organic and biochemical environments. Apart from a high natural abundance, this nucleus is characterized by a low Larmor frequency and a relatively large quadrupolar moment which makes it a challenge to work with from an NMR point of view. In order to compare the spectra produced by either QCPMG or single-pulse MAS experiments, simulated spectra of a  $^{14}\text{N}$ -site having parameters corresponding to parameter set P3 are displayed in Figure 2. In Figure 2, the calculated QCPMG spectra in column A correspond to a two-site jump process whereas the spectra in column C are due to a six-site jump process. Comparing columns A and C, an efficient narrowing of the width of the overall lineshape in column C is clearly seen at faster jump rates whereas major changes in the overall lineshape except for the width are observed in column A. This is in good agreement with results obtained previously<sup>2,76</sup> stating that the motional averaged quadrupole coupling constant,  $C_Q$ , for three-site or higher order jump processes in the fast limit is  $\bar{C}_Q = C_Q(1/2)(3\cos^2(\beta_{\text{PC},v}^Q) - 1)$ . It is noted that the average is zero if  $\beta_{\text{PC},v}^Q$  is the magic angle. In addition, severe broadening of the spin-echo sidebands is observed for  $k=10^4$  Hz in column C that almost collapses into a lineshape.

The MAS spectra in Figure 2 are calculated for a two-site jump (column B) and a six-site jump (column D). Significant spectral differences are observed when comparing columns B and D corresponding to a two- and six-site jump process, respectively. In column B, the spinning sideband manifold is collapsed into a lineshape for  $k=10^5$ – $10^6$  Hz whereas the severe motional broadening is observed in the range  $k=10^4$ – $10^6$  Hz for the six-site jump in column D. Besides this effect, a more pronounced overall line narrowing effect is observed as in the QCPMG spectra (columns A and C). Comparing the effects of dynamics as evaluated by QCPMG or MAS experiments both experiments are subjected to line broadening of either spin-echo sidebands or spinning sidebands. Moreover an overall change in lineshape due to averaging of the EFG-tensor is observed. While the latter effect is similar for the two experiments, the line broadening effect of the spinning sidebands in the MAS is more pronounced than for the spin-echo sidebands in the QCPMG experiments. This means that the line broadening effect is more efficiently induced by modulation of the spatial part of the Hamiltonian than by modulation of the spin-part of the Hamiltonian.



**Figure 2** Simulated  $^{14}\text{N}$  (43.34 MHz) QCPMG spectra corresponding to a two-site jump process (column A) or a six-site jump process (column C) and MAS spectra corresponding to a two-site jump process (column B) or a six-site jump process (column D). All simulations employed parameter set P3 in [Table 1](#). The logarithm of the rate constant  $k$  is indicated at each row of spectra.



**Figure 3** Maximum intensity as a function of  $\log(k)$  for simulated  $^{14}\text{N}$  (43.34 MHz) spectra using parameter set P3. The intensity profile for a two-site jump is shown by a solid line for the MAS experiments and by squares for the QCPMG experiments. For the six-site jump process, the triangles correspond to the intensity profile for the MAS experiment and the filled circles for the QCPMG experiment.

The intensity profiles displayed in Figure 3 illustrate the effect of two- and six-site jump processes for either MAS or QCPMG experiments. In case of the two-site jump process, no significant gain is obtained at higher jump rates whereas intensity gains by 5.8 (QCPMG) and 7.6 (MAS) are observed for the six-site jump. However, the intensity of the spectra in the intermediate regime is lower for the higher order processes. The higher intensity gain in the MAS spectra reflects that the line narrowing effect due to fast dynamics not only narrows the overall line-shape but also the individual spinning sidebands.

#### 4.2. Dynamic effects in $^{14}\text{N}$ MAS spectra by SQ or DQ coherences

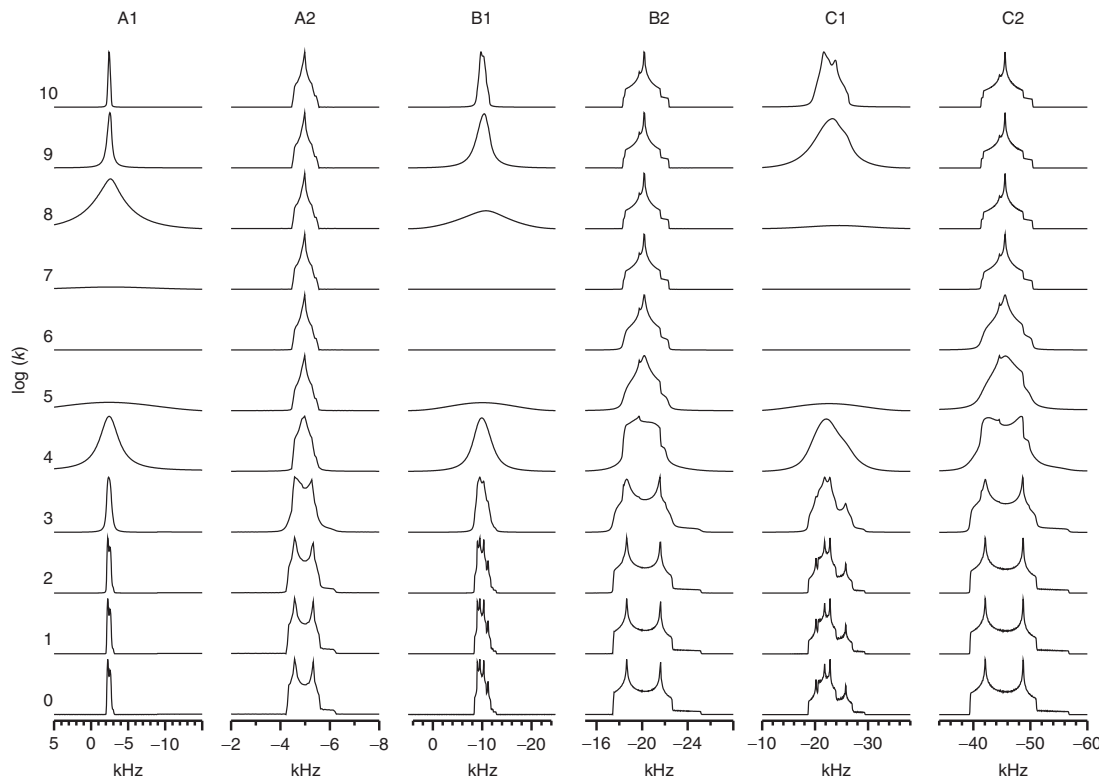
For half-integer quadrupolar nuclei, the effect of dynamics may be probed by analysis of the central transition.<sup>61–64,70</sup> This transition is not influenced by the first-order quadrupolar interaction but only by the second-order quadrupolar interaction. Studies of this transition are not an option for nuclei having integer spin-quantum numbers but the second-order quadrupolar interaction may be studied by rotor-synchronized acquisition of MAS spectra as the first-order quadrupolar interaction is averaged out whereas the centerband is influenced by the second-order quadrupolar interaction and the CSA. Recently a whole range of correlation experiments involving  $^{14}\text{N}$  have been suggested. Such experiments pave the way for NMR analysis of proteins having all isotopes present in natural abundance. Among these experiments are the  $^1\text{H}/^{13}\text{C}$ - $^{14}\text{N}$  HMQC experiments<sup>47–50</sup> in which DQ  $^{14}\text{N}$  coherence is correlated with SQ coherence of either H or C in proteins. One benefit of choosing the DQ transition is that this is not affected by

the first-order quadrupole Hamiltonian. Similar to the central transition in half-integer quadrupolar nuclei. In sulfa drugs,  $C_Q$ s ranging from 2.2 to 4.4 MHz were reported<sup>77</sup> and for polypeptides and thiourea  $C_Q$ s around 3 MHz were obtained.<sup>47,78</sup> In order to explore  $^{14}\text{N}$  MAS as a general tool for dynamic studies of such sites a series of simulations corresponding to parameter sets P6–P8 in Table 1 were performed. Acquisition of the full spinning sideband manifold for a site having parameter sets P7 and P8 would be prohibited by the  $Q$  of most NMR probes and therefore the focus is on rotor-synchronized acquisition. Rotor-synchronized MAS spectra for  $^{14}\text{N}$  corresponding to a two-site jump process employing parameter sets P6–P8 observing either SQ or DQ coherences are displayed in Figure 4 columns A1, B1 and C1 (SQ coherence) and A2, B2, and C2 (DQ coherence), respectively. Similar effects of molecular dynamics on the SQ coherence are observed for all parameter sets. Starting from the slow motion limit, a line broadening effect sets in when the dynamic process becomes faster, then an intermediate regime with zero intensity spectra is reached and hereafter the line-shape starts narrowing due to faster dynamics. From these spectra, it is evident that the intermediate region is a function of the magnitude of  $C_Q$  and that this region becomes broader when  $C_Q$  is increased. For parameter set P6, three ‘zero intensity’ spectra for  $k=10^5$ – $10^7$  Hz are obtained whereas four of such spectra for  $k=10^5$ – $10^8$  Hz are present for parameter set P8. The effect of the second-order quadrupolar shift ( $\text{SOQE} = (C_Q^2/40\nu_0)(1 + (\eta_Q^2/3))$ ) is also very prominent. For the spectra of the corresponding DQ coherences, the effect of dynamics is quite different. Starting from slow dynamics, a slight line broadening sets in at  $k=10^2$  (P6) or  $10^3$  (P7,P8) Hz followed by a change in lineshape occurs in the intermediate regime  $k=10^3$ – $10^5$  (P6) or  $k=10^3$ – $10^7$  (P7,P8) Hz. No further changes in the line-shape appear at faster jump rates. In Figure 5A, the intensity profile for the SQ coherences is presented whereas the profiles for the DQ coherences are displayed in Figure 5B. The profiles are significantly different. While the intensity of the SQ coherences exhibits a broad minimum in the regime  $k=10^5$ – $10^8$  Hz, the intensity profile of the DQ coherences is of almost sigmoidal shape with a slight intensity decrease in the regime between start and end level. It is seen that the DQ-spectra are not broadened beyond detection at any rate for the two-site jump and that the most significant motional effects take place in the regime  $10^3$ – $10^7$  Hz. This actually makes DQ-correlated  $^{14}\text{N}$  experiments more attractive than SQ-correlated experiments as the line broadening effects are much more shallow and it is possible to follow the dynamic process through several orders of magnitude.

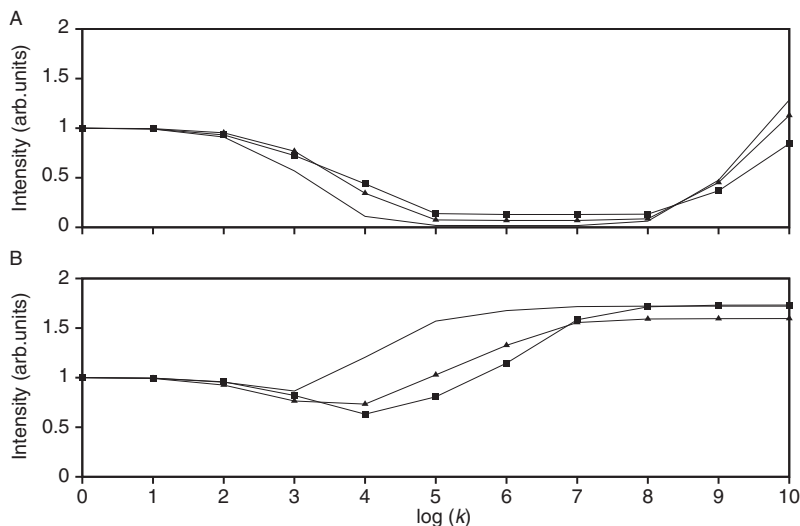
It should be noted that the DQ-spectra presented here are obtained assuming ideal excitation. To accurately simulate the DQ projections from the HMQC experiments, real time rf-pulses should be included and the calculations should be performed for the indirect dimension of the HMQC sequence.

### 4.3. Multi-axis jump processes

Jumps around multiple axes are of course more complex to deal with than rotations around just one axis. A number of studies were performed on such systems.<sup>30,33,51</sup> Presently, a comparison of the  $^2\text{H}$  single-pulse MAS (ideal excitation) and the



**Figure 4** Simulated  $^{14}\text{N}$  (43.34 MHz) rotor-synchronized MAS spectra corresponding to a two-site jump process and detection of either single-quantum (columns A1, B1, C1) or double-quantum coherence (columns A2, B2, C2). The spectra in columns A (A1,A2) are calculated using parameter set P6, whereas parameter sets P7 and P8 are used for columns B (B1, B2) and C (C1, C2), respectively. Gaussian line broadenings of 75 (A1, B1, C1), 50 (A2, B2) or 100 (C2) Hz were applied prior to Fourier transformation. The logarithm of the rate constant  $k$  is indicated at each row of spectra.

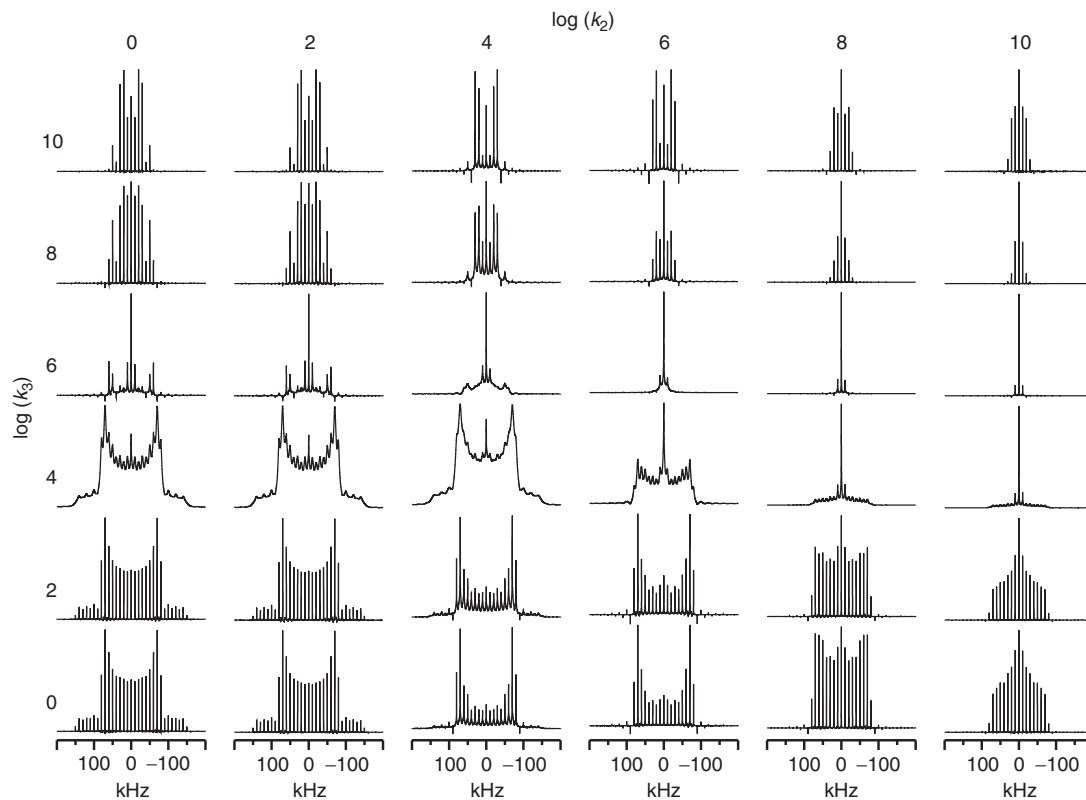


**Figure 5** Maximum intensity as a function of  $\log(k)$  for simulated  $^{14}\text{N}$  (43.34 MHz) MAS spectra of a two-site jump process detecting either (A) single-quantum coherence or (B) double-quantum coherence. In both plots, the solid line corresponds to parameter set P6, the solid triangles to parameter set P7 and the solid squares to parameter set P8.

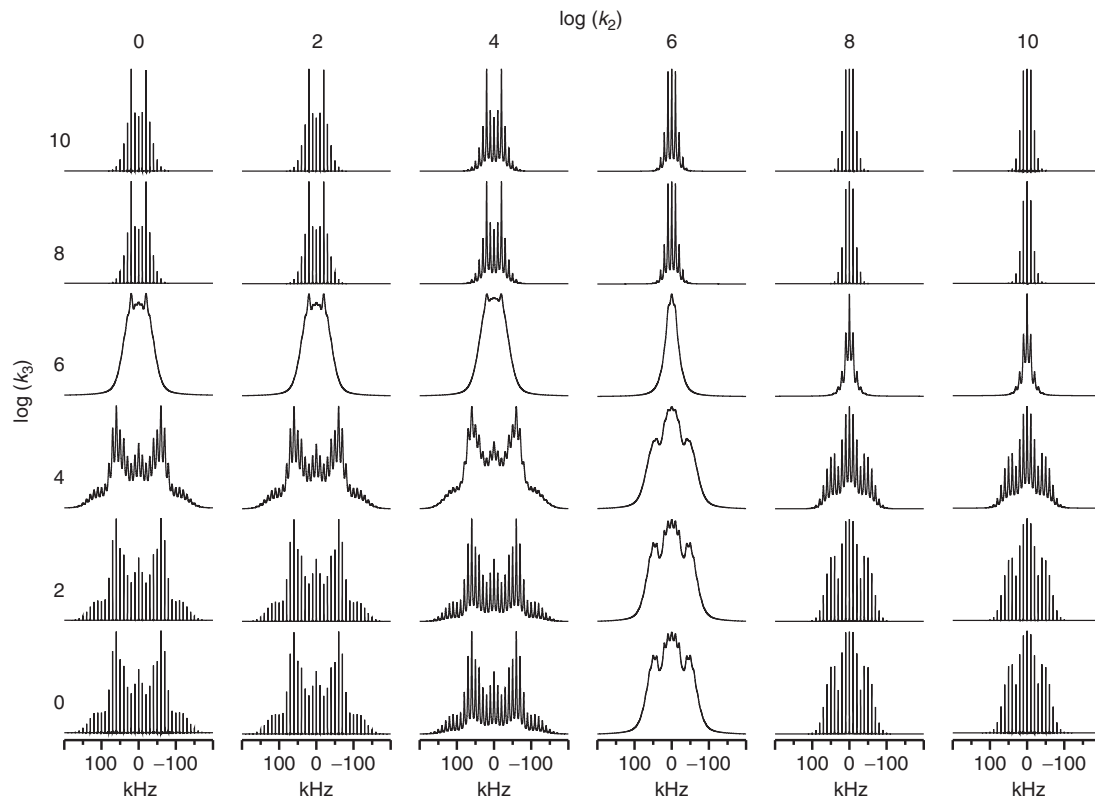
QCPMG (real pulses) experiments is performed in order to verify if different effects are observed when modulating either the spin-part (QCPMG) or the spatial part (MAS) of the Hamiltonian. The results for a rotation around a  $C_3$ -axis (rate constant  $k_3$ ) followed by rotation around a  $C_2$ -axis (rate constant  $k_2$ )—similar to what is observed in DMS- $d_6$ —are displayed in Figures 6 and 7. At room temperature and above the three-site jump in DMS- $d_6$  is extremely fast and usually only the two-site jump is considered for this compound. This effect can be followed in the upper row of both figures where  $k_3 = 10^{10}$  Hz and  $k_2$  is varied. In the  $^2\text{H}$  QCPMG spectra (Figure 6), it is noted that only minor differences for  $k_3 = 10^8$  Hz are observed when comparing the first two columns corresponding to  $k_2 = 1$  and 100 Hz. Besides these two columns, comparison of either rows or columns in the remaining part of the figure reflects changes in either overall lineshape or line width of spin-echo sidebands when at least one rate constant is changed by at least two orders of magnitude. A rather interesting feature is the dramatic narrowing of the overall lineshape for  $k_3 = 10^6$  Hz and  $k_2 = 10^6$ – $10^{10}$  Hz. Moreover, a major broadening of the spin-echo sidebands is observed for  $k_3 = 10^4$  Hz and all  $k_2$ -values.

The corresponding  $^2\text{H}$  MAS spectra (Figure 7) display different features. First of all, the columns corresponding to  $k_2 = 1$  and 100 Hz are identical. Likewise for the rows corresponding to  $k_3 = 1$  and 100 Hz. In addition only minor differences between the columns  $k_2 = 10^8$  and  $10^{10}$  Hz as well the rows for  $k_3 = 10^8$  and  $10^{10}$  Hz are observed. This indicates that no changes are observed when any of the rate constants are in the slow or the fast limit.





**Figure 6** Simulated  $^2\text{H}$  (73.58 MHz) QCPMG spectra corresponding to a 3-by-2-site jump process using parameter set P2b in [Table 1](#) and the single-frame set of Euler angles were<sup>69</sup>: (0.0, 124.0, 0.0), (57.594, 55.006, 91.716), (302.406, 55.006, 268.206), (0.0, 124.0, 180.0), (57.594, 55.006, 271.716), (302.406, 55.006, 88.206). The logarithm of the rate constants  $k_3$  and  $k_2$  are indicated at each row and column of the spectra. All spectra were apodized by Gaussian line broadening of 50 Hz prior to Fourier transformation.

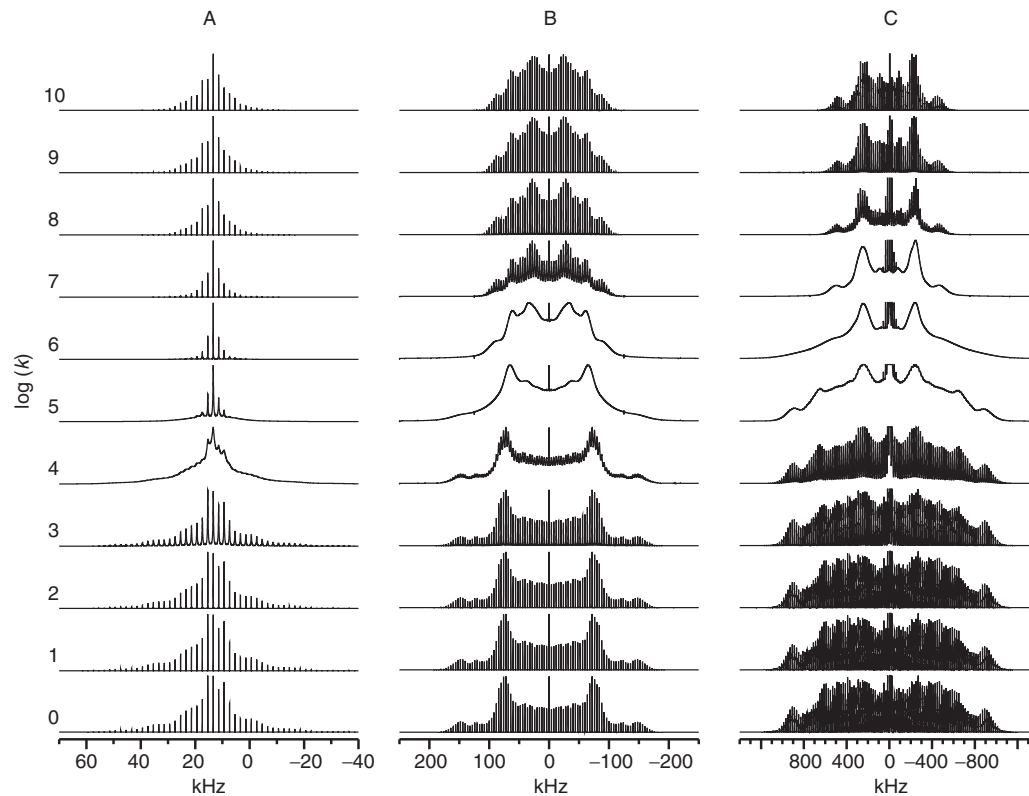


**Figure 7** Simulated  $^2\text{H}$  (73.58 MHz) MAS spectra corresponding to a 3-by-2-site jump process the same parameter set as in [Figure 6](#). The logarithm of the rate constants  $k_3$  and  $k_2$  are indicated at each row and column of the spectra. All spectra were apodized by Gaussian line broadening of 50 Hz prior to Fourier transformation.

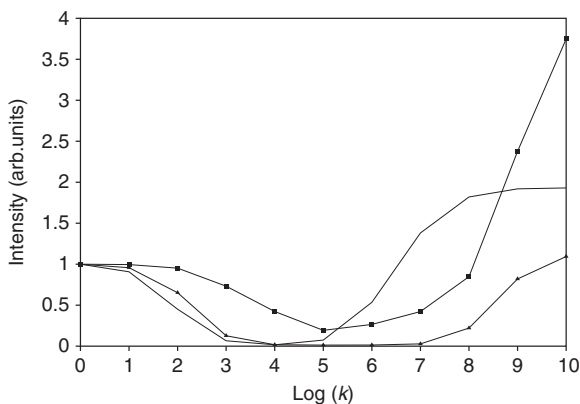
Comparison of the MAS and the QCPMG spectra reveals a range of differences, in particular when comparing the rows corresponding to  $k_3 = 10^6$  Hz or the columns for  $k_2 = 10^6$  Hz. In both cases, the spinning sideband manifold of the MAS spectra is heavily broadened whereas significant line broadening in the QCPMG spectra is only observed for  $(k_3, k_2) = (10^4, 10^6)$  Hz and  $(10^6, 10^4)$  Hz and to a lesser extent  $(10^6, 10^6)$  Hz. Besides the intermediate regime, obvious differences between QCPMG and MAS spectra are also observed when comparing rows for  $k_3 = 10^8$  and  $10^{10}$  Hz as well as columns for  $k_2 = 10^8$  and  $10^{10}$  Hz. In both cases, these rows and columns are identical for the MAS spectra whereas differences are observed in the QCPMG spectra. Likewise, differences in the QCPMG spectra for the two rows corresponding to  $k_3 = 1$  or 100 Hz were observed whereas these two rows were identical in the MAS spectra. This suggests that the QCPMG experiment is more sensitive towards motional changes if one of the rate constants is in the fast regime or if  $k_3$  is in the slow regime. Overall the differences between the MAS and QCPMG spectra illustrate that the effect of motion affects the spin-part and the spatial part of the Hamiltonian by different mechanisms.

#### 4.4. Half-integer quadrupolar nuclei

Half-integer quadrupolar nuclei span a large part of the periodic table and covers spins from  $3/2$  to  $9/2$ . Regarding observation of these nuclei by solid-state NMR spectroscopy, the experiments of choice depend upon the magnitude of the quadrupolar coupling constant,  $C_Q$ , in particular. To demonstrate the effects of dynamics on nuclei having different  $C_Q$ s, Larmor frequencies and spin-quantum numbers, examples of two-site jumps for MAS spectra of  $^{133}\text{Cs}$ ,  $^{23}\text{Na}$  and  $^{39}\text{K}$  using parameter sets P9, P10 and P11a, respectively, are displayed in Figure 8. The purpose of this figure is to compare motional effects on the spinning sideband manifolds and therefore the signal corresponding to the central transition in  $^{23}\text{Na}$  and  $^{39}\text{K}$  is cut off at the maximum intensity of the spinning sidebands. Overall the effects of the dynamics follow the same trend. At slow jump rates, the spectra are not affected by dynamics, then in the intermediate regime line broadening sets in and at faster jump rates the spinning sidebands become narrow. It must be noted that the overall width of the spinning sideband manifold at fast jump rates is smaller than at very slow dynamics. Comparison of columns A, B and C reveals that the jump rate at which the line broadening effect induced by motion sets in depends on the magnitude of  $C_Q$ , spin-quantum number and Larmor frequency. Comparing columns A and B, significant line broadening was noted for  $k = 10^3$ – $10^5$  Hz for  $^{133}\text{Cs}$  and  $k = 10^4$ – $10^7$  Hz for  $^{23}\text{Na}$ . In column B, the spinning sideband manifold was even broadened to what looks like a static lineshape when  $k = 10^5$ – $10^6$  Hz. Column C corresponds to a  $^{39}\text{K}$  site with a rather large  $C_Q$  and in this case the motional line broadening affects the dynamic regime  $k = 10^4$ – $10^8$  Hz with ‘static lineshapes’ for  $k = 10^5$ – $10^7$ . Altogether, these observations demonstrate that motional line broadening sets in at lower jump rates for smaller quadrupole effects and that the regime of severe line broadening (‘static lineshape’) is extended for larger quadrupole effects. Figure 9 displays the corresponding intensity profiles. In agreement with the line broadening observed in Figure 8,



**Figure 8** (A) Simulated MAS spectra of  $^{133}\text{Cs}$  (52.45 MHz) (column A),  $^{23}\text{Na}$  (105.8 MHz) (column B) and  $^{39}\text{K}$  (23.325 MHz) (column C) corresponding to a two-site jump process and ideal excitation. Parameter sets P9, P10 and P11 have been employed, respectively. The logarithm of the rate constant  $k$  is indicated at each row of spectra. Gaussian line broadening of 20 (A), 50 (B) and 200 (C) Hz were added prior to Fourier transformation.

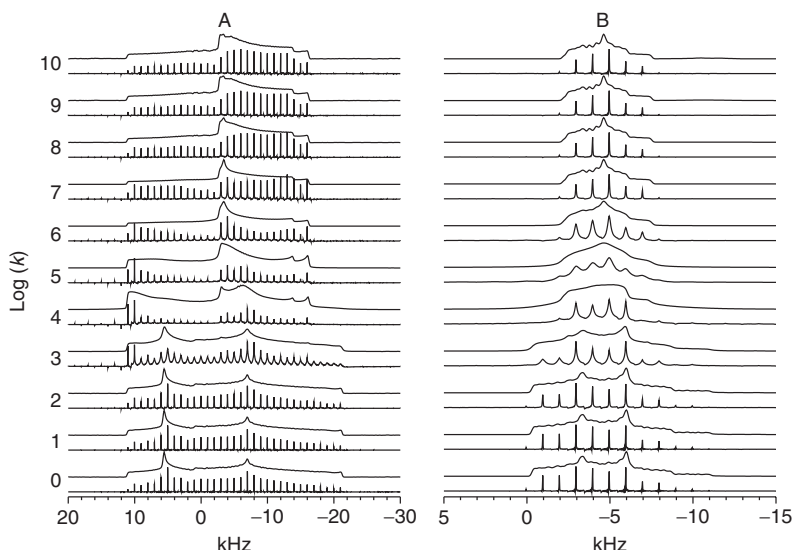


**Figure 9** Maximum intensity as a function of  $\log(k)$  for simulated MAS spectra of a two-site jump process for  $^{133}\text{Cs}$  (parameter set P9, solid line),  $^{23}\text{Na}$  (parameter set P10, solid triangles) and  $^{39}\text{K}$  (parameter set P11, solid squares).

the intensity profile, for example,  $^{133}\text{Cs}$  shows a minimum in the range  $=10^3\text{--}10^5$  Hz whereas broader minima were observed for the two other nuclei. Besides this, the intensity gain in the fast jump limit reflects the overall line broadening of the lineshape. This effect is most pronounced for  $^{39}\text{K}$  and  $^{133}\text{Cs}$  where gains of 3.7 and 1.9, respectively, are obtained. For  $^{23}\text{Na}$ , the gain is only 1.1 due to only minor reduction in the width of the overall lineshape.

When larger  $C_Q$ s are presented, it is often an advantage to study the central transition as this is not affected by the first-order quadrupole Hamiltonian. The effects of two-site jump dynamics on a  $^{39}\text{K}$  site observed by QE, QCPMG (parameter set P11a), MAS (parameter set P11b) and QCPMG–MAS (parameter set P11c) experiments are shown in Figure 10. In column A, the static QE and QCPMG spectra are displayed whereas the MAS and QCPMG–MAS spectra are shown in column B. In both columns, the motional line broadening is initially observed for  $k=10^2$  Hz in the QCPMG as well as the QCPMG–MAS spectra. More severe line broadening is observed in all spectra  $k=10^3$  Hz and at faster jump rates changes in particular the overall lineshape and the width of the spin–echo sidebands in the QCPMG–MAS spectra are detected. At jump rates  $k=10^6$  Hz, a line narrowing effect sets in and above  $k=10^8$  Hz only minor line narrowing of the spin–echo sidebands were observed for the QCPMG–MAS spectra. From this comparison, the QCPMG–MAS experiment looks very promising as effects on both overall lineshape as well as broadening/narrowing of the spin–echo sidebands were present in the regime  $k=10^3\text{--}10^7$  Hz.

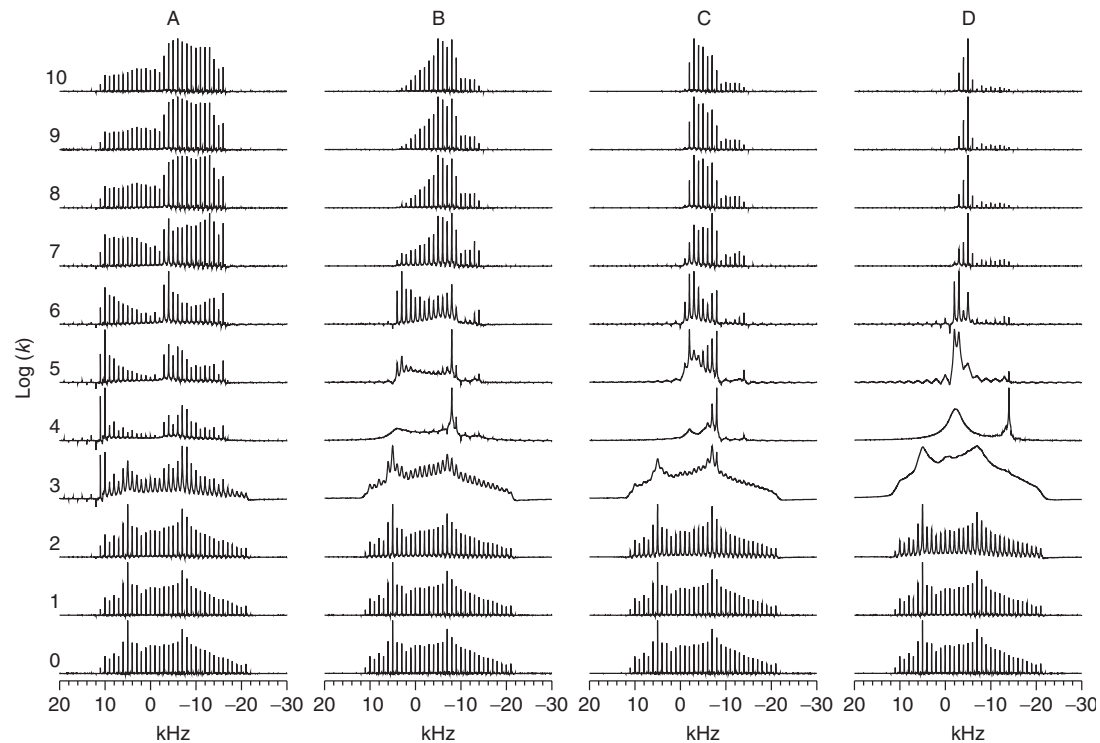
Taking an experimental point of view variable temperature experiments used for dynamics studies are easiest to perform under static conditions as rotation of the sample cause frictional heating and at very high or very low temperatures it may be difficult to construct MAS probe that would allow sufficiently fast spinning when studying half-integer quadrupolar nuclei. This makes the



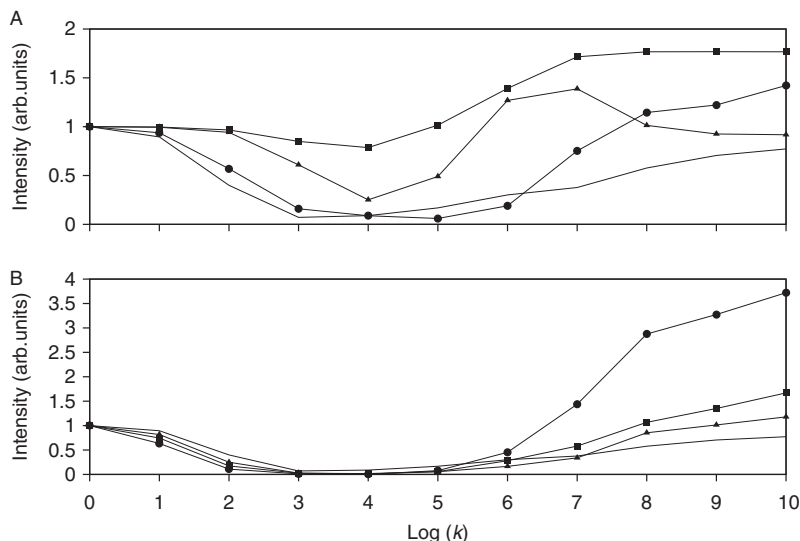
**Figure 10** (A) Simulated  $^{39}\text{K}$  (23.325 MHz) QE and QCPMG spectra (column A) employing parameter set P11a ( $M=0$  and acquisition of 1224 points for the QE spectra) and single-pulse MAS (parameter set P11b) and QCPMG–MAS spectra (parameter set P11c) corresponding to a two-site jump process. In column A, the upper spectra for each rate constant correspond to the QE spectra and in column B the single-pulse MAS spectra are the upper spectra for each rate constant. The logarithm of the rate constant  $k$  is indicated at each row of spectra. The QCPMG and QCPMG–MAS spectra were apodized by Gaussian line broadening of 25 Hz prior to Fourier transformation, whereas line broadenings for 250 and 200 Hz were employed for the QE and single-pulse MAS spectra, respectively.

QCPMG experiment a good choice as it is sensitive to motion and is more sensitive than the QE experiment. In Figure 11, effects of 2-, 3-, 4-, and 6-site jumps on a  $^{39}\text{K}$  site using parameter set P11a are displayed. At slow jump rates the spectra are similar in the four columns but even at  $k=100$  Hz motional line broadening of the spin-echo sidebands is observed in columns B (three-site jump), C (four-site jump) and in particular D (six-site jump). In the intermediate regime  $k=10^3$ – $10^8$  Hz, changes in both overall lineshape and width of spin-echo sidebands are observed. The latter is most pronounced for three-site jumps or higher. No changes in the overall lineshape were observed for  $k > 10^8$  Hz. For spin-1 nuclei, it has been demonstrated that for three-site jumps or higher the lineshape in the fast jump regime is the same.<sup>2,76</sup> Looking at the spectra in Figure 11 for the fast limit ( $k=10^{10}$  Hz), it is evident that they become narrower as the order of the jump process becomes higher and does not converge towards the same lineshape at fast dynamics.

This is in good agreement with the intensity profiles in Figure 12B that clearly shows that the intensity in the fast limit increases when the order of the jump process is increased. In the regime  $k=10^3$ – $10^5$  Hz, it is noted that the intensity of the two-site jump is not as heavily reduced as in the higher order jump processes.



**Figure 11** (A) Simulated  $^{39}\text{K}$  (23.325 MHz) QCPMG spectra employing parameter set P11a corresponding to a two-site jump (column A), three-site jump (column B), four-site jump (column C) or a six-site jump (column D), respectively. The logarithm of the rate constant  $k$  is indicated at each row of spectra. All spectra were apodized by Gaussian line broadening of 25 Hz prior to Fourier transformation.



**Figure 12** Maximum intensity as a function of  $\log(k)$  for simulated  $^{39}\text{K}$  spectra shown in Figures 10 and 11. (A) The intensity profiles for a two-site jump using the QE (solid triangles), the QCPMG (solid line), the QCPMG-MAS (solid circles) and the single-pulse MAS (solid squares) experiments. (B) The intensity profiles of the QCPMG experiment for a two-site (solid line), three-site (solid triangles), four-site (solid squares) and a six-site (solid circles) jump process.

Going back to the four experiments examined in Figure 10, the corresponding intensity profiles are shown in Figure 12A. It is noted that the maximum intensity of all experiments is reduced in the regime  $k = 10^3 - 10^5$  Hz, but the level of reduction is quite different. The smallest reduction was observed for the MAS experiment and secondly the QE experiment whereas the QCPMG (static or MAS) experiments were more significantly reduced. At jump rates faster than  $10^5$  Hz, the intensity increases steadily for all but the QE experiment. The reason for the local intensity maximum is ascribed to the singularity around  $-3.5$  kHz in the QE spectrum. This singularity is broadened at faster jump rates.

## 5. CONCLUSIONS

In this work, it has been demonstrated that periodic modulation of the Hamiltonian describing a dynamic process introduces spectral effects that depend upon the nature of the modulations. For both MAS and QCPMG experiments, sidebands are broadened in the intermediate dynamic regime and a significant narrowing of the sideband manifold is observed for higher order jump processes due to averaging of the anisotropic part of the quadrupolar tensor.



Both experiments are applicable for acquisition of  $^2\text{H}$  and  $^6\text{Li}$  spectra and for these nuclei only first-order EFG- and CSA-terms in the Hamiltonian are required. For  $C_{\text{QS}}$  below 750 kHz, both  $^{14}\text{N}$  QCPMG and MAS experiments are applicable at 14.1 T but above this  $C_{\text{Q}}$  limit the hardware demands make it very difficult to employ the QCPMG experiment and single-pulse MAS must be the method of choice for such applications. For larger  $C_{\text{QS}}$ , indirect detection of either  $^{14}\text{N}$  SQ or DQ coherences using rotor-synchronized acquisition is suggested. In this context, the DQ lineshape is not as severely broadened as the SQ lineshape as it is not affected by the first-order quadrupolar Hamiltonian.

Two-axis  $^2\text{H}$  dynamics for a system with a  $C_3$ -axis rotating around a  $C_2$ -axis have also been explored and these results suggest that the QCPMG experiment is more sensitive than the MAS experiment towards motional effects if either of the two rate constants is in the fast regime.

For half-integer nuclei, MAS experiments have also been explored focussing on the effect of the spinning sideband manifold. Similar to what is observed for spin-1 nuclei, significant line broadening of the spinning sidebands was observed in a regime that depends on  $C_{\text{Q}}$ ,  $I$  and the Larmor frequency.

The sensitivity of the QE, QCPMG, MAS and QCPMG–MAS experiments towards motional effects was also compared and even though the QCPMG–MAS were most sensitive due to effects on overall lineshape as well as on spin-echo sidebands, the QCPMG experiment is considered the best suited experiment for practical purposes. Effects of 2-, 3-, 4- and 6-site jumps in QCPMG experiments of a second-order quadrupolar broadened lineshape showed that the spectrum in the fast limit becomes narrower when the order of the jump process is increased. This is in contrast to what is observed for spin-1 nuclei. In common for all the quadrupolar nuclei examined in this work, a more severe line broadening mechanism was observed in the presence of  $H_{\text{Q}}^{(1)}$  than if only  $H_{\text{Q}}^{(2)}$  were present. The latter was shown for the central transition in half-integer quadrupolar nuclei and DQ coherences in spin-1 nuclei.

## ACKNOWLEDGEMENTS

The author wish to acknowledge financial support from the 'Biofunctional Carbohydrates—BioFunCarb' project (project no. 2101-08-0068) funded by the Danish Council for Strategic Research.

## REFERENCES

1. M. Vogel and E. Rössler, *J. Phys. Chem. B*, 2000, **104**, 4285.
2. B. Boddenberg and R. Grosse, *Z. Naturforsch.*, 1986, **41a**, 1361.
3. L. M. Bull, A. K. Cheetham, B. M. Powell, J. A. Ripmeester and C. I. Ratcliffe, *J. Am. Chem. Soc.*, 1995, **117**, 4328.
4. S. Nishikiori, T. Kitazawa, C.-H. Kim and T. Iwamoto, *J. Phys. Chem. A*, 2000, **104**, 2591.
5. J. R. Gardinier, P. J. Pellechia and M. D. Smith, *J. Am. Chem. Soc.*, 2005, **127**, 12448.
6. Y. Hiayama, J. V. Silverton, D. A. Torchia, J. T. Gerig and S. J. Hammond, *J. Am. Chem. Soc.*, 1986, **108**, 2715.
7. A. E. Aliev, K. D. M. Harris, I. J. Shannon, C. Glidewell, C. M. Zakaria and P. A. Schofield, *J. Phys. Chem.*, 1995, **99**, 12008.

8. M. E. Hatcher, D. L. Mattiello, G. A. Meints, J. Orban and G. P. Drobny, *J. Am. Chem. Soc.*, 1998, **120**, 9850.
9. K. Liu, J. Williams, H. Lee, M. M. Fitzgerald, G. M. Jensen, D. B. Goodin and A. E. McDermott, *J. Am. Chem. Soc.*, 1998, **120**, 10199.
10. L. Vugmeyster, D. Ostrovsky, J. J. Ford, S. D. Burton, A. S. Lipton, G. L. Hoatson and R. L. Vold, *J. Am. Chem. Soc.*, 2009, **131**, 13651.
11. L. Vugmeyster, D. Ostrovsky, J. J. Ford and A. S. Lipton, *J. Am. Chem. Soc.*, 2010, **132**, 4038.
12. G. L. Olsen, M. F. Bardaro, Jr., D. C. Echodu, G. P. Drobny and G. Varani, *J. Am. Chem. Soc.*, 2010, **132**, 303.
13. E. L. Hahn, *Phys. Rev.*, 1950, **80**, 580.
14. I. Solomon, *Phys. Rev.*, 1958, **110**, 61.
15. J. H. Davis, K. R. Jeffrey, M. Bloom, M. I. Valic and T. P. Higgs, *Chem. Phys. Lett.*, 1976, **42**, 390.
16. H. W. Spiess and H. Sillescu, *J. Magn. Reson.*, 1981, **42**, 381.
17. R. J. Wittebort, E. T. Olejniczak and R. G. Griffin, *J. Chem. Phys.*, 1987, **86**, 5411.
18. M. S. Greenfield, A. D. Ronemus, R. L. Vold, R. R. Vold, P. D. Ellis and T. E. Raidy, *J. Magn. Reson.*, 1987, **72**, 89.
19. M. Bloom, J. H. Davis and M. I. Valic, *Can. J. Phys.*, 1980, **58**, 1510.
20. T. M. Barbara, M. S. Greenfield, R. L. Vold and R. R. Vold, *J. Magn. Reson.*, 1986, **69**, 311.
21. M. H. Levitt, *Prog. NMR Spectrosc.*, 1986, **18**, 61.
22. D. P. Raleigh, E. T. Olejniczak and R. G. Griffin, *J. Magn. Reson.*, 1989, **81**, 455.
23. F. H. Larsen, H. J. Jakobsen, P. D. Ellis and N. C. Nielsen, *J. Phys. Chem. A*, 1997, **101**, 8597.
24. F. H. Larsen, H. J. Jakobsen, P. D. Ellis and N. C. Nielsen, *Chem. Phys. Lett.*, 1998, **292**, 467.
25. C. Schmidt, B. Blümich and H. W. Spiess, *J. Magn. Reson.*, 1988, **79**, 269.
26. S. Kaufmann, S. Wefing, D. Schaefer and H. W. Spiess, *J. Chem. Phys.*, 1990, **93**, 197.
27. D. Schaefer and H. W. Spiess, *J. Chem. Phys.*, 1992, **97**, 7944.
28. D. Schaefer, J. Leisen and H. W. Spiess, *J. Magn. Reson. A*, 1995, **115**, 60.
29. J. H. Kristensen, H. Bildsøe, H. J. Jakobsen and N. C. Nielsen, *J. Magn. Reson.*, 1992, **100**, 437.
30. J. H. Kristensen, G. L. Hoatson and R. L. Vold, *Solid State Nucl. Magn. Reson.*, 1998, **13**, 1.
31. J. H. Kristensen, G. L. Hoatson and R. L. Vold, *J. Chem. Phys.*, 1999, **110**, 4533.
32. O. Weintraub and S. Vega, *Solid State Nucl. Magn. Reson.*, 1995, **4**, 341.
33. J. Huang, R. L. Vold and G. L. Hoatson, *J. Chem. Phys.*, 2006, **124**, 104504.
34. J. H. Kristensen, H. Bildsøe, H. J. Jakobsen and N. C. Nielsen, *J. Magn. Reson.*, 1999, **139**, 314.
35. D. J. Siminowitch, M. Rance and K. R. Jeffrey, *J. Magn. Reson.*, 1984, **58**, 62.
36. T.-H. Lin, J. A. DiNatale and R. R. Vold, *J. Am. Chem. Soc.*, 1994, **116**, 2133.
37. S. Antonijevic and E. Persson, *J. Chem. Phys.*, 2007, **126**, 014504.
38. M. Mizuno, Y. Suzuki, K. Endo, M. Murakami, M. Tansho and T. Shimizu, *J. Phys. Chem. A*, 2007, **111**, 12954.
39. C. P. Grey and N. Dupré, *Chem. Rev.*, 2004, **104**, 4493.
40. R. Siegel, J. Hirschinger, D. Carlier, S. Matar, M. Ménétrier and C. Delmas, *J. Phys. Chem. B*, 2001, **105**, 4166.
41. Z. Xu and J. F. Stebbins, *Solid State Nucl. Magn. Reson.*, 1995, **5**, 103.
42. Z. Xu and J. F. Stebbins, *Science*, 1995, **270**, 1332.
43. G. Jeschke and M. Jansen, *Angew. Chem. Int. Ed.*, 1998, **37**, 1282.
44. H. J. Jakobsen, H. Bildsøe, J. Skibsted and T. Giavani, *J. Am. Chem. Soc.*, 2001, **123**, 5098.
45. T. Giavani, H. Bildsøe, J. Skibsted and H. J. Jakobsen, *J. Magn. Reson.*, 2004, **166**, 262.
46. F. Lindström, P. T. F. Williamson and G. Gröbner, *J. Am. Chem. Soc.*, 2005, **127**, 6610.
47. Z. Gan, *J. Am. Chem. Soc.*, 2006, **128**, 6040.
48. S. Cavadini, A. Lupulescu, S. Antonijevic and G. Bodenhausen, *J. Am. Chem. Soc.*, 2006, **128**, 7706.
49. S. Cavadini, A. Abraham, S. Ulzega and G. Bodenhausen, *J. Am. Chem. Soc.*, 2008, **130**, 10850.
50. S. Cavadini, *Prog. Nucl. Magn. Reson.*, 2010, **56**, 46.
51. A. J. Vega and Z. Luz, *J. Chem. Phys.*, 1803, **1987**, 86.
52. J. H. Kristensen and I. Farnan, *Chem. Phys.*, 2001, **270**, 109.
53. E. A. Behrens, D. M. Poojary and A. Clearfield, *Chem. Mater.*, 1998, **10**, 959.
54. M. Nyman, F. Bonhomme, R. S. Maxwell and T. M. Nenoff, *Chem. Mater.*, 2001, **13**, 4603.
55. P. D. Southon and R. F. Howe, *Chem. Mater.*, 2002, **14**, 4209.

56. L.-S. Du and J. F. Stebbins, *J. Non-Cryst. Sol.*, 2003, **315**, 239.
57. S. Sham and G. Wu, *Inorg. Chem.*, 2000, **39**, 4.
58. C. V. Grant, V. Frydman and L. Frydman, *J. Am. Chem. Soc.*, 2001, **122**, 11743.
59. A. S. Lipton, T. A. Wright, M. K. Bowman, D. L. Reger and P. D. Ellis, *J. Am. Chem. Soc.*, 2002, **124**, 5850.
60. A. S. Lipton, R. W. Heck and P. D. Ellis, *J. Am. Chem. Soc.*, 2004, **126**, 4735.
61. J. H. Kristensen and I. Farnan, *J. Chem. Phys.*, 2001, **114**, 9608.
62. J. H. Kristensen and I. Farnan, *J. Magn. Reson.*, 2002, **158**, 99.
63. M. Witschas, H. Eckert, H. Freiheit, A. Putnis, G. Korus and M. Jansen, *J. Phys. Chem. A*, 2001, **105**, 6808.
64. R. W. Schurko, S. Wi and L. Frydman, *J. Phys. Chem. A*, 2002, **106**, 51.
65. L. van Wüllen, L. Hildebrandt and M. Jansen, *Solid State Ionics*, 2005, **176**, 1449.
66. M. Kotecha, S. Chaudhuri, C. P. Grey and L. Frydman, *J. Am. Chem. Soc.*, 2005, **127**, 16701.
67. G. M. Bowers, D. L. Bish and R. J. Kirkpatrick, *J. Phys. Chem. C*, 2008, **112**, 6430.
68. D. Carlier, M. Blangero, M. Ménétrier, M. Pollet, J.-P. Doumerc and C. Delmas, *Inorg. Chem.*, 2009, **48**, 7018.
69. R. L. Vold and G. L. Hoatson, *J. Magn. Reson.*, 2009, **198**, 57.
70. F. H. Larsen, *J. Magn. Reson.*, 2004, **171**, 293.
71. F. H. Larsen, *Solid State Nucl. Magn. Reson.*, 2007, **31**, 100.
72. F. J. Dyson, *Phys. Rev.*, 1949, **75**, 486.
73. G. J. Bowden and W. D. Hutchison, *J. Magn. Reson.*, 1986, **67**, 403.
74. E. Anderson, Z. Bai, C. Bischof, S. Blackford, J. Demmel, J. Dongarra, J. Du Croz, A. Greenbaum, S. Hammarling, A. McKenney and D. Sorensen, *LAPACK Users' Guide*. Society for Industrial and Applied Mathematics, Philadelphia, PA, 1999. <http://www.netlib.org/lapack/>.
75. S. K. Zaremba, *Ann. Mat. Pura Appl.*, 1966, **73**, 293.
76. R. G. Barnes, *Adv. Nucl. Quadrupole Reson.*, 1974, **1**, 335.
77. R. Blinc, J. Seliger, A. Zidansek, V. Zagar, F. Milia and H. Robert, *Solid State Nucl. Magn. Reson.*, 2006, **30**, 61.
78. D. H. Smith and R. M. Cotts, *J. Chem. Phys.*, 1954, **41**, 2403.

## NMR Studies of Disorder in Condensed Matter Systems

**K. P. Ramesh**

---

<b>Contents</b>		
	1. Introduction	140
	2. Dipolar Glasses	141
	2.1. Method of detection	143
	2.2. Line shape analysis	144
	2.3. Spin–lattice relaxation studies	144
	2.4. 1-Dimensional and 2-dimensional O–D–O deuteron exchange NMR	145
	3. NMR Study of Relaxor Ferroelectrics	158
	3.1. Lead magnesium niobate PMN	160
	3.2. Uniaxial relaxors—strontium barium niobate	162
	4. Conducting Polymers	163
	4.1. Disorder in conducting polymers	163
	4.2. Charge transport in conducting polymers	164
	4.3. NMR in conducting polymers/organic conductors	166
	4.4. Dimensionality and $1/T_1$ versus frequency plot	168
	4.5. Method of detection	168
	4.6. Sample preparation and experimental methods	169
	5. Conclusions	172
	References	172

---

### Abstract

This review summarizes nuclear magnetic resonance (NMR) studies in condensed matter systems exploring the effects of disorder. Highly ordered systems have a well-defined order parameter, which is zero at high-temperature phase and finite at low temperatures. In contrast to magnetic spin glasses, dipolar glasses show that the cusp in the dielectric susceptibility is rounded and the freezing takes place over an unusually large-temperature interval far above the glass transition temperature  $T_G$ . Many a times, it is difficult to define a

Department of Physics, Indian Institute of Science, Bangalore, India

Annual Reports on NMR Spectroscopy, Volume 71  
ISSN 0066-4103, DOI: 10.1016/S0066-4103(10)71005-X

© 2010 Elsevier Ltd.  
All rights reserved.

glass transition temperature for a given system. The microscopic origin of this behaviour is quite interesting and is a subject of intensive research.

Origin of disorder is different in different systems. In dipolar glasses, the origin of disorder is traced to the shuttling of H-bonds between the possible positions. In parent compounds, at higher temperatures, there is equal probability of H-bonds being found between the two oxygens of the two adjacent  $\text{PO}_4$  groups, while below a particular temperature  $T_f$  (defined as the ferroelectric (FE) transition temperature), they freeze to one of the possible positions. In a dipolar glass system (FE + AFE mixed system), the system goes to a frustrated state with the disappearance of the phase transition resulting in an orientational disorder. As a result of this, the rate of H-bond motion in these systems, now will have a wide range of distribution starting from  $10^{-3}$  to  $10^{-12}$  s. Similarly in FE relaxors, one can find substitutional disorder due to the changes in the charges of the different cations resulting in random-fields (RFs) and random bonds. The main sources of disorder in conducting polymers (CPs) are  $\text{sp}^2$  defects in the chain, chain ends, chain entanglements, voids, morphological and doping defects. CPs are partially crystalline and partially amorphous, the volume fraction of the crystalline regions and the size of the crystalline coherence length play a dominant role in the charge transport. In general, the disorder induced localization plays a dominant role in the transport properties of CPs.

Our main aim in this review is to study the effect of disorder in dipolar glasses, FE relaxors and CPs. NMR is a powerful local probe for providing information about the distribution and dynamics of local RFs, and characteristic of such systems. While the quadrupole-perturbed NMR line shape analysis gives details about the distribution of local RFs, spin–lattice relaxation studies can give information on the dynamics in the frustrated state of these systems. Many modifications and new methods have been adopted to use NMR to explore the effects of disorder on measurable quantities. Other than hydrogen, many NMR friendly nuclei such as deuterium,  $^{87}\text{Rb}$ ,  $^{45}\text{Sc}$ ,  $^{93}\text{Nb}$ ,  $^{207}\text{Pb}$ ,  $^{205}\text{Tl}$ , etc. are used to study these systems. Further, two-dimensional deuterium NMR exchange spectroscopy is also applied to study these materials.

**Key Words:** Dipolar glasses, Ferroelectric relaxors, Conducting polymers, NMR line shape, Disorder, Local polarization related to the line shape, Symmetric/asymmetric quadrupole-perturbed NMR, H-bonded systems, Spin–lattice relaxation, Edwards–Anderson order parameter, Dimensionality of conduction, Proton, Deuteron tunnelling.

---

## 1. INTRODUCTION

Disorder in condensed matter system is a vast area of research and has seen tremendous progress due to the addition of new systems and techniques. Nuclear magnetic resonance (NMR) being a local probe has played an important role in exploring the rich physics hidden in these systems.

Disordered systems can be broadly classified into spin glasses, dipolar glasses/pseudo-spin glasses, canonical glasses, conducting polymers (CPs),

amorphous systems, etc. In this chapter, we have attempted to briefly bring out the use of NMR, in particular pulsed NMR technique in these systems. In this review, we have concentrated only on the NMR studies in dipolar glasses, ferroelectric (FE) relaxors and CPs. Even among these systems, we have taken only a few representative systems to discuss the analysis of NMR data and their interpretation. Our main aim is to show, how a traditional technique like NMR and its measurable parameters can be used to unravel the rich physics in disordered materials. In this respect it may not be a comprehensive review, but aids the students/researchers to practice applicability of NMR to new systems. Typical examples have been discussed in detail whenever the clarity is needed.

## 2. DIPOLAR GLASSES

The condensed matter systems of proton/deuteron pseudo-spin glasses have captured the attention of both experimentalists and theorists for quite some time. In contrast, to magnetic spin glasses the cusp in the dielectric susceptibility is rounded and the freezing takes place over an unusually large-temperature interval far above the glass transition temperature  $T_G$ . The microscopic origin of this behaviour in dipolar glasses points towards a basic difference between dipolar and spin glasses. These are absent in spin glasses but present in proton and deuteron glasses. There is still another feature which distinguishes proton and deuteron glasses from spin glasses, namely, the occurrence of random-fields (RFs). The term dipolar glasses refers to the systems of regular lattice, some of whose sites are occupied by constituents containing a dipole or quadrupole moments. These moments have orientational degrees of freedom. They interact with one another and below some freezing temperature " $T_f$ " their motion slows down and they freeze into a configuration which is devoid of long-range dipolar order.<sup>1</sup> These systems can be prepared by mixing an FE and an anti-ferroelectric (AFE) material which are isostructural. The most common example of this type is the mixed system of the FE rubidium dihydrogen phosphate (RDP) and AFE ammonium dihydrogen phosphate (ADP). It has been found that this mixed system  $(\text{NH}_4)_x\text{Rb}_{1-x}\text{H}_2\text{PO}_4$  (RADP), for a certain concentration range ( $0.22 < x < 0.74$ ), shows frustration effects at low temperatures.<sup>2</sup> Other members of this family are listed in Table 1.

The origin of disorder is traced to the shuttling of H-bonds between the possible positions. At higher temperatures, there is equal probability of H-bonds being found between the two oxygens of the two adjacent  $\text{PO}_4$  groups. In parent compounds, they freeze to one of the possible positions below a particular temperature  $T_f$  defined the FE transition temperature. In an FE + AFE mixed system, the following new interactions arise. For example, in RADP, there is what is called as RF because of the electric charges sitting on the corresponding cations, random bond as the bond between the cations are different in mixed systems.<sup>19</sup>

A brief review of the literature on the mixed crystals of  $\text{KH}_2\text{PO}_4$  (KDP) is available which covers the early part of the preparation and characterization of these systems. Over 30 different parent compounds have been identified.

**TABLE 1** List of FE + AFE systems studied by NMR technique

System	Nuclei investigated	References
$\text{Rb}_{1-x}(\text{NH}_4)_x\text{H}_2\text{PO}_4$ ( $0.2 < x < 0.8$ )	Proton and $^{87}\text{Rb}$ NMR	3
$\text{Rb}_{1-x}(\text{ND}_4)_x\text{D}_2\text{PO}_4$ ( $x = 0.45$ )	Deuteron and $^{87}\text{Rb}$ NMR	4–7
$\text{Rb}_{1-x}(\text{NH}_4)_x\text{H}_2\text{AsO}_4$ ( $x = 0.32$ )	Deuteron NMR, $^{75}\text{As}$ NQR	8
$\text{Rb}_{1-x}(\text{Nd}_4)_x\text{D}_2\text{AsO}_4$ ( $x = 0.32$ )	Deuteron NMR, $^{75}\text{As}$ NQR	9,10
$\text{K}_{1-x}(\text{NH}_4)_x\text{H}_2\text{PO}_4$ ( $x = 0.25, 0.51, 0.61$ )	Proton NMR	11
$\text{Rb}_{1-x}\text{Ti}_x\text{H}_2\text{PO}_4$ ( $x = 0.3$ )	$^{205}\text{Tl}$ and $^{87}\text{Rb}$ NMR	12
$\text{BP}_x\text{BPI}_{(1-x)}$	$^1\text{H}$ NMR	13,14
$\text{BP}_x\text{GPI}_{(1-x)}$	$^1\text{H}$ NMR	15,16
$\text{DBP}_{(1-x)}\text{DBPI}_x$	$^2\text{D}$ NMR	17,18

Further their deuterated analogues along with their mixed crystals offer a wide variety of substances with lot of interesting physical properties.<sup>20</sup> Since then, there are many techniques which have been used to explore the novel physics hidden in them.

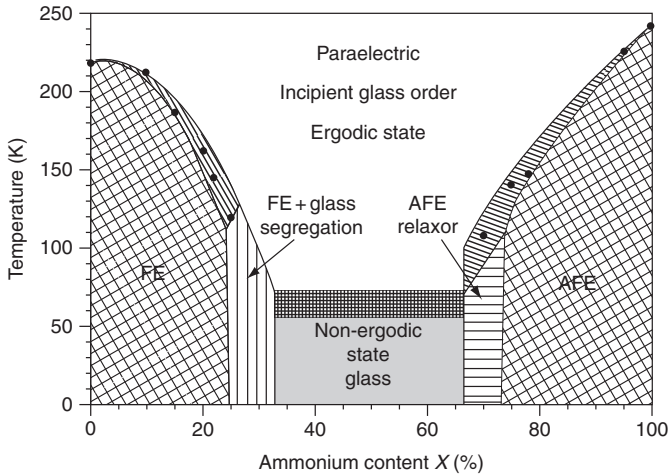
NMR is a powerful technique for providing information about the distribution and dynamics of local RFs, characteristic of such systems. While the quadrupole-perturbed NMR line shape analysis gives details about the distribution of local RFs, spin–lattice relaxation (SLR) studies can give information on the dynamics in the frustrated state of these systems. From the literature, it can be seen that most of the NMR experiments have been carried out in RADP mixed systems and its deuterated analogues. ETH group published a number of results<sup>21–23</sup> on various mixed crystals.

As mentioned earlier, one can have a range of parent compounds which can form such mixed systems which show a wide range of concentration and they have well-defined phase diagram as a function of concentration.<sup>24</sup> Depending upon the ionic radii of the parent compounds, their FE or AFE transition temperature and structural details, the phase diagram (Figure 1) may be symmetric (isostructural) or asymmetric (otherwise).

In strongly disordered systems such as spin glasses where there is an infinite number of order parameters the situation is radically different, as there is no long-range structural ordering and no sharp change in the NMR frequency at any temperature. The NMR technique<sup>4</sup> is nevertheless capable of providing useful information about strongly disordered systems as the quadrupole-perturbed NMR frequency of a given nucleus depends on the local RF  $h_i$  and the NMR line shape reflects the distribution and dynamics of the local RFs  $v_i(t) = v_i(h_i(t))$ .

NMR measurements in these systems have allowed for the following. A determination of the local-polarization distribution function  $W(p)$  and the Edwards–Anderson order parameter  $q_{\text{EA}}$  in the weak substitutional disorder limit ( $x = 0.5$ ) ongoing through  $T_c$ . The results showed that  $W(p)$  is asymmetric below  $T_c$  and symmetric above  $T_c$  and that  $q_{\text{EA}}$  makes a discontinuous jump on going through  $T_c$  in view of first-order nature of this transition.

Use of NMR technique for the study of mixed systems is mainly by R. Blinc's group from J. Stefan Institute, University of Ljubljana. Proton and deuteron



**Figure 1** Phase diagram of deuterated RADP  $(\text{NH}_4)_x\text{Rb}_{1-x}\text{H}_2\text{PO}_4$  as a function of  $x$ .

glasses are solid solutions of H-bonded FE (e.g.  $\text{RbH}_2\text{PO}_4$ ) and AFE (e.g.  $\text{NH}_4\text{H}_2\text{PO}_4$ ) crystals, where randomly competing interactions lead in a certain concentration range  $x_{\min} \leq x \leq x_{\max}$  to frustration and the occurrence of a glassy phase without FE and AFE long-range order. Another feature which distinguishes proton and deuteron glasses from spin glasses, namely the occurrence of RFs, which are absent in spin glasses.<sup>25</sup>

## 2.1. Method of detection

A pulsed NMR spectrometer, with a variable frequency and variable temperature facility is best suited for the study of these disordered systems.<sup>26,27</sup> For dipolar glasses and relaxor systems, a spin echo Fourier transformation NMR spectra of the system have been measured in a wide bore superconducting magnet ( $\sim$  typically at 9.2 T).

In this section, we will be concentrating mainly on the use of NMR technique based literature on dipolar glasses and the information obtained from them. The NMR nuclei studied in dipolar glasses are  $^1\text{H}$ ,  $^2\text{H}$  and  $^{87}\text{Rb}$  and  $^{31}\text{P}$ .  $^{207}\text{Pb}$ ,  $^{45}\text{Sc}$  and  $^{93}\text{Nb}$  are other nuclei which are studied in relaxor materials.

Generally, the relaxation in these materials is attributed to the reorientation of the symmetric groups and motion of hydrogen bonds. The normal behaviour of (1) single exponential magnetization recovery, (2) relaxation time versus temperature exhibiting a BPP behaviour, (3) FE and AFE phase transition observed in parent compounds will disappear in the mixed system. New features observed are (a) the recovery of the non-equilibrium magnetization is non-exponential, showing a signature of spatial inhomogeneity, resulting from a cluster distribution (b) anomalous line broadening of the line width requiring  $\omega\tau_c \gg 1$ , and



$\omega_L \tau_{c2} \ll 1$ , suggests the distribution of  $\tau_{c2}$  from  $10^{-10}$  to  $10^{-3}$  s. (c) The existence of a  $T_1$  minimum in the region of onset of dielectric losses implies a tremendous slowing down of the proton intra-bond (O–H–O) switching motion from  $10^{-11}$  to  $10^{-8}$  s, not observed in  $\text{KH}_2\text{PO}_4$ -type crystals. Our main concern is to interpret this behaviour with proper reasoning. The range of  $\tau_c$  observed in the mixed system raises a question whether a glass transition temperature  $T_G$  can be defined at all. Many NMR methods<sup>3</sup> have been adopted to explore their properties which are discussed in the following sections.

## 2.2. Line shape analysis

In disordered materials, there will be an inhomogeneous distribution of resonance frequency  $f(\nu)$  arising from each physically non-equivalent site in the unit cell, instead of a single homogeneous resonance line as in translationally invariant crystalline materials. The inhomogeneous broadening of the resonance lines has different origins in different types of glasses. In magnetic spin glasses, the randomly distributed local magnetic fields are responsible for this, whereas in the proton (deuteron) pseudo-spin glasses or in quadrupolar glasses the randomly distributed electric field gradients (EFGs) which interact with nuclei of non-zero electric quadrupole moment are responsible for the broadening. Because of the spatial disorder, EFG tensor components are randomly distributed in both orientation and magnitude. The resulting inhomogeneity of the electric quadrupole interaction is essentially static in nature and reflect quenched random disorder in the lattice. A study of the inhomogeneous frequency distribution (line shape) thus provides useful information with respect to static disorder in these glassy systems. A 2D NMR inhomogeneous versus homogeneous line shape separation technique can be used to separate out the inhomogeneous and homogeneous part of the line shape.<sup>28</sup> In  $^{87}\text{Rb}$   $^2\text{D}$  NMR experiment in the proton glass (PG) system  $(\text{ND}_4)_x\text{Rb}_{1-x}\text{D}_2\text{PO}_4$  with  $x=0.44$ , Dolinšek<sup>28</sup> have shown that the homogeneous line shape is Lorentzian while the broad, highly asymmetric inhomogeneous line shape is given<sup>4,29</sup> by Equation (1).

$$W(p) = \frac{1}{\beta\bar{J}(2\pi(q + \bar{\Delta}))^{1/2}} \frac{1}{1 - p^2} \exp\left(-\frac{1}{2} \frac{(\tanh^{-1}p)^2}{\beta^2\bar{J}^2(q + \bar{\Delta})}\right) \quad (1)$$

## 2.3. Spin–lattice relaxation studies

Apart from extracting the local RF distribution and the determination of  $q_{\text{EA}}$  from the analysis of NMR line shapes, SLR studies can reveal the molecular dynamics characteristics of PGs. Most of the SLR studies in these systems have been performed using the quadrupolar nuclei like  $^{87}\text{Rb}$  and  $^2\text{D}$ , other than  $^1\text{H}$ , the advantage being that the quadrupolar interaction can provide a probe for studying either structural variations or molecular motions in the vicinity of the quadrupolar nuclei and this being especially useful in monitoring the deuteron dynamics in the O–D---O bonds, as the freeze-out of protons (deuterons) in this bond is a

characteristic feature of the PG state. Furthermore, quadrupolar interactions being electrostatic in nature are sensitive to the effects of electric dipolar disorder. The other NMR nuclei in RADP/D-RADP systems namely  $^1\text{H}$  and  $^{31}\text{P}$  which are spin-1/2 nuclei are not that extensively used as the quadrupolar nuclei. However many PG properties, such as freezing of polarization cluster ordering, stretched exponential relaxation behaviour, etc. can be observed by means of dipolar relaxation of a spin-1/2 nucleus. There is also an advantage in using spin-1/2 nuclei in that the quadrupolar nuclei will have multiple transitions from the unequally spaced energy levels, whereas the spin-1/2 nuclei have got only a single transition. Owing to the multiple transitions in quadrupolar nuclei, it is often difficult to separate out the effects due to a distribution of correlation times from the multi-level quadrupolar effects.<sup>30</sup>

The reason why NMR spectroscopy is so successful in the study of D-RADP system is the existence of local and non-local NMR probes in this system. While, the covalently bonded deuteron sees only the local polarization, but not the polarization of the neighbouring deuteron, the ionically bonded Rb observes a range about  $\pm 2$  lattice constants and is thus capable of distinguishing between different spatial correlations of deuteron order. Furthermore, the characteristic time scale of NMR for time averaging is in the order of millisecond, and can be extended to the order of 100 s by means of 2D NMR exchange measurements. It can thus be considered as a quasi-static investigation method.<sup>24</sup>

## 2.4. 1-Dimensional and 2-dimensional O-D---O deuteron exchange NMR

1-Dimensional (1D) NMR, using line shape, estimating the Edwards–Anderson parameter  $q_{\text{EA}}$ , is applicable to systems, on the time scale of the order  $10^{-3}$ – $10^{-8}$  s and this method fails for the direct determination of  $q_{\text{EA}}$  on longer time scales.

The use of quadrupole-perturbed 1D  $^2\text{H}$  NMR spectroscopy and in particular two-dimensional (2D)  $^2\text{H}$  NMR exchange spectroscopy do look very promising as regards elucidating the details of the hydrogen dynamics. Such investigations are also expected to give new insight into the discrepancy between the higher rates of chemical exchange and lower electrical conductivity (DBP)—and vice versa (DBPI)—recently observed.

The 2D deuterium NMR exchange spectroscopy has been made using the technique of Schmidt et al.<sup>31</sup> The corresponding pulses sequence selects the signal of the form

$$F_{\text{CC}}(t_1, t_2, t_m) = e^{-t_m/T_1} e^{-(t_1+t_2)/T_2} \begin{bmatrix} a_{AA}(t_m) \cos(\omega_A t_1) \cos(\omega_A t_2) + \\ a_{BB}(t_m) \cos(\omega_B t_1) \cos(\omega_B t_2) + \\ a_{AB} \cos(\omega_A t_1) \cos(\omega_B t_2) + \\ a_{BA}(t_m) \cos(\omega_B t_1) \cos(\omega_A t_2) \end{bmatrix} \quad (2)$$

The first two terms in the bracket give—after a 2D Fourier transform—the diagonal peaks in the spectrum, where as the last two terms give the cross-peaks.

The ratio of the intensities of the cross-peaks and the diagonal peaks are related to the glass order parameter  $q_{EA}$

$$R(x \rightarrow \infty) = \frac{1 - q_{EA}}{1 + q_{EA}} \quad (3)$$

$R$  is always smaller than 1. If  $q_{EA} \neq 0$ . A 2D NMR experiment, thus always the measurement of  $R(x \rightarrow \infty)$ , and always the determination of  $q_{EA}$ , in the slow motion regime, where the determination of  $q_{EA}$  from line shape is no longer possible.

#### 2.4.1. RADP system (deuterated)

The problem which makes experimental studies of proton and deuteron glasses so difficult is that the Edwards–Anderson order parameter  $q_{EA}$  characterizing the deuteron glass has no macroscopic conjugate field and is therefore hard to measure. Here, Blinc et al.<sup>5</sup> have shown that quadrupole-perturbed NMR allows a direct experimental determination of the average local-polarization distribution function  $W(p)$  and its second moment, the Edwards–Anderson order parameter  $q_{EA}$ . Thus an experimental determination of  $f(v)$  (line shape function) immediately yields the probability distribution of local polarization  $W(p)$  or the second moment of  $f(v)$  is directly proportional to the Edwards–Anderson order parameter. One should note that there is a clear separation line between high temperature ergodic pseudo-spin-glass phase characterized by a single-order parameter  $q = q_{EA}$  from the non-ergodic low temperature phase characterized by an order parameter function  $q(x)$  with  $0 < x < 1$ .

Deuteron and  $^{87}\text{Rb}$  NMR data have been reported for D-RADP-55. The temperature dependence of both the O–D–O deuteron and the  $^{87}\text{Rb } \frac{1}{2} \rightarrow -\frac{1}{2}$  SLR rates show broad and asymmetric minima near 90 K. This has to be contrasted with the findings in the pure compounds.

Line shape studies of  $^{87}\text{Rb}$  and deuteron NMR lines have thrown more light on the frustration in the system. Blinc et al.<sup>5</sup> have shown clearly the measurement of second moment can be related to the Edwards–Anderson spin-glass order parameter in the glass phase.

Blinc et al.<sup>4</sup> in a classic paper on the NMR line shapes in PGs have presented the relation between the RF distribution and the quadrupole-perturbed NMR line shape for both first-order and second-order quadrupole effects. Static as well as time fluctuating RFs have been considered. By evaluating the local RF distribution, Blinc et al.<sup>4</sup> have evaluated the Edwards–Anderson ( $q_{EA}$ ) order parameter.

The Edwards–Anderson spin-glass order parameter is defined as<sup>32</sup>

$$q_{EA} = \frac{1}{N} \sum_i \langle S_i^Z \rangle^2 = \left[ \langle S_i^Z \rangle^2 \right]_{Av} \quad (4)$$

where  $N$  is the number of lattice sites,  $\langle \dots \rangle$  represents the thermal average, while  $[\dots]_{Av}$  denotes the disorder average that is, the simultaneous average over random bonds and RFs. It has to be noted that  $S^Z = \pm 1$  represents the two possible positions of the reorientable dipole in the case of proton/deuteron pseudo-spin glasses.

The average probability distribution of the local polarization  $\mathbf{p}$  is defined as

$$W(p) = \frac{1}{N} \sum_i \delta(p - \langle S_i^Z \rangle) = [\delta(p - \langle S_i^Z \rangle)]_{Av} \quad (5)$$

It is well known that the first moment of the distribution  $W(p)$  is the total polarization  $P$ , which is zero in the absence of a homogeneous external electric field, while its second moment is related to the  $q_{EA}$  order parameter<sup>5</sup> as

$$q_{EA} = \int dp p^2 W(p) \quad (6)$$

In the case of RADP or D-RADP,  $W(p)$  can be evaluated using the Ising pseudo-spin model with infinitely ranged random interaction and quenched RFs.<sup>33,34</sup> The Hamiltonian is expressed as

$$H = -\frac{1}{2} \sum_{i,j} J_{ij} S_i^Z S_j^Z - \sum_i f_i S_i^Z \quad (7)$$

where  $J_{ij}$  denotes the infinite-range quenched random interactions between the pseudo-spins  $S_i^Z$  and  $f_i$  represents the random local longitudinal field at the site  $i$ . The random interactions  $J_{ij}$  and fields  $f_i$  are independently distributed according to the Gaussian distribution,

$$\begin{aligned} D(J_{ij}) &= \frac{1}{\sqrt{2\pi}J^2} \exp\left(-\frac{J_{ij}^2}{2J^2}\right) \\ D(f_i) &= \frac{1}{\sqrt{2\pi}\Delta} \exp\left(-\frac{f_i^2}{2\Delta}\right) \end{aligned} \quad (8)$$

where  $J^2$  and  $\Delta$  are the variance of the distributions with mean zero. In order to perform the average over the disorder in Equation (8), the replica formalism as known from the theory of spin glasses is used.<sup>35</sup> For the replica symmetric phase, the average probability distribution of the local polarization is given as

$$W(p) = \frac{1}{\beta \bar{J} (2\pi(q + \bar{\Delta}))^{1/2}} \frac{1}{1 - p^2} \exp\left(-\frac{1}{2} \frac{(\tanh^{-1} p)^2}{\beta^2 \bar{J}^2 (q + \bar{\Delta})}\right) \quad (9)$$

Blin et al.<sup>4</sup> have plotted the distribution function for  $\Delta = 0.35$  and several values of reduced temperature  $T/J$ . For  $T < T_G \equiv J$ ,  $W(p)$  exhibits a two peak structure with maxima near  $p = \pm 1$ . At  $T \approx T_G$ ,  $W(p)$  flattens out and for  $T > T_G$ , it becomes bell-shaped distribution with a maximum at  $p = 0$ . With increasing temperatures, the width of  $W(p)$  decreases and for extremely high temperatures it behaves asymptotically as  $\lim_{T \rightarrow \infty} W(p) = \delta(p)$ . They have measured the O-D · · · O deuteron and <sup>87</sup>Rb ½ → -½ quadrupole-perturbed NMR spectra for RADP single crystals with  $x = 0.44$ , at an orientation where the relation between  $\omega$  and  $p$  is close to being linear. The inhomogeneous broadening has been found to be much larger than the

homogeneous line width  $\nu$  measured by the Hahn echo. By subtracting the contribution due to the homogeneous line width, they have obtained the temperature dependence of the Edwards–Anderson order parameter from the second moment of the  $^{87}\text{Rb } \frac{1}{2} \rightarrow -\frac{1}{2}$  line shapes. The temperature dependence of the parameter  $q_{\text{EA}}$  could not be fitted either using a pure glass-transition model ( $J^2 \neq 0, \Delta \approx 0$ ) or by a pure RF model ( $J^2 = 0, \Delta \neq 0$ ) for any value of  $J$  or  $\Delta$ . This indicates an RF smearing of the Ising pseudo-spin glass transition in D-RADP as predicted by Pirc et al.<sup>33</sup> To extract the local-polarization distribution function from the NMR data, they have studied the O–D---O deuteron line shapes as a function of temperature.<sup>4</sup> The experimental deuteron line shapes and  $W(p)$  have shown the predicted change from a single-peaked structure at high temperature to a double peaked structure at low temperature. All the line shape results have been obtained in the fast motion regime. To conclude the section on the relevance of line shape analysis as applied to proton/deuteron glasses, the following points are worth mentioning again: (1) The determination of the quadrupole-perturbed NMR line shape allows for a determination of the local RF distribution  $W(p)$  and a determination of the Edwards–Anderson spin-glass order parameter  $q_{\text{EA}}$  and (2) the deuteron as well as Rb quadrupole-perturbed NMR data show that in these systems one deals with an “RF smearing random-bond” type pseudo-spin glass transition and not with an RF type freezing or a classical random bond type spin-glass transition.

$^{87}\text{Rb}$  and  $^2\text{H}$  NMR in D-RADP-55 have been reported by Blinc et al.<sup>6</sup> In this work, they have demonstrated that the distribution of the RFs which breaks the local symmetry of the high-temperature phase can be extracted from the difference between the inhomogeneous and homogeneous NMR line shapes. Their SLR data show that the local freezing dynamics is determined by the randomly biased freeze-out of the O–D---O deuteron intra-bond motion. The temperature dependence of both the O–D---O deuteron and the  $^{87}\text{Rb } (\frac{1}{2} \rightarrow -\frac{1}{2})$  SLR rates show broad and asymmetric minima near 90 K. The anomalous diffusion of  $\text{D}_3\text{PO}_4$  defects is thought to determine the  $^{87}\text{Rb}$  and  $^2\text{H}$  relaxation at low temperatures. The minimum in the  $^2\text{H}$  NMR  $T_1$  around  $T = 180$  K is attributed to the relaxation due to the  $\text{ND}_4$  reorientation and it follows a BPP behaviour with temperature.

Dolinšek et al.<sup>7</sup> have reported the existence of quantum tunnelling in these systems. This has been observed from the temperature-independent behaviour of  $^{87}\text{Rb}$  and  $^2\text{H}$  NMR SLR times at low temperatures ( $1.6 < T < 10$  K). Quantum tunnelling in these systems refers to the tunnelling of protons/deuterons in the double-well potential. In a  $^{31}\text{P}$  NMR relaxation time measurements by Chen et al.<sup>30</sup> in D-RADP systems, have found an additional  $T_1$  minimum at low temperatures apart from the BPP  $T_1$  minimum at high temperatures. The low temperature minimum has been attributed to the extreme slowing down of the O–D---O intra-bond motion which is unique to the glassy phase.

#### 2.4.2. RADP system (protonated)

Salient experimental features exhibited by RADP/D-RADP type mixed systems are (1) diffuse scattered intensities at temperatures less than 100 K, (2) a broad rather than a sharp Cusp in the dielectric susceptibility experiment at the PG transition temperature (unlike in spin glasses), (3) deviation of the temperature

dependence of the lattice constant from normal anharmonic behaviour, (4) the appearance of well-defined librational modes of cations at temperatures less than 100 K, (5) the extreme slowing down of proton/deuteron dynamics resulting in additional  $T_{1\min}$  in the PG state, (6) quantum tunnelling phenomenon at very low temperatures ( $T < 10$  K), (7) appearance of double peaks in the NMR spectrum as well as asymmetric broadening of the NMR spectrum in the PG phase, (8) the different phases exhibited by these systems with a change in the ammonium concentration and (9) isotope effect.

$^{87}\text{Rb}$  and  $^1\text{H}$  SLR rate as a function of temperature is a very important parameter which shows the suppression of phase transition and reveals the frustration in the mixed system. Temperature dependence of  $T_1$  in any ordered system can be described by the well known Bloembergen-Purcell-Pound (BPP) type expression. However, disordered systems show deviations from BPP behaviour, showing a broad distribution of relaxation times. The magnetization recovery shows a stretched exponential recovery of magnetization following  $M(\tau) = M_0(1 - 2^* \exp(-\tau/T_1^*)^\alpha)$  where  $\alpha$  is the stretched exponent.

Slak et al.<sup>3</sup> have measured the  $^{87}\text{Rb}$  and  $^1\text{H}$  NMR SLR rates in  $\text{Rb}_{0.35}(\text{NH}_4)_{0.65}\text{H}_2\text{PO}_4$  as a function of temperature at a Larmor frequency of 30.78 MHz. The proton  $T_1$  is dominated by the  $\text{NH}_4$  reorientations and exhibits a broad minimum near 175 K. The activation energy for the  $\text{NH}_4$  reorientation is found to be 13.4 kJ/mol (138 meV) and the correlation coefficient is of the order of  $10^{-13}$  s. From room temperature, down to 120 K, the temperature dependence of  $T_1$  could be explained by the BPP theory. The departure from the BPP behaviour below  $\sim 120$  K is attributed to a distribution in the relaxation times.

From 300 to 120 K, the  $^{87}\text{Rb}$  SLR time  $T_1$  slowly increases with decreasing temperature which is attributed to  $90^\circ$  reorientations of the  $\text{H}_2\text{PO}_4$  groups. Below 120 K, the  $^{87}\text{Rb}$  SLR time starts decreasing with cooling and passes through a minimum around 30 K and then increases with a further decrease in temperature. The process of intra-bond jump has been invoked to explain the relaxation behaviour below 120 K. The intra-bond hydrogen jump modulates the EFG around the  $^{87}\text{Rb}$  nucleus thereby affecting the relaxation. The minimum occurs when the intra-bond jump becomes of the order of the nuclear Larmor frequency ( $\omega_0\tau_c = 1$ ). The authors have proposed two models to explain the  $^{87}\text{Rb}$   $T_1$  behaviour; in one model they have proposed an Arrhenius law with a temperature-dependent distribution of hindering barriers and in the other model they have assumed a Vogel-Fulcher law<sup>36</sup> with a temperature-independent distribution of activation energies.

NMR is rather limited in its frequency range. It has however the important advantage that it is site-specific and allows the detailed determination of the local behaviour of a given elementary dipole. Blinc et al.<sup>4</sup> has carried out NMR experiment to verify the deuteron intra-bond motion in deuteron glasses is a pure Arrhenius-like thermally activated process or whether deuteron tunnelling effects become important at low temperatures.

Blinc et al.<sup>4</sup> have carried out a measurement of the  $^{87}\text{Rb}$  SLR rate in a  $\text{Rb}_{0.58}(\text{ND}_4)_{0.42}\text{D}_2\text{PO}_4$  single crystal in a wide temperature range allowed for a discrimination between classical thermally activated deuteron jumping across the

potential barrier between the two equilibrium sites in the H-bond and phonon-assisted incoherent deuteron tunnelling. The results show that thermally activated deuteron intra-bond jumping dominates above 55 K whereas at lower temperatures phonon-assisted deuteron tunnelling becomes rate determining. This result seems to be the first direct evidence for incoherent phonon-assisted deuteron tunnelling in H-bonded systems.

Kind et al.<sup>37</sup> reported on the first observation of the dynamics of correlated hydrogen switching among the six Slater  $D_2PO_4$  configurations, induced by unpaired  $D_3PO_4$  and  $DPO_4$  Takagi group diffusion in a deuteron glass  $Rb_{0.5}ND_{4(0.5)}D_2PO_4$ . The results obtained by 2D  $^{31}P$  exchange NMR prove the validity of the Slater–Takagi ice rules and allow for the direct determination of the correlation time for the unpaired Takagi group visits to a  $D_2PO_4$  group. Their experimental method is based on the fact that  $^{31}P$  chemical shift tensors discriminate among different  $H_2PO_4$  configurations.

**2.4.2.1. Low temperature properties of proton and deuteron glasses** Solid solutions of hydrogen-bonded FE and AFE crystals such as  $Rb_{1-x}(NH_4)_xH_2PO_4$  form in a certain concentration range a glassy phase, where no macroscopic symmetry change occurs on cooling down to the lowest temperatures reached. It is usually assumed that the motion of the protons or deuterons in the double-well O–H···O potentials is randomly frozen out at low temperatures implying a static quenched disorder characteristic of orientational glasses.<sup>38,39</sup>

In view of the fact that specific heat measurements<sup>40</sup> show the presence of dynamic disorder and possible quantum tunnelling at low temperatures. To check this hypothesis, Blinc et al.<sup>41</sup> have performed a site-specific search for this motion. Deuteron intra-H-bond motion seemed to be the most likely candidate for this kind of dynamic disorder. Blinc et al.<sup>41</sup> have measured  $^{87}Rb$ , deuteron SLR time at low temperatures, as well as performed a 2D deuteron exchange NMR experiment on the O–D···O deuterons in D-RADP and  $Rb_{0.68}(ND_4)_{0.32}D_2AsO_4$  (DRADA-32).

At lower temperatures, the  $A' \leftrightarrow B$  and  $A \leftrightarrow B'$  intra-H-bond exchange time becomes low on the NMR time scale so that we are in the slow motion regime ( $\Delta\omega \gg 1$ ). The deuteron NMR frequency now depends on the instantaneous value of the pseudo-spin  $S_i^Z$

$$\nu_i = \nu_0 + \nu_2 + \nu_1 S_i^Z \quad (10)$$

Here, the information on deuteron motion can be obtained by 2D exchange NMR<sup>41</sup> where the observation window—determined by the mixing period (Figure 2)—for intra-H-bond exchange is extended by five orders of magnitude into the  $10^2$ – $10^3$  s region.

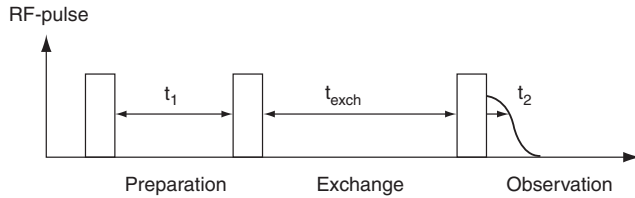
When no chemical exchange between two physically non-equivalent sites A and B takes place, one finds in such an experiment in the  $\omega_1$ – $\omega_2$  plane only diagonal peaks at positions  $\omega_{AA}$ – $\omega_{BB}$ . If however chemical exchange does take place, cross-peaks appear at  $\omega_{AB}$ – $\omega_{BA}$  A positions.

The X-bond O–D···O, 2D deuteron exchange NMR spectrum in DRADA with  $x=0.32$  at 40 K is shown in Figure 3 at mixing times  $t_{mix}=10$  and 30 s. Cross-peaks

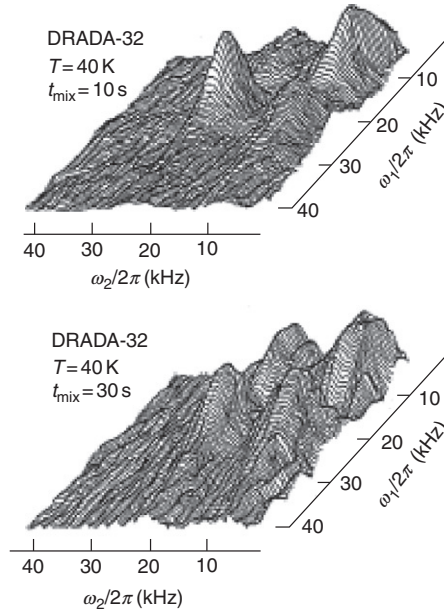
are clearly visible at  $t_{\text{mix}}=10$  s and become as strong as the diagonal peaks at  $t_{\text{mix}}=30$  s. From the time dependence of the relative intensities of the cross-peaks

$$R = \frac{I_{AB}}{I_{AA}} = \tanh\left(\frac{t_{\text{mix}}}{\tau_{\text{exch}}}\right) \quad (11)$$

Their measurements showed  $\tau_{\text{exch}} \approx 15$  s at 45 K and 236 s at  $T=24$  K. This demonstrates that dynamic intra-H-bond deuteron disorder  $\text{O}-\text{D}\cdots\text{O} \leftrightarrow \text{O}\cdots\text{D}-\text{O}$  is still present in DRADA at low temperatures in the glassy phase. A measure-



**Figure 2** Radio frequency pulse sequence for a 2D deuteron exchange NMR experiment.



**Figure 3** 2D  $\text{O}-\text{D}\cdots\text{O}$  deuteron exchange NMR spectra of DRADA-32 at  $T=40$  K for  $t_{\text{mix}}=10$  and 30 s. In addition to the diagonal peaks, the  $\text{O}-\text{D}\cdots\text{O} \leftrightarrow \text{O}\cdots\text{D}-\text{O}$  exchange cross-peaks are clearly visible.



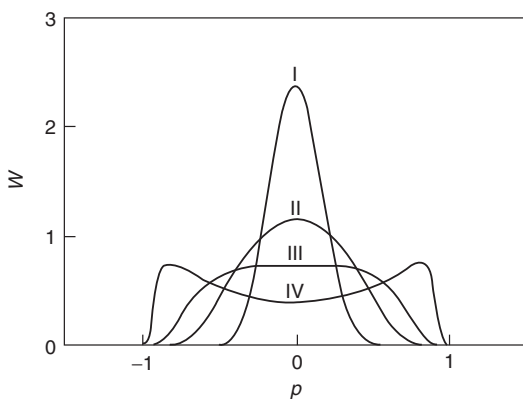
ment of the temperature dependence of the intensities of the O-D $\cdots$ O deuteron lines relative to (ND<sub>4</sub>)<sub>1-x</sub>(KI)<sub>x</sub> with  $x=0.2$  showed that no intensity is lost between 100 and 20 K so that in  $\tau_{\text{exch}}$  all O-D $\cdots$ O deuterons move from one equilibrium site in the H-bond to another ( $A \leftrightarrow B$ ).

2D deuteron exchange NMR and  $^{87}\text{Rb}$  SLR time measurements in (DRADA-32) PGs show that the O-H $\cdots$ O dipoles are not completely frozen out at low temperatures but show dynamic features characteristic of incoherent tunnelling. RADP and D-RADP are thus quantum glasses. A comparison of  $W_n^{-1}$  SLR rates show that minima occur at 90 K for D-RADP-42, whereas at 25 K for RADP-50, thus demonstrating the tremendous isotope effect in the intra-H-bond dynamics.

Specific heat measurements<sup>40</sup> indicate that the assumption of static frozen glass disorder at low temperatures may be too restrictive and that the intra-H-bond hydrogen motion may still persist in the form of quantum tunnelling. To check this hypothesis, 2D deuteron NMR and  $^{87}\text{Rb}$  and  $^2\text{H}$  SLR measurements were carried out at low temperatures. With site-specific NMR measurements, it was also hoped to identify the microscopic nature of the “two-level” states which determine the low  $T$  glassy properties of these systems.

$$T_G = \frac{J}{k_B}, \quad T_\Delta = \frac{\sqrt{\Delta}}{k_B}, \quad T_\Omega = \frac{\Omega}{k_B} \quad (12)$$

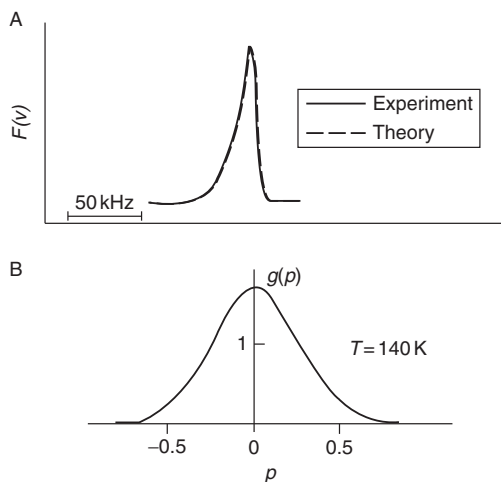
In Figure 4, the local-polarization distribution  $W(p)$  is shown as a function of  $p$  at zero temperature for a fixed RF variance  $\Delta/J^2=0.1$  and various values of  $\Omega/J=T_\Omega/T_G=2, 1.2, 1$  and  $0.75$ . Whereas  $W(p)$  is single peaked for cases I, II, and III (i.e. at large  $T_\Omega/T_G$ ), it becomes double peaked in case IV where  $T_\Omega/T_G < 1$ . The decrease of  $\Omega$  has here a similar effect on  $W(p)$  as the decrease in temperature in the RB-RF model without tunnelling.



**Figure 4** Local-polarization distribution  $W(p)$  at zero temperature for a fixed RF variance  $\Delta/J^2=0.1$  and various values of the tunnelling frequency  $\Omega/J=T_\Omega/T_G=2$  (I), 1.2 (II), 1 (III), and 0.75 (IV).

Blinç et al.<sup>29</sup> have carried out studies on the temperature and angular dependence of the  $\text{ND}_4$  deuteron using FT NMR spectra for a series of mixed  $\text{Rb}_{1-x}(\text{ND}_4)_x\text{D}_2\text{PO}_4$  single crystals at 42.462 MHz. The temperature dependence of the  $\text{ND}_4$  deuteron NMR line shape shows a doublet spectrum between 290 and 158 K. They have observed acid deuteron freeze-out for above  $T_G$  in the title compound and the results are interpreted as a result of RF smearing induced by substitutional disorder which acts as an ordering field conjugate to the Edwards–Anderson spin-glass order parameter and induces a finite value of the order parameter far above the nominal transition temperature  $T_G$ . This results in a random gradual O–D–O deuteron freeze-out which in turn produces a broadening of the NMR line.

$^{87}\text{Rb}$  ( $\frac{1}{2} \rightarrow -\frac{1}{2}$ ) NMR spectra were measured by Blinç et al.<sup>6</sup> in  $\text{Rb}_{0.45}(\text{ND}_4)_{0.55}\text{D}_2\text{PO}_4$  by FT of the off-resonance spin echoes of the above single crystal. The  $^{87}\text{Rb}$  magnetization recovery was found to be describable by a “stretched” exponential recovery function, while in pure RDP it was single exponential, for the same orientation of the crystal. The shift of  $^{87}\text{Rb}$   $T_1$  minimum from 30 K in the un-deuterated system to 90 K in the deuterated one demonstrates the importance of the H-bond dynamics in the transition. The  $\tau$  values deduced from the fit show a tremendous slowing down of the deuteron intra-bond motion from  $10^{-13}$  s at room temperature to more than  $10^{-2}$  s at 30 K that dominates the  $^{87}\text{Rb}$  as well as the freezing dynamics. The formation of quasi-static, randomly oriented, locally polarized clusters is best seen from the asymmetry of the inhomogeneous  $^{87}\text{Rb}$  ( $\frac{1}{2} \rightarrow -\frac{1}{2}$ ) line shape (Figure 5A) for  $c \parallel H_0$ . The observed asymmetry of the line shape shows that the principal source of line broadening is static



**Figure 5** (A)  $^{87}\text{Rb}$  ( $\frac{1}{2} \rightarrow -\frac{1}{2}$ ) NMR line shape for  $c \parallel H_0$  and  $T=140\text{ K}$ . The solid line represents the fit to theoretical expressions. (B) Static and quasi-static RF distributions  $g(p)$  deduced from inhomogeneous  $^{87}\text{Rb}$  line shape.

on a  $T_2$  time scale. The obvious explanation is that nuclei in differently polarized clusters have different resonance frequencies and that ergodicity is broken on the NMR time scale as  $p$  is non-zero. The distribution of resonance frequencies  $f(v)$  is then simply related to the spatial distribution  $g(p)$  of static RFs (Figure 5B).

Thus,  $^{87}\text{Rb}$  NMR studies on  $\text{Rb}_{0.45}(\text{ND}_4)_{0.55}\text{D}_2\text{PO}_4$  reveal that the deuteron “pseudo-spin-glass” transition is just not a simple kinetic slowing down process, but due to a gradual condensation of randomly polarized clusters. The results provide novel information on the temperature dependence and distribution of local RFs and their dynamics. Further, the NMR data suggest that the “pseudo-spin O–D–O deuteron intra-bond motion determines freezing dynamics.

$$f(v) dv = g(p) dp \quad (13)$$

#### 2.4.3. $\text{Rb}_{1-x}(\text{NH}_4)_x\text{H}_2\text{AsO}_4$ systems

Sobol et al.<sup>8</sup> have measured proton SLR time ( $T_1$ ) in  $\text{Rb}_{1-x}(\text{NH}_4)_x\text{H}_2\text{AsO}_4$  systems in the range 100–4.2 K. Magnetization recovery was found to be non-exponential in the entire range of temperature. The MR data fit to a stretched exponential recovery and the exponent  $\alpha$  was found to be temperature dependent implying broadening of the distribution of microscopic correlation times  $\rho(\tau')$  with decreasing temperature.

It is not clear, whether the experimentally observed random local freezing of the deuterons in the O–D–O bonds in deuteron glasses corresponds to a true thermodynamic phase transition or whether one deals with a dynamic phenomenon which only seems static because of the finite observation time of the experimental techniques. The recently observed<sup>42</sup> splitting between the field-cooled and zero-field dielectric susceptibilities below an instability temperature  $T_i$  seems to speak for the occurrence of an Almeida–Thouless-like thermodynamic phase transition in deuteron glasses. It is well known that 1D NMR and EPR allow a direct measurement of the Edwards–Anderson order parameter  $q_{\text{EA}}$  only on time scales of  $10^{-3}$ – $10^{-8}$  s and 2D exchange NMR possibly seems to be a better technique for such slow motions.

An important open question regarding PGs, in general is that whether in these systems one deals with an equilibrium phase transition or with a metastable kinetic phenomenon observed because of the finite experimental observation time. It is known that on the frequency observation scales of SLR and line shape studies ( $10^3$ – $10^8$  Hz), the deuteron/PG phase appears static. But 2D exchange NMR extends the frequency of observation window into the millihertz region. Dolinšek et al.<sup>9</sup> have measured (1) Proton and deuteron SLR time (2)  $^2\text{D}$  exchange NMR O–D–O deuteron study in  $\text{Rb}_{0.68}(\text{ND}_4)_{0.32}\text{D}_2\text{AsO}_4$  single crystal to verify the random pseudo-spin Ising model, namely the O–H–O bonds are the elementary reorientable two position dipoles. They determined O–D–O deuteron intra-bond exchange time  $\tau_{\text{exch}}$  in  $\text{Rb}_{0.68}(\text{ND}_4)_{0.32}\text{D}_2\text{AsO}_4$  as a function of temperature. They have detected very slow fluctuations in the H-bond double minimum potential which averages out the H-bond asymmetry and the glass order parameter to zero at long-enough times. They have concluded that the glass state in PGs is not a thermodynamic long-lived state but a kinetic phenomenon.

Blinic et al.<sup>10</sup> have reviewed the present understanding of two recent advances in proton and deuteron glasses namely, (a) the determination of  $q_{EA}$  and  $W(p)$  in the “weak substitutional disorder” limit ( $J_o > J$ ) via  $^{75}\text{As}$  NQR and NMR and (b) the application of 2D “exchange” deuteron NMR to the study of deuteron inter- and intra-bond transfer rates in deuteron glasses on time scales  $1\text{--}10^3$  s.

Blinic et al.<sup>10</sup> have performed 2D exchange NMR experiments to find the direct determination of intra- and inter-H-bond deuteron exchange in  $\text{Rb}_{0.68}(\text{ND}_4)_{0.32}\text{D}_2\text{AsO}_4$ , containing the case that the two sites, between which exchange takes place, giving rise to clearly resolved distinct absorption peaks. The results agree with the basic predictions of the random bond RF Ising pseudo-spin model of deuteron and PGs.

#### 2.4.4. $\text{K}_{1-x}(\text{NH}_4)_x\text{H}_2\text{PO}_4$ systems

In order to fully understand these systems, Kannan et al.<sup>11</sup> have taken up detailed investigations in the mixed systems composed of FE potassium dihydrogen phosphate (KDP) and anti-ferroelectric ADP. The results of the investigations carried out in these mixed systems  $(\text{NH}_4)_x\text{K}_{1-x}\text{H}_2\text{PO}_4$  (KADP) for  $x = 0.25, 0.49, 0.61$ , using  $^1\text{H}$  NMR SLR time measurements as a function of temperature down to 4.2 K. Their  $T_1$  experiments have revealed, apart from the  $T_1$  minimum due to the ammonium group reorientation at higher temperatures, additional  $T_1$  minima at low temperatures. Further, they have found that the nuclear magnetisation recovery follows a stretched exponential on decreasing the temperature of the sample, which is a typical characteristic of glassy systems.<sup>43</sup> Surprisingly, they found that on further cooling, at very low temperatures ( $T < 20$  K), the nuclear magnetisation recovery tends to become single exponential.

#### 2.4.5. $\text{Rb}_{0.7}\text{Tl}_{0.3}\text{H}_2\text{PO}_4$

Wu et al.<sup>12</sup> have investigated PG behaviour in  $\text{Rb}_{0.7}\text{Tl}_{0.3}\text{H}_2\text{PO}_4$ —using  $^{205}\text{Tl}$  and  $^{87}\text{Rb}$  NMR. A solid solution of FE  $\text{RbH}_2\text{PO}_4$  and AFE  $\text{TlH}_2\text{PO}_4$  (TDP) with  $x = 0.3$  has been prepared to look for substitutional disorder of  $\text{Rb}^+$  ions by  $\text{Tl}^+$  ions. Thallium-doped RDP system shows a PG behaviour around 50 K, exhibiting a  $T_1$  minimum in thallium NMR. This indicates the tremendous slowing down of proton intra-bond (O–H–O) jump motion. They also observed an onset of PG behaviour (progressive freezing) starts around 147 K itself, revealed as a deviation of thallium  $T_1$  as well as the appearance of double exponential magnetization recovery of  $^{87}\text{Rb}$  NMR. The high value of  $T_1$  observed in thallium system shows that magnetic dipolar interactions are responsible for relaxation in this system in contrast to RADP system which is quadrupolar in nature.

$^{87}\text{Rb}$  NMR showed a single exponential recovery of magnetization.  $T_1$  initially started decreasing with decreasing temperature and exhibited a shallow minimum at about 147 K, on further cooling below this temperature, the magnetization recovery showed a double stretched exponential with intensity ratio of 45:55. This demonstrated the existence of two  $^{87}\text{Rb}$  sites with a spatial inhomogeneity resulting in a cluster distribution.

#### 2.4.6. Betaine phosphate/phosphate mixed crystals (protonated)

Blinic and co-workers have extensively studied, the disordered systems RADP and RADA and to a much lesser extent KADP and KADA and their deuterated analogues<sup>3,4,26–29</sup> using  $^2\text{H}$  and  $^{87}\text{Rb}$  NMR. In these systems, O–H---O bonds form a three-dimensional (3D) network of hydrogen bonds connecting the phosphate tetrahedra. On the other hand, in the BP–BPI family, the H-bonds linking the phosphate or phosphite groups, form quasi-1D chains, resulting in highly anisotropic characteristics. The reduced effective dimensionality of the dipolar coupling has also stimulated considerable theoretical interest in the BP–BPI family. Thus, disordered systems like  $\text{BPI}_{(1-x)}\text{BP}_x$ , prepared from a combination of FE and AFE compounds, are very interesting to investigate, particularly, to know how structural (site-specific) or orientational disorder may affect the dynamics of the proton groups, as a function of temperature. The underlying microscopic randomness due to local fluctuations of composition can result in static lattice strains which can have notable effect on the SLR time as observed in NMR experiments.<sup>44</sup>

Mixed systems made from a combination of FE and AFE compounds exhibit various effects of disorder in different temperature regions, and the type of effects observed depend on the technique and the window of observation employed. Dielectric studies<sup>45,46</sup> in  $\text{BPI}_{(1-x)}\text{BP}_x$ , with H-bonded networks, have revealed deviations from Curie–Weiss law, a progressive broadening of dielectric loss curves and dispersion of dielectric constant at sufficiently low temperatures, which were ascribed to the gradual freezing of the O–H–O dipoles in random orientations. These systems are interesting to investigate, particularly regarding the effect of structural (site-specific local variations) or orientational disorders on the dynamics of proton groups as a function of temperature. In these systems, inter-proton magnetic dipolar interaction, modulated by the internal motions—both classical reorientation as well as quantum rotational tunnelling is largely responsible for the proton SLR and  $^1\text{H}$  NMR SLR is therefore an appropriate technique to study the dynamics of symmetric proton groups like  $\text{CH}_3$ , trimethylammonium (TrMA), etc. in the presence of disorder.

In this section, we have discussed  $\text{BPI}_{(1-x)}\text{BP}_x$  and its deuterated analogues. Other system which is taken up for study is  $\text{BP}_x\text{GPI}_{(1-x)}$  where BP is AFE and GPI (glycine phosphate) is FE. In contrast to  $\text{BPI}_{(1-x)}\text{BP}_x$  system, one can expect severe deviations as both cation and anion are different and also their cell dimensions also have quite a bit of mismatch.

Ramanuja et al.<sup>13</sup> have carried out proton NMR relaxation measurements in AFE betaine phosphate (BP), FE betaine phosphite (BPI) and the mixed system  $\text{BPI}_{(1-x)}\text{BP}_x$  at 11.4 and 23.3 MHz from 300 to 80 K for  $x=0.0, 0.25, 0.45, 0.85$ , and 1.0. The temperature dependence of SLR time  $T_1$  exhibits two minima as expected from the BPP model in parent compounds BP and BPI. The Larmor frequency dependence of  $T_1$  in the mixed system is rather unusual and exhibits different slopes for the low-temperature wings at the two frequencies, which is a clear experimental evidence of the presence of different methyl groups with different activation energies ( $E_a$ ) indicating disorder.

$^1\text{H}$  SLR time ( $T_1$ ) measurements<sup>14</sup> have been extended to much lower temperatures (100–4 K) in  $\text{BPI}_{(1-x)}\text{BP}_x$  in the same frequency range to study the

effects of disorder. The  $T_1$  data have been analysed following Lourens' model, which show a gradual transition from classical reorientations to quantum tunnelling motions. At lower temperatures (when thermal motions become too slow), differences (due to disorder) in the local environments of the reorienting groups result in a distribution in the activation energy ( $E_a$ ) and the energy gap of the ground to the first excited torsional level ( $E_{01}$ ). Below 50 K, the system moves into the quantum tunnelling regime and the magnetization recovery shows biexponential behaviour which is another signature of disorder.

Proton NMR relaxation measurements have been carried out by Ramanuja et al.<sup>15</sup> in the mixed system of AFE betaine phosphate (BP) and FE glycine phosphate (GPI),  $\text{BP}_x\text{GPI}_{1-x}$  at 11.4 and 23.3 MHz from 300 to 100 K for  $x=0.3, 0.4, 0.5, 0.6, 0.7$  and  $0.8$ . The temperature dependence of SLR time follows the BPP model in the parent compounds, while the Larmor frequency dependence of  $T_1$  in the mixed system is rather unusual. The  $T_1$  curve exhibits different slopes for the low-temperature wings at the two frequencies, which is a clear experimental evidence of the presence of different methyl groups with different activation energies ( $E_a$ ), indicating disorder. For  $x=0.3$  and  $0.4$ , biexponential recovery of magnetization has been observed below 190 K, showing that the degree of disorder varies with the concentration. The temperature dependence of relaxation time data has been interpreted in terms of  $\text{NH}_3$ , trimethylammonium and methyl group reorientations.

The  $^1\text{H}$  NMR  $T_1$  study<sup>15</sup> of mixed systems of  $\text{BP}_x\text{GPI}_{1-x}$  in the temperature range  $300 > T > 100$  K shows the following features. In all these mixed systems, the  $T_1$  dependence on temperature does not show the expected features of the BPP model of relaxation. The activation energies of the  $\text{NH}_3$ , TrMA and  $\text{CH}_3$  groups exhibit a distribution with concentration and Larmor frequency. These observations are attributed to the presence of disorder in the mixed system varying as a function of the relative concentrations. In the concentrations 0.3 and 0.4, the magnetization recovery becomes non-exponential below 190 K and two values of  $T_1$ , viz. a short  $T_{1S}$  component corresponding to the mobile set of protons and along  $T_{1L}$  component corresponding to the non-reorienting set of protons, were observed, which is ascribed to disorder.

$^1\text{H}$  NMR SLR time ( $T_1$ ) studies<sup>16</sup> in  $(\text{BP}_x\text{GPI}_{1-x})$  have been extended down to low temperature range 100–4 K, at two Larmor frequencies 11.4 and 23.3 MHz. Analysis of  $T_1$  data indicates the presence of a number of inequivalent methyl groups and a gradual transition from classical reorientations to quantum tunnelling rotations. At lower temperatures, microstructural disorder in the local environments of the methyl groups, results in a distribution in the activation energy ( $E_a$ ) and the torsional energy gap ( $E_{01}$ ). For certain values of  $x$ , the magnetization recovery shows biexponential behaviour at lower temperatures.

#### 2.4.7. Betaine phosphate/phosphate mixed crystals (deuterated)

1D NMR parameters such as SLR time and line shape measurements give information about the dynamics of the intra-bond O–H–O motion along with reorientational motion of symmetric groups in the dipolar glasses. However, the information obtained from such studies is limited hence reports of such studies are meagre. In the corresponding deuterated analogues much more information

can be obtained as quadrupolar interactions being electrostatic in nature, are sensitive to the effects of electric dipolar disorder (orientational disorder).

With this in view, 1D and 2D  $^2\text{H}$  NMR measurements on selected single crystals of  $\text{DBP}_{1-x}\text{DBPI}_x$  mixed crystals, were performed by Totz et al.<sup>17</sup> in order to study the static and dynamic behaviour of the deuterium atoms in the hydrogen bridges and in the methylene groups. In the  $^2\text{H}$  NMR spectra of the mixed crystals, it is possible to distinguish between DBP and DBPI molecules. Furthermore, for all deuterons the EFG tensors could be determined. A characteristic dependency of the high-temperature phase transition on the phosphate concentration  $x$  was derived from the changes of the 1D  $^2\text{H}$  NMR spectra. Authors suggested a model, which describes this dependency qualitatively, underlines the anti-ferrodistortive character of this transition. Furthermore, from the line shape variations, the occurrence of processes of exchange between several deuterons, including DBP and DBPI molecules, was concluded. The presence of exchange between different molecules in the chains was confirmed by means of analyzing the cross-peaks of 2D  $^2\text{H}$  NMR exchange experiments. The observation of this charge-transport process along the chains from the microscopic point of view is very important for the understanding of electrical conductivity processes in these crystals.

The 2D deuterium NMR exchange spectroscopy is applied to study<sup>18</sup> the hydrogen mobility in partially deuterated mixed crystals of betaine phosphate (DBP) and betaine phosphite (DBPI),  $\text{DBP}_{1-x}\text{DBPI}_x$ . In these crystals, chemical exchange processes of deuterons between different hydrogen bridges occur which are studied by the 2D  $^2\text{H}$  NMR technique over a wide temperature range in the slow-exchange regime. For the case of  $\text{DBP}_{1-x}\text{DBPI}_x$  with several deuteron sites taking part in the exchange, the analysis of the quantitative exchange behaviour required a combination of time-domain analysis of our 2D NMR data with mixing-time and temperature-dependent measurements. Different exchange rates for each two-site exchange, all showing Arrhenius behaviour, were obtained for  $\text{DBP}_{0.3}\text{DBPI}_{0.7}$ . For crystals with different phosphite concentration  $x$ , the differences towards  $\text{DBP}_{0.3}\text{DBPI}_{0.7}$  were established. A good correlation between NMR results with conductivity data (from dielectric measurements) was drawn and an estimation of charge carrier densities was made.

### 3. NMR STUDY OF RELAXOR FERROELECTRICS

There are many questions about relaxors. Are they similar to dipolar glasses where elementary dipoles exist on the atomic scale or is the relaxor state indeed characterized by the presence of nanosized polar cluster of variable sizes and orientations.

Relaxor ferroelectrics<sup>47–49</sup> (RFEs) have attracted considerable attention in recent years due to their unusual physical behaviour. Relaxors are technologically important as transducer/actuator materials. Relaxors are intermediate between dipolar glasses and classical FEs and exhibit both substitutional and charge disorder. They exhibit very large dielectric, piezoelectric, and electromechanical

responses and hence are technologically important for many applications<sup>47,48</sup> such as capacitors and piezoelectric devices.<sup>50</sup> The key to the understanding of the nature of relaxors is their local structure. At any temperature between 1000 and 4 K the average symmetry of PMN, for instance, is cubic. This is true even on the micrometric scale. Experiments on the nanometric scale have however, shown that the local structure is different from the average structure. Burns et al.<sup>51</sup> suggested that randomly oriented polar nanostructure appears below 925 K. Very little is known about the microscopic nature of these nanoclusters. Unlike a normal FE, the dielectric constant of an RFE exhibits a high peak, over a broad temperature range, with strong frequency dispersion; which clearly indicates relaxation processes at multiple time scales.<sup>52</sup> Their common feature is site and charge disorder as different cations with different charges and ionic radii randomly occupy equivalent lattice sites. They exhibit strongly dispersive giant dielectric and electrostrictive anomalies at  $T_m$ , but in contrast to normal FEs no symmetry change down to 0 K. Hence, they do not exhibit regular FE phase transitions. Thus, relaxors are substitutionally disordered complex perovskites.

Substitutional charge disorder in FEs giving rise to quenched electric RFs is probably at the origin of their relaxor behaviour.<sup>53</sup> Fluctuating polar nanoregions (PNR) in the paraelectric regime are related to the spatial fluctuations of the RFs. Meta stable pinned nanodomains in the FE regime are at the origin of non-Debye dielectric response, non-exponential relaxation, ageing and memory effects.

In analogy to spin glasses and dipolar glasses, they also show a great difference between the field-cooled and zero-field cooled susceptibilities demonstrating breaking of ergodicity. Their behaviour seems to be determined by “polar nanoclusters” embedded into a neutral matrix. NMR study of these relaxor systems is expected throw light on the question, whether, the relaxor transition is a transition to a dipolar glass state or FE state broken up into nanodomains due to quenched RFs.

A number of important questions, however, still remain open. The first is which ion displacements Pb or Nb/Mg/Sc are responsible for the formation of polar regions? What is the nature of non-polar matrix into which polar clusters are assumed to be embedded? Are the polar clusters and the non-polar matrix dynamic or static entities? Another still open important problem in PMN relaxor is related to microscopic inhomogeneities in the site occupancy of the  $\text{Mg}^{2+}$  and  $\text{Nb}^{5+}$  cations and their role in the formation of the polar regions. An existence of a 1:1 Mg/Nb ordered microregions is still discussed in literature. Since the 1:1 Sc/Nb chemical order in  $\text{PbSc}_{1/2}\text{Nb}_{1/2}\text{O}_3$  really exists, a comparative study of the high-temperature local structure of these two relaxors is of interest.

It should be stressed that the diffraction methods do not provide complete characterization of lattice distortions and ionic shifts in relaxors due to the compositional disorder of these materials and nanometric scale of polar order. Thus, local methods such as magnetic resonance and, in particular, NMR can be extremely useful in this case. In NMR experiments, the nuclei are sensitive to their local environment at a distance less than 1–2 nm. In addition, NMR operates at a much longer time scale ( $10^5$ – $10^8$  s) in comparison with the neutron or X-ray



methods that also provide the possibility to distinguish between static and dynamic ion shifts.

The systems and their abbreviations used for RFE are as follows:

$\text{PbSc}_{1/2}\text{Nb}_{1/2}\text{O}_3$	PSN
$\text{PbMg}_{1/3}\text{Nb}_{2/3}\text{O}_3$	PMN
$(1-x)\text{Pb}(\text{Zn}_{1/3}\text{Nb}_{2/3})\text{O}_3:x\text{PbTiO}_3$	PZN:PT
$\text{Pb}(\text{Sc}_{1/2}\text{Ta}_{1/2})\text{O}_3$	PST
$\text{Sr}_x\text{Ba}_{1-x}\text{Nb}_2\text{O}_6$	SBN
Tetragonal tungsten bronze oxides	

Tinte et al.<sup>54</sup> have reviewed the literature on FE relaxors. It is generally accepted that RFE properties are associated with an intrinsic local structure of PNR,<sup>55,56</sup> the precise nature of which remains controversial. Phenomenological models for solids with random chemical disorder show how local dipole moments (e.g. o-centered ions) in a polarizable lattice can lead to relaxor behaviour,<sup>57</sup> but do not address nanoscale short-range chemical order that enhances relaxor properties in the important family of  $\text{Pb}(\text{B}_x\text{B}'_{(1-x)})\text{O}_3$  perovskites.<sup>58</sup> Previous simulations<sup>59,60</sup> of microscopic models for PSN and PMN indicated a very strong spatial correlation between PNR and short-range chemically ordered regions, but no conclusive evidence of a relaxor state was found; for example, the Burns temperature<sup>61</sup>  $T_B$  was not located.

Tinte et al.<sup>54</sup> have carried out molecular dynamic simulations of first-principles based effective Hamiltonian for PSN under pressure and of PMN at ambient pressure that clearly exhibit a relaxor state in the paraelectric phase. Analysis of the short-to-medium range polar order allows them to locate Burns temperature  $T_B$ . Burns temperature is identified as the temperature below which dynamic nanoscale polar clusters form. Below  $T_B$ , the relaxor state characterized by enhanced short-to-medium range polar order (PNR) pinned to nanoscale chemically ordered regions. The calculated temperature–pressure phase diagram of PSN demonstrates that the stability of the relaxor state depends on a delicate balance between the energetics that stabilize normal ferroelectricity and the average strength of quenched “random” local fields.

### 3.1. Lead magnesium niobate PMN

Lead magnesium niobate,  $\text{PbMg}_{1/3}\text{Nb}_{2/3}\text{O}_3$  PMN, is probably the best investigated relaxor crystal. Salient features observed in this system are (1) it displays high dielectric permittivity over a broad temperature range with a significant frequency dispersion ( $\epsilon' \approx 20,000$  at  $T_m \approx 265$  K) and ( $f = 1$  kHz) and giant electrostriction.<sup>48</sup> Contrary to normal FEs, such anomalies are not directly linked to a structural phase transition but related to relaxational processes. Indeed X-ray and neutron-diffraction studies in PMN showed no evidence for a structural phase transition down to 5 K; the symmetry remains cubic on an average, at all temperatures,<sup>62</sup> contrary to the  $\text{PbSc}_{1/2}\text{Nb}_{1/2}\text{O}_3$  PSN relaxor, which undergoes a spontaneous cubic-rhombohedral phase transition at  $T_m \approx 355$  K.<sup>63,64</sup> Structural refinement results have shown that the local structure is different from the

average cubic one for both of the relaxors, and even at  $T \gg T_m$ . For instance,  $\text{Pb}^{2+}$  ions are randomly shifted below  $\approx 650$  K, that is, far above  $T_m$ .<sup>63,64</sup> At this high temperature, the optic index of refraction  $n(T)$  deviates from a linear temperature dependence as it was first evidenced by Burns and Dacol.<sup>65</sup> They assumed that this unexpected high-temperature deviation arises from small, randomly oriented, very local regions of non-reversible polarization that begin to appear with in the otherwise non-polar crystal structure below  $T_d$ , which is called the Burns temperature. The formation of PNR was also confirmed by observation in the PMN X-ray and neutron diffuse scattering that appears below  $T_d$ .<sup>62,66</sup>

Since the first synthesis<sup>67</sup> of the classic  $\text{PbMg}_{1/3}\text{Nb}_{2/3}\text{O}_3$  (PMN) material in 1961, relaxor FEs have been the subject of ongoing experimental and theoretical investigations due to their fundamental scientific interest and their importance in technological applications such as capacitors and piezoelectric devices.<sup>50</sup> Relaxors exhibit a wealth of interesting physical phenomena, which first appear at the so-called Burns temperature ( $T_B$ ) significantly above the Curie temperature  $T_C$ . Most prominently, below  $T_B$ , relaxor systems display a deviation of the inverse dielectric constant ( $1/\epsilon$ ) from the Curie–Weiss law<sup>68</sup> [Figure 1(a)] as well a strong dependence of the frequency. Microscopically, modelling of the frequency dependence has revealed a wide range of relaxation times and divergence of the longest relaxation times close to  $T_C$ .<sup>69,70</sup> Since the landmark paper of Burns and Dacol,<sup>61</sup> these effects have been ascribed to the appearance of PNR at the Burns temperature and their subsequent growth as the temperature is lowered. The PNRs are postulated to consist of groups of many correlated dipoles that move together slowly and would explain the long relaxation times that are observed.<sup>55,71</sup> Grinberg<sup>72</sup> has reviewed the literature on PMN relaxor. Despite the intense research, the structure and dynamics of PNR and the relaxor phase in general on an atomistic level remain poorly understood.

The  $^{93}\text{Nb}$  and  $^{45}\text{Sc}$  NMR spectra in  $\text{PbSc}_{1/2}\text{Nb}_{1/2}\text{O}_3$  (PSN) and  $\text{PbMg}_{1/3}\text{Nb}_{2/3}\text{O}_3$  (PMN) disordered relaxor FEs at the temperature  $T > T_m$ , where  $T_m \approx 355$  and 265 K for PSN and PMN respectively, have been studied by Laguta et al.<sup>73</sup> Spectral analysis was performed on the base both of the analytical description of NMR lines shapes, allowing for homogeneous and inhomogeneous broadening related to a random distribution of the EFGs and numerical Monte Carlo method taking into account EFGs originated from random distribution of Mg, Sc and Nb ions (which may be shifted or not) over B-type cation sites. The observed  $1/2 \leftrightarrow -1/2$  transition spectrum of the  $^{93}\text{Nb}$  and  $^{45}\text{Sc}$  nuclei in the PSN was shown to contain a narrow (3–4 kHz) almost isotropic part and a broad strongly anisotropic part. These two components of NMR spectra are related to 1:1 Sc/Nb ordered and compositionally disordered regions of the crystal, respectively. It was shown that in the disordered regions  $\text{Sc}^{3+}$ ,  $\text{Nb}^{5+}$  and  $\text{O}^{2-}$  ions are shifted from their cubic lattice sites in one of three possible directions. On the contrast, in PMN the NMR spectrum of  $^{93}\text{Nb}$  contains practically only the broad component. The portion of unbroadened spectrum that may correspond to ideal 1:2 regions accounts only for 1–2% of the total integral intensity. No evidence was obtained about existence of the 1:1 regions in PMN. The NMR data demonstrate that in PMN the cubic symmetry at  $T > T_m$  is locally broken due to ions' shifts similar to that in disordered PSN.

The values of the ion shifts were estimated in the point charges point dipoles approximation of the EFGs calculation both in the PSN and PMN.

Probably<sup>74</sup> the primary cause of RL behaviour is the electric charge disorder giving rise to quenched RFs. Their fluctuations are at the origin of polar nanodomains, which create disordered domain states upon cooling provided that the order parameter has continuous symmetry.<sup>75</sup> A remarkable exception is 3D uniaxial systems, whose ground state is ordered as expected for the RF Ising model (RFIM) system. They are expected to reveal new criticality due to a  $T=0$  fixed point<sup>76</sup> and strongly decelerated critical dynamics.<sup>77</sup> In the archetypical solid solution  $\text{PbMg}_{1/3}\text{Nb}_{2/3}\text{O}_3$  (PMN),<sup>78</sup> no RFIM criticality is observed due to the high pseudo-spin dimension of the order parameter,  $P$ , which might be described by an eight state Potts model.<sup>79</sup> Very probably the low- $T$  ground state is a glassy one as described within the mesoscopic spherical random bond RF (SRBRF) theory.<sup>80</sup>

Blinc et al.<sup>71</sup> have carried out  $^{207}\text{Pb}$  NMR in an electric field. They have observed separately the anisotropic  $^{207}\text{Pb}$  spectra of FE like polar clusters and isotropic spectra of spherical glass matrix into which the polar clusters are embedded, confirming the model proposed by Burns and Dacol. They concluded that PMN to be an incipient FE.

### 3.2. Uniaxial relaxors—strontium barium niobate

Strontium barium niobate (SBN) is a prototypical relaxor system, which belongs to the tetragonal tungsten bronze oxide family. Cubic relaxors like  $\text{PbMg}_{1/3}\text{Nb}_{2/3}\text{O}_3$  contain fluctuating PNR in the paraelectric regime, which are related to the spatial fluctuations of relaxor FEs which destroy the FE phase transition and give rise to a glassy state, while, uniaxial systems like  $\text{Sr}_{1-x}\text{Ba}_x\text{Nb}_2\text{O}_6$  exhibit RFIM behaviour with non-classical critical exponents, for example  $\alpha \approx 0$ .

The uniaxial RL crystal  $\text{Sr}_{0.61-x}\text{Ce}_x\text{Ba}_{0.39}\text{Nb}_2\text{O}_6$  (SBN61:Ce,  $0 \leq x < 0.02$ ) with its two-component polar order parameter fulfils the conditions of a ferroic RFIM.<sup>81</sup> At temperatures  $T > T_c$ , polar precursor clusters have been evidenced for example by linear birefringence<sup>82</sup> and susceptibility<sup>83</sup> experiments. After freezing into a metastable domain state at  $T < T_c$ , nanodomains with a fractal size distribution have been observed using high resolution piezoresponse force microscopy.<sup>84</sup>

There are always questions about relaxors, that whether, the relaxor transition is a transition to a dipolar glass state or FE state broken up into nanodomains due to quenched RFs.

The relaxor transition in cubic perovskite relaxors (PMN, PSN and PST) and tungsten bronze relaxor (SBN) has been studied by NMR.<sup>85</sup> The observed spectra consist of a narrow  $\frac{1}{2} \leftrightarrow -\frac{1}{2}$  central transition superimposed on a broad background due to satellite transitions. The chemical heterogeneity, responsible for relaxor properties is reflected in the structure of the central transition part. The latter is composed of two components, one due to ordered and the other due to disordered regions. Despite of the fact that the macroscopic symmetry does not change when relaxor transition occurs, a non-zero quadrupole coupling constant

determined from NMR clearly demonstrates the broken local symmetry by forming nanodomains due to quenched fields. Thus NMR study in these relaxors clearly shows that they do not exhibit regular FE phase transitions, but their behaviour seems to be determined by “polar nanoclusters” embedded into a neutral matrix.

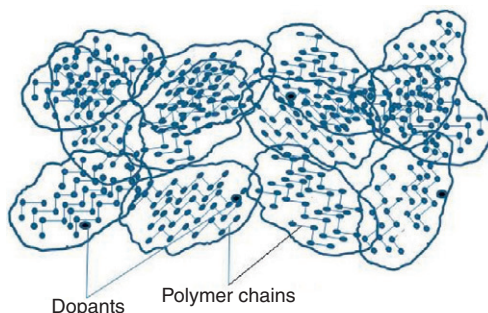
$^{93}\text{Nb}$  NMR investigations relaxor FE PMN at 450 K have been studied by Glinchuk et al.<sup>86</sup> The peculiar features of the observed NMR lines are wide shoulders and a very narrow central peak, the line shape being strongly asymmetrical in the case of  $B\parallel[001]$  and practically symmetrical for  $B\parallel[011]$ . The analytical description of NMR lines, allowing for homogeneous and inhomogeneous broadening related to a random distribution of the EFG has been performed. The fitting of the theory and observed line shapes had shown the existence of microregions with  $\langle 001 \rangle$ ,  $\langle 011 \rangle$  and  $\langle 111 \rangle$  ion shift directions.

The temperature dependence of the Edwards–Anderson order parameter  $q_{\text{EA}}$  and the local-polarization distribution function  $W(p)$  have been determined in a PMN single crystal using 2D- $^{93}\text{Nb}$  NMR by Blinc et al.<sup>87</sup> A glass like freezing of reorientable polar clusters occurs in the temperature range of the diffuse relaxor transition, whereas the NMR spectra corresponding to pinned nanodomains do not change with temperature. The obtained form of  $W(p)$  as well as the temperature dependence of  $q_{\text{EA}}$  can be well described by a newly proposed spherical random bond–random field (SRBRF) model of relaxor FEs.

## 4. CONDUCTING POLYMERS

### 4.1. Disorder in conducting polymers

Charge transport in CPs is dictated by a variety of phenomena that is generally accounted as due to the *disorder*. The main sources of disorder in CP are  $\text{sp}^2$  defects in the chain, chain ends, chain entanglements, voids, morphological and doping defects.<sup>88</sup> CPs are partially crystalline and partially amorphous, the volume fraction of the crystalline regions and the size of the crystalline coherence length play a dominant role in the charge transport. In general, the disorder induced localization plays a dominant role in the transport properties of CPs. Furthermore, the extent of disorder, depends on the parameters controlled in the preparative conditions of CPs, which depends on various methods of synthesis like casting films of molecules with high molecular weight from the solution, electrochemical deposition of polymer chains from solution of monomers, evaporation of molecules and other chemical methods. Consequently, on the microscopic level each film is different. However, by variation in synthesis conditions like temperature, current control in case of electropolymerization, solvent and spin casting conditions, give a handle to control the extent of disorder and consequently, the macroscopic transport properties in these systems (Figure 6).



**Figure 6** Disorder in conducting polymers.

## 4.2. Charge transport in conducting polymers

Even though these materials are being studied from over two decades, there are many questions about, the nature of charge carriers and the dimensionality of electrical conduction.

Charge transport studies in CP as a function of temperature, and magnetic field have given lot of insight into the conduction mechanisms. A charge carrier population in these systems can do one of the following processes, depending on the temperature. At high temperatures, they get thermally excited and move from trap to the free band, with an activation energy equal to the traps-“free” band difference. At low temperatures, they can perform Variable Range Hopping (VRH), and at much lower temperatures, when the thermal energy is not enough for VRH, they may tunnel between localized states.

The M-I transition in doped CPs is mainly governed by the extent of disorder, inter-chain interaction and doping level.<sup>88,89</sup> It is well known that disorder potentials can localize the electronic states. If the random component of the disorder potential is large with respect to the bandwidth, then the localization of electronic wave functions can occur. In the presence of strong disorder, the overlap of the wave functions drops off exponentially and the system moves towards the insulating regime.

In CPs both fibrillar and globular morphologies have been observed. In fibrillar morphology, the chains are extended; as a result, it is possible to have delocalized states along the chain length. In globular morphology, the chains are coiled up, which tends to localize the electronic states and favours the formation of granular-type material. Since CPs are partially crystalline and partially amorphous, the volume fraction of the crystalline regions and the size of the crystalline coherence length play dominant roles in the charge transport.

The electronic wave functions in the crystalline domains are delocalized with respect to that in amorphous region. If the volume fraction of crystalline regions exceeds 50% and wave function of the delocalized states overlaps quite well, then the system “sees” only an averaged-over disorder potential; moreover, in this case, some metallic features can be observed.<sup>89</sup> On the other hand, when there are large-scale inhomogeneities, as in amorphous regions, granular regions, metallic

islands, etc., then the random fluctuations in disorder potentials are high. As a result, the intrinsic metallic features are suppressed and the system moves towards the insulating regime. In general, the disorder induced localization plays a dominant role in M-I transition and in the transport properties of CPs.<sup>88,89</sup>

CPs are distinguished from other polymers because they possess  $sp^2$  hybridized backbone. They are important because of their light weight, easy processability and electrical properties of metals. Further, their use in making devices such as LED and molecular detection make their study more important.<sup>89A</sup> Application of conductive polymers more directly linked to their conductive nature, which depend on the doping. The conductivity will change considerably in the presence of oxidizing and reducing environment, hence can be used as sensing elements. PPY and PANI can be used as gas sensors for gases like  $NO_x$ ,  $SO_2$  and  $H_2S$ . Polypyrrole (PPY) is one of the most studied CPs due to its environmental stability, ease of fabrication and high conductivity when doped. Because PPY films expand and contract in response to applied electrochemical potentials, they have been proposed for use as soft actuators.<sup>90</sup> Even though these materials are being studied from over two decades, there are many questions about (1) the nature of charge carriers, (2) the dimensionality of electrical conduction. CP films of the type polypyrrole (PPY), polyaniline (PA), poly thiophene, poly 3-methyl thiophene (P3MT) and many other organic conductors belong to another family of disordered materials. Poly (3-alkylthiophenes) (P3ATs) show great promise as electronic and optoelectronic devices such as light-emitting diodes and field effect transistors. Particularly, the regioregular versions of P3ATs have received much attention because they show high crystallinity and high conductivity.<sup>91</sup>  $^{13}C$  NMR in P3BT has been carried out by Yazawa et al.<sup>91</sup> to investigate the structure and molecular dynamics around 340 K, the phase transition temperature for poly 3-butyl thiophene (P3BT). They observed a shoulder signal for  $C4'$  (methyl) carbon below 33 K, indicating the presence of at least two chemically inequivalent methyl carbons.

Even though the charge transport studies in CPs as a function of temperature, and magnetic field have given lot of insight into the conduction mechanisms like VRH, polarons, etc., NMR being a local microscopic probe, would give a better understanding of the systems. A correlation between NMR data and transport mechanism can unambiguously give a comprehensive information about the system. Many reviews related to NMR study of CPs are available for example Kahol et al.,<sup>92</sup> Mehring<sup>93</sup> and Mizoguchi.<sup>94</sup>

In this review, we have concentrated mainly on the NMR study of these systems. NMR being a local microscopic probe, it is expected to reveal the information about the type of charge carriers, their dynamics and dimensionality of motion, etc. Further, it is interesting to derive such information from NMR observables, looking for any universality in their behaviour, etc. have been addressed. All these polymers being organic based ones, with hydrogen being one of the important constituent in the polymers backbone is an added advantage, as hydrogen atom has the highest sensitivity with respect to NMR because of its high  $\gamma$  (gyro magnetic ratio). Further, in addition to the hydrogen in the backbone, there are some alkyl reorienting groups like  $CH_3$ ,  $C_2H_5$ , etc. Fluorine is contained in the dopant of the polymer, while  $^{13}C$  in some enriched samples.

Spin dynamics methods have widely proved to be a powerful tool to study the dynamics of polarons and thus the transport properties in CPs at the chain scale.<sup>95–97</sup> This is of particular interest in CP since disorder which is present at every scale in most of them makes the intrinsic transport properties difficult to be observed using conventional macroscopic techniques. One of these methods is based on measurements of the nuclear SLR time,  $T_1$  as a function of the NMR frequency. Obviously this method fails when the relaxation is not exponential and no  $T_1$  can be clearly determined. Such a situation has been observed several times in CP<sup>98,99</sup> and is generally attributed to the existence of heterogeneities. As a matter of fact, a granular structure is invoked to account for several different experimental data, of which inhomogeneous doping is often considered to be the origin. Mabboux et al.<sup>100</sup> has theoretically investigated the NMR relaxation in heterogeneously doped CPs and found it to be non-exponential.

It should be mentioned here that there are other resonance methods like ESR,<sup>94,101</sup> whose line width can be used to derive complimentary information about the spin dynamics, which is not discussed here.

### 4.3. NMR in conducting polymers/organic conductors

NMR experiments on representative systems like CPs and organic conductors are presented in the next section. Majority of the work reported in CP and organic conductors are concentrated on doped polyacetylene (PANI), polypyrrole (PPY) and poly thiophene (PT). But, before discussing the experimental results, it is better to review the NMR theory as applicable to CPs/organic conductors. A brief presentation of the same has been given here for the ready reference.

#### 4.3.1. NMR theory for conducting polymers

There are many theories which are proposed to explain the temperature and frequency dependence of relaxation rate in CPs and the details of which can be obtained from any of them. However, Soda et al.<sup>102</sup> has discussed it in more detail, which is used to analyse the experimentally observed  $T_1$  data in CPs with relevance to the corresponding physics.

The determination of the conduction mechanism in CPs is a key missing piece of information in the understanding of these important materials. NMR  $T_1$  data and Korringa type analysis<sup>103</sup> of  $T_1$  data can help to explore the important issues concerning the nature of conduction mechanism. The starting point is the relaxation mechanism developed for metals (Li, Al and Cu) which is discussed in detail in literature. NMR  $T_1$  data metals are interpreted in terms of the interaction of the conduction electrons with the nucleus. There are two parts which are responsible for such electron nuclear interaction (1) the well known contact term, (2) dipolar interaction between charge carriers and nuclear magnetic moment. If the contact term is the only mechanism responsible for relaxation then the  $1/T_1$  versus  $T$  follows Korringa relation, that relates the  $T_1$  to the Knight shift in metals. However, when the other interactions are present then the  $1/T_1$  temperature will show deviations from Korringa relation. There are many possible models which have been proposed to explain the NMR experimental data in CPs. In this section, we



have considered some representative systems and discussed the data interpretation. Some new understanding and conclusions have been derived which are presented.

Inherent in the derivation of the Korringa equation were assumptions of spherically symmetric nuclear wave functions and independent electron block wave functions. CPs are morphologically very different from metals. Spherically symmetric wave functions cannot accurately describe the asymmetry of the  $sp^2$  hybridized polymer backbone. Furthermore, electron correlations and Coulombic repulsions are not dealt with in the Korringa theory which make significant contributions in CPs. NMR relaxation studies have been reported on charge transfer complexes such as TTF-TCNQ [Soda et al.<sup>102</sup>], fluoroanthrene<sub>2</sub> (PF<sub>6</sub>) [Sachs et al.<sup>104</sup>]. The CT complexes provide an intermediate step towards a theory for  $T_1$  relaxation in CP. The first theoretical approach to a Korringa type equation for organic conductors was done by Soda et al. on the TTF-TCNQ system.

The "modified" Korringa equation can be written as

$$\frac{1}{T_1} = \kappa^2 S_k C_O T, \quad C_O = \frac{4\pi k_B}{\hbar} \left( \frac{\gamma_n}{\gamma_e} \right)^2 \quad (14)$$

In this equation,  $\kappa$  is the isotropic Knight shift and  $S_k$  is the Korringa enhancement factor, which takes into account the low dimensionality or anisotropy of the conduction as well as electron correlations. Thus,  $S_k$  lumps all the complications into one parameter and is given by

$$S_k = \left\{ \frac{1}{2} \left( \frac{\tau_{\perp}}{\tau_s} \right)^{1/2} \left[ \frac{3}{5} \varepsilon J(\omega_n) + \left( 1 + \frac{7}{5} \varepsilon \right) J(\omega_e) \right] K_O(\alpha) + (1 + 2\varepsilon) K_{2K_F}(\alpha) \right\} \quad (15)$$

In this expression  $\tau_{\perp}$  is the inter-chain hopping time and  $\tau_s$  is the phonon scattering time along a chain. The quantity  $\varepsilon = (d^2/a^2)$  is the ratio of the anisotropic to isotropic contribution of the hyperfine interaction and  $J(\omega)$  is the spectral density of the interaction, with  $\omega_e$  and  $\omega_n$  being electron and nuclear precession frequencies respectively,

$$J(\omega) = \left[ \frac{(1 + \omega^2 \tau_{\perp}^2)^{1/2} + 1}{2(1 + \omega^2 \tau_{\perp}^2)} \right] \quad (16)$$

In addition  $K_O(\alpha)$  and  $K_{2F}(\alpha)$  are given by the following equations:

$$K_O(\alpha) = (1 - \alpha)^{1/2}, \quad K_{2F}(\alpha) = \frac{(1 - \alpha)^2}{[1 - \alpha F(2k_F)]^2} \quad (17)$$

Korringa enhancement factor is a function of four parameters: the Coulombic repulsion energy ( $\alpha$ ), the two correlation times ( $\tau_{\perp}$  and  $\tau_s$ ) and the hyperfine anisotropy ( $\varepsilon$ ). These are fit parameters to fit  $T_1$  data. For a classical metal,  $\varepsilon$  and  $\alpha=0$  which gives  $S_k=1$ , the Korringa result. In a highly anisotropic conduction charge transfer complex  $S_k$  ranges from 50 to 500, indicating the a large deviation from a normal metal.<sup>105</sup>



Thus measuring the SLR time as a function of temperature gives a simple diagnostic tool for assessing, whether the hyperfine relaxation is dominant in the system. Similarly, the plot of relaxation rate ( $1/T_1$ ) as a function of Larmor frequency ( $\omega$ ) gives information about the dimensionality of conduction.

The spectral density function,  $f(\omega)$ , reflects the electronic spin motion and depends sensitively on the dimensionality of the process. For 1D diffusion,

$$f(\omega) = (1/2D_{\parallel} \parallel \omega)^{1/2} \quad (18)$$

where  $D_{\parallel}$  is the intra-chain diffusion rate.

#### 4.4. Dimensionality and $1/T_1$ versus frequency plot

Following the above equation it is obvious that if a plot of  $1/T_1$  versus  $1/\omega$  is linear, the system is categorized as 1D. At low frequency, the 1D diffusion breaks down because of inter-chain hopping and 2D or 3D behaviour is expected. In two dimensions,  $f(\omega)$  displays a logarithmic divergence, while in three dimensions, it is nearly constant. The crossover between 1D and 2D or 3D regimes occurs at  $\omega \approx D_{\perp}$ , which is the inter-chain diffusion rate.<sup>106</sup>

The frequency dependence of NMR SLR time is a powerful method to study the spin dynamics in CPs.<sup>107</sup> They reveal the microscopic dynamics of the charge carrier, polaron or conduction electrons. Therefore, interpretation of the NMR relaxation rate is useful, but difficult as other additional mechanisms like the localized paramagnetic centres and molecular motions of reorienting symmetric groups also make considerable contributions to the NMR  $T_1$ .

In the same way,  $1/T_1$  versus temperature behaviour also give a wealth of information. At all temperatures measurements on a given nucleus have values of  $1/T_1T$  that decrease with increasing field. This behaviour is different from the frequency and field-independent behaviour associated with relaxation due to conduction electrons in a conventional 3D metal. Clark et al.<sup>108</sup> has carried out  $1/T_1T$  measurements in PPYPF<sub>6</sub> and P3MT samples.

The power spectrum of the local magnetic field fluctuations shows different features at different Larmor frequency and temperature. The interpretation of the results is that the dominant source of these fluctuations is spatial transport of the electrons along the polymer chains and the frequency and temperature dependences reflect the details of their motions.

#### 4.5. Method of detection

NMR being a window-dependent technique, the range of Larmor frequency plays an important role in the study of CPs. In CPs there are many interactions which are possible for SLR. Whenever the relaxation has contributions from additional mechanisms such as reorientation of symmetric groups present in the dopants such as PF<sub>6</sub>, AsF<sub>6</sub>, etc. and presence of moisture then the scenario becomes more complicated and one has to carefully analyse the data. Further, the lower frequency measurements show 3D behaviour while at high frequencies the system

shows a typical quasi-1D behaviour. These issues will be addressed while discussing the NMR results in representative systems. Generally experimentalists in this area have used<sup>109</sup> Larmor frequencies ranging from 10 to 960 MHz. Many other workers have worked from 300 K down to few milli Kelvin. Such extreme experimental conditions are known to sort out many unresolved issues or may lead to additional information.

## 4.6. Sample preparation and experimental methods

Several conjugated polymers such as polyaniline, polypyrrole and poly thiophene have been prepared by chemical methods using doping. The electrical conductivity of these polymers has been controlled by (i) the type of dopant, (ii) the concentration of doping, (iii) the conditions of doping (the current density, temperature of reaction, etc.)

Samples are chopped into tiny pieces to avoid skin-depth problems at the Larmor frequency. Spin echo ( $\pi/2-\tau-\pi/2$ ,  $90^\circ$  phase shifted) or free induction decay (FID) ( $\pi-\tau-\pi/2$ ) sequences are used for  $T_1$  measurement depending on the sample and the sensitivity of the spectrometer.

Some of the features observed in CPs are

- (1) Frequency dependence of  $1/T_1$ .
- (2)  $1/T_1$  versus temperature data showing deviations from Korringa-relation.

Some representative systems like CPs and organic conductors on which NMR experiments have been conducted giving information about the dimensionality, power law behaviour are presented in the next section.

### 4.6.1. NMR in CP films

Majority of the work reported in CP films are focused on doped polyacetylene (PANI), polypyrrole (PPY) and poly thiophene (PT).

$1/T_1$  versus  $1/f^{1/2}$  fit clearly shows the one-dimensionality of the system deviations have been observed at low frequencies. Many such reports are known in the literature. Even though, many experimental studies of  $1/T_1$  versus temperature are reported, no explicit model have been proposed to explain this data.

Nechtschein et al.<sup>106,110</sup> have carried out a detailed study of  $1/T_1$  with frequency and temperature, both in undoped and doped polyacetylene (PA). Their data analysis shows that PA is quasi-1D system throughout the temperature range of study, except at very low temperatures. Their analysis further, showed that, the intra-chain diffusion follows power law behaviour,  $T^n$ ;  $n=0.65$  above 50 K, and  $T^n$ ;  $n=1.5$  below 50 K. These arguments along with Sach's model<sup>111</sup> may result in an empirical model for  $1/T_1$  versus temperature data in a limited range of temperature.

Mizoguchi et al.<sup>112</sup> also have carried experiments of  $1/T_1$  versus temperature as well as frequency dependence studies in FSO<sub>3</sub>-doped PA ( $10^5$  S/cm). They have done the experiments at considerably low NMR frequencies and over a wide temperature range. Their  $T_1$  analysis with frequency shows quasi-1D

behaviour at high frequencies, while the fit deviates at lower frequencies. They conclude that the system tends to behave like a 3D system at low frequencies. Their observation of  $1/T_1$  maximum at high temperature at all the three frequencies is ascribed to the molecular motion of  $\text{FSO}_3$  groups, moisture and other reorienting groups.

Proton  $1/T_1$  of heavily doped polyacetylene films with different dopants such as  $\text{FSO}_3\text{H}$ ,  $\text{HClO}_4$ , iodine, bromine and potassium was measured by Shimizu et al.<sup>113</sup> and the behaviour expected for a quasi-1D metal was not found. Some of them showed a time dependence of  $1/T_1$ . They have deduced the temperature dependence of resistivity from the  $1/T_1$  and  $1/T_1$  versus temperature shows  $T^{1.5}$  behaviour above 40 K and deviates from such behaviour below 40 K. Mizoguchi and Kuroda<sup>107</sup> have given a comprehensive review of many investigations of NMR relaxation of both  $^1\text{H}$  and  $^{13}\text{C}$  in undoped polyacetylene.

$^1\text{H}$  NMR study of  $\text{I}_2$  doped poly[2-butoxy-5-methoxy phenylene vinylene] (PBMPV) has been carried out by Lee et al.<sup>114</sup> They found magnetization recovery to follow a stretched-exponential form  $M(t) = M_0[1 - \exp(-t/T_1)^n]$  with  $n = 0.8 \pm 0.03$ , which is characteristic of a system with distribution of the correlation time.  $1/T_1$  versus  $\nu^{-1/2}$  in samples with different conductivity follows  $\nu^{-1/2}$  dependence over 20–40 MHz range indicating the main SLR is 1D spin diffusion. A correlation between  $1/T_1$  and dc conductivity has been made which is found follow a simple power law.

$^1\text{H}$   $T_1$  studies in metallic PPyPF<sub>6</sub> have been carried out by Clark et al.<sup>109</sup> and Singh et al.<sup>115</sup> at 960 and 383 MHz over 1.7–55 and 1.7–200 K respectively. The rate at lower frequency is 2–8 times faster than that at high frequency depending on temperature. Although the microscopic details do not fit the model for 1D diffusion, the dominant proton  $T_1$  relaxation is due to conduction electron motion. They found that at high field and low temperatures where the Zeeman energy,  $g\mu_B H \gg k_B T$ , below which the Spin Diffusion Paramagnetic Centres (SDPC) is expected to freeze-out; hence  $T_1$  measurements at such low temperatures eliminate nuclear spin diffusion to paramagnetic centers as a competing mechanism leaving only relaxation by translational motion of electrons.

#### 4.6.2. NMR in organic conductors

Wieland et al.<sup>116</sup> have carried out frequency-dependent proton SLR rate studies in organic metal  $(\text{PERYLENE})_2(\text{AsF}_6)_{0.75}(\text{PF}_6)_{0.35}x0.85\text{CH}_2\text{Cl}_2$ .  $1/T_1$  versus  $(\nu_L)^{-1/2}$  showed a linear dependence showing a signature of a 1D motion of the spins.  $1/T_1$  versus temperature in the range 300–180 K showed a linear variation as expected of an organic metal. Below 180 K, it exhibited a phase transition from a organic metal (above 180 K) to a semiconducting conductor below 180 K.  $1/T_1$  maximum observed around 50 K, which was ascribed to their coupling to the  $^{19}\text{F}$  spins of reorienting  $\text{PF}_6$  groups. This also supports the view that  $^1\text{H}$  relaxation shows signatures of relaxation due to 1D motion of spins as well as reorienting groups depending on which process dominates at the temperature under consideration.

Sachs et al.<sup>104</sup> have carried out  $^1\text{H}$   $T_1$  measurements in  $(\text{FA})_2\text{PF}_6$  organic conductor over a wide range of frequencies from 14 to 200 MHz at 293 K.  $1/T_1$

versus  $(\nu_L)^{-1/2}$  data at high Larmor frequencies follow linear behaviour at 293 K, supporting the evidence of 1D diffusive motion. Lattice imperfections are known to spoil the one-dimensionality of the sample.

Alexandrowicz et al.<sup>117</sup> have carried spatial mapping and density of the conduction electrons in  $(\text{FA})_2\text{PF}_6$  using 2D ESR imaging maps of the conduction electron density and mobility. The maps generally show pronounced inhomogeneity of both density and mobility on the scale of  $\sim 30\text{--}300\ \mu\text{m}$ . Highly mobile regions were identified and the mobility was quantitatively evaluated using theoretical models.

Höptner et al.<sup>118</sup> have carried out  $^1\text{H}$  and  $^{19}\text{F}$  SLR time as a function of temperature. Fluorines are known to be relaxed mainly by the reorientational motion of the anions and by the interaction with fixed paramagnetic impurities, the protons are relaxed additionally above 150 K predominantly by highly mobile paramagnetic species, whose concentration could be determined directly via the NMR signal amplitude. Korringa relation observed for proton relaxation shows that it is metallic above 183 K. Further,  $1/T_1$  versus  $(\nu_L)^{-1/2}$  dependence of the proton relaxation supports the 1D spin transport and also confirms that only protons of the cation stacks are relaxed by the highly mobile paramagnetic species.

Soda et al.<sup>102</sup> have measured  $T_1^{-1}$  as function of magnetic field for various temperatures and pressures in TTF and TCNQ chains. In general the properties of quasi-1-D metals depend on the values of the dimensionless parameters, namely  $t_\perp/E_F$  and  $\hbar/E_F\tau_v$ . The material is 1D for  $(t_\perp/E_F \ll 1)$  or 3D for  $(t_\perp/E_F \approx 1)$ . The value of  $\hbar/E_F\tau_v$  gives the degree of cleanliness. For  $\hbar/E_F\tau_v \ll 1$ , the material is clean and its properties should be dominated by the coherence length  $\xi$ , while for  $\hbar/E_F\tau_v \geq 1$ . It is dirty and the mean free path  $A = v_F\tau_v$  has a dominant effect on electronic properties. They have attempted to show how the various materials can be presented on one-dimensionality versus cleanliness diagram. For,  $\hbar/\tau_v \leq t_\perp$ , one gets a true 1D metal (i.e. coherent electronic motion along the chains and diffusive one perpendicular to the chains), for  $t_\perp < \hbar/\tau_v < E_F$ ; a low mobility semiconductor. Temperature and pressure affect mainly  $\tau_v$  and in some materials  $\tau_\perp$  and this causes the materials to move on this diagram. In this way, the picture derived from the systematic measurement of the NMR relaxation times gives us an overall view of quasi-1D metals.

Kaiser et al.<sup>119</sup> have studied  $^{19}\text{F}$  NMR in  $(\text{Pyrene})_{12}(\text{SbF}_6)_7$  cation salt. The rotational motion of those  $\text{SbF}_6$  anions of this salt can be best discriminated by the analysis of the temporal evolution of the  $^1\text{H}$  Overhauser shift of the conduction electron ESR line. Temperature dependence of the Overhauser shift detected proton-SLR rate recorded at 9.46 GHz electron spin and 14.4 MHz proton NMR frequency. It is important to note that the proton relaxation reflects only the low temperature BPP-peak of  $\text{SbF}_6$  anion rotation, in addition to conduction electron contribution. This salt undergoes a 3D-ordered Peierls transition at  $\approx 113\ \text{K}$ , which is due to the freezing of the anion motion.

Charge transfer salt (CTS)  $(\text{TMTTF})_2\text{SbF}_6$  has been studied by Yu et al.<sup>120</sup> using  $^{13}\text{C}$  NMR spectroscopy. It is known that at ambient pressure, a transition to a

charge-ordered (CO) state occurs at  $T_{CO}=156$  K, and anti-ferromagnetic (AF) order is observed below  $T_N=8$  K.

## 5. CONCLUSIONS

In this review, we have seen a variety of new physics due to disorder and new methodologies based on NMR probe to explore the same. In dipolar glasses one finds an orientational disorder of electric dipoles, resulting in a non-exponential or stretched exponential behaviour indicating the distribution of correlation times. The energy landscape of  $E_a$  is also anticipated in these systems. The inhomogeneous distribution of NMR frequency points to the presence of each physically non-equivalent site in the unit cell, resulting in a highly asymmetric inhomogeneous line shape. This leads to local dependence to local RF distribution and estimation of  $q_{EA}$  Edwards–Anderson order parameter. SLR time exhibiting unexpected, broad and asymmetric minima (indirectly observed using  $^{87}\text{Rb}$ ,  $^{207}\text{Tl}$   $T_1$ ) shows the evidence of slow motion of H-bonds.

SLR time results provide novel information on the temperature dependence and distribution of local RFs and their dynamics. A direct evidence for incoherent phonon-assisted deuteron tunnelling in H-bonded systems has been observed from NMR experiments. The use of quadrupole-perturbed 1D  $^2\text{H}$  NMR spectroscopy and in particular 2D  $^2\text{H}$  NMR exchange spectroscopy has found to be very promising as regards elucidating the details of the hydrogen dynamics.

$\text{BP}_x\text{BPI}_{1-x}$  and  $\text{BP}_x\text{GPI}_{1-x}$  systems have shown a distribution of  $E_a$  for the motion of symmetric groups due to the presence of disorder. In relaxors, these experiments have shown the presence of short-to-medium range PNR below  $T_B$  Burns temperature and their subsequent growth as the temperature is lowered. In CPs,  $T_1$  versus temperature analysis, yields a fitting parameter ( $S_k$ ), known as the Stoner enhancement factor, which takes into account the low dimensionality or anisotropy of conduction as well as electron correlations. In a highly anisotropic conduction charge transfer complex  $S_k$  ranges from 50 to 500, indicating a large deviation from a normal metal.  $1/T_1$  versus  $1/\sqrt{f}$  reveals information about the dimensionality of the system, while  $T_1$  versus temperature shows a power law behaviour. Effect of reorientation of symmetric rotors is seen in some cases.

## REFERENCES

1. U. T. Hochli, K. Knorr and A. Loidl, *Adv. Phys.*, 1990, **39**, 405.
2. E. Courtens, *Phys. Rev. Lett.*, 1984, **52**, 69.
3. J. Slak, R. Kind, R. Blinc, E. Courtens and S. Zumer, *Phys. Rev. B*, 1984, **30**(1), 85.
4. R. Blinc, S. Zumer, M. Koren and D. C. Ailion, *Phys. Rev. B*, 1988, **37**(13), 7276.
5. R. Blinc, J. Dolinšek, R. Pirc, B. Tadic, B. Zalar, R. Kind and O. Liechti, *Phys. Rev. Lett.*, 1989, **63**(20), 2248.
6. R. Blinc, D. C. Ailion, B. G\"unther and S. Zumer, *Phys. Rev. Lett.*, 1986, **57**(22), 2826.
7. J. Dolinšek, D. Arcon, B. Zalar, R. Pirc, R. Blinc and R. Kind, *Phys. Rev. B*, 1996, **54**(10), R6811.
8. W. T. Sobol, I. G. Cameron, M. M. Pintar and R. Blinc, *Phys. Rev. B*, 1987, **35**(13), 7299.
9. J. Dolinšek, B. Zalar and R. Blinc, *Phys. Rev. B*, 1994, **50**(2), 805.

10. R. Blinc, J. Dolinšek, B. Zalar and F. Milia, *J. Non-Cryst. Solids*, 1994, **172–174**, 436.
11. R. Kannan, K. P. Ramesh, and J. Ramakrishna, *DAE Symposium*, 2001
12. G. Wu, W. G. Clark, K. P. Ramesh, S. Subramanian, and R. Menon, *Proceedings of the DAE Solid State Physics Symposium, held at BARC & TIFR, Mumbai 400085*, PP 89, December 5–9, 2005
13. M. N. Ramanuja, K. P. Ramesh and J. Ramakrishna, *Mol. Phys.*, 2006, **104**, 3213.
14. M. N. Ramanuja, K. P. Ramesh and J. Ramakrishna, *Mol. Phys.*, 2008, **106**, 745.
15. M. N. Ramanuja, K. P. Ramesh and J. Ramakrishna, *Magn. Reson. Chem.*, 2007, **45**, 1027.
16. M. N. Ramanuja, K. P. Ramesh and J. Ramakrishna, *Mol. Phys.*, 2009, **107**, 643.
17. J. Totz, H. Braeter and D. Michel, *J. Phys. Condens. Matter*, 1999, **11**, 1575.
18. J. Totzt, D. Michell, Yu.N. Ivanov, I. P. Aleksandrova, J. Petersson and A. Klöpperpieper, *Appl. Magn. Reson.*, 1999, **17**, 243–263.
19. E. Courtens, *J. Phys. Lett. Paris*, 1982, **43**, 199.
20. E. Courtens, *Ferroelectrics*, 1987, **72**, 229.
21. P. Bastchi, B. Matthias, W. Merz and P. Sherrer, *Helv. Phys. Acta*, 1945, **18**, 238.
22. B. Matthias and W. Merz, *Helv. Phys. Acta*, 1946, **19**, 227.
23. B. Matthias, W. Merz and P. Sherrer, *Helv. Phys. Acta*, 1947, **20**, 273.
24. N. Korner, Ch. Pfammatter and R. Kind, *Phys. Rev. Lett.*, 1993, **70**(9), 1283.
25. S. Iida and H. Terauchi, *J. Phys. Soc. Jpn.*, 1983, **52**, 4044.
26. R. Blinc, B. Zalar, V. V. Laguta and M. Itoh, *Phys. Rev. Lett.*, 2005, **94**, 147601.
27. R. Blinc, J. Dolinšek, D. Arcon and B. Zalar, *J. Phys. Chem. Solids*, 1996, **57**, 1479.
28. J. Dolinšek, *J. Mag. Res.*, 1991, **92**, 312.
29. R. Blinc, J. Dolinšek, V. H. Schmidt and D. C. Ailion, *Europhys. Lett.*, 1988, **6**(1), 55.
30. S. Chen, D. C. Ailion and G. Laicher, *Phys. Rev. B*, 1993, **47**(6), 3047.
31. B. Schmidt, Blumich and H.W. Spiess, *J. Magn. Reson.*, 1988, **79**, 269.
32. S. F. Edwards and P. W. Anderson, *J. Phys. F*, 1975, **5**, 965.
33. R. Pirc, B. Tadic and R. Blinc, *Phys. Rev. B*, 1987, **36**(16), 8607.
34. R. A. Cowley, T. W. Ryan and E. Courtens, *Z. Phys. B*, 1986, **65**, 181.
35. K. Binder and A. P. Young, *Rev. Mod. Phys.*, 1986, **58**(4), 802.
36. H. Vogel, *Z. Phys.*, 1921, **22**, 645.
37. R. Kind, P. M. Cereghetti, C. A. Jeiziner, B. Zalar, J. Dolinšek and R. Blinc, *Phys. Rev. Lett.*, 2002, **88**(19), 195501.
38. Z. Kutnjak, C. Filipič, A. Levstik and R. Pirc, *Phys. Rev. Lett.*, 1993, **70**, 4015.
39. Z. Kutnjak, R. Pirc, A. Levstik, I. Levstik, C. Filipič, R. Blinc and R. Kind, *Phys. Rev. B*, 1994, **50**, 12421.
40. J. F. Berret, M. Meissner, S. K. Watson, R. O. Pohl and E. Courtens, *Phys. Rev. Lett.*, 1991, **67**, 93.
41. R. Blinc, J. Dolinsek and B. Zalar, *Z. Phys. B*, 1997, **104**, 629.
42. A. Levstik, C. Filipic, S. Kutnjak, I. Levstik, R. Pirc, B. Tadic and R. Blinc, *Phys. Rev. Lett.*, 1991, **66**, 2368.
43. R. G. Palmer, D. L. Stein, E. Abrahams and P. W. Anderson, *Phys. Rev. Lett.*, 1984, **53**(10), 958.
44. W. Winterlich, A. Titze, G. Hinze and R. Böhmer, *Phys. Rev. B.*, 1998, **57**(22), 14158.
45. M. L. Santos, J. C. Azevedo, A. Almeida, M. R. Chaves, A. R. Pires, H. E. Muser and A. Kloppeper, *Ferroelectrics*, 1993, **108**, 363.
46. M. L. Santos, M. R. Chaves, A. Almeida, A. Kloppeper, H. E. Muser and J. Albers, *Ferroelectr. Lett.*, 1993, **15**, 17.
47. G. A. Smolensky, *J. Phys. Soc. Jpn.*, 1970, **28**, 26.
48. L. E. Cross, *Ferroelectrics*, 1987, **76**, 241.
49. G. A. Smolenskii and A. I. Agranovskaya, *Sov. Phys. Solid State*, 1959, **1**, 429.
50. S. E. Park and T. R. Shrout, *J. Appl. Phys.*, 1804, **1997**, 82.
51. G. Burns and F. H. Dacol, *Ferroelectrics*, 1990, **104**, 25, *Phys. Rev. B*, 1983, **28**, 2527.
52. G. A. Samara, *Phys. Rev. Lett.*, 1996, **77**, 314.
53. W. Kleeman, J. Dec, S. Miga and R. Pankrath, *Ferroelectrics*, 2004, **302**, 247.
54. S. Tinte, B. P. Burton, E. Cockayne and U. V. Waghmare, *Phys. Rev. Lett.*, 2006, **97**, 137601.
55. R. Blinc, V. V. Laguta and B. Zalar, *Phys. Rev. Lett.*, 2003, **91**, 247601.
56. I. K. Jeong, *Phys. Rev. Lett.*, 2005, **94**, 147602.
57. B. E. Vugmeister and H. Rabitz, *Phys. Rev. B*, 1988, **57**, 7581.

58. B. E. Vugmeister, *Phys. Rev. B*, 2006, **73**, 174117.
59. B. P. Burton, E. Cockayne and U. V. Waghmare, *Phys. Rev. B*, 2005, **72**, 064113.
60. B. P. Burton, E. Cockayne, S. Tinte and U. V. Waghmare, *Phase. Transit.*, 2006, **79**, 91.
61. G. Burns and F. H. Dacol, *Solid State Commun.*, 1983, **48**, 853.
62. P. Bonneau, P. Garnier, G. Calvarin, E. Husson, J. R. Gavarri, A. W. Hewat and A. Morell, *J. Solid State Chem.*, 1991, **91**, 350.
63. C. Malibert, B. Dkhil, J. M. Kiat, D. Durand, J. F. Berar and A. Spasojevic-deBire, *J. Phys.: Condens. Matter*, 1997, **9**, 7485.
64. P. Bonneau, P. Garnier, E. Husson and A. Morell, *Mater. Res. Bull.*, 1989, **24**, 201.
65. G. Burns and F. H. Dacol, *Solid. State Commun.*, 1973, **13**, 423, *Phys. Rev. B*, 1988, **28**, 2527.
66. A. Naberezhnov, S. Vakhrushev, B. Dorner, D. Stranch and H. Moudde, *Euro. Phys. J. B*, 1999, **11**, 13.
67. G. A. Smolenskii, V. A. Isupov, A. I. Agranovskaya and S. N. Popov, *Sov. Phys. Solid State*, 1961, **2**, 2584.
68. D. Viehland, S. J. Jang, L. E. Cross and M. Wuttig, *Phys. Rev. B*, 1992, **46**, 8003.
69. R. Pirc, R. Blinc and V. Bobnar, *Phys. Rev. B*, 2001, **63**, 054203.
70. V. Bovtun, S. Veljko, S. Kamba, J. Petzelt, S. Vakhrushev, Y. Yakymenko, K. Brinkman and N. Setter, *J. Eur. Ceram. Soc.*, 2006, **26**, 2867.
71. R. Blinc, V. V. Laguta and B. Zalar, *Phys. Rev. Lett.*, 2003, **391**, 247601-1.
72. I. Grinberg, Y. HanShin and A. M. Rappe, *Phys. Rev. Lett.*, 2009, **103**, 197601.
73. V. V. Laguta, M. D. Glinchuk, S. N. Nokhrin, I. P. Bykov, R. Blinc, A. Gregorovic and B. Zalar, *Phys. Rev. B*, 2003, **67**, 104106.
74. V. Westphal, W. Kleemann and M. D. Glinchuk, *Phys. Rev. Lett.*, 1992, **68**, 847.
75. I. Imry and S. K. Ma, *Phys. Rev. Lett.*, 1975, **35**, 1399.
76. D. P. Belanger and A. P. Young, *J. Magn. Magn. Mater.*, 1991, **100**, 272.
77. D. S. Fisher, *Phys. Rev. Lett.*, 1986, **56**, 416.
78. G. A. Smolenski and V. A. Isupov, *Dokl. Acad. Nauk SSSR*, 1954, **97**, 653.
79. H. Qian and L. A. Bursill, *Int. J. Mod. Phys. B*, 1996, **10**, 2027.
80. R. Blinc, J. Dolinsek, A. Gregorovic, B. Zalar, C. Filipic, Z. Kutnjak, A. Levstik and R. Pirc, *Phys. Rev. Lett.*, 1999, **83**, 424.
81. W. Kleemann, J. Dec, P. Lehnen, R. Blinc, B. Zalar and R. Pankrath, *Europhys. Lett.*, 2002, **57**, 14.
82. P. Lehnen, W. Kleemann, Th. Woike and R. Pankrath, *Eur. Phys. J. B*, 2000, **14**, 633.
83. J. Dec, W. Kleemann, V. Bobnar, Z. Kutnjak, A. Levstik, R. Pirc and R. Pankrath, *Europhys. Lett.*, 2001, **55**, 781.
84. P. Lehnen, W. Kleemann, Th. Woike and R. Pankrath, *Phys. Rev. B*, 2001, **64**, 224109.
85. R. Blinc, B. Zalar and A. Gregorovic, *Sci. Sinter.*, 2002, **34**, 3-11.
86. M. D. Glinchuk, S. N. Nokhrin, I. P. Bykov, V. V. Laguta, R. Blinc, A. Gregorovic and B. Zalar, *Phys. Stat. Sol. (b)*, 2001, **228**, 757.
87. R. Blinc, J. Dolinšek, A. Gregorovič, B. Zalar, C. Filipič, Z. Kutnjak, A. Levstik and R. Pirc, *Phys. Rev. Lett.*, 1999, **83**(2), 424.
88. R. Menon, C. O. Yoon, D. Moses and A. J. Heegerin, in: *Hand Book of Conducting Polymers*, T. A. Skotheim, R. L. Elsenbaumer, and J. R. Reynolds (eds.), 2nd edn. Marcel Dekker, New York, 1988.
89. H. S. Nalwa(ed.) (1998). *In Hand Book of Organic Conductive Molecules and Polymers*, Vols. 1-4. Wiley, New York, 1998.
- 89A. H. A. Al. Altar, A. P. Monkman, M. Tavasli, S. L. Beltington and M. R. Bryce, *Appl. Phys. Lett.*, 2005, **86**, 1.
90. C.-H. Tso, J. D. Madden and C. A. Michal, *Synth. Met.*, 2007, **157**, 460.
91. K. Yazawa, Y. Inoue, T. Yamamoto and N. Asakawa, *Phys. Rev. B*, 2006, **74**, 094204.
92. P. K. Kahol, G. C. Clark and M. Mehrling, in: *Conjugated Conducting Polymers*, (H. Kiess ed.), Springer-Verlag, Berlin, Heidelberg, New York, 1992, Vol. 102, p. 217.
93. M. Mehrling, in: *Low-Dimensional Conductors and Superconductors*, D. Jerome and L. G. Caron (eds.), Plenum, New York, 1987, Vol. 155, p. 185.
94. K. Mizoguchi, *Jpn. J. Appl. Phys.*, 1995, **34**, 1.
95. F. Devreux and H. Lecavelier, *Phys. Rev. Lett.*, 1987, **59**, 2585.

96. J. P. Travers, P. Le Guyader, P. N. Adams, P. J. Laughlin and A. P. Monkman, *Synth. Met.*, 1994, **65**, 159.
97. K. Mizoguchi, M. Nechtschein, J. P. Travers and C. Menardo, *Phys. Rev. Lett.*, 1989, **63**, 66.
98. F. Masin, G. Gusman and R. Deltour, *Solid State Commun.*, 1981, **40**, 291.
99. P. Le Guennec, J. P. Travers and Y. F. Nicolau, *Synth. Met.*, 1993, **55**, 672.
100. P. Y. Mabboux, B. Beau, J. P. Travers and Y. F. Nicolau, *Synth. Met.*, 1997, **84**, 985.
101. M. Nechtschein, *Hand book of conducting polymers*, Chapter 5, p. 141
102. G. Soda, D. Jerome, M. Weger, J. Alizon, J. Gallice, H. Robert, J. M. Fabre and L. Giral, *J. Phys. (Paris)*, 1977, **38**, 931.
103. J. Korringa, *Physica*, 1950, **16**, 601.
104. G. Sachs, E. Dormann and M. Schwoeres, *Solid State Commun.*, 1985, **53**, 73.
105. D. Kongeter and M. Mehring, *Phys. Rev. B*, 1989, **39**, 6361.
106. M. Nechtschein, F. Devreux, R. L. Greene, T. C. Clarke and G. B. Street, *Phys. Rev. Lett.*, 1980, **44**, 356.
107. K. Mizoguchi and S. Kuroda, in: *Hand book of Organic Conductive Molecules and Polymers*, Vol. 3, Chapter 6, page 251. in: *Conducting Polymers Spectroscopy and Physical Properties* (C. Nalwa ed.), John Wiley and Son Ltd, 1997, p.301.
108. Clark et al., private communication.
109. W. G. Clark, K. Tanaka, S. E. Brown, R. Menon, F. Wudl, W. G. Moulton and P. Kuhns, *Synth. Met.*, 1999, **101**, 343.
110. M. Nechtschein, F. Devreux, F. Genoud, M. Guglielmi and K. Holczer, *Phys. Rev. B*, 1983, **27**, 61.
111. G. Sachs and E. Dorman, *Synth. Met.*, 1988, **25**, 157.
112. K. Mizoguchi, F. Shimizu and K. Kume, *Synth. Met.*, 1991, **41**, 185.
113. F. Shimizu, K. Mizoguchi, S. Masubuchi and K. Kume, *Synth. Met.*, 1995, **69**, 43–44.
114. C. H. Lee, Cheol Eui Lee, J. I. Jin and B. K. Nam, *Phys. Rev. B*, 1896, **1996**, 53.
115. K. J. Singh, W. G. Clark, K. P. Ramesh and M. Reghu, *J. Phys.: Condens Matter*, 2008, **20**, 465208.
116. J. Wieland, U. Haebleren, D. Schweitzer and H. J. Keller, *Synth. Met.*, 1987, **19**, 393.
117. G. Alexandrowicz, T. Tashma, A. Feintuch, A. Grayevsky, E. Dormann and N. Kaplan, *Phys. Rev. Lett.*, 2000, **84**, 2973.
118. W. Höpftner, M. Mehring, J. U. Von Schütz, H. C. Wolf, B. S. Morra, V. Enkelmann and G. Wegner, *Chem. Phys.*, 1982, **73**, 253.
119. A. Kaiser, B. Pongs, G. Fischer and E. Dormann, *Phys. Lett.*, 2001, **282**, 125.
120. W. Yu, F. Zhang, F. Zaborszky, B. Alavi, A. Baur, C. A. Merlic and S. E. Brown, *Phys. Rev. B*, 2004, **70**, 121101.



# SUBJECT INDEX

## A

Anti-ferroelectric (AFE) material, 141, 156  
Arrhenius law, 149  
Asymmetric inhomogeneous line, 144

## B

Betaine phosphate/phosphate mixed crystals  
  deuterated  
    2D deuterium NMR, 158  
    1D NMR parameters, 158  
  protonated  
    relaxation measurements, 157  
    temperature dependence, 158  
BlochLib, 100  
Bloembergen-Purcell-Pound (BPP) behaviour, 149

## C

Conducting polymers (CP)  
  charge transport  
    applications, 165  
    disorder potential, 164  
    electronic wave functions, 164–165  
    fibrillar and globular morphologies, 164  
    films, 165  
    gyro magnetic ratio, 165  
    sp<sup>2</sup> hybridized backbone, 165  
    spin dynamics methods, 166  
    VRH, 164  
  dimensionality and 1/T<sub>1</sub> vs. frequency plot, 168  
  disorder in, 163–164  
  Larmor frequency, 168–169  
  NMR theory  
    Korringa type analysis, 166–167  
    spectral density function  $f(\omega)$ , 168  
    T<sub>1</sub> data, 166  
  preparation and methods  
    NMR films, 169–170  
    organic conductors, NMR, 170–172

## D

Dipolar glasses  
  detection method, 143–144  
  deuteron exchange NMR, 1D and 2D  
    betaine phosphate/phosphate mixed  
      crystals, 156–158

K<sub>1-x</sub>(NH<sub>4</sub>)<sub>x</sub>H<sub>2</sub>PO<sub>4</sub>, 155  
RADP system, 146–150  
Rb<sub>0.7</sub>Tl<sub>0.3</sub>H<sub>2</sub>PO<sub>4</sub>, 155  
Rb<sub>1-x</sub>(NH<sub>4</sub>)<sub>x</sub>H<sub>2</sub>AsO<sub>4</sub>, 154–155  
line shape analysis, 144  
spin-lattice relaxation (SLR) studies, 144–145

## E

Edwards-Anderson order parameter ( $q_{EA}$ ), 142,  
  145–146, 148, 153–154, 163  
Electric field gradient (EFG) tensors, 144, 158  
Equivalent nuclides, molecular species  
  crystalline solids, 8  
  gases, 6–7  
  non-viscous liquids, 7  
Equivalent spin-1/2 nuclides. *See* Systems  
  magnetic resonance, 5–23  
Exchange actions and interactions  
  electrons, 5–6  
  nuclei, 6  
Exchange degeneracy, 10

## F

Fluxional molecules  
  bullvalene, 18  
  CH<sub>5</sub><sup>+</sup> cation, 17  
  cyclohexane, 18  
  PF<sub>5</sub>, 17

## G

GAMMA C++ library, 81–83

## H

Half-integer quadrupolar nuclei  
  <sup>39</sup>K QE and QCPMG spectra, 131–132  
  line broadening effect, 129–130  
  quadrupolar coupling constant, 129  
  spin-quantum number and Larmor  
    frequency, 129  
Hydrogen–deuterium exchange mass  
  spectroscopy (HXMS), 44

## K

Korringa enhancement factor ( $S_K$ ), 167  
K<sub>1-x</sub>(NH<sub>4</sub>)<sub>x</sub>H<sub>2</sub>PO<sub>4</sub>, 155

## L

- Larmor frequency, 168–169
- Lead magnesium niobates (PMN)
  - vs.* PSN,  $^{93}\text{Nb}$  and  $^{45}\text{Sc}$  NMR spectra, 161–162
  - RF Ising model (RFIM), 162
  - salient features, 160
  - structural refinement, 160–161
- Line shape analysis, dipolar glasses, 144
- Liouville-von-Neumann equation, 85, 106

## M

- Matter systems condensation
  - conducting polymers
    - charge transport, 164–166
    - disorder, 163–164
    - Larmor frequency, 168–169
    - NMR theory, 166–168
    - preparation and methods, 169–172
    - $1/T_1$  *vs.* frequency plot, 168
  - dipolar glasses
    - cusp, 141
    - definition, 141
    - detection method, 143–144
    - deuterated RADP, phase diagram, 142–143
    - deuteron exchange NMR, 1D and 2D, 145–158
    - line shape analysis, 144
    - random-fields occurrence, 141
    - spin-lattice relaxation (SLR) studies, 144–145
  - disordered systems, 140
  - relaxor ferroelectrics
    - Burns temperature, 160
    - cubic symmetry, 159
    - disordered complex perovskites, 159
    - field-cooled and zero-field cooled susceptibility, 159
    - lead magnesium niobates (PMN), 160–162
    - static and dynamic ion shifts, 160
    - strontium barium niobate (SBN), 162–163
- Molecular motion simulation. *See* Quadrupolar nuclei, 104–110, 112–124, 126, 128–134
- Molecule selection, equivalences
  - benzene
    - ground-state, 17
    - valence isomers, 16
  - cyclopropane, 17
  - fluxional molecules
    - bullvalene, 18
    - $\text{CH}_5^+$  cation, 17
    - cyclohexane, 18
    - $\text{PF}_5$ , 17
  - hydrazine, 14–15
  - methane, 14

- molecular hydrogen
  - dipole–dipole interaction, 13–14
  - magnetic properties, 12

## MR motion effects

- intermittent crystal rotations, 8–9
- internal molecular rotations and interchanges, 8
- random molecular rotations, 9
- sample rotations, 9–10

## Multi-axis jump processes

- $^2\text{H}$  MAS spectra, 126, 128

MAS *vs.* QCPMG, 129

## N

- $^{14}\text{N}$  MAS spectra dynamic effects, 123–124
- NMR disorder studies. *See* Matter systems condensation, 140–172
- NMR spectroscopy
  - biomolecular, 46–47
  - chemical shifts (CSs), 48–49
  - H–D exchange, 56–57
  - heteronuclear relaxation experiments and analysis, 52–55
  - information, 47–48
  - nuclear overhauser effect, 49
  - paramagnetic relaxation enhancement (PRE), 55–56
  - residual dipolar couplings (RDCs), 51
  - scalar couplings, 50

## P

- Paramagnetic relaxation enhancement (PRE), 55–56
- PMN. *See* Lead magnesium niobates, 160–162
- Protein dynamics
  - biological processes
    - intrinsically disordered and unfolded proteins, 66–69
    - sub- $\tau_c$  motions, 63–66
    - supra- $\tau_c$  motions, 58–63
  - exploring techniques
    - ECD and VCD spectroscopy, 43
    - electron microscopy, 43
    - hydrogen–deuterium exchange mass spectroscopy (HXMS), 44
    - molecular modelling, 45–46
    - UV fluorescence, 43–44
    - X-ray diffraction, 44–45
  - motions and time scales, 38–39
- NMR spectroscopy
  - biomolecular, 46–47
  - chemical shifts (CSs), 48–49
  - H–D exchange, 56–57

heteronuclear relaxation experiments and  
analysis, 52–55  
information, 47–48  
nuclear overhauser effect, 49  
paramagnetic relaxation enhancement  
(PRE), 55–56  
residual dipolar couplings (RDCs), 51  
scalar couplings, 50  
and structure, 39–42  
Proton and deuteron glasses  
incoherent tunnelling, 152  
local-polarization distribution, zero  
temperature, 152  
radio frequency pulse sequence, 150–151  
<sup>87</sup>Rb NMR line shape, 153  
resonance frequency distribution, 153–154  
X-bond O-D-O, 150–151

## Q

Quadrupolar Carr-Purcell-Meiboom-Gill  
(QCPMG) experiment, 105  
Quadrupolar nuclei  
dynamic effects, <sup>14</sup>N MAS spectra, 123–124  
EXPRESS simulation program, 106  
half-integer  
<sup>39</sup>K QE and QCPMG spectra, 131–132  
line broadening effect, 129–130  
quadrupolar coupling constant, 129  
spin-quantum number and Larmor  
frequency, 129  
half-integer quadrupolar nuclei, 129–134  
<sup>2</sup>H dynamics determination, 104–105  
multi-axis jump processes  
<sup>2</sup>H MAS spectra, 126, 128  
MAS *vs.* QCPMG, 129  
numerical simulations  
half-integer quadrupolar nuclei, 118–119  
parameters, 117  
spin-1 nuclei, 118  
QCPMG experiment, 105  
spin-1 nuclei  
intensity profiles, 123  
MAS and QCPMG spectra, 119–121  
<sup>14</sup>N QCPMG spectra, two-site jump process,  
121–122  
numerical simulations, 118  
theory  
2-by-2-site jump, 114–115  
2-by-3-site jump, 115–117  
density operator formalism, 106  
Dyson time-ordering operator, 107  
Liouville-von-Neumann equation, 106  
L-matrix, N-site jump, 110  
orthonormal operators, 107

spatial tensors, laboratory frame, 109  
spin-1 nuclei, 112–114  
standard Zeeman basis, 108  
two-axis jump processes, 114

## R

RADP system  
deuterated  
Edwards-Anderson spin-glass order  
parameter, 146  
Gaussian distribution, 147  
local polarization, average probability  
distribution, 147  
quantum tunnelling, 148  
protonated  
Arrhenius law, 149  
Bloembergen-Purcell-Pound (BPP)  
behaviour, 149  
proton and deuteron glass, low temperature  
properties, 150–154  
Slater-Takagi ice rules, 150  
Vogel-Fulcher law, 149  
Relaxor ferroelectrics  
Burns temperature, 160  
cubic symmetry, 159  
disordered complex perovskites, 159  
field-cooled and zero-field cooled  
susceptibility, 159  
lead magnesium niobates (PMN), 160–162  
static and dynamic ion shifts, 160  
strontium barium niobate (SBN), 162–163  
Residual dipolar couplings (RDCs), 51

## S

Solid-state NMR spectra. *See* Quadrupolar nuclei,  
104–110, 112–124, 126, 128–134  
Spectral degeneracy, 23  
Spherical random bond-random field (SRBRF)  
model, 163  
Spin Diffusion Paramagnetic Centres  
(SDPC), 170  
Spin-Hamiltonian parameters  
coupling parameters  
asymmetric matrices *Y*, 22  
entanglement, 21–22  
measurements, 22–23  
Zeeman term  
asymmetry *g*, 21  
<sup>o</sup>PH, 19–20  
situation *g* isotropic, 21  
squared parameter matrix, 20–21  
Spin-lattice relaxation, 144–145  
Spin-1 nuclei  
intensity profiles, 123

Spin-1 nuclei (*cont.*)

MAS and QCPMG spectra, 119–121

<sup>14</sup>N QCPMG spectra, two-site jump process, 121–122

numerical simulations, 118

Spin-1/2 nuclides. *See* Systems magnetic resonance, 5–23

SQ/DQ coherences, 123–124

Strontium barium niobate (SBN), 162–163

Systems magnetic resonance

equivalent nuclides, molecular species

crystalline solids, 8

gases, 6–7

non-viscous liquids, 7

exchange actions and interactions

electrons, 5–6

nuclei, 6

exchange degeneracy, 10

molecules selection, equivalences

benzene and isomers, 15–17

cyclopropane, 17

fluxional molecules, 17–18

hydrazine, 14–15

methane, 14

molecular hydrogen, 12–14

motion effects

intermittent crystal rotations, 8–9

internal molecular rotations and interchanges, 8

random molecular rotations, 9

sample rotations, 9–10

sets spin–spin interactions, distinct particles

first-order multiplets, 11

homonuclear couplings, 12

isotropic part, 10

permutation groups, 11–12

spin-Hamiltonian parameters

coupling parameters, 21–22

measurements, 22–23

spectral degeneracy, 23

Zeeman term, 19–21

## T

Two-axis jump processes, 114

## U

Uniaxial relaxors, 162–163

UV fluorescence, 43–44

## V

Variable range hopping (VRH), 164

Virtual magnetic resonance spectroscopy (MRS)

applications and implications

metabolite function uses, 91

metabolite prior information, 89

pulse sequence development, 94–99

pulse sequence optimization, 92

RF pulses and spatially varying artefacts, 92–94

spectral fitting routines, 90

BlochLib, 100

computer simulations, magnetic resonance, 99–100

GAMMA spectral simulation library, 81–83

physics to object-oriented programming

computational objects, 85

design considerations, 88–89

expectation value, 84

Liouville–von Neumann equation, 85

metabolites, 83

mixed state, 84

simulated pulse sequence coding, 85–88

PJNMR, 100

POMA, 99

SIMPSON, 100

spectral simulation techniques

definition, 78–79

GAMMA C++ library, 81–83

software overview, 80–81

SPINEVOLUTION, 100–101

virtual NMR spectrometer, 100

VRH. *See* Variable range hopping, 164

## X

X-ray diffraction, 44–45

## Z

Zeeman term

asymmetry  $g$ , 21<sup>o</sup>PH, 19–20situation  $g$  isotropic, 21

splitting parameter matrices, 4

squared parameter matrix, 20–21